

THROUGH THE MAGMA MUSH: TRACING MAGMA EVOLUTION FROM THE
MANTLE, THROUGH THE CRUST, AND TO THE SURFACE USING THE
GEOCHEMISTRY OF ERUPTED MELTS AND MINERALS

By

Christopher Svoboda

A DISSERTATION

Submitted to
Michigan State University
in partial fulfillment of the requirements
for the degree of

Geological Sciences – Doctor of Philosophy

2022

ABSTRACT

THROUGH THE MAGMA MUSH: TRACING MAGMA EVOLUTION FROM THE MANTLE, THROUGH THE CRUST, AND TO THE SURFACE USING THE GEOCHEMISTRY OF ERUPTED MELTS AND MINERALS

By

Christopher Svoboda

Studies synthesizing field work, numerical simulations, petrology, geochemistry, and geophysical observations indicate that the compositional diversity of lavas results from evolution of mantle-derived basaltic magmas by mixing, assimilation, and fractional crystallization. These studies indicate this evolution occurs within dispersed complexes called transcrustal magmatic systems, rather than tank-like magma chambers. The processes within these magmatic systems have implications for understanding the evolution of continental crust, the breakup of continental landmasses, and the hazards associated with volcanism. We present three studies in various tectonic and magmatic settings, using the geochemistry of whole rocks and minerals to relate magmatic processes within transcrustal magma systems and their inputs from the mantle to large-scale plate tectonic and geodynamic questions. In a study of magnesium-rich andesites from the Taupo Volcanic Zone, I link primitive mineral compositions in Mg-depleted melts to the growth of magma accommodation zones in a rifting segment of arc crust. Mineral constraints on temperature and pressure indicate that the plumbing system first formed at mid- to lower-crustal pressures (3.5-7.0±2.8 kbar). I interpret the mafic mineralogy and presence of disequilibrium features as evidence that these andesites and their crystal cargo represent the products of a developing magmatic system in the middle to lower crust. This study addresses the question of how magmatic systems initially form and evolve. I examine lavas from the back arc of Patagonian Argentina, where volcanism is displaced from the magmatic arc due to subduction of oceanic

spreading centers. I demonstrate using thermodynamic models that the source regions for melts contain volumes of pyroxenite (3-11%), and were generated at high pressures (2.6-2.7 GPa). These melting conditions have been consistent since the Eocene. I interpret these results as evidence of detachment of pyroxene-rich lithosphere that was created by magma-lithosphere interaction during the Mesozoic breakup of Gondwana. These results show a link between prior magmatic events the role of pyroxene-rich mantle lithologies in subsequent mantle melting episodes. Finally, I present a study that probes the evolution of late-stage magmas in the failed 1.1-billion-year-old Mid-Continent Rift that are analogous to packages of lava and sediment that are buried during the final stages of continental breakup. I present evidence showing magma mixing between primitive and evolved residual magma controls the magma composition in these lavas. The highly negative ϵ_{Hf} and ϵ_{Nd} isotopic characteristics of these magmas, supported by modeling outcomes, suggest extensive assimilation (15%) of continental crust accompanying fractional crystallization of olivine, plagioclase feldspar, and spinel at 4 kbar pressure and 1060° C. I interpret this as a renewed pulse of magma that has exploited a preexisting transcrustal magmatic system. I posit that this system had its magma supply exhausted at the end of the main stage of volcanism but remained partially molten due to residual heat from the main stage. The results of this study have implications for the persistence of these magmatic systems through time. Each individual study, while from disparate time periods and tectonic settings, demonstrates that the transcrustal magmatic system (and the transcrustal system's link to the mantle) provides a suitable conceptual framework for modeling and describing the evolution of magmas. These systems are not static but rather change with time to respond to geodynamic forces and rates of magma delivery.

I dedicate this work to the incredible foundation of personal support that I am so fortunate to have:

- my wife, Alexandria, who I love so dearly and am so grateful to for your endless support.
- my mother and father, who I want to make proud of their son.
- my angelic daughter Olive, who joined us only recently but has been such an immense source of joy and inspiration.
- my siblings by birth (Erin) and marriage (Oliver, rest in peace brother), who always kept me grounded.
- all the pets (Lola, Leon, Lucy, Loretta, Uzi), even those departed, who provided emotional support and companionship in times of darkness and despair.
- my best friends of so many years Tom Moshos, Dennis Goers, Chris Boehringer, and Danny Dancey, who have gathered with me every summer in recent memory to shake off the year's stresses.
- and my in-laws Cindy and Enrique Salfate, who have provided childcare and the hand of their daughter in marriage

All the love and support these individuals provided are what gave me the strength to carry through this seemingly insurmountable task. I am forever in your debt.

ACKNOWLEDGEMENTS

This work was financially supported by the Michigan State University Department of Earth and Environmental Sciences, the Michigan State University Graduate School, the Geological Society of America Student Research Grants (2017, 2019), the Michigan Space Grant Consortium, and National Science Foundation Grant 1549764. This work was greatly supported in myriad intellectual and physical ways by all members of my research group through many years. These include but are not limited to Andrew LaVigne, Brandon Chiasera, Susan Krans, Alex Steiner, Jacob Bonessi, Madison Kortas, Mariah Bennett, and (William) Ray Davis. I am grateful to my dissertation committee members Allen McNamara, Susannah Dorfman, and Michael Velbel, who have provided me with support and guidance both individually and as a group. Finally, this work would have been impossible without the patience and mentorship of my advisor Dr. Tyrone Rooney. Thank you all.

TABLE OF CONTENTS

LIST OF TABLES	ix
LIST OF FIGURES	x
1. INTRODUCTION.....	1
BIBLIOGRAPHY	6
2. TRANSCRUSTAL MAGMATIC SYSTEMS : EVIDENCE FROM ANDESITES OF THE SOUTHERN TAUPO VOLCANIC ZONE	10
2.1 Introduction	10
2.2 Geological Setting	13
2.3 Samples.....	18
2.4 Methods	18
2.5 Results.....	20
2.5.1 Petrography	20
2.5.2 Major Elements: Whole Rocks, Groundmass Glasses, and Interstitial Melts	25
2.5.3 Trace Elements: Whole Rocks, Groundmass Glasses, and Interstitial Melts	27
2.5.4 Mineral Geochemistry	30
2.6 Discussion	33
2.6.1 Evolution of Arc Magmas in Deep Crustal Hot Zones.....	33
2.6.1.1 Crystallization at Ohakune.....	35
2.6.1.2 Mineral Transport and Entrainment at Ohakune	36
2.6.1.3 Contamination at Ohakune	37
2.6.1.4 Pressure and Temperature Constraints on the Ohakune Magma Plumbing System.....	39
2.6.1.5 Synthesis	43
2.6.2 Maturation of Hot Zones into Transcrustal Magmatic Systems	46
2.7 Conclusions	48
BIBLIOGRAPHY	50
3. IMPLICATIONS OF PYROXENITE IN THE SOURCE OF CENOZOIC (EOCENE- RECENT) MAGMATISM IN THE TRIPLE JUNCTION PROVINCE OF PATAGONIAN ARGENTINA.....	56
3.1 Introduction	56
3.2 Geologic Background	58
3.2.1 Cenozoic Magmatism in the Andean Arc and Back Arc.....	58
3.2.2 Ridge-Trench Interaction and Patagonian Slab Windows	63
3.2.3 Tectonic and Magmatic History of the Deseado Massif	64
3.3 Materials and Methods	66
3.3.1 Samples	66
3.3.2 Whole Rock Major & Trace Elements.....	69
3.3.3 Ar-Ar Isotopic Dating.....	70

3.4 Results	73
3.4.1 Petrography	73
3.4.1.1 La Angelita (Plio-Pleistocene)	73
3.4.1.2 Cerro Mojon (Miocene-Pliocene).....	78
3.4.1.3 Basalto de las Lagunas sin Fondo (Mid-Miocene).....	78
3.4.1.4 Basalto Alma Gaucha (Early Miocene)	78
3.4.1.5 Cerro del Doce (Eocene)	79
3.4.1.6 Summary of Petrographic Observations.....	80
3.4.2 Ar-Ar Isotopic Dating.....	80
3.4.3 Major Element Whole Rock Chemistry	85
3.4.3.1 La Angelita (Plio-Pleistocene)	85
3.4.3.2 Cerro Mojon (Miocene-Pliocene).....	90
3.4.3.3 Basalto de las Lagunas sin Fondo (Mid-Miocene).....	90
3.4.3.4 Basalto Alma Gaucha (Early Miocene).....	91
3.4.3.5 Cerro del Doce (Eocene)	91
3.4.4 Whole Rock Trace Element Geochemistry.....	92
3.4.4.1 La Angelita (Plio-Pleistocene)	96
3.4.4.2 Cerro Mojon (Miocene-Pliocene).....	98
3.4.4.3 Basalto de las Lagunas sin Fondo (Mid-Miocene).....	98
3.4.4.4 Basalto Alma Gaucha (Early Miocene).....	99
3.4.4.5 Cerro del Doce (Eocene)	99
3.4.5 Unconstrained Samples	99
3.5 Discussion	101
3.5.1 The Effects of Crustal Contamination on Patagonian Triple Junction Province Magmas.....	101
3.5.2 The Temporal Progression of Triple Junction Province Magmatism Relative to Slab Windows.....	106
3.5.3 Estimation of Mantle-Equilibrated Primary Magmas using PRIMACALC2 ...	109
3.5.4 Exploring Adiabatic Mantle Melting of Patagonian Back Arc Basalts using Ocean Basalt Simulator version 1 (OBS-1)	114
3.5.5 Dripping Pyroxenite in the Source of Eocene-Recent Patagonian Triple Junction Province Magmas.....	125
3.6 Conclusions	128
BIBLIOGRAPHY	130
4. FRACTIONAL CRYSTALLIZATION AND CRUSTAL CONTAMINATION: EVOLUTION OF LATE-STAGE MAGMAS FROM THE PORCUPINE MOUNTAINS IN THE 1.1 GA MID-CONTINENT RIFT	138
4.1 Introduction	138
4.2 Geologic Background	141
4.2.1 Defining the Mid-Continent Rift	141
4.2.2 Structural and Magmatic Evolution of the Mid-Continent Rift	143
4.2.2.1 Mid-Continent Rift Development Prior to Initiation of Magmatism	143
4.2.2.2 Extent and Timing of Magmatism of the Keweenaw Large Igneous Province	144
4.2.3 The Porcupine Mountains Volcanic Complex.....	148

4.2.4 Temporal Constraints on Portage Lake and Porcupine Mountains Volcanism	152
4.3 Materials and Methods	153
4.3.1 Samples	153
4.3.2 Whole Rock Major & Trace Elements.....	154
4.3.3 Isotopes.....	154
4.4 Results.....	155
4.4.1 Petrography	155
4.4.1.1 Lake of the Clouds Basalts & Fe-Ti Basalts.....	155
4.4.1.2 Granophyres	156
4.4.1.3 Rhyolites	156
4.4.2 Major Elements.....	156
4.4.2.1 Lake of the Clouds Basalts	156
4.4.2.2 Granophyres	159
4.4.2.3 Fe-Ti Basalts	159
4.4.2.4 Lower Type 1 Rhyolites	159
4.4.2.5 Upper Type 2 Rhyolites	160
4.4.3 Trace elements.....	160
4.4.3.1 Lake of the Clouds Basalts	160
4.4.3.2 Granophyres	165
4.4.3.3 Fe-Ti Basalts	165
4.4.3.4 Lower Type 1 Rhyolites	166
4.4.3.5 Upper Type 2 Rhyolites	166
4.4.4 Isotopes.....	166
4.4.5 Alteration	168
4.5 Discussion	170
4.5.1 Magmatic Pulses Evident in the Porcupine Mountains & Inferences from the Volcanic Stratigraphy.....	170
4.5.2 Formation of Porcupine Mountains Rhyolites	171
4.5.3 Assimilation and Fractional Crystallization in the Genesis of the Porcupine Mountains Volcanics Fe-Ti Basalts	172
4.5.3.1 Comparison to Group 5 at Mamainse Point	172
4.5.3.2 Trace Element REAFC/AFC/FC Modeling Rationale and Procedure	174
4.5.3.3 Modeling Outcomes & Implications for Rift Volcanism	182
4.5.4 The Genesis and Evolution of the Lake of the Clouds Basalts	184
4.5.4.1 The Lake of the Clouds Magmatic Pulse.....	184
4.5.4.2 Modeling Procedure	185
4.5.4.3 Modeling Results	186
4.5.4.4 Modeling Conclusions & Synthesis.....	189
4.5.4.5 Implications of Different Assimilants Used in Modeling Outcomes	190
4.5.5 Porcupine Mountains Volcanic Complex and the Local Cessation of Main Stage Volcanism.....	194
4.6 Conclusions	197
BIBLIOGRAPHY	200
5. CONCLUSION AND SYNTHESIS	206
BIBLIOGRAPHY	209

LIST OF TABLES

Table 3.1 Table summarizing results of $^{40}\text{Ar}/^{39}\text{Ar}$ sample dating for the Patagonian Triple Junction Province magmas collected in this study. Apparent eruption ages range from 2.52-40.18 Ma. Maximum eruption ages are given as the lowest single step age from $^{40}\text{Ar}/^{39}\text{Ar}$ results.....	82
Table 3.2 Table summarizing the results of PRIMACALC2 modeling simulations to back correct for olivine fractionation and establish Primary magma compositions. Sample names have had the 0000 between the TOR and the -## omitted and replaced with a dash (-) to save space. F% is percent partial melt; %XFrac represents the weight percent of olivine that has been added back into the primary melt; P is pressure; TWC is wet temperature in °C; TDC is dry temperature in °C; $\text{Fe}^{2+}/\text{Fe}^T$ is the calculated percentage of Fe in the 2+ oxidation state over the total Fe in the sample; MgO PM is the weight percent of MgO calculated for the mantle in equilibrium with the sample. $(\text{La}/\text{Sm})_N$ from non-corrected magmas is shown for a comparison to predicted F%.....	112
Table 3.3 Table summarizing the result of OBS1 simulations on Patagonian triple junction province melts that were first back corrected in PRIMACALC2 to reflect equilibrium with the mantle. Melting models are melt metasomatism (T) and melt-melt mixing (X), discussed in text.	122
Table 4.1 Trace elements considered in the constant mass REAFC model, with explanation for their incorporation.....	176
Table 4.2 Run conditions and compositions used in the various REAFC/AFC/FC models to describe the evolution of the Fe-Ti basalts. For assimilant compositions, (a) indicates that the value used is the average of three granite gneisses presented in Seifert et al., 1992 while (b) indicates that the value used is the leucosome of Steiner, 2014. For REAFC, the starting magma and recharging magma are the same composition.	178

LIST OF FIGURES

Figure 1.1 A schematic diagram of a generalized transcrustal magmatic system illustrating the various parts of the overall system that are investigated in this dissertation. The figure is not drawn to scale. The green areas in the mantle melting region represent pyroxenite pods3

Figure 2.1 Study location and geologic setting of the Taupo Volcanic Zone (TVZ) of New Zealand. (a) GeoMapApp DEM base map of the North Island of New Zealand. Black outline shows the modern boundary of the TVZ, an actively extending rifting arc. Rifting is driven by oblique subduction of oceanic crust from the west that meets the North Island at the Hikurangi trench (barbed line; barbs shown on overriding plate). The direction and velocity of subduction is shown by the arrow in the lower right. The TVZ is segmented into three distinct zones: a central rhyolite producing, caldera forming region flanked to the northeast and southwest by andesite producing zones. The approximate zones of these boundaries are shown by the dashed black lines. (b) Area inset from red box in (a). The major Quaternary andesite-producing volcanoes of the Togariro Volcanic center are shown, with the edifices discussed in this study highlighted. Ruapehu is one of the central stratovolcanoes in the southern andesite zone along with Tongariro and Ngauruhoe. Ohakune and Pukeonake are satellite vents. Names used consistent with Price et al. (2012) and Beier et al. (2017), and references therein.15

Figure 2.2 Plot of Mg# ($100 \times \text{molar Mg}/(\text{Mg}+\text{Fe})$ with total Fe) vs SiO₂ of High-Mg andesites and dacites (HMAD) magmas from Ruapehu and around the Taupo Volcanic Zone (colored squares and diamonds), compared with other non-HMAD eruptive products from the stratovolcano Ruapehu (gray diamonds). Data from Fig. 1B of Conway et al. 2020.16

Figure 2.3 Representative images of petrographic phases and textures observed in Ohakune andesites, views all in crossed polars. (a) A blackened (oxidized) and embayed olivine surrounded by a rim of ortho- and clinopyroxene. (b) An embayed (non-oxidized) olivine exhibiting corona texture next to a 1mm single crystal of clinopyroxene. (c) Abundant embayed olivine with various-sized orthopyroxene coronae. (d) A radiating rosette-shaped glomerocryst of clinopyroxene and orthopyroxene set in a groundmass of clinopyroxene + plagioclase microlites. (e) Irregular clinopyroxene and orthopyroxene glomerocryst with an interstitial glass at the center of the glomerocryst. Image also shows vesicularity typical of Ohakune scoriae. (f) Disaggregated quartzite xenolith.....22

Figure 2.4 (a) Representative backscattered scanning electron microscope of a clinopyroxene (medium gray) and orthopyroxene (darker gray) glomerocryst from Sample 5021D. Note the thin light gray area rimming the exterior of the pyroxenes of this glomerocryst. This is due to Fe-rich rims. We interpret these rims as evidence of brief storage in an Mg poor magma chamber prior to eruption. Inset area at bottom left of (a) has had contrast and levels digitally adjusted to show the Fe-rich rims more clearly. (b) Photomicrograph of 5021A clinopyroxene and orthopyroxene glomerocryst in crossed polar view. Red and blue dots indicate laser ablation sites of crystal types as indicated in the legend. Analyses with red boxes have Lo-Al chemical signature.....24

Figure 2.5 Major element X-Y bivariate diagrams of Ohakune whole rocks (circles), groundmass glasses (squares), and interstitial glasses (crosses). Orange circles and diamonds are whole rocks and melt inclusions respectively from the Pukeonake edifice for comparison (Beier et al. 2017).

Black arrows in the first two panels (SiO_2 vs. MgO and Al_2O_3) show postulated mineral accumulation trends.....26

Figure 2.6 CI chondrite (Sun and McDonough 1989) normalized rare earth element (REE) concentrations of Ohakune whole rocks, groundmass glasses, and interstitial glasses (left frames), as well as REE concentrations of pyroxenes collected during this study (right frames). Also shown are REE patterns for the Te Herenga Formation (Conway et al. 2018). Shaded gray regions indicate the overall range of compositions in Ohakune samples28

Figure 2.7 Primitive mantle (Sun and McDonough 1989) normalized trace element abundance diagrams for whole rocks, groundmass glasses, interstitial glasses, and all analyses superimposed. The bottom two frames also show trace element patterns for Te Herenga Formation andesites of Ruapehu (Conway et al. 2018). Shaded gray regions indicate the overall range of compositions in Ohakune andesites29

Figure 2.8 X-Y bivariate diagrams showing olivine Fo vs. Ni and Ca. Included on these diagrams for comparison are global datasets (e.g. MORB olivine from Table S2A of Sobolev et al. (2007) and references, and arc olivine collated from GEOROC; see Supplemental Document 3, Tables C1 & C2 for full data and sources). Ohakune olivine fall into the low-Ca field defined by arc olivine. Also shown is the average of three analyses of San Carlos olivine (cyan diamond) showing the composition of mantle olivine31

Figure 2.9 Selected major and minor element bivariate X-Y diagrams of ortho- and clinopyroxenes in Ohakune andesites. Cyan open circles represent high-aluminum orthopyroxenes, while navy open circles represent low-aluminum orthopyroxenes. Red rectangles represent high-aluminum clinopyroxenes, while yellow rectangles represent low-aluminum clinopyroxenes32

Figure 2.10 Diagram showing pressure and temperature constraints provided by thermobarometry modeled from pyroxene compositions using the spreadsheet and equations of Putirka (2008, 2015). Samples have been subdivided based on Lo-Al and Hi-Al crystal pairs, although we find no systematic differences between the two groups other than a wider spread of predicted temperatures for the Hi-Al group. Pressure is constrained using Equation 39 of Putirka (2008), while temperature is constrained using Equation 36 in the same work. Error on the estimates of temperature are $\pm 38^\circ\text{C}$ and estimates of pressure are ± 2.8 kbar (Putirka 2008); error bars are shown in the center of the figure to represent the uncertainty of the temperature and pressure estimates on each clinopyroxene-orthopyroxene pair.41

Figure 2.11 Diagrammatic figure (not to scale) that indicates the processes active in the Ohakune hot zone from the mantle to the surface.45

Figure 3.1 Overview map of Patagonia (South America) showing important tectonic and magmatic features. The purple lines represent plate boundaries such as the Chile Rise oceanic spreading center and the Chile Trench. Earthquakes are represented by yellow circles (Global Catalog of Earthquakes - Humanitarian Data Exchange (USGS ANSS Comprehensive Catalog)), while Holocene and Pliocene volcanoes are shown as red triangles (Smithsonian Institution & Venzke, 2013a, 2013b). The location and ages of Cenozoic lavas are shown by the colored

polygons (Gómez et al., 2019). The names of each of the Cenozoic back-arc magmatic provinces are shown in italicized text. Dashed areas show the approximate boundaries of the two Patagonian massifs, the Deseado and Somun Cura (Ramos, 2008). The area of this study is located within the Deseado Massif; see Figure 3.2.....60

Figure 3.2 Map of the study area showing the extent of Cenozoic and Mesozoic magmatic rocks in the Deseado Massif, Santa Cruz province, Argentina. Colored areas represent the full extent of mapped lava flows from each unit, and circles indicate individual sampling locations. Mesozoic units are shown here to illustrate how closely associated Cenozoic magmatic units are in space with these Mesozoic volcanics. Inset shows the extent of this mapped area in South America. Base imagery is Google satellite imagery.68

Figure 3.3 Photographs of various mineral phases and textures observed in Patagonian Triple Junction province magmas. Scale bars are shown in the bottom left of individual images. (A) La Angelita sample TOR0000TH in cross polarized light (XPL) showing olivine and plagioclase feldspar phenocrysts, as well as a rounded pyroxene nodule. Scale bar 500 μm . (B) Vesicular La Angelita sample TOR0000TM in XPL showing rounded pyroxene nodule. Scale bar 500 μm . (C) Cerro Mojon sample TOR0000TF in XPL showing olivine phenocrysts and coarse feldspar groundmass. Scale bar 500 μm . (D) Cerro Mojon sample TOR0000TD in XPL showing feldspar-rich sample with no phenocryst olivine. Scale bar 1 mm. (E) Basalto de las Lagunas sin Fondo (BLSF) sample TOR0000U2 in XPL showing two subsets of olivine crystals. One subset is small, altered crystals, and the other subset is larger fresh crystals. Also of note is the extremely fine-grained groundmass which is characteristic of BLSF flows in this study. Scale bar 200 μm . (F) Basalto Alma Gaucha sample TOR0000TT in plane polarized light (PPL) showing pink titaniferous groundmass augite. Scale bar 200 μm . (G) Cerro del Doce sample TOR0000U7 in PPL showing green & gray pyroxene and clear olivine. Scale bar 500 μm . (H) Same field of view as (G), but in XPL. Scale bar 500 μm . (I) Cerro del Doce sample TOR0000UA in PPL showing brown-pink titaniferous pink groundmass pyroxene, and also altered olivine. Scale bar 200 μm . (J) Cerro del Doce sample TOR0000U8 in XPL showing spinel inclusions within olivine. Scale bar 200 μm . (K) Cerro del Doce sample TOR0000U0 in XPL showing clinopyroxene nodule. Note oscillatory zoning of the large pyroxene that forms the bulk of the nodule. Scale bar 200 μm . (L) Cerro del Doce sample TOR0000U9 in XPL showing feldspar nodule. Scale bar 200 μm75

Figure 3.4 Column showing the stratigraphic sequence of sampled Alma Gaucha basalts. Below the sample names are the phases observed petrographically and the mineral proportions by volume (Ol = olivine, Pl = plagioclase feldspar). Also shown are major element oxides MgO, CaO, and Al₂O₃ in weight percent to illustrate how these elements change throughout the section, reflecting crystallization of Mg-rich olivine and Ca-rich plagioclase feldspar.79

Figure 3.5 Isotopic spectra showing graphical results of ⁴⁰Ar/³⁹Ar dating for Patagonian Triple Junction Province magmas83

Figure 3.6 Bivariate total alkali silica diagram, where total alkali is major element oxides Na₂O+K₂O. Data from all Holocene volcanic centers in the Patagonian Triple Junction province shown (Gorring & Kay, 2001).87

Figure 3.7 Bivariate diagrams of major element oxides vs. MgO in weight percent for Patagonian Triple Junction province magmas. Data from all Holocene volcanic centers in the Patagonian Triple Junction province shown (Gorring & Kay, 2001).89

Figure 3.8 Rare earth element concentrations normalized to CI Chondrite (McDonough & Sun, 1995) for Triple Junction Province Patagonian magmas. Promethium (Pm) is not found in terrestrial rock samples, but laboratory convention is to include it on these diagrams to remove an abrupt jump from Sm to Nd. The interpolated Pm values are calculated as the geometric mean of adjacent chondrite-normalized values of elements Nd and Sm. The gray fields represent the entire dataset from maximum to minimum extremes.93

Figure 3.9 Bivariate diagram showing $(La/Sm)_N$, or CI Chondrite-normalized (McDonough & Sun, 1995) lanthanum over samarium concentrations, vs $(Tb/Yb)_N$ for the various Patagonian Triple Junction Province magmas. This diagram is another way to visualize the slope of rare earth element diagrams (Figure 3.8, above) and shows the relative REE slopes of various groups. $(La/Sm)_N$ represents the overall rare earth element slope, which is sensitive to partial melting percentage; $(Tb/Yb)_N$ shows the heavy rare earth element slope, which is sensitive to garnet in the mantle.. Because $(La/Sm)_N$ can be sensitive to fractional crystallization, this ratio is also shown plotted vs. MgO. There is some correlation of $(La/Sm)_N$ with MgO, especially in the Eocene Cerro del Doce groups. However, because only the highest-MgO samples were chosen for modeling, the effects of crystallization changing the ratio are not important when considering mantle melting.95

Figure 3.10 Trace element spider diagram showing elemental concentrations normalized to pyrolite or Primitive Mantle (PM) (McDonough & Sun, 1995) for the various Patagonian Triple Junction Province magmas. The gray fields represent the entire dataset from maximum to minimum extremes. Also shown for comparison are the dated magmas from Gorring & Kay (2001).97

Figure 3.11 Bivariate plots showing trace element concentrations and ratios that are associated with crustal contamination, after Sjøger et al. (2013). UCC is upper continental crust and LCC is lower continental crust. These values are based on those recommended for these reservoirs in Rudnick et al. (2003). OIB and N-MORB are shown for comparison of Patagonian melts with uncontaminated reservoirs; compositions for these two mantle end members are derived from those given in Sun and McDonough (1989). Arrows indicate possible contamination vectors. Also shown are the three continental contamination indicators versus MgO to rule out variation of these elements due to fractional crystallization.103

Figure 3.12 OBS1 trace element spider profile (normalized to primitive mantle of Sun & McDonough, 1989) of sample TOR0000TE (Cerro Mojon, Mio-Pliocene) using the pyroxenite composition G2, considered a successful fit and therefore a possible solution. Slope on heavily incompatible elements (the right side of the diagram) was considered a critical constraint on the success of the fit. The dark blue line represents the melt calculated by OBS1 because of mixing the three end members in user-specified proportions: PYROX, green (in this instance the G2 pyroxenite composition of Brown et al. (2020)); PERI_2, bright blue, which represents the primitive or previously unmelted mantle; and PERI_1, yellow, which represents the depleted

mantle component. The pink line represents the measured composition of the lava. Elements are displayed as concentrations divided by primitive mantle (PM); in this case PM values are from (Sun & McDonough, 1989).....119

Figure 3.13 Monte Carlo simulation fitting window from OBS1 that was the second control on successful fit for elements. The view has been split into two to fit within the width constraints of this document. 25/26 elements match between the observed and the simulated melt. In this case K was slightly outside of the window of success at 32.2 of an acceptable 30 relative deviation % limit. However, considering the low percentage relative deviation (RD%) for the right side of the diagram (i.e., the bottom row of elements in the figure; also, the most incompatible) we considered the slight mismatch excess of 2.2% relative deviation on the element potassium to be within acceptable tolerances.....121

Figure 4.1 Gravity (A) and magnetic (B) anomaly maps of the Midwest region of the United States of America defining the extent of the Mid-Continent Rift (MCR). The Fort Wayne Rift (FWR) structure and East Continent Gravity High (ECGH) structure are considered by S. Stein et al. (2018) to be extensions of the mid-continent rift. Black arrow in each figure points to this study's geographic area in northern Michigan. Figures modified from S. Stein et al. (2018),.....142

Figure 4.2 Map of the Lake Superior region showing the various locations where MCR/Keweenawan magmatic rocks are exposed. Red areas represent reversed magnetic polarity, while blue areas represent normal polarity. Figure modified from Swanson-Hysell et al. (2014).
.....146

Figure 4.3 Geologic map of the Porcupine Mountains volcanic complex. Colored regions indicate the mapped extent of each unit from Cannon et al. (1995), while the points represent the sampling sites of rocks described in this study. This map figure was initially created by Jacob Bonessi and modified by Chris Svoboda for use in this document. Lake of the Clouds basalt, Fe-Ti Basalt, and Upper & Lower Rhyolite are designations from this study. Inset map in upper right-hand corner shows Google Earth aerial imagery of the Lake Superior region, and the red square indicates the extent of the map area shown.....149

Figure 4.4 Stratigraphic column showing the various igneous and sedimentary rock units in the Porcupine Mountains. Developed from the map of Cannon et al. (1995)......151

Figure 4.5 Bivariate diagrams of major element oxides vs. MgO in weight percent for Porcupine Mountains volcanics samples. Sample group abbreviations in key are as follows: Fe-Ti = Fe-Ti basalts; LT1R = Lower Type 1 rhyolite; GRN = Granophyre; PLV = Portage Lake Volcanics; LOC = Lake of the Clouds basalts; UT1R = Upper Type 2 rhyolite. These abbreviations will be used consistently among all figures in this paper to identify these groups. FeO shown is Fe²⁺ and represents 85% of FeO^T.....158

Figure 4.6 Rare earth element (REE) diagrams showing concentrations of REE in Porcupine Mountains magmas normalized to chondrite (Boynton, 1984). The element Pm is not found in nature and its value in this figure represents the geometric mean of the adjacent elements Nd & Sm.....161

Figure 4.7 Bivariate diagram showing Eu/Eu^* (measured/interpolated Eu) vs. MgO and Sr for Porcupine Mountains magmas.162

Figure 4.8 Trace element spider diagrams showing concentrations of incompatible trace elements in Porcupine Mountains magmas normalized to the Primitive Mantle (Sun & McDonough, 1989).
.....163

Figure 4.9 Plot of chondrite-normalized La/Yb vs chondrite-normalized Tb/Yb in Porcupine Mountains volcanic rocks (samples labeled with prefix A). Shown for comparison are Mamainse Point Volcanic Group magmas; Types 5a, b, and c (grp. B samples in legend) are divided to show similarities between these groups remaining Mamainse Point magmas are undivided. Evolved rocks from the Porcupine Mountains are not shown on this plot as mineral phases can affect these elements.....164

Figure 4.10 Bivariate diagrams showing chondrite-normalized La/Sm and Tb/Yb vs. MgO in all Porcupine mountains volcanic rocks. These elemental ratios in Lake of the Clouds basalts and Fe-Ti basalts do not co-vary with MgO , indicating that these ratios are not altered by fractional crystallization. We observe a large spread in $(La/Sm)_{CN}$ and $(Tb/Yb)_{CN}$ in the rhyolites (LT1R and UT2R).....165

Figure 4.11 Age-corrected ($i =$ initial at 1100 Ma) isotopic results (Hf , Nd) for Porcupine Mountains magmatic rocks (samples with prefix A in the legend). Mamainse Point formation samples (those with prefix B in the legend) shown for reference. Groups 5a, 5b, and 5c of the Latent Stage at Mamainse Point are selected for comparison and remaining Mamainse Point isotopes are shown but are undifferentiated. Shown for reference is the Mantle Array (Chauvel et al., 2008). The precise compositions of the end members given here (plume, continental crust, and the depleted mantle (DM)) are not well constrained and they are therefore illustrated as gray hexagons representing this uncertainty. Isotope end members from Rooney et al., 2022.....167

Figure 4.12 Trace element spider diagram that shows similarities between Group 5c basalts from Mamainse Point and the Fe-Ti basalts from the Porcupine Mountains.173

Figure 4.13 Results of trace element magma evolution simulations for magmas TOR00005E, TOR00005G, and TOR0000JZ. Legend entry abbreviations are as follows: REAFC = Recharge, evacuation, assimilation, fractional crystallization (blue line); AFC = assimilation-fractional crystallization (orange line); FC = fractional crystallization (green line); Assim = Assimilation (pure mixing between parental magma and assimilant; red line). High- MgO sample TOR00005E in the first set of plots is omitted from further diagrams.181

Figure 4.14 Results of trace element magma evolution simulations showing a possible solution using TOR00008D as the parental and recharging magma, and the leucosome granitoid melt liquid composition of Steiner (2014) as the assimilant. Legend entry abbreviations are as follows: REAFC = Recharge, evacuation, assimilation, fractional crystallization (blue line); AFC = assimilation-fractional crystallization (orange line); FC = fractional crystallization (green line);

Assim = Assimilation (pure mixing between parental magma and assimilant; red line). User specified mineral in the second header column is spinel.....188

1. INTRODUCTION

Volcanism is a fundamental physical process observed on Earth that impacts human civilization and is part of the long-term evolution of Earth. Volcanism is linked to convective flow in the Earth's solid mantle (Bercovici 2003; Schmerr et al. 2010). It is also commonly associated with plate boundaries and plate tectonics. Beneath a volcano, volumes of mantle material partially melt at depth; melts percolate upwards through the mantle; they are then stored in the crust and react with their surroundings before eventually reaching the surface at a vent (Ito and Mahoney 2005; Weyer and Ionov 2007; Cashman et al. 2017). Therefore, a consensus has recently emerged that volcanoes of all scales and settings sit at the top of a vertically extensive column of magma mush, i.e., melts and solids, that spans from the mantle, through the crust where the magmas evolve, and to the surface (Bachmann et al. 2007; Price et al. 2012; Cashman et al. 2017; Ganne et al. 2018; Davis et al. 2021).

Because magmatic columns spanning the crust and mantle often form and evolve on geologic timescales (i.e., tens of thousands to millions of years), it is impossible make observations and interpretations of these processes based only on geophysical methods (Conway et al. 2016; Cashman et al. 2017). Recent studies have examined the geochemical characteristics of erupted lavas, their mineral cargo, and relict intrusive complexes within the context of this model to determine the processes active in these mush columns (Walker et al. 2015; Ganne et al. 2018; Bachmann and Huber 2019; Conway et al. 2020). Geochemical studies can therefore be used to infer the evolutionary systematics of these columns. These inferences can inform models for the evolution of continents, plate tectonics, supercontinent cycles, and predicting geologic hazards (Condie 1998; Gamble et al. 2003; Nance and Murphy 2013; Garnero et al. 2016; Stein et al. 2018).

This dissertation presents an examination of processes within magmatic columns at various sites and scales using geochronological, petrographic, major element, trace element, and isotopic geochemical data from lavas and minerals. Our investigations focus on three separate field sites, presented in order of their chapters in this dissertation: (1) the Taupo Volcanic Zone, which is an actively rifting arc on the north island of New Zealand (Harrison and White 2004); (2) the back-arc magmatic province of the Deseado Massif in Argentina that has a history of 40 million years of periodic low-volume magmatism throughout the Cenozoic (Kay et al. 2004); and (3) the failed billion-year old North American Mid-Continent Rift (Stein et al. 2018).

Each chapter of this dissertation probes a different part of the magmatic column from crust to mantle: chapter two probes the deep mafic roots of the transcrustal magmatic system; chapter three examines the connection of the magmatic system with the mantle; and chapter four examines the interface of an evolved, long-lived transcrustal system with the surrounding wall-rock. Within the crust, this column can be thought of as a series of sills and dikes holding and transmitting magmas in various levels of crystallinity, but where large-volume melt lenses that are typically thought of as magma chambers are absent (Solano et al. 2012; Cashman et al. 2017; Bachmann and Huber 2019). In the mantle, the column is a heterogeneous, veined volume of plutonic/metamorphic rock where some minerals & lithologies (e.g., pyroxene, pyroxenite rock) can melt preferentially (Morgan 2001; Kogiso et al. 2004; Tackley 2008). A 2-D schematic diagram of a transcrustal magmatic system with the various portions of the system investigated is shown below in Figure 1.1.

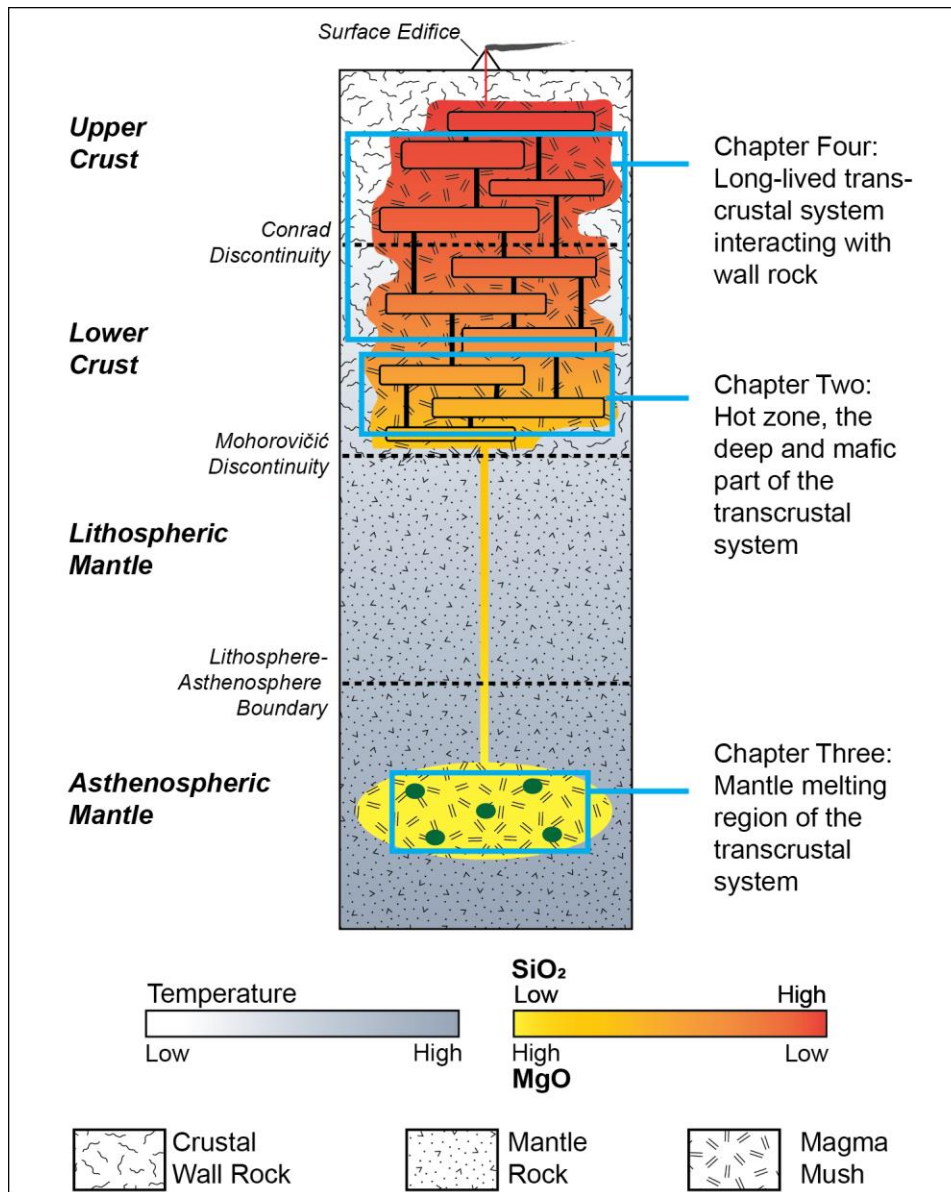


Figure 1.1

A schematic diagram of a generalized transcrustal magmatic system illustrating the various parts of the overall system that are investigated in this dissertation. The figure is not drawn to scale. The green areas in the mantle melting region represent pyroxenite pods.

In chapter two focusing on the Taupo Volcanic Zone, I probe the southward propagation of magmatism in the rift and provide insights into the growth and evolution of expanding magmatic plumbing systems. These insights can be applied to interpretations of other rifting and subducting

volcanic environments. In chapter three I investigate the lithological and physical characteristics of the magma source region to link melting with the presence of pyroxenite heterogeneity, which is implicated in the source of some basalts globally (Sobolev et al. 2007; Brown and Leshner 2014; Brown 2020). Chapter four focuses on magmatic evolution within a developed magmatic system at the termination of magmatism in the Proterozoic Mid-Continent Rift, and the implications of these observations in the process of continental breakup that cannot be observed elsewhere (McDermott et al. 2018; Stein et al. 2018).

I apply modern numerical tools to constrain physical properties and elucidate evolutionary pathways of the magmatic systems I investigate. These numerical tools include: mineral thermometers and barometers that can be used to infer the depth and extent of crystallization and plumbing systems (Putirka 2008); forward mantle melting simulations that constrain pressure, temperature, and compositional characteristics of magma source regions (Kimura and Kawabata 2015); forward models that thermodynamically constrain the stable phase assemblages along crystallization paths of a magma (Gualda and Ghiorso 2015); inverse models that calculate the composition of magmas last in equilibrium with the mantle (Kimura and Ariskin 2014); and models that simulate the combined effects of magma recharge, eruption, crystallization, and assimilation in an evolving magma system at a given depth in the crust (Lee et al. 2014). Furthermore, I use these models to synthesize and build upon the existing literature from these areas and then integrate these results into a global tectonic and geodynamic context. For example, the results of the numerically modeled geochemical data can be compared to geophysical observations at modern rifting & subducting volcanic margins. Similarly, the physical constraints these models provide can be compared to field-scale observations in other parts of the same province (e.g. the Lake of the Clouds results can be compared to observations of the Duluth

complex in the Mid Continent Rift) or at exposed analogs of relict or extinct systems (e.g. the depths of the hot zone can be compared to physical measurements of depths in exposed, uplifted magma plumbing systems in subduction zones). Finally, I propose new mechanisms to explain debated phenomena at these field sites.

BIBLIOGRAPHY

BIBLIOGRAPHY

- Bachmann, O. and Huber, C. 2019. The inner workings of crustal distillation columns; the physical mechanisms and rates controlling phase separation in silicic magma reservoirs. *Journal of Petrology*, **60**, 3–18.
- Bachmann, O., Miller, C.F. and de Silva, S.L. 2007. The volcanic–plutonic connection as a stage for understanding crustal magmatism. *Journal of Volcanology and Geothermal Research*, **167**, 1–23, <https://doi.org/10.1016/j.jvolgeores.2007.08.002>.
- Bercovici, D. 2003. The generation of plate tectonics from mantle convection. *Earth and Planetary Science Letters*, **205**, 107–121, [https://doi.org/10.1016/S0012-821X\(02\)01009-9](https://doi.org/10.1016/S0012-821X(02)01009-9).
- Brown, E.L. 2020. Markov chain Monte Carlo inversion of mantle temperature and source composition, with application to Reykjanes Peninsula, Iceland. *Earth and Planetary Science Letters*, 15.
- Brown, E.L. and Leshner, C.E. 2014. North Atlantic magmatism controlled by temperature, mantle composition and buoyancy. *Nature Geoscience*, **7**, 820–824.
- Cashman, K.V., Sparks, R.S.J. and Blundy, J.D. 2017. Vertically extensive and unstable magmatic systems: A unified view of igneous processes. *Science*, **355**, eaag3055, <https://doi.org/10.1126/science.aag3055>.
- Condie, K.C. 1998. Episodic continental growth and supercontinents: a mantle avalanche connection? *Earth and Planetary Science Letters*, **163**, 97–108.
- Conway, C.E., Leonard, G.S., Townsend, D.B., Calvert, A.T., Wilson, C.J., Gamble, J.A. and Eaves, S.R. 2016. A high-resolution $^{40}\text{Ar}/^{39}\text{Ar}$ lava chronology and edifice construction history for Ruapehu volcano, New Zealand. *Journal of Volcanology and Geothermal Research*, **327**, 152–179.
- Conway, C.E., Chamberlain, K.J., Harigane, Y., Morgan, D.J. and Wilson, C.J. 2020. Rapid assembly of high-Mg andesites and dacites by magma mixing at a continental arc stratovolcano. *Geology*, **48**, 1033–1037.
- Davis, W.R., Collins, M.A., Rooney, T.O., Brown, E.L., Stein, C.A., Stein, S. and Moucha, R. 2021. Geochemical, petrographic, and stratigraphic analyses of the Portage Lake Volcanics of the Keweenaw CFBP: implications for the evolution of Main stage volcanism in Continental Flood Basalt Provinces. *Geological Society, London, Special Publications*, SP518-2020–2221, <https://doi.org/10.1144/SP518-2020-221>.
- Gamble, J.A., Price, R.C., Smith, I.E., McIntosh, W.C. and Dunbar, N.W. 2003. $^{40}\text{Ar}/^{39}\text{Ar}$ geochronology of magmatic activity, magma flux and hazards at Ruapehu volcano, Taupo Volcanic Zone, New Zealand. *Journal of Volcanology and Geothermal Research*, **120**, 271–287.

- Ganne, J., Bachmann, O. and Feng, X. 2018. Deep into magma plumbing systems: Interrogating the crystal cargo of volcanic deposits. *Geology*, **46**, 415–418, <https://doi.org/10.1130/G39857.1>.
- Garnero, E.J., McNamara, A.K. and Shim, S.-H. 2016. Continent-sized anomalous zones with low seismic velocity at the base of Earth's mantle. *Nature Geoscience*, **9**, 481–489.
- Gualda, G.A. and Ghiorso, M.S. 2015. MELTS _ E xcel: AM icrosoft E xcel-based MELTS interface for research and teaching of magma properties and evolution. *Geochemistry, Geophysics, Geosystems*, **16**, 315–324.
- Harrison, A.J. and White, R.S. 2004. Crustal structure of the Taupo Volcanic Zone, New Zealand: Stretching and igneous intrusion. *Geophysical Research Letters*, **31**, <https://doi.org/10.1029/2004GL019885>.
- Ito, G. and Mahoney, J.J. 2005. Flow and melting of a heterogeneous mantle: 1. Method and importance to the geochemistry of ocean island and mid-ocean ridge basalts. *Earth and Planetary Science Letters*, **230**, 29–46, <https://doi.org/10.1016/j.epsl.2004.10.035>.
- Kay, S.M., Gorrington, M. and Ramos, V.A. 2004. Magmatic sources, setting and causes of Eocene to Recent Patagonian plateau magmatism (36°S to 52°S latitude). 13.
- Kimura, J. and Kawabata, H. 2015. OceanBasaltSimulator version (OBS1): Trace element mass balance in adiabatic melting of a pyroxenite-bearing peridotite. *Geochemistry, Geophysics, Geosystems*, **16**, 267–300, <https://doi.org/10.1002/2014GC005606>.
- Kimura, J.-I. and Ariskin, A.A. 2014. Calculation of water-bearing primary basalt and estimation of source mantle conditions beneath arcs: PRIMACALC2 model for WINDOWS. *Geochemistry, Geophysics, Geosystems*, **15**, 1494–1514, <https://doi.org/10.1002/2014GC005329>.
- Kogiso, T., Hirschmann, M.M. and Pertermann, M. 2004. High-pressure partial melting of mafic lithologies in the mantle. *Journal of Petrology*, **45**, 2407–2422.
- Lee, C.-T.A., Lee, T.C. and Wu, C.-T. 2014. Modeling the compositional evolution of recharging, evacuating, and fractionating (REFC) magma chambers: Implications for differentiation of arc magmas. *Geochimica et Cosmochimica Acta*, **143**, 8–22, <https://doi.org/10.1016/j.gca.2013.08.009>.
- McDermott, C., Lonergan, L., Collier, J.S., McDermott, K.G. and Bellingham, P. 2018. Characterization of seaward-dipping reflectors along the South American Atlantic margin and implications for continental breakup. *Tectonics*, **37**, 3303–3327.
- Morgan, J.P. 2001. Thermodynamics of pressure release melting of a veined plum pudding mantle. *Geochemistry, Geophysics, Geosystems*, **2**.
- Nance, R.D. and Murphy, J.B. 2013. Origins of the supercontinent cycle. *Geoscience Frontiers*, **4**, 439–448.

- Price, R.C., Gamble, J.A., Smith, I.E.M., Maas, R., Waight, T., Stewart, R.B. and Woodhead, J. 2012. The Anatomy of an Andesite Volcano: a Time–Stratigraphic Study of Andesite Petrogenesis and Crustal Evolution at Ruapehu Volcano, New Zealand. *Journal of Petrology*, **53**, 2139–2189, <https://doi.org/10.1093/petrology/egs050>.
- Putirka, K.D. 2008. Thermometers and Barometers for Volcanic Systems. *Reviews in Mineralogy and Geochemistry*, **69**, 61–120, <https://doi.org/10.2138/rmg.2008.69.3>.
- Schmerr, N., Garnero, E. and McNamara, A. 2010. Deep mantle plumes and convective upwelling beneath the Pacific Ocean. *Earth and Planetary Science Letters*, **294**, 143–151.
- Sobolev, A.V., Hofmann, A.W., et al. 2007. The amount of recycled crust in sources of mantle-derived melts. *science*, **316**, 412–417.
- Solano, J.M.S., Jackson, M.D., Sparks, R.S.J., Blundy, J.D. and Annen, C. 2012. Melt Segregation in Deep Crustal Hot Zones: a Mechanism for Chemical Differentiation, Crustal Assimilation and the Formation of Evolved Magmas. *Journal of Petrology*, **53**, 1999–2026, <https://doi.org/10.1093/petrology/egs041>.
- Stein, S., Stein, C.A., et al. 2018. Insights from North America’s failed Midcontinent Rift into the evolution of continental rifts and passive continental margins. *Tectonophysics*, **744**, 403–421, <https://doi.org/10.1016/j.tecto.2018.07.021>.
- Tackley, P.J. 2008. Layer cake or plum pudding? *Nature geoscience*, **1**, 157–158.
- Walker, B.A., Bergantz, G.W., Otamendi, J.E., Ducea, M.N. and Cristofolini, E.A. 2015. A MASH Zone Revealed: the Mafic Complex of the Sierra Valle Fértil. *Journal of Petrology*, **56**, 1863–1896, <https://doi.org/10.1093/petrology/egv057>.
- Weyer, S. and Ionov, D.A. 2007. Partial melting and melt percolation in the mantle: the message from Fe isotopes. *Earth and Planetary Science Letters*, **259**, 119–133.

2. TRANSCRUSTAL MAGMATIC SYSTEMS : EVIDENCE FROM ANDESITES OF THE SOUTHERN TAUPO VOLCANIC ZONE

2.1 Introduction

In active arc environments, the seismically defined stratified structure of the crust is typically described as a mafic lower crust and a felsic upper crust (e.g., Harrison and White 2004). These inferences are supported by studies of exposed, tilted arc sections where remnants of the arc magma plumbing system are revealed, showing a similar stratification (Greene et al. 2006; Walker et al. 2015; Barnes et al. 2016). Such studies have highlighted the central role of magmatic differentiation processes such as fractional crystallization, magma mixing, contamination or assimilation, and homogenization in controlling the structure of arc crust (e.g., Hildreth and Moorbath 1988). Furthermore, in products erupted from these arc magmatic systems, the melt is often out of equilibrium with the crystal cargo contained within (Cashman et al. 2017 and references therein; Ganne et al. 2018). Both petrologic studies of exposed crustal sections (e.g., Greene et al. 2006; Walker et al. 2015) and numerical modeling simulations (e.g., Annen et al. 2006; Solano et al. 2012) suggest this variability is the result of differentiation of many batches of magma within intrusive complexes stacked throughout the crust.

These igneous complexes have been given multiple monikers, including MASH zones (Hildreth and Moorbath 1988), hot zones (Annen et al. 2006), and transcrustal magmatic systems (Cashman et al. 2017). While these terms are not necessarily all identical, they broadly describe the vertically extensive magma storage zones beneath volcanoes where melts differentiate and interact with the surrounding crust, especially in magmatic arcs. Lower crustal hot zones are used in accordance with the previous work of Annen et al. (2006), referring to the mafic roots of the

plumbing systems. They may be the first parts of the plumbing system to form. A transcrustal magmatic system is then defined as the hot zone plus more felsic zones higher in the crust that form through sustained intrusion and differentiation. We will retain the hot zone nomenclature throughout this document because we are specifically referring to the mafic lower-crustal components of the magmatic plumbing system. These hot zones may be the earliest differentiation zones to develop beneath new volcanic edifices, before mature transcrustal magmatic systems are fully established.

Within transcrustal magmatic systems there are thought to be two discrete zones: a lower zone (the hot zone) where mafic magmas initially lose heat and differentiate; and an upper zone where intermediate magmas extracted from the mafic zone accumulate, homogenize and differentiate further (Annen et al. 2006; Price et al. 2012; Jackson et al. 2018). In well-developed volcanic arcs, the processes active in the mafic lower portions of the hot zone are difficult to investigate as the erupted magmatic products typically originate largely from the upper more felsic zone (e.g., Price et al. 2012). This may be due to filtering of the mafic material as melts and crystals are processed through the upper felsic zone.

Exposed arc plutonic crustal cross sections do provide some insights into the development of these hot zones. However, there are several reasons that they lack information about the initial stages of the establishment of the hot zone: 1) The record of magma evolution is often overprinted in the plutonic rocks by a myriad of processes that might include metamorphism; 2) The complementary volcanic products are poorly exposed or completely missing due to uplift and erosion; 3) Some of the mafic lower crust may have developed a density instability that resulted in recycling back into the mantle (Cashman et al. 2017). Many such sections are thus not ideal for the specific study of the hot zones within arcs. The scarcity of exposed crustal cross sections of

arcs that include the lower crustal component presents a distinct challenge for characterizing the igneous processes active in the lower crust of arc magmatic zones. This requires us to identify and examine volcanic products that directly sample these deep components without an overprinting of the overlying upper crustal magmatic system. Those exposed arc sections that do exist, however, (e.g., the Sierra Valle Fertil complex of Argentina - Walker et al. 2015; and the Wooley Creek batholith in California - Barnes et al. 2016) have a lower-crustal mafic component that is composed of tens to hundreds of mafic and ultramafic cumulate bodies. These mafic cumulate bodies are described as “complex and non-regular” (Walker et al. 2015). This is consistent with the complex of sills that form active hot zones. This style of emplacement of igneous bodies as dozens of discrete sills in the lower crust is also consistent with the assumptions underpinning numerical simulations and geochemical studies (e.g., Annen et al. 2006; Price et al. 2012; Solano et al. 2012). These models suggest an evolution from an early mafic zone restricted to the mid- to lower crust towards a fully developed system that contains mafic and felsic zones spanning the entire crust.

Another strategy to understand the development of mafic arc crustal roots in hot zones is to examine immature volcanic edifices in active arcs like the Taupo Volcanic Zone (TVZ). In this study we examine the products of a small, monogenetic edifice – Ohakune. We then contrast those findings with Ruapehu, which has been active for up to 340 ka (Tost et al. 2016). There, magmas are processed through a much more complex magmatic and mature plumbing system that evolved with sustained intrusion over time (Price et al. 2012). We consider both the solid residues (intrusive) and liquid extracts (extrusive) in the system, and utilize the crystal cargo and xenoliths present in erupted materials to help deconvolve the processes of melting, melt extraction, fractionation, and assimilation (Bachmann et al. 2007; Cashman et al. 2017; Ganne et al. 2018).

Below we outline evidence from our study that sheds light on differentiation processes in the lower crust. Our data indicates that mafic material erupted within andesites represents the products of basaltic differentiation that amalgamates melts and crystals from multiple levels of the crust prior to eruption. In essence, they are mafic mushes crystallized from basalt in the mid- to lower-crust mixed with intermediate melts stored in the mid- to upper- crust. These differentiation products erupt without experiencing the significant upper crustal storage, assimilation, and differentiation typically observed at most mature stratovolcanoes.

2.2 Geological Setting

The TVZ on the North Island of New Zealand (Fig. 2.1a) is an actively rifting arc (Cole 1990; Gamble *et al.* 1990; Wilson *et al.* 1995). In the northern and southern portions of the TVZ, at the boundaries of the rifting arc section, andesitic volcanism is predominant. In the central TVZ, rhyolitic magmas are dominant with subordinate basalt and intermediate magmas (Wilson *et al.* 1995; Fig. 1a). Ruapehu is the most southerly andesitic stratovolcano in the TVZ. It is part of a complex of volcanic edifices called the Tongariro Volcanic Center. These include other stratovolcanoes (e.g., Tongariro, Ngauruhoe) as well as smaller satellite vents such as Pukeonake (Fig. 2.1b).

Work at Ruapehu established that the magmatic plumbing system there experienced temporal evolution over the last 250 ka (Price *et al.* 2012; Conway *et al.* 2016). The oldest exposed eruptive products at Ruapehu, the Te Herenga Formation (Fig. 1b), evolved mostly in the lower crust based on isotopic and trace element constraints (Price *et al.* 2012). More recent Ruapehu magmas (e.g., those of the Wahainoa, Mangawhero, and Whakapapa formations) ascended through a plumbing system that was more vertically extensive. Much of the transcrustal magmatic

system sampled by these Ruapehu eruptions occupies the upper- and middle crust (Price *et al.* 2012). The 250-180 ka Te Herenga Formation at Ruapehu contains plagioclase as a phenocryst phase and olivine with Fo₆₉₋₈₅ (Fo = Forsterite, mineral molar Mg/Mg+Fe; Conway *et al.* 2016, 2018). The range of Fo observed in Te Herenga and the presence of plagioclase suggest that Ruapehu sampled an intermediate portion of the transcrustal system at that time. Furthermore, petrography and geochemical data derived from distal mass flow deposits on Ruapehu from Tost *et al.* (2016) indicate that a magmatic system had developed at Ruapehu more than 340 ka ago. The Ohakune scoria cones mark the southern termination of the TVZ just southwest of Ruapehu and are traditionally considered to be satellite vents of Ruapehu (Graham and Hackett 1987). Graham and Hackett (1987) recognized that basaltic andesites at Ohakune contained phenocrysts of olivine, clinopyroxene, and orthopyroxene but did not contain phenocrysts, antecrysts, or xenocrysts of plagioclase. These scoriae are among the most primitive products of the Ruapehu system. They belong to a group of lavas found at Ruapehu and elsewhere in the TVZ called high-Mg andesite-dacite (HMAD) (Conway *et al.* 2020). These HMAD are interpreted to be formed by mixing of intermediate magmas stored as mush zones and olivine-bearing mafic magmas (Conway *et al.* 2020; Fig. 2.2). Ohakune also is the southernmost volcanic edifice in the Taupo Volcanic Zone at the tip of the propagating rift (Fig. 2.1b). We thus contend that Ohakune might provide a window into the elusive hot zone portion of a transcrustal magmatic system.

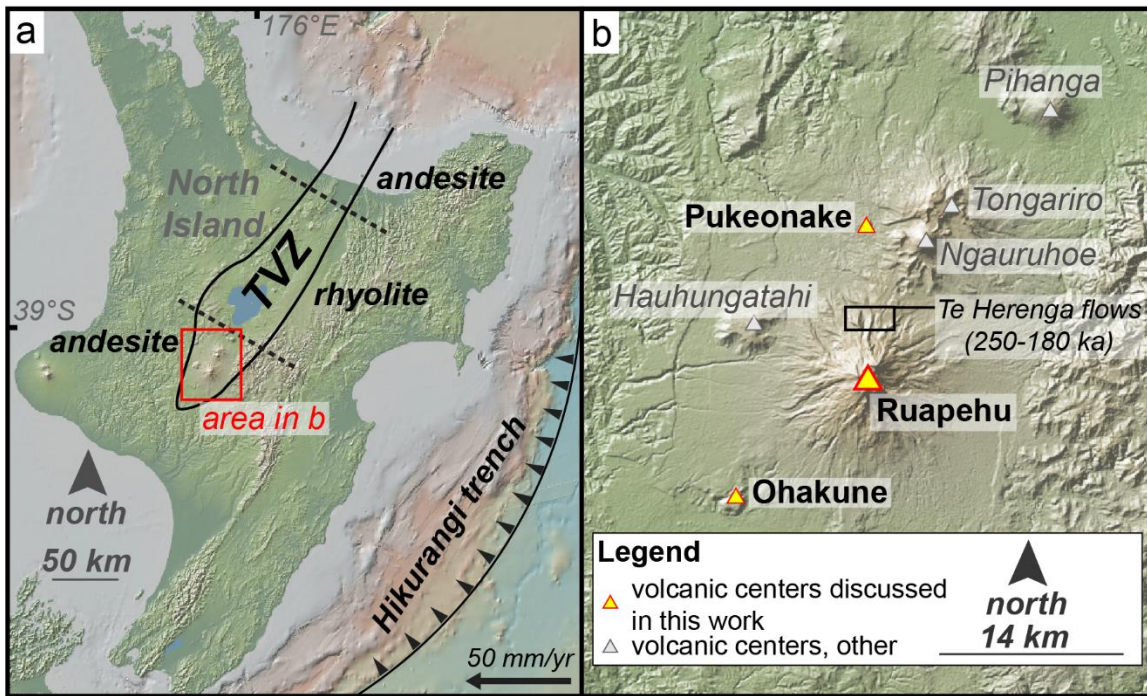


Figure 2.1

Study location and geologic setting of the Taupo Volcanic Zone (TVZ) of New Zealand. (a) GeoMapApp DEM base map of the North Island of New Zealand. Black outline shows the modern boundary of the TVZ, an actively extending rifting arc. Rifting is driven by oblique subduction of oceanic crust from the west that meets the North Island at the Hikurangi trench (barbed line; barbs shown on overriding plate). The direction and velocity of subduction is shown by the arrow in the lower right. The TVZ is segmented into three distinct zones: a central rhyolite producing, caldera forming region flanked to the northeast and southwest by andesite producing zones. The approximate zones of these boundaries are shown by the dashed black lines. (b) Area inset from red box in (a). The major Quaternary andesite-producing volcanoes of the Tongariro Volcanic center are shown, with the edifices discussed in this study highlighted.

Figure 2.1 (cont'd.)

Ruapehu is one of the central stratovolcanoes in the southern andesite zone along with Tongariro and Ngauruhoe. Ohakune and Pukeonake are satellite vents. Names used consistent with Price et al. (2012) and Beier et al. (2017), and references therein.

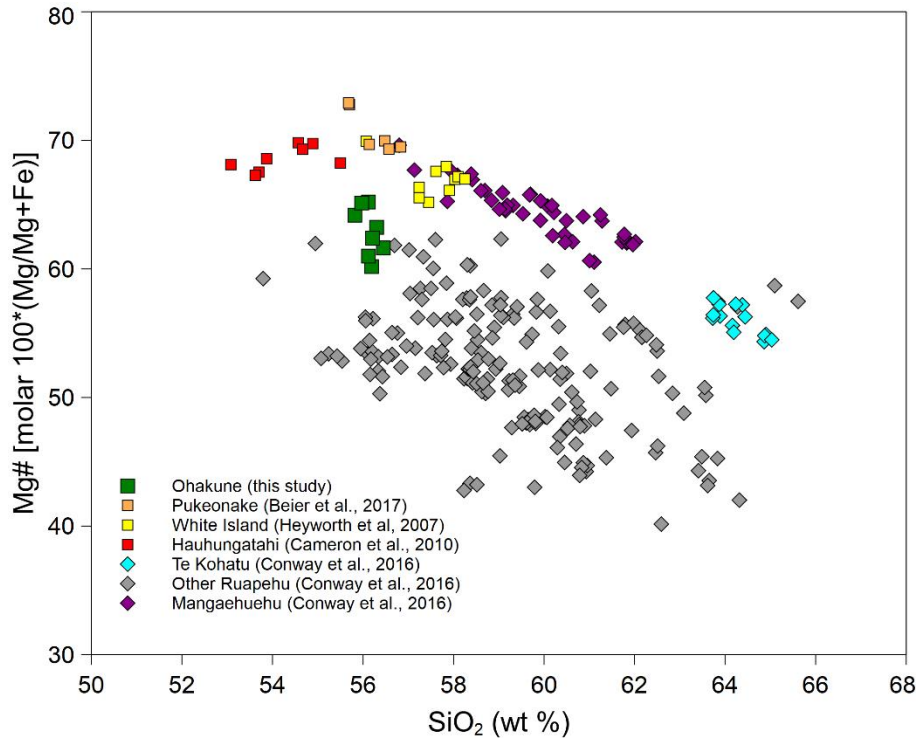


Figure 2.2

Plot of Mg# ($100 \times \text{molar Mg}/(\text{Mg}+\text{Fe})$ with total Fe) vs SiO₂ of High-Mg andesites and dacites (HMAD) magmas from Ruapehu and around the Taupo Volcanic Zone (colored squares and diamonds), compared with other non-HMAD eruptive products from the stratovolcano Ruapehu (gray diamonds). Data from Fig. 1B of Conway et al. 2020.

Here we examine the magmatic products of the Ohakune Craters, a scoria cone 20 km southwest of Ruapehu that erupted 31.5 ka ago (Froggatt and Lowe 1990). Kósik et al. (2016) report eruptions at the Ohakune Craters were from fissures aligned with the Ohakune fault.

Eruptions were mixed fire fountaining, Strombolian explosions, and phreatomagmatic blasts that left behind 100-200m craters, with a total eruptive volume of $28.83 \times 10^6 \text{ m}^3$. Despite their young age that contrasts with the presumed long existence of the Ruapehu mature hot zone, these HMAD products may constitute important windows into a primarily lower crustal hot zone. This may be due to the location at the current termination of the TVZ, and the hot zone may be developing as the rifting process continues southward.

The textural populations observed in Ohakune scoriae may indicate a dispersed magmatic system (i.e., a series of sills) wherein mafic crystals are forming. The Ohakune andesites and their crystalline cargo provide a record of these magmatic systems in their earliest stages. The behaviors we observe in this hot zone include: the crystallization, transport, and accumulation of primitive olivine; the crystallization of high-Mg# (Mg# = molar $\text{Mg}/(\text{Mg} + \text{Fe}^{\text{II}})$) pyroxenes in the mid crust; and brief storage of these mafic minerals in an intermediate melt prior to eruption. We integrate our observations of the Ohakune magmatic system with the predictions of numerical models (e.g., Annen *et al.* 2006; Solano *et al.* 2012) as well as the petrology of nearby Ruapehu stratovolcano and the Pukeonake satellite vent. These results have implications for our understanding of the evolution of hot zones, and models for the evolution of continental crust.

2.3 Samples

Fresh scoria samples were collected from strombolian bed layers at the Ohakune Craters scoria cone (Locality 1, Houghton and Hackett 1984 or CSC of Kósik et al. 2016). Eight samples from this sequence of units, named progressively from 5021A at the base to 5021I at the top of the sequence (Supplemental Document 1, Table A1), were selected for geochemical analysis. Whole rock scoria samples represent individual blocks and bombs of material removed from the deposits in Ohakune. They are dense, unwelded, and vesicular (20-55% total void space). Ohakune scoriae are porphyritic (5-20% phenocrysts) with visible clots of mafic minerals that are 1-2 mm, suspended in a glassy to microcrystalline groundmass.

2.4 Methods

Whole rock samples were cut, polished, washed in deionized water, and powdered in an alumina mill. They were then fused into lithium tetraborate glass disks. These disks are 3 grams rock flour, 9 grams borate flux, and 1 gram ammonium nitrate oxidizer to convert all Fe into Fe³⁺, mixed in a platinum crucible, and then oscillated over a burner for 25 minutes before being quenched in platinum molds. These disks were analyzed at Michigan State University for major elements using a Bruker S4 X-ray fluorescence spectrometer (following methods contained in Rooney *et al.* 2012), and for trace elements by laser-ablation inductively coupled plasma mass spectrometry (LA-ICP-MS) using a Photon-Machines Analyte G2 excimer laser and Thermo Scientific ICAP Q quadrupole ICP-MS (following methods contained in Rooney *et al.* 2015).

Four petrographic thin sections (5021A, C, F, G-B) that contained all major textural groups were selected for analysis. Clinopyroxene, orthopyroxene, olivine, interstitial glass within glomerocrysts, and groundmass glasses were analyzed with a common method including 48 major

and trace elements using the same LA-ICP-MS apparatus as above. The methods of Rooney *et al.* (2015) were followed. In brief, the laser pulse was set at 10 Hz with a 4.1 J/cm^2 fluence, with 30 μm spots, scaled to the size of individual crystals. Ablated material was conveyed to the ICP-MS by a 0.75 mL/min flow of He through a 2-volume 15×15 cm HeIEx cell. The ICP-MS was used in kinetic energy discrimination mode, where the reduced polyatomic isobaric interferences allowed for precise quantification of major elements with low detection limits. Calibration was performed on a combination of fused reference material rock powders and natural and synthetic basalt glasses (Supplemental Document 2, Table B6). Silicon was collected twice on the ICP-MS, once as an unknown, and once as an internal standard applied to all elements. Silicon contents used as internal standard for unknown mineral analyses were set to 50 wt. % SiO_2 (a value roughly representative of silica contents in mafic minerals). From there, the sum of all internal-standard-corrected major element oxides was calculated, and all major and trace element concentrations were subsequently normalized to the actual sum of major element oxides in anhydrous silicate minerals, i.e., 100 wt. %. Samples were bracketed by analyses of fused glass standards BHVO-1 and JB-1a every hour during analyses to monitor and correct linearly for drift. Mineral standards Smithsonian Institution olivine NMNH-11312-44 and diopside NMNH-117733 were analyzed three times as unknown (secondary standard) (see Supplemental Document 2, Table B6). Uncertainties resulting from instrument reproducibility and accuracy of calibration standards combined are 2-5% on most elements and are 10% or less on all analyzed elements (see Supplemental Document 2, Table B6). Major element results for Fe were converted into FeO , Fe_2O_3 , and FeO_T in whole rocks, groundmass glasses, and interstitial glasses using the $\text{Fe}^{3+}/\Sigma\text{Fe}$ ratio 0.15 for back-arcs reported in Kelley and Cottrell (2009).

Thin sections 5021 C, D, and F were examined on an Oxford Instruments JEOL 6610LV Scanning Electron Microscope (SEM) using backscattered electron imaging of carbon-coated slides with an accelerating voltage of 15 kV at Michigan State University's Center for Advanced Microscopy.

2.5 Results

2.5.1 Petrography

Ohakune scoriae contain an assemblage of olivine, clinopyroxene, and orthopyroxene crystals (Fig. 2.3). Glomerocrysts and individual crystals (phenocrysts/antecrysts) represent 5-20 volume %, while total crystallinity of Ohakune scoriae ranges from 15-70%. The groundmass is glassy to microcrystalline (glass = 10-45% of groundmass), with plagioclase and clinopyroxene as major groundmass phases. Samples are vesicular, with large (>0.5-1 mm in diameter, e.g., Fig. 2.3c, central vesicle) voids occupying 1-20% of the observed volume and microvesicles (<50-100 micrometers; see black areas in Fig. 2.4a for reference) occupying from 20-60% of the groundmass volume. Total vesicularity ranges are calculated to be 20-55% of the volume of the samples. Full petrographic details are contained in Supplemental Document 1, Table A1.

Olivine is ~1 mm, embayed, with evidence of disequilibrium from partial resorption (e.g., Fig. 2.3c). All olivine crystals either have coronae of orthopyroxene or are contained within a glomerocryst of ortho- and clinopyroxene (Fig. 2.3a, b, c). Zoning is not apparent in olivine crystals petrographically or via backscattered SEM imaging.

Clinopyroxene and orthopyroxene commonly occur with equilibrium textures including euhedral polycrystalline glomerocrysts and single variably sized (0.1-1 mm) euhedral individual crystals. Glomerocrysts occur in all Ohakune samples. Glomerocrysts are irregularly shaped with

visible triple junctions and equilibrium grain boundaries, consistent with fragments of a mafic mush (Holness *et al.* 2007). Some glomerocrysts occur as rosettes (Fig. 2.3d, e). Interstitial glass is observed within some glomerocrysts. Clinopyroxene are commonly twinned. Core to rim direct zoning, oscillatory zoning, and exsolution lamellae are not evident under backscattered SEM imaging. Backscattered SEM images do show discontinuous zoning in the form of Fe-rich rims in a two-pyroxene glomerocryst in Sample 5021 (Fig. 2.4a). Polycrystalline, fine-grained (grains 0.05-0.3 mm), disaggregated quartzite xenoliths (Fig. 2.3f) are abundant in the lower units of the Ohakune strombolian sequence (samples 5021 A-E) but are not observed in upper units.

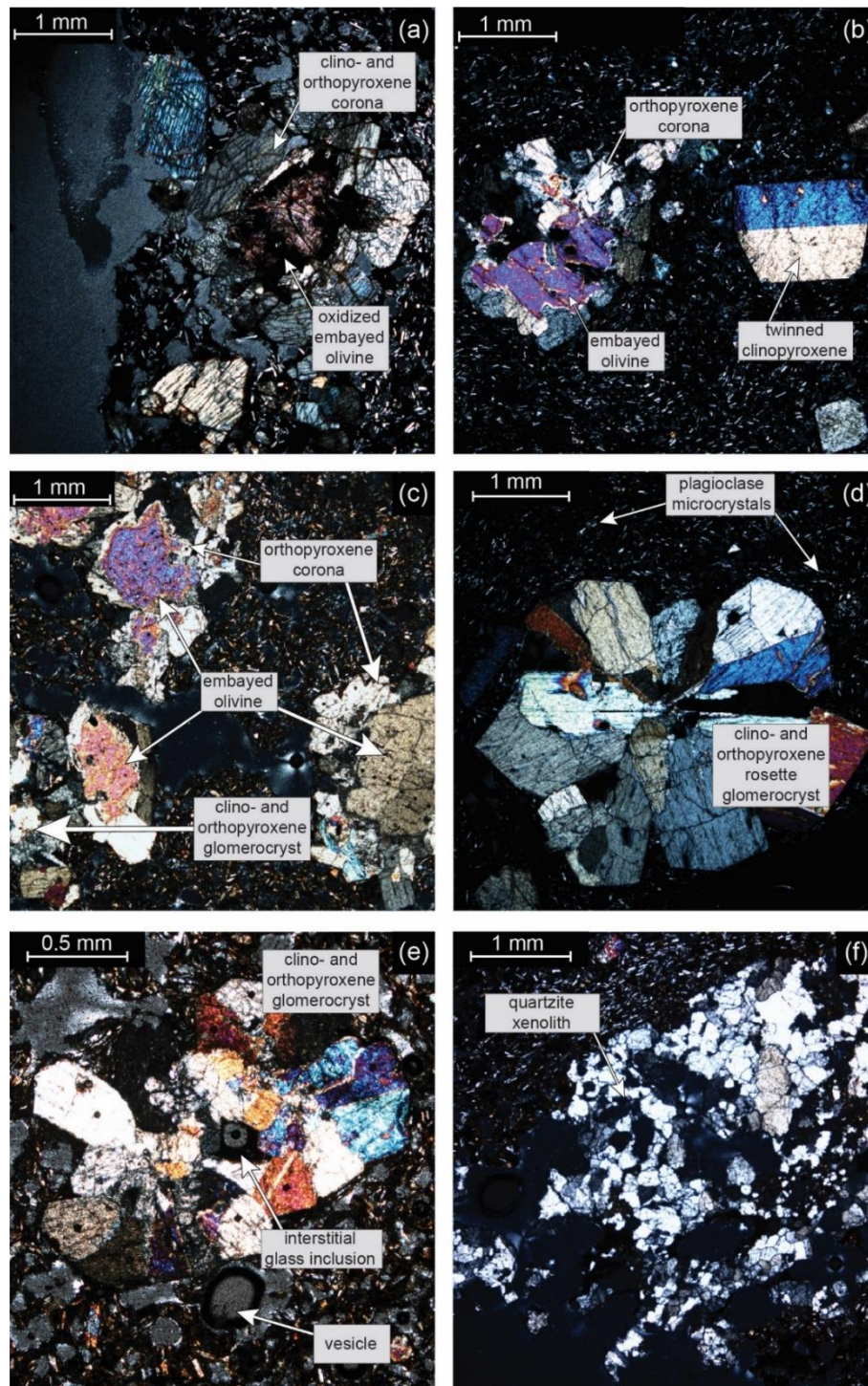


Figure 2.3

Representative images of petrographic phases and textures observed in Ohakune andesites, views all in crossed polars. (a) A blackened (oxidized) and embayed olivine surrounded

Figure 2.3 (cont'd)

by a rim of ortho- and clinopyroxene. (b) An embayed (non-oxidized) olivine exhibiting corona texture next to a 1mm single crystal of clinopyroxene. (c) Abundant embayed olivine with various-sized orthopyroxene coronae. (d) A radiating rosette-shaped glomerocryst of clinopyroxene and orthopyroxene set in a groundmass of clinopyroxene + plagioclase microlites. (e) Irregular clinopyroxene and orthopyroxene glomerocryst with an interstitial glass at the center of the glomerocryst. Image also shows vesicularity typical of Ohakune scoriae. (f) Disaggregated quartzite xenolith.

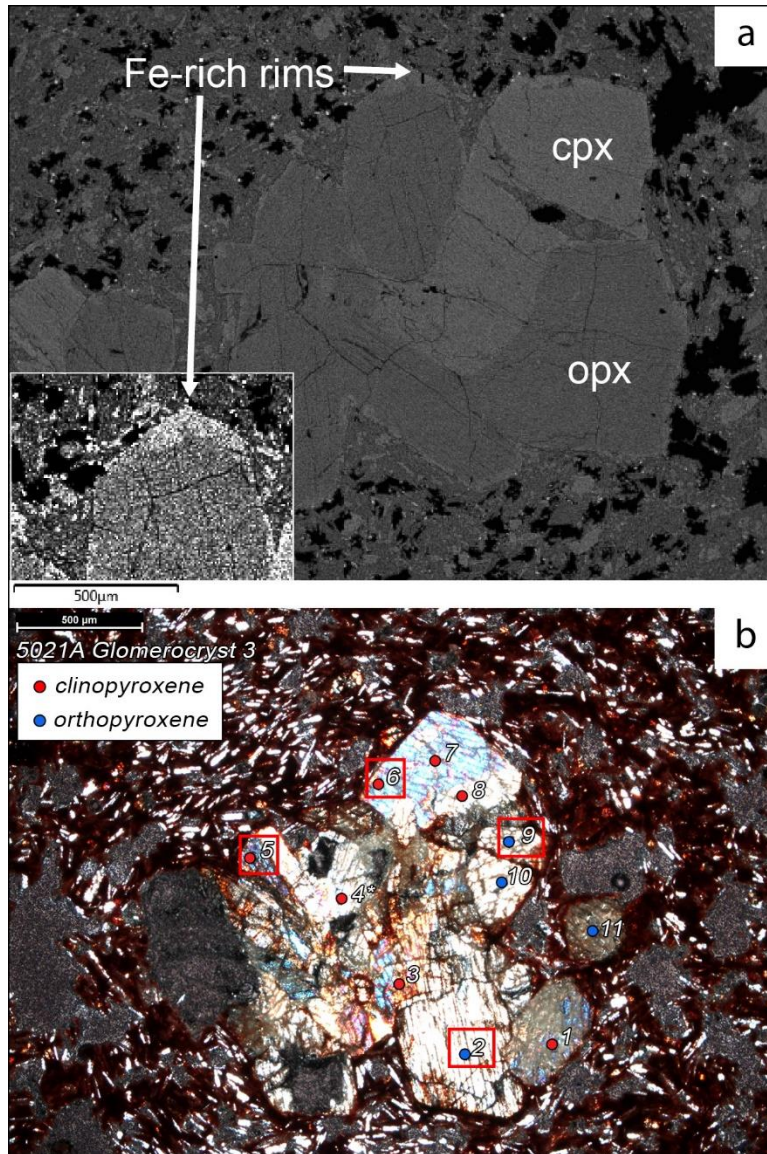


Figure 2.4

(a) Representative backscattered scanning electron microscope of a clinopyroxene (medium gray) and orthopyroxene (darker gray) glomerocryst from Sample 5021D. Note the thin light gray area rimming the exterior of the pyroxenes of this glomerocryst. This is due to Fe-rich rims. We interpret these rims as evidence of brief storage in an Mg poor magma chamber prior to eruption. Inset area at bottom left of (a) has had contrast and levels digitally adjusted to show the Fe-rich rims more clearly. (b) Photomicrograph of 5021A clinopyroxene and orthopyroxene

Figure 2.4 (cont'd)

glomerocryst in crossed polar view. Red and blue dots indicate laser ablation sites of crystal types as indicated in the legend. Analyses with red boxes have Lo-Al chemical signature

2.5.2 Major Elements: Whole Rocks, Groundmass Glasses, and Interstitial Melts

Whole-rock measurements of Ohakune scoriae lie along the basaltic andesite-andesite boundary of the Total Alkali Silica (TAS) diagram of Le Maitre (1989) and have high Mg#. Groundmass glasses are andesite, while interstitial glasses are more evolved and are largely dacitic in composition. Such glass compositions are uncommon in subduction zone volcanoes globally (Reubi and Blundy 2009). Whole rock Mg# are 60-65 (average (avg.) 63, standard deviation (s.d.) 1.9) and are considerably higher than expected for rocks with this andesitic SiO₂ content, but fit on the HMAD trend of Conway et al. (2020) (Fig. 2.2). Groundmass and interstitial glasses and have higher SiO₂ concentrations (Fig. 2.5) and lower Mg# than the whole rocks (groundmass glasses range 30-46, avg. 38 s.d. 6.9; interstitial glasses range 25-44, avg. 31 s.d. 5.8); see Supplemental Document 2, Tables B3 & B4. Major element oxides CaO and Al₂O₃ form a negative-sloped trend against increasing SiO₂ in the groundmass glasses and interstitial melts, while TiO₂, MnO, and K₂O form a positive sloped trend vs. increasing SiO₂; FeO is largely scattered.

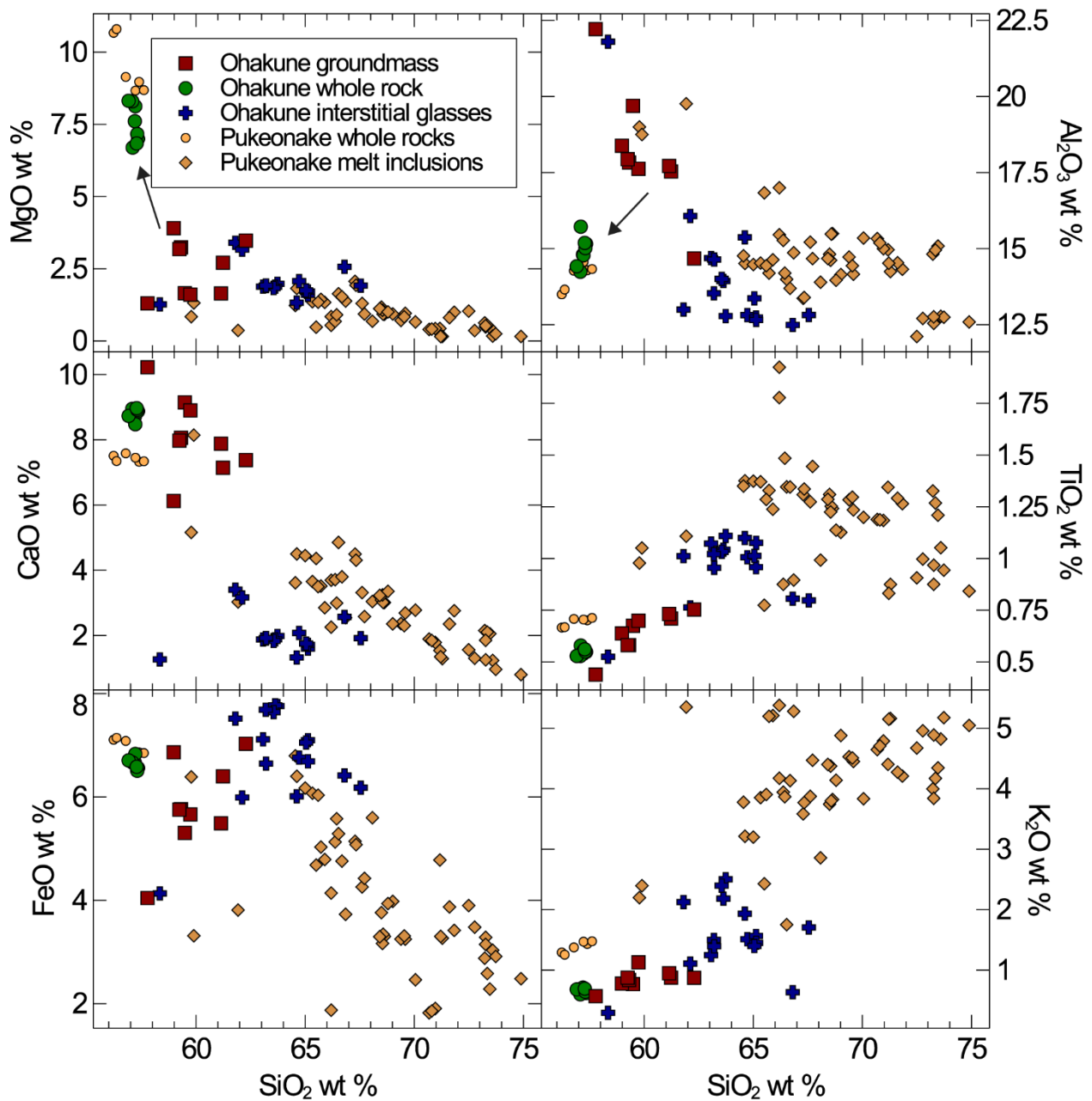


Figure 2.5

Major element X-Y bivariate diagrams of Ohakune whole rocks (circles), groundmass glasses (squares), and interstitial glasses (crosses). Orange circles and diamonds are whole rocks and melt inclusions respectively from the Pukeonake edifice for comparison (Beier et al. 2017). Black arrows in the first two panels (SiO_2 vs. MgO and Al_2O_3) show postulated mineral accumulation trends

2.5.3 Trace Elements: Whole Rocks, Groundmass Glasses, and Interstitial Melts

Strontium forms a negative trend vs. increasing SiO₂ in all samples (i.e., whole rocks, groundmass glasses, and interstitial glasses), while V, Zr, and Rb form positively sloped trends. First-row transition metals Ni and Cr are at higher concentrations in whole rock analyses than in interstitial melts and groundmass glasses (whole rock Ni avg. = 50 ppm s.d. 10, Cr avg. = 262 ppm s.d. 73; groundmass glass Ni avg. = 9.4 ppm s.d. 5.1 and Cr = 6.5 ppm s.d. 7.7; interstitial glass Ni avg. = 10.3 ppm s.d. 9.6, Cr avg. = 28.7 ppm s.d. 35.5) (see Supplemental Document 2, Tables B3 & B4). The interstitial glasses with the highest SiO₂ contents are not necessarily those with the most elevated incompatible trace element concentrations. Interstitial melts extend to higher overall incompatible trace element enrichment than groundmass glasses or whole rocks.

Rare earth elements (REE) normalized to CI chondrite (Sun and McDonough 1989) for whole rocks, groundmass glasses, and interstitial melts show a homogeneous pattern at variable levels of enrichment (Fig.2.6). The pattern is tilted upwards from Eu-La, then flat from Lu-Eu. La_N/Yb_N in all melts ranges from a minimum of 2.53 to a maximum of 3.97, with an average of 3.23 and standard deviation 0.35. Trace element abundance diagrams normalized to Primitive Mantle (PM, Sun and McDonough 1989) show these same parallel patterns, with notable depletions in Nb and Ta (Fig. 2.7).

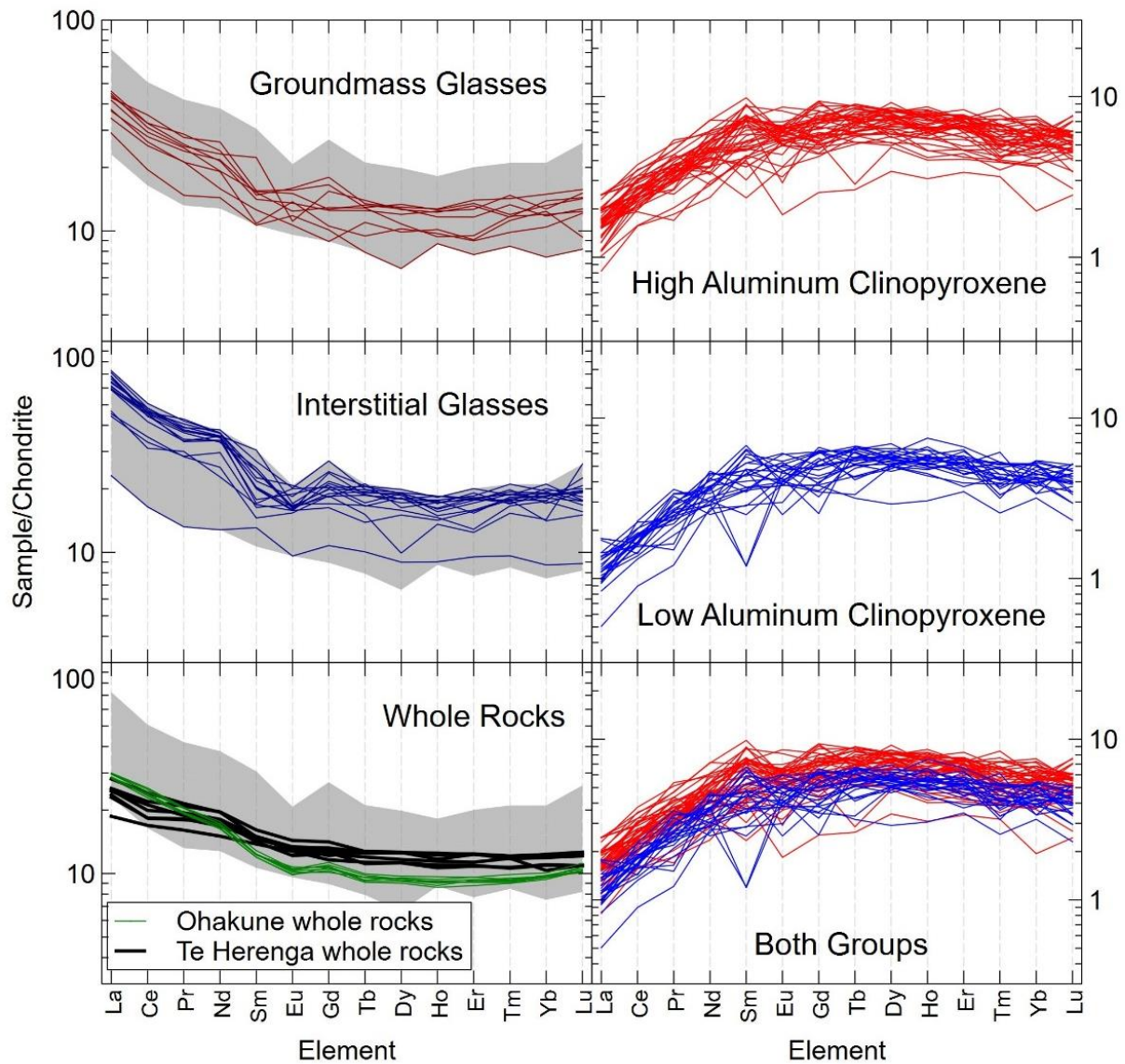


Figure 2.6

CI chondrite (Sun and McDonough 1989) normalized rare earth element (REE) concentrations of Ohakune whole rocks, groundmass glasses, and interstitial glasses (left frames), as well as REE concentrations of pyroxenes collected during this study (right frames). Also shown are REE patterns for the Te Herenga Formation (Conway et al. 2018). Shaded gray regions indicate the overall range of compositions in Ohakune samples

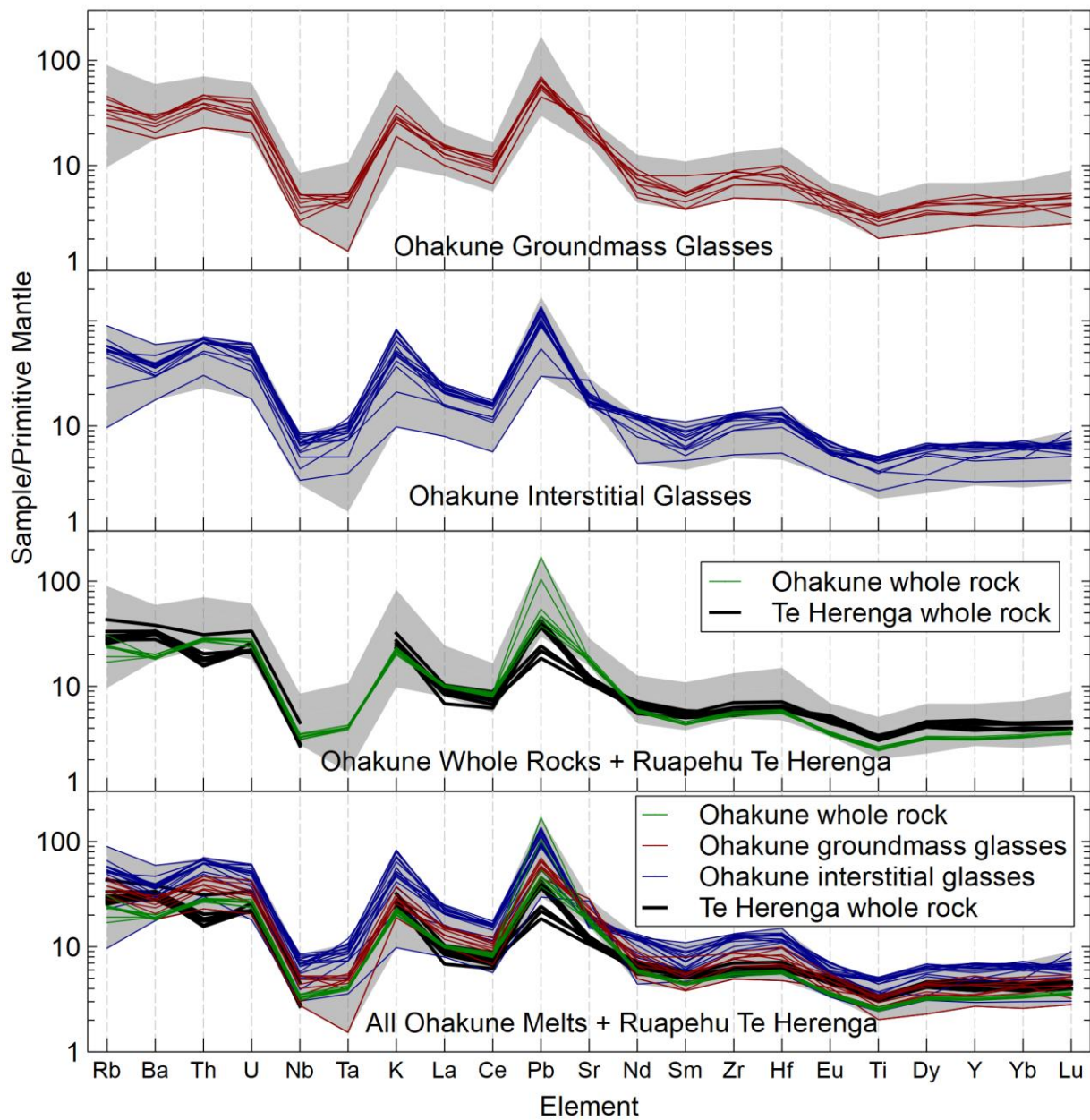


Figure 2.7

Primitive mantle (Sun and McDonough 1989) normalized trace element abundance diagrams for whole rocks, groundmass glasses, interstitial glasses, and all analyses superimposed. The bottom two frames also show trace element patterns for Te Herenga Formation andesites of Ruapehu (Conway et al. 2018). Shaded gray regions indicate the overall range of compositions in Ohakune andesites

2.5.4 Mineral Geochemistry

Olivine crystals in Ohakune andesites are Mg-rich, with Fo₈₅₋₉₁ (avg. 87.5, s.d. 1.4; Fig. 2.8). Pyroxenes are also Mg-rich, with Mg# for clinopyroxene ranging from 81-88 (avg. 83 s.d. 1.4) and Mg# for orthopyroxene ranging from 76-83 (avg. 81 s.d. 1; Fig. 2.9). Orthopyroxenes can be divided into two groups: a low-aluminum group (henceforth Lo-Al, Al₂O₃ = 0.8-1.2 wt %), and a high-aluminum group (Hi-Al opx Al₂O₃ = 1.5-3.1 wt %) (Fig. 2.9). There may be a similar division of clinopyroxenes, although it is not as clear as with orthopyroxene; we have marked our divisions for both clino- and orthopyroxenes in Fig. 2.9. Lo-Al and Hi-Al pyroxenes compositions can be found in the same glomerocrysts. In several instances, the Lo-Al and Hi-Al signature appears in different regions of the same crystal (one such instance shown in Fig. 2.4b). Lo-Al orthopyroxenes have elevated SiO₂ and MnO, and lower TiO₂, Cr, and V relative to Hi-Al pyroxenes (Fig. 2.9). REE patterns for both Hi-Al and Lo-Al groups of pyroxenes overlap and have a similar shape with slopes that are only displaced parallel up or down to one another. Hi-Al clinopyroxenes encompass a wider range of REE enrichments than the Lo-Al group. (Fig. 2.6).

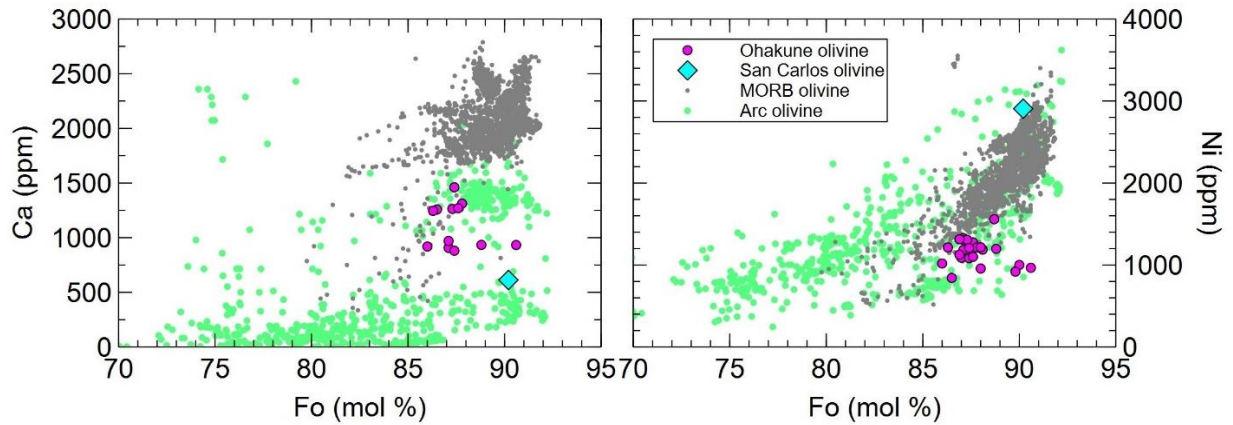


Figure 2.8

X-Y bivariate diagrams showing olivine Fo vs. Ni and Ca. Included on these diagrams for comparison are global datasets (e.g. MORB olivine from Table S2A of Sobolev et al. (2007) and references, and arc olivine collated from GEOROC; see Supplemental Document 3, Tables C1 & C2 for full data and sources). Ohakune olivine fall into the low-Ca field defined by arc olivine. Also shown is the average of three analyses of San Carlos olivine (cyan diamond) showing the composition of mantle olivine

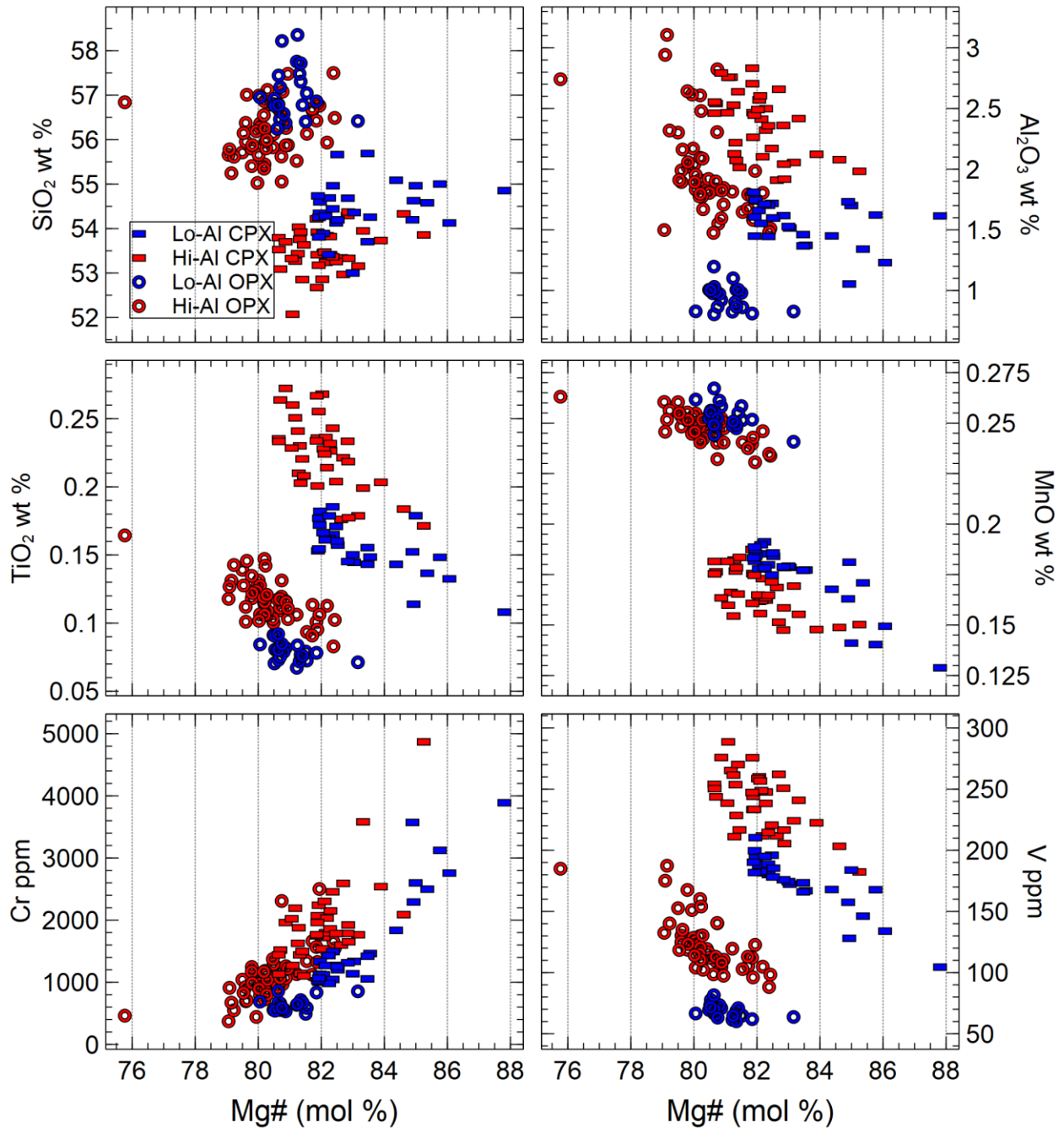


Figure 2.9

Selected major and minor element bivariate X-Y diagrams of ortho- and clinopyroxenes in Ohakune andesites. Cyan open circles represent high-aluminum orthopyroxenes, while navy open circles represent low-aluminum orthopyroxenes. Red rectangles represent high-aluminum clinopyroxenes, while yellow rectangles represent low-aluminum clinopyroxenes

2.6 Discussion

2.6.1 Evolution of Arc Magmas in Deep Crustal Hot Zones

The volcanic products erupted in magmatic arcs around the globe are thought to be processed gradually throughout the crust, forming extensive vertical structures referred to as transcrustal magmatic systems (e.g., Cashman *et al.* 2017). The lowermost parts of these structures where mafic magmas ascend into, stall and differentiate, referred to as hot zones (Annen *et al.* 2006), are difficult to thoroughly investigate. Their magmatic products typically differentiate further in the upper crust (e.g., Bachmann and Huber 2019). How these hot zones initially form and how they evolve are important considerations for understanding the formation and modification of Earth's continental crust.

Below we outline evidence for our interpretation of andesites from Ohakune as the product of a hot zone. These andesites are processed with limited subsequent evolution in the upper crust. The most notable features of Ohakune andesites are their lack of plagioclase, and high-Mg# whole-rock composition at the observed SiO₂ contents. High-Mg# andesites (HMA) are recognized globally at subduction zones (Kelemen 1995) including in the TVZ and at Ruapehu (Conway *et al.* 2020) and are thought to play an important role in the construction of the continental crust. Numerous models have been proposed to explain the genesis of HMAs, including as mantle partial melts (Grove *et al.* 2005), hybridization of mantle-derived basalts and dacites (Straub *et al.* 2011), and through assimilation and fractional crystallization (Price *et al.* 2012). Here, we argue for their origin from lower crustal differentiation of basalt magmas.

Ohakune whole rock compositions are characterized by Mg#, Cr, and Ni that are elevated over measurements of groundmass and interstitial glasses. This is consistent with the ferromagnesian phenocryst assemblage having crystallized from the interstitial and groundmass

glasses. Similarly, groundmass and interstitial glasses are more evolved than the whole rocks in terms of SiO₂, alkalis, and Zr. These signatures are more evolved than what would be expected for volcanic rocks with such high whole rock Mg#.

Our results show that these magnesian minerals are out of Fe-Mg equilibrium with the host groundmass glasses. Equilibrium calculations were performed using mineral-melt Fe-Mg K_D of 0.25 for both clinopyroxene and orthopyroxene (Bédard 2007, 2010). Ohakune clinopyroxenes are in equilibrium with a magma with an average Mg# of 54, while Ohakune orthopyroxenes are in equilibrium with a magma with an average Mg# of 51 (n=75). Putirka (2008) suggests a mineral-melt Fe-Mg K_D of 0.283 may be more appropriate for clinopyroxene-melt equilibria at the conditions of relevance; this brings the average Mg# of magma in equilibrium with the clinopyroxene to 57.5. Measurements of the groundmass glasses, on the other hand, have an average Mg# of 38, indicating that the pyroxenes are not in Fe-Mg equilibrium with their host melts.

Recent studies (e.g., Putirka 2008; Mollo *et al.* 2013; Neave *et al.* 2019) cast some doubt on the use of Fe-Mg K_D values to assess equilibrium of pyroxenes with their host melts. These studies suggest that a more robust test for equilibrium is to compare the DiHd (diopside-hedenbergite) component observed in pyroxenes with that predicted from the composition of the host melt. A one-to-one match indicates equilibrium. When we perform these tests for equilibrium on Ohakune pyroxenes and groundmass glass compositions, we find observed DiHd components in pyroxene of 0.71-0.78 and predicted DiHd components from the host melt of 0.65-0.72. At Ohakune, observed and predicted components vary from each other by 0.05-0.07, indicating some disequilibrium within the DiHd system. There is a 1σ uncertainty associated with Mollo *et al.*'s (2013) modeling (standard error of the estimate = 0.06), meaning that observed and predicted DiHd

in Ohakune pyroxenes do overlap within uncertainty. Thus, the disequilibrium present at Ohakune cannot be extensive.

In backscattered SEM imagery we observe thin (~6-35 μm) Fe-rich rims at the margins of glomerocrysts of ortho- and clinopyroxene (Fig. 2.4a); this piece of evidence may also support disequilibrium of minerals with their host melts. Embayed olivine also indicates a period of dissolution, possibly during ascent due to entrainment with an upwelling melt or mush. Rims of orthopyroxene on this embayed olivine may be the result of introduction into an SiO_2 -rich magma. These olivine subsequently underwent a peritectic transformation to orthopyroxene via the reaction $\text{Forsterite} + \text{SiO}_2 \rightarrow \text{Enstatite}$ (Zellmer *et al.* 2016). Some olivine does not exhibit this orthopyroxene reaction rim, but is simply contained within a network of ortho- and clinopyroxene (e.g. Fig 2.-3a). These observations suggest to us at least two phases of crystallization, as well as two phases of mineral transport and accumulation evident in the erupted Ohakune magmas.

2.6.1.1 Crystallization at Ohakune

The most Mg-rich silicate phase, and thus the first to crystallize from melts at Ohakune, is olivine. A study of olivine xenocrysts in mafic enclaves hosted within rhyolites from the Central TVZ found Fo content ranging from 79-86 concluded that these xenocrysts reflected the products of primitive basaltic melts (Barker *et al.* 2020). We observe olivine at Ohakune with Fo between 84.5-90.6. Ohakune olivine have equivalent and higher Fo contents than these rhyolite-hosted olivine. This suggests that Ohakune olivine are indeed the product of primitive mantle melts.

Given the Fo content of the Ohakune olivine, and assuming a Mg-Fe K_D of 0.30 (Roeder and Emslie 1970), the crystals should be in equilibrium with melts that have Mg# between 63.6 and 75.5. Perfit *et al.* (1980) suggested that primitive island arc basalt should have Mg# >65. Thus, the olivine in Ohakune samples is in equilibrium with, and plausibly crystallized from, a primitive

basaltic melt. Inclusions of spinel, visible in backscattered SEM imagery, also suggest a similar origin. Geophysical studies indicate that the crust below the southern TVZ is thick (up to 40 km at the far southern extent) and the lower crust is made of metamorphosed oceanic crust (Salmon *et al.* 2011). This is another possible source of the olivine, albeit unlikely given the refractory nature of olivine in oceanic crust.

When compared to olivine from the global MORB database (Sobolev *et al.* 2007) and arc magmas (compiled from the GEOROC database, Supplemental Document 3, Table C1), the Ohakune olivine best fits the arc compositional field, in Ni vs Fo space, and even more closely within Ca vs Fo space (Fig. 2.8). Petrographically, the olivine exists as embayed single crystals, not as nodules or cumulate fragments as might be expected from anatexis of refractory oceanic crust. Thus, the most simple and likely interpretation is that the Ohakune olivine originated as the earliest differentiation products of a primitive arc basalt.

The next phase of crystallization at Ohakune is that of two pyroxenes. The clinopyroxenes in Ohakune samples are slightly more magnesian than the orthopyroxenes. While the melts in equilibrium with these samples have slightly different Mg# (avg. 51 for orthopyroxene vs. avg. 54 for clinopyroxene), it is plausible that both pyroxenes are in equilibrium with the same melt, based on petrographic evidence (e.g., that they are contained in the same glomerocrysts with visible triple junctions). We interpret these minerals as having crystallized from melts with Mg# lower than that of olivine (Mg# 64-75), but higher than the melts they are contained within (Mg# 35-50).

2.6.1.2 Mineral Transport and Entrainment at Ohakune

The first phase of mineral transport at Ohakune occurs when olivine is entrained within an upwelling magma. The embayments observed in Ohakune olivine could be the result of dissolution via decompression melting on transport within levels of the differentiation zone (Ferguson *et al.*

2016). These embayments are filled with orthopyroxene in some samples, and other embayed olivine are contained in a network of clino- and orthopyroxene (see Fig. 2.3a). We interpret this as evidence that the entrained olivine crystals were stored in the same area where the pyroxenes crystallized. There is also evidence of olivine reacting with the melt to form orthopyroxene overgrowths because of this transport. We observe orthopyroxene that forms as antecrysts derived from mafic magma, but also as overgrowths of orthopyroxene. These overgrowths indicate a peritectic reaction between SiO_2 in the melt and the olivine that was transported (Zellmer *et al.* 2016). This recrystallization could have been precipitated by a mixing event between mafic crystals and an evolved melt.

The final stage of petrogenesis in Ohakune andesites is a second phase of crystal transport and brief storage in the magma with which they were erupted. Evidence for this stage of crystal uptake comes from the geochemical disequilibrium of the crystals and the groundmass glasses. Further evidence comes from Fe-rich rims (e.g., Fig. 2.4b). This rim is an indication that the minerals may have resided for some time in the melt they were erupted with (i.e., the groundmass glass melt). Other studies in the TVZ have calculated pre-eruptive storage times on the order of days to a year (Beier *et al.* 2017; Conway *et al.* 2020). It is also possible that these rims grew because of overgrowth from being in the host melt. Regardless of the cause of these overgrowths (diffusion or growth), these overgrowths indicate storage in a melt that is not in equilibrium with the crystals. We suggest here that this storage is outside of the main differentiation zone, either in a shallow staging chamber or during ascent to the surface.

2.6.1.3 Contamination at Ohakune

A key observation is that Ohakune orthopyroxenes (and to a lesser extent the clinopyroxenes) can be divided into two distinct geochemical groups (Lo-Al and Hi-Al). One

possible explanation for the observed Lo-Al and Hi-Al pyroxene groups may be due to sector zoning in pyroxene. This process is well documented (e.g., Nakamura 1973; Watson and Liang 1995; Neave *et al.* 2019; Ubide *et al.* 2019). Although our SEM observations do not show clear evidence for this process in Ohakune minerals, there are some geochemical similarities we observe that may support sector zoning. The most notable of these geochemical similarities are Al, Ti, Si, and Mg variation among the groups, which are commonly associated with this type of zoning in igneous minerals (Ubide *et al.* 2019). Ubide *et al.* (2019) note that transition metals do not necessarily partition into these sectors. In Ohakune minerals, we do observe variations in transition metals Cr and V. It is plausible that Ohakune minerals are sector zoned, resulting in our observations of varying Al, Ti, Si, Mg, and other elements.

Another possibility to explain the Hi-Al and Lo-Al groups comes from Kushiro (1960), who showed that Al, Cr, Ti, and Fe³⁺ increasingly substitute into the clinopyroxene structure as SiO₂ concentration decreases in a magma. We observe this relationship of increased SiO₂ and depleted Al₂O₃, Cr, V, and TiO₂ clearly in Ohakune orthopyroxene groups, and a similar distribution of these elements in the clinopyroxenes (Fig. 2.9). Thus, the presence of the Hi- and Lo-Al groups could be due to the increasing SiO₂ concentration of the host magma.

The SiO₂ increase could have been the result of magma evolution driven by crystallization. In this case, we would expect to observe a continuous core to rim zoning (i.e., Mg rich at the core to Fe rich at the rim) and associated core-to-rim Mg# decrease in crystals due to the changing concentration of these elements and SiO₂ in the magma (e.g. Nakagawa *et al.* 2002). Since we do not observe this type of zoning in Ohakune pyroxenes, we instead suggest that the SiO₂ increase of mafic melts prior to their arrival in the differentiation zone is dominantly the result of contamination rather than crystallization.

There is evidence of quartzite in the lower crust, which is a possible source of SiO₂ in the Ohakune hot zone. Our microscopic observations revealed disaggregated quartzite xenoliths (Fig. 3f). Graham and Hackett (1987) also found fragments of sediments from the Cenozoic-aged marine Torlesse terrane in the Ohakune scoriae. This material could have been taken up in ascending melts, and then partially dissolved during adiabatic ascent. This decompression melting of Torlesse sediments presents a plausible vector for the addition of SiO₂; we attribute the two pyroxene groups to this addition. This could also explain upwelling magmas with mafic character and high Mg#, but also SiO₂ enrichment, arriving in the differentiation zone.

2.6.1.4 Pressure and Temperature Constrains on the Ohakune Magma Plumbing System

Pressure and temperature constraints on the crystallization of the Ohakune pyroxenes can be used to infer the extent of the hot zone. Coexistence of two pyroxenes allow the application of calibrated geological thermometers and barometers (Putirka 2008). In these calculations the estimates of temperature ($\pm 38^\circ\text{C}$, eqn. 36; Putirka 2008) are relatively well constrained, while pressure estimates exhibit large uncertainties (± 2.8 kbar, or roughly ± 7 -10.5 km, eqn. 39; Putirka 2008). The temperatures and pressures are derived iteratively using equations 36 and 39 of Putirka (2008) and the spreadsheet model for two pyroxenes (Putirka 2015).

Our method was to take analyses of crystals within individual glomerocrysts (e.g. orthopyroxene and clinopyroxene crystals found in Glomerocryst 5021A Glom 1) and apply the thermometers and barometers presented by Putirka (2008) using the provided spreadsheet (Putirka 2015). We find that the crystals have variable opx-cpx Fe-Mg equilibrium constants, K_D . Putirka (2015) indicates that for magmatic systems a K_D of 1.09 ± 0.14 is appropriate, while in subsolidus systems a value of 0.7 ± 0.2 is more appropriate. We find equilibrium constants within the ranges for magmatic systems and subsolidus systems. This is consistent with the hypothesis that some of

the crystals (i.e., the pairs with K_D between 0.95 and 1.23) were crystallizing from a mafic melt directly, while others (i.e., pairs with K_D between 0.5 and 0.9) were those that were contained in sills that had achieved a subsolidus state prior to their disaggregation and incorporation in the Ohakune magmas. This also supports the hypothesis that crystals aggregated into the final eruption were drawn from a series of multiple sills in various states of crystallization.

We observe clinopyroxene and orthopyroxene pairs that return temperatures of 990-1065±38°C and crystallization pressures of 3.5-7±2.8 kbar (Fig. 2.10). These results are consistent with those obtained from the same geothermobarometer by Kósik *et al.* (2016) for Ohakune pyroxenes, which returned results of 4.8-5.4±2.8 kbar (~17-19 km depth) and 1034-1053°C. These depths are shallower, but within uncertainty of, those obtained by (Deering *et al.* 2011), who reported 1137-1154 °C and 6.5 kbar (23 km depth) using a clinopyroxene-liquid geothermobarometer. These results together broadly suggest that magmas crystallized in the middle to lower crust.

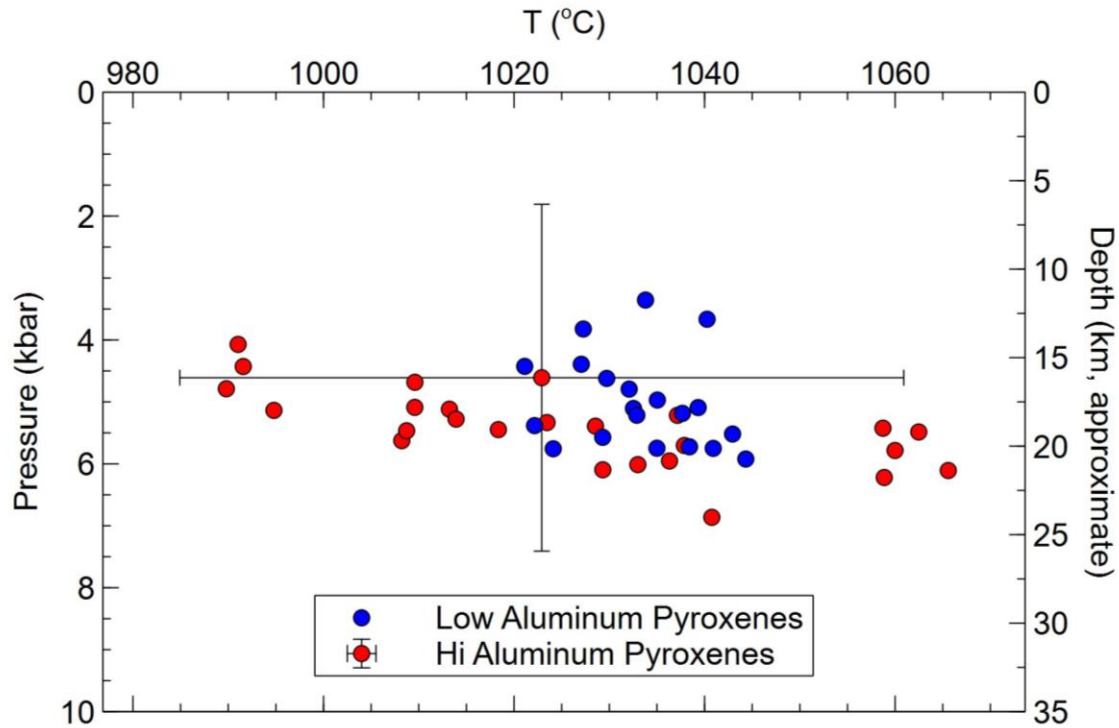


Figure 2.10

Diagram showing pressure and temperature constraints provided by thermobarometry modeled from pyroxene compositions using the spreadsheet and equations of Putirka (2008, 2015). Samples have been subdivided based on Lo-Al and Hi-Al crystal pairs, although we find no systematic differences between the two groups other than a wider spread of predicted temperatures for the Hi-Al group. Pressure is constrained using Equation 39 of Putirka (2008), while temperature is constrained using Equation 36 in the same work. Error on the estimates of temperature are $\pm 38^{\circ}\text{C}$ and estimates of pressure are ± 2.8 kbar (Putirka 2008); error bars are shown in the center of the figure to represent the uncertainty of the temperature and pressure estimates on each clinopyroxene-orthopyroxene pair.

The high and low aluminum pyroxene signatures observed at Ohakune could potentially reflect polybaric differentiation. Gasparik (1985) and Putirka *et al.* (1996) showed experimentally that with increasing pressure of crystallization, clinopyroxene will exhibit a higher proportion of

jadeite (Jd, $\text{NaAlSi}_2\text{O}_6$). Our data show that the Hi-Al clinopyroxenes have a slightly higher average Jd component (Hi-Al mean Jd = 0.0148, Lo-Al mean Jd = 0.0115). Outcomes of crystallization simulations on TVZ basalts using MELTS_Excel performed in this study (see Supplemental Document 4 for details) suggest that pressure could explain some of the compositional difference between the two groups. The Jd of the Hi Al clinopyroxenes is approximated by crystallization runs at 8 kbar, while the Jd of the Lo Al clinopyroxenes is approximated by crystallization at 5.3 kbar. The possibility of a polybaric differentiation system that spans the crust from ~5-8 kbar is, therefore, plausible based on these results. However, polybaric differentiation does not necessarily explain observed differences in TiO_2 , V, or Cr in these pyroxenes. Thus, the contamination described in the section “Contamination at Ohakune” remains a necessary process in describing the different pyroxene groups.

We have demonstrated that both pressure- and composition-driven changes to the system could be responsible for the observed dichotomy of pyroxenes. It is possible that both effects impacted Ohakune pyroxenes, and the various disparate crystals were mixed before eruption. The MELTS modelling outcomes also support the results of thermobarometric modelling: crystallization took place at pressures consistent with the mid- to lower crust (5-8 kbar). These results may also be explained by sector zoning; as a result of disequilibrium crystallization, at least one group of sectors records an inaccurate pressure of formation.

In their model for a magmatic mush column (i.e. a hot zone), Ganne *et al.* (2018) related the SiO_2 in a melt to the temperature, and to a lesser extent the depth, at which it crystallized. When our results are compared to the magmatic mush column model (e.g. Figs. 2.3A and B of Ganne *et al.* (2018)), the temperatures and SiO_2 contents do suggest an intermediate mush in the middle crust. In the Southern Rocky Mountain Volcanic field, from which the magmatic

mush column model in Ganne *et al.* (2018) is derived, the depths and densities of the different zones are based on an interpretive model created with geophysical and petrological constraints (Lipman and Bachmann 2015). This model, while not a perfect analogy to the TVZ, has similarities: the Southern Rocky Mountain Volcanic field is a continental rift, situated on ~45 km thick crust (Lipman and Bachmann 2015), whereas the TVZ is a rifting arc located on ~40 km thick crust (Gamble *et al.* 1990; Wilson *et al.* 1995; Villamor and Berryman 2006; Deering *et al.* 2011; Salmon *et al.* 2011). This similarity could indicate that hot zones in rifts and arcs evolve via common processes and pathways.

2.6.1.5 Synthesis

When taken together, our observations indicate the petrogenesis of the Ohakune andesites occurred by multiple stages of crystallization and mixing of intermediate melts with mafic crystal cargoes. This is consistent with formation within a hot zone. We have demonstrated through pyroxene thermobarometry and MELTS crystallization simulations that this hot zone is likely vertically extensive and may span from 3.5-8 kbar pressures (~12.5-28 km depth). Thus, this differentiation zone is best approximated by a series of sills with basaltic magmas in various states of crystallization. This is consistent with the petrographic textures of glomerocrysts reported here, as well as modeled cpx-opx equilibrium constants from the thermobarometry.

We have shown evidence that Ohakune magmas initially crystallize primitive olivine. The base of a hot zone may hence be defined as a region where high Fo olivine (Fo~80-90) crystallizes from a primitive basalt. At Ohakune, this olivine is transported, forms embayments during decompression, and is incorporated into slightly more evolved magmas and/or mushes. Magmas may be variably contaminated with SiO₂ during ascent through the lower crust. Melts move upward in the hot zone, carrying entrained olivine, where they continue to evolve through the

crystallization of pyroxenes. Batches of crystals are finally amalgamated together in an evolved melt prior to their final eruption. These processes are detailed in Fig. 2.11.

Diagram of the Ohakune Hot Zone

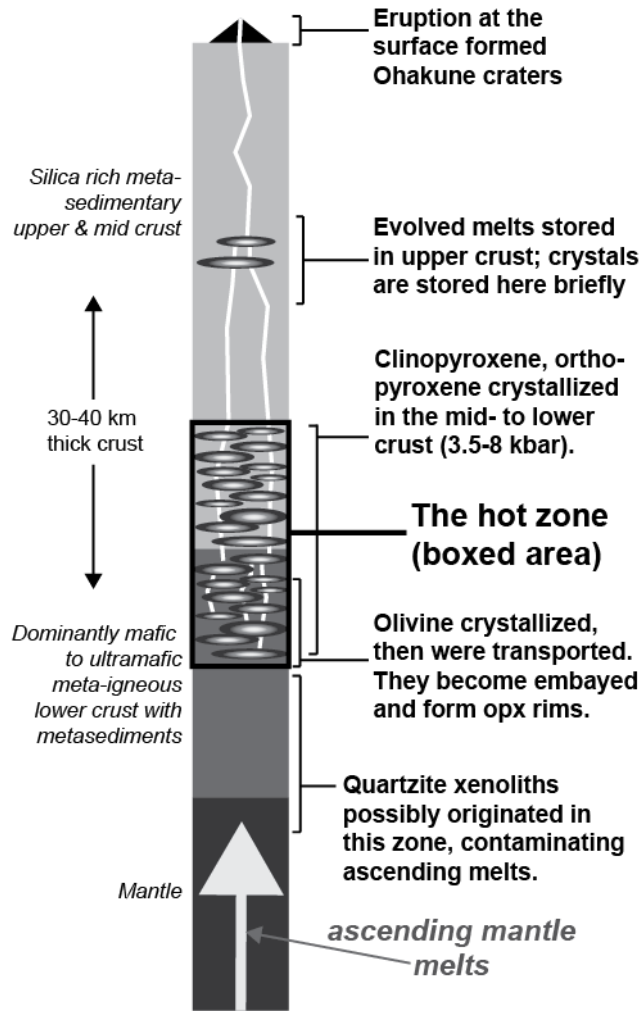


Figure 2.11

Diagrammatic figure (not to scale) that indicates the processes active in the Ohakune hot zone from the mantle to the surface.

Mixing of mafic and felsic materials appears commonly in descriptions of TVZ HMAD products - Conway *et al.* (2020) conclude that HMAD erupted at Ruapehu formed by mixing of mafic, forsterite-bearing magmas with felsic mid-crustal mushes. At Pukeonake, another satellite vent to Ruapehu (Fig. 1b), Beier *et al.* (2017) concluded that the HMAD found there is due to a multi-stage mixing of felsic melts with ferromagnesian minerals. We suggest there is a similar process operating with Ohakune andesites, whereby the whole-rock compositions are mixtures of

intermediate glasses “contaminated” by the high MgO and low Al₂O₃ mineral assemblage of olivine and two pyroxenes (Fig. 2.5; data shown from Beier *et al.* (2017) for comparison).

2.6.2 Maturation of Hot Zones into Transcrustal Magmatic Systems

There are several lines of evidence that support Ohakune eruptive products being drawn from deep, primitive levels of a magmatic plumbing system. In our samples, we observe olivine, orthopyroxene, and clinopyroxene with Mg# values that are too primitive to be in equilibrium with the measured groundmass glass composition. The predicted and observed DiHd components of pyroxenes are also not 1-to-1, suggesting disequilibrium. This disequilibrium, the match between predicted and observed jadeite components, and the range of crystallization pressures recorded by thermobarometry suggests that the crystalline cargo erupted at Ohakune was derived from a mush or series of mushes stored in the lower to middle crust that were remobilized and incorporated into andesitic melt stored in the upper crust. The evidence presented here supports the petrogenesis of Ohakune andesites in a stacked series of sills in the middle to lower crust by the mixing of mafic crystals and intermediate melts, consistent with a hot zone (Fig. 2.11).

The magmatic system sampled by Ohakune contains more primitive material than that sampled in modern magmatism in the nearby Ruapehu magmatic system. Glasses at Ohakune are more primitive than those found in andesites from Pukeonake or Ruapehu (Price *et al.*, 2012; Beier *et al.*, 2017). Olivine at Ohakune has a higher Fo than all Ruapehu formations that are younger than ca. 180 ka (Fo 55-70; Price *et al.*, 2012; Conway *et al.*, 2016). The primitive material sampled by Ohakune might be interpreted as products of the lower portions of the laterally more extensive nearby Ruapehu magmatic system. It may also represent a newly developing system occurring at the southern terminus of the propagating TVZ rift. With the data presented herein, it is not possible to unambiguously distinguish between these two models. Whether it is from a new system or

scavenged from the deep parts of Ruapehu's plumbing, the materials at Ohakune do represent products of the deep system that are unseen at well-developed edifices. At the opposite termination of the TVZ, at White Island, high Mg# andesites bearing high-Fo olivine phenocrysts (Heyworth *et al.* 2007) may be evidence of another deep hot zone. These materials from a different segment of the TVZ define a symmetry together with Ohakune.

A body of work suggests that a thermal maturation of the crust is necessary before more felsic magmas begin to emerge (e.g., De Silva *et al.* 2006; Bachmann *et al.* 2007). As more batches of magma intrude the continental crust, they release heat and assimilate increasing amounts of wall rock to further contaminate the magmas that differentiate within the hot zone. Our evidence supports this; we observe intermediate glasses at Ohakune that are less evolved than those found at Ruapehu and Pukeonake. These intermediate glasses represent melts that are sampled infrequently at arc volcanoes (Reubi and Blundy 2009). This is another piece of evidence that supports Ohakune materials being sourced from the deep system. We conclude that the deepest parts of transcrustal magmatic systems (i.e., where mafic melts evolve in hot zones) can be investigated by observing edifices found at the termination of structures such as the TVZ.

Evidence of transitional levels between the hot zone probed by Ohakune and the more mature upper parts of the transcrustal magmatic system may also be preserved within Pukeonake and older Ruapehu magmatic deposits. Tost *et al.* (2016) studied the petrography and geochemistry of distal mass-flow sediments derived from Ruapehu volcanics, which extended the initiation of volcanism at Ruapehu to >340 ka and as old as 490 ka ago. They concluded that the magmatic system at that time was a dispersed, small scale system in the middle to upper crust (Tost *et al.* 2016). The 250-180 ka Te Herenga Formation exhibits trace element compositions like that of the Ohakune eruptives and very different to other Ruapehu rocks (Figs. 2.5, 2.6; Price *et al.* 2012),

suggesting a somewhat immature system. This is consistent with the presence of primitive olivine in these rocks. However, the presence of phenocryst plagioclase requires shallower fractionation and points towards a potentially more transitional phase of the development of the transcrustal magmatic system. At Pukeonake, pyroxenes are still more primitive than the melts that contain them, but they are more evolved than those at Ohakune; plagioclase is also present there. Rocks erupted at Pukeonake exhibit sloped trace element patterns indicative of enhanced crustal assimilation (Price *et al.* 2012; Beier *et al.* 2017). Thus, Te Herenga & Pukeonake lavas may sample a transitional part (i.e., the middle levels) of the transcrustal magmatic system. Meanwhile, modern Ruapehu products likely sample the uppermost parts of the fully established transcrustal magmatic system. Our results, when integrated with these data from other edifices, thus constitute important contributions to our understanding of the structures and processes operating within the hot zones at the origin of arc magmatism.

2.7 Conclusions

Andesites erupted at Ohakune, a parasitic vent of Ruapehu in the Taupo Volcanic Zone, have high Mg# that is not a feature of the primary magmatic liquid but is instead due to entrainment of mafic minerals (olivine, orthopyroxene, and clinopyroxene) into a lower-Mg#, evolved melt. These crystals are not in equilibrium with their host melts. They are interpreted to be fragments of middle and lower crustal mushes that crystallized between 3.5-8 kbar based on constraints provided by this study. This conclusion is supported by other studies from the TVZ (Deering *et al.* 2011; Kósik *et al.* 2016).

There is evidence of possible SiO₂ contamination of ascending mafic melts or sector zoning at Ohakune that results in two distinct groups of pyroxenes, a high-Al group, and a low-Al group.

This contamination is a regional phenomenon influenced by specific lower crustal geology and is not the same as crustal assimilation that is later observed more globally as hot zones evolve, which manifest as sloped trace element patterns, incompatible element enrichments, and isotopic effects. Nearby within the TVZ, there is evidence for a transitional stage of hot zone development at Pukeonake and in Te Herenga deposits at Ruapehu. The modern eruptive products of Ruapehu with their geochemically and modally diverse mineralogy (Price *et al.* 2012; Conway *et al.* 2018, 2020) probably represent a mature transcrustal magmatic system. The textures and geochemical attributes of Ohakune eruptives show the processes active in a hot zone: periods of crystallization, crystal transport, magma-crystal mixing, and incorporation of crustal material.

A fully time-integrated view of evolving crustal differentiation systems relies on further constraining the physical, chemical, and temporal systematics in the development of transcrustal magmatic systems. Active volcanoes, extinct volcanoes, and satellite vents in subduction zones globally are the laboratories where these systematics will be refined. This is especially true at or near the termination of volcanic segments, and anywhere high-Mg# andesites are found.

BIBLIOGRAPHY

BIBLIOGRAPHY

- Annen, C., Blundy, J.D. and Sparks, R.S.J. 2006. The Genesis of Intermediate and Silicic Magmas in Deep Crustal Hot Zones. *Journal of Petrology*, **47**, 505–539, <https://doi.org/10.1093/petrology/egi084>.
- Bachmann, O. and Huber, C. 2019. The inner workings of crustal distillation columns; the physical mechanisms and rates controlling phase separation in silicic magma reservoirs. *Journal of Petrology*, **60**, 3–18.
- Bachmann, O., Miller, C.F. and de Silva, S.L. 2007. The volcanic–plutonic connection as a stage for understanding crustal magmatism. *Journal of Volcanology and Geothermal Research*, **167**, 1–23, <https://doi.org/10.1016/j.jvolgeores.2007.08.002>.
- Barker, S.J., Rowe, M.C., et al. 2020. What lies beneath? Reconstructing the primitive magmas fueling voluminous silicic volcanism using olivine-hosted melt inclusions. *Geology*, **48**, 504–508, <https://doi.org/10.1130/G47422.1>.
- Barnes, C.G., Coint, N. and Yoshinobu, A. 2016. Crystal accumulation in a tilted arc batholith. *American Mineralogist*, **101**, 1719–1734, <https://doi.org/10.2138/am-2016-5404>.
- Bédard, J.H. 2007. Trace element partitioning coefficients between silicate melts and orthopyroxene: parameterizations of D variations. *Chemical Geology*, **244**, 263–303.
- Bédard, J.H. 2010. Parameterization of the Fe=Mg exchange coefficient (Kd) between clinopyroxene and silicate melts. *Chemical Geology*, **274**, 169–176, <https://doi.org/10.1016/j.chemgeo.2010.04.003>.
- Beier, C., Haase, K.M., Brandl, P.A. and Krumm, S.H. 2017. Primitive andesites from the Taupo Volcanic Zone formed by magma mixing. *Contributions to Mineralogy and Petrology*, **172**, 33.
- Cashman, K.V., Sparks, R.S.J. and Blundy, J.D. 2017. Vertically extensive and unstable magmatic systems: A unified view of igneous processes. *Science*, **355**, eaag3055, <https://doi.org/10.1126/science.aag3055>.
- Cole, J.W. 1990. Structural control and origin of volcanism in the Taupo volcanic zone, New Zealand. *Bulletin of Volcanology*, **52**, 445–459, <https://doi.org/10.1007/BF00268925>.
- Conway, C.E., Leonard, G.S., Townsend, D.B., Calvert, A.T., Wilson, C.J., Gamble, J.A. and Eaves, S.R. 2016. A high-resolution ⁴⁰Ar/³⁹Ar lava chronology and edifice construction history for Ruapehu volcano, New Zealand. *Journal of Volcanology and Geothermal Research*, **327**, 152–179.
- Conway, C.E., Gamble, J.A., Wilson, C.J., Leonard, G.S., Townsend, D.B. and Calvert, A.T. 2018. New petrological, geochemical, and geochronological perspectives on andesite-dacite

- magma genesis at Ruapehu volcano, New Zealand. *American Mineralogist: Journal of Earth and Planetary Materials*, **103**, 565–581.
- Conway, C.E., Chamberlain, K.J., Harigane, Y., Morgan, D.J. and Wilson, C.J. 2020. Rapid assembly of high-Mg andesites and dacites by magma mixing at a continental arc stratovolcano. *Geology*, **48**, 1033–1037.
- De Silva, S., Zandt, G., Trumbull, R. and Viramonte, J. 2006. Large-scale silicic volcanism—The result of thermal maturation of the crust. *In: Advances in Geosciences: Volume 1: Solid Earth (SE)*. 215–230.
- Deering, C.D., Bachmann, O., Dufek, J. and Gravley, D.M. 2011. Rift-Related Transition from Andesite to Rhyolite Volcanism in the Taupo Volcanic Zone (New Zealand) Controlled by Crystal–melt Dynamics in Mush Zones with Variable Mineral Assemblages. *Journal of Petrology*, **52**, 2243–2263, <https://doi.org/10.1093/petrology/egr046>.
- Ferguson, D.J., Gonnermann, H.M., Ruprecht, P., Plank, T., Hauri, E.H., Houghton, B.F. and Swanson, D.A. 2016. Magma decompression rates during explosive eruptions of Kīlauea volcano, Hawaii, recorded by melt embayments. *Bulletin of Volcanology*, **78**, 1–12.
- Froggatt, P.C. and Lowe, D.J. 1990. A review of late Quaternary silicic and some other tephra formations from New Zealand: their stratigraphy, nomenclature, distribution, volume, and age. *New Zealand journal of geology and geophysics*, **33**, 89–109.
- Gamble, J.A., Smith, I.E.M., Graham, I.J., Peter Kokelaar, B., Cole, J.W., Houghton, B.F. and Wilson, C.J.N. 1990. The petrology, phase relations and tectonic setting of basalts from the taupo volcanic zone, New Zealand and the Kermadec Island arc - havre trough, SW Pacific. *Journal of Volcanology and Geothermal Research*, **43**, 253–270, [https://doi.org/10.1016/0377-0273\(90\)90055-K](https://doi.org/10.1016/0377-0273(90)90055-K).
- Ganne, J., Bachmann, O. and Feng, X. 2018. Deep into magma plumbing systems: Interrogating the crystal cargo of volcanic deposits. *Geology*, **46**, 415–418, <https://doi.org/10.1130/G39857.1>.
- Gasparik, T. 1985. Experimentally determined compositions of diopside-jadeite pyroxene in equilibrium with albite and quartz at 1200–1350°C and 15–34 kbar. *Geochimica et Cosmochimica Acta*, **49**, 865–870, [https://doi.org/10.1016/0016-7037\(85\)90178-4](https://doi.org/10.1016/0016-7037(85)90178-4).
- Graham, I.J. and Hackett, W.R. 1987. Petrology of calc-alkaline lavas from Ruapehu Volcano and related vents, Taupo Volcanic Zone, New Zealand. *Journal of petrology*, **28**, 531–567.
- Greene, A.R., DeBARI, S.M., Kelemen, P.B., Blusztajn, J. and Clift, P.D. 2006. A Detailed Geochemical Study of Island Arc Crust: the Talkeetna Arc Section, South–Central Alaska. *Journal of Petrology*, **47**, 1051–1093, <https://doi.org/10.1093/petrology/egl002>.
- Grove, T.L., Baker, M.B., Price, R.C., Parman, S.W., Elkins-Tanton, L.T., Chatterjee, N. and Müntener, O. 2005. Magnesian andesite and dacite lavas from Mt. Shasta, northern

- California: products of fractional crystallization of H₂O-rich mantle melts. *Contributions to Mineralogy and Petrology*, **148**, 542–565.
- Harrison, A.J. and White, R.S. 2004. Crustal structure of the Taupo Volcanic Zone, New Zealand: Stretching and igneous intrusion. *Geophysical Research Letters*, **31**, <https://doi.org/10.1029/2004GL019885>.
- Heyworth, Z., Turner, S., et al. 2007. ²³⁸U–²³⁰Th–²²⁶Ra–²¹⁰Pb constraints on the genesis of high-Mg andesites at White Island, New Zealand. *Chemical Geology*, **243**, 105–121.
- Hildreth, W. and Moorbath, S. 1988. Crustal contributions to arc magmatism in the Andes of Central Chile. *Contributions to Mineralogy and Petrology*, **98**, 455–489, <https://doi.org/10.1007/BF00372365>.
- Holness, M.B., Anderson, A.T., Martin, V.M., MacLennan, J., Passmore, E. and Schwindinger, K. 2007. Textures in Partially Solidified Crystalline Nodules: a Window into the Pore Structure of Slowly Cooled Mafic Intrusions. *Journal of Petrology*, **48**, 1243–1264, <https://doi.org/10.1093/petrology/egm016>.
- Houghton, B.F. and Hackett, W.R. 1984. Strombolian and phreatomagmatic deposits of Ohakune Craters, Ruapehu, New Zealand: a complex interaction between external water and rising basaltic magma. *Journal of volcanology and geothermal research*, **21**, 207–231.
- Jackson, M.D., Blundy, J. and Sparks, R.S.J. 2018. Chemical differentiation, cold storage and remobilization of magma in the Earth's crust. *Nature*, **564**, 405–409, <https://doi.org/10.1038/s41586-018-0746-2>.
- Kelemen, P.B. 1995. Genesis of high Mg# andesites and the continental crust. *Contributions to Mineralogy and Petrology*, **120**, 1–19.
- Kelley, K.A. and Cottrell, E. 2009. Water and the Oxidation State of Subduction Zone Magmas. *Science*, **325**, 605–607, <https://doi.org/10.1126/science.1174156>.
- Kósik, S., Németh, K., Kereszturi, G., Procter, J.N., Zellmer, G.F. and Geshi, N. 2016. Phreatomagmatic and water-influenced Strombolian eruptions of a small-volume parasitic cone complex on the southern ringplain of Mt. Ruapehu, New Zealand: facies architecture and eruption mechanisms of the Ohakune Volcanic Complex controlled by an unstable fissure eruption. *Journal of Volcanology and Geothermal Research*, **327**, 99–115.
- Kushiro, I. 1960. Si-Al relation in clinopyroxenes from igneous rocks. *American journal of science*, **258**, 548–554.
- Le Maitre, R.W. 1989. A classification of igneous rocks and glossary of terms. *Recommendations of the international union of geological sciences subcommission on the systematics of igneous rocks*, **193**.
- Lipman, P.W. and Bachmann, O. 2015. Ignimbrites to batholiths: Integrating perspectives from geological, geophysical, and geochronological data. *Geosphere*, **11**, 705–743.

- Mollo, S., Putirka, K., Misiti, V., Soligo, M. and Scarlato, P. 2013. A new test for equilibrium based on clinopyroxene–melt pairs: clues on the solidification temperatures of Etnean alkaline melts at post-eruptive conditions. *Chemical Geology*, **352**, 92–100.
- Nakagawa, M., Wada, K. and WOOD, C.P. 2002. Mixed magmas, mush chambers and eruption triggers: evidence from zoned clinopyroxene phenocrysts in andesitic scoria from the 1995 eruptions of Ruapehu volcano, New Zealand. *Journal of petrology*, **43**, 2279–2303.
- Nakamura, Y. 1973. Origin of sector-zoning of igneous clinopyroxenes. *American Mineralogist: Journal of Earth and Planetary Materials*, **58**, 986–990.
- Neave, D.A., Bali, E., Guðfinnsson, G.H., Halldórsson, S.A., Kahl, M., Schmidt, A.-S. and Holtz, F. 2019. Clinopyroxene–liquid equilibria and geothermobarometry in natural and experimental tholeiites: the 2014–2015 Holuhraun eruption, Iceland. *Journal of Petrology*, **60**, 1653–1680.
- Perfit, M.R., Gust, D.A., Bence, A.E., Arculus, R.J. and Taylor, S.R. 1980. Chemical characteristics of island-arc basalts: Implications for mantle sources. *Chemical Geology*, **30**, 227–256, [https://doi.org/10.1016/0009-2541\(80\)90107-2](https://doi.org/10.1016/0009-2541(80)90107-2).
- Price, R.C., Gamble, J.A., Smith, I.E.M., Maas, R., Waight, T., Stewart, R.B. and Woodhead, J. 2012. The Anatomy of an Andesite Volcano: a Time–Stratigraphic Study of Andesite Petrogenesis and Crustal Evolution at Ruapehu Volcano, New Zealand. *Journal of Petrology*, **53**, 2139–2189, <https://doi.org/10.1093/petrology/egs050>.
- Putirka, K. 2015. *Two-Pyroxene Thermometers and Barometers*. Excel.
- Putirka, K., Johnson, M., Kinzler, R., Longhi, J. and Walker, D. 1996. Thermobarometry of mafic igneous rocks based on clinopyroxene-liquid equilibria, 0-30 kbar. *Contributions to Mineralogy and Petrology*, **123**, 92–108, <https://doi.org/10.1007/s004100050145>.
- Putirka, K.D. 2008. Thermometers and Barometers for Volcanic Systems. *Reviews in Mineralogy and Geochemistry*, **69**, 61–120, <https://doi.org/10.2138/rmg.2008.69.3>.
- Reubi, O. and Blundy, J. 2009. A dearth of intermediate melts at subduction zone volcanoes and the petrogenesis of arc andesites. *Nature*, **461**, 1269–1273.
- Roeder, P.L. and Emslie, Rf. 1970. Olivine-liquid equilibrium. *Contributions to mineralogy and petrology*, **29**, 275–289.
- Rooney, T.O., Hart, W.K., Hall, C.M., Ayalew, D., Ghiorso, M.S., Hidalgo, P. and Yirgu, G. 2012. Peralkaline magma evolution and the tephra record in the Ethiopian Rift. *Contributions to Mineralogy and Petrology*, **164**, 407–426.
- Rooney, T.O., Morell, K.D., Hidalgo, P. and Franceschi, P. 2015. Magmatic consequences of the transition from orthogonal to oblique subduction in P anama. *Geochemistry, Geophysics, Geosystems*, **16**, 4178–4208.

- Salmon, M.L., Stern, T.A. and Savage, M.K. 2011. A major step in the continental Moho and its geodynamic consequences: the Taranaki-Ruapehu line, New Zealand. *Geophysical Journal International*, **186**, 32–44.
- Sobolev, A.V., Hofmann, A.W., et al. 2007. The amount of recycled crust in sources of mantle-derived melts. *science*, **316**, 412–417.
- Solano, J.M.S., Jackson, M.D., Sparks, R.S.J., Blundy, J.D. and Annen, C. 2012. Melt Segregation in Deep Crustal Hot Zones: a Mechanism for Chemical Differentiation, Crustal Assimilation and the Formation of Evolved Magmas. *Journal of Petrology*, **53**, 1999–2026, <https://doi.org/10.1093/petrology/egs041>.
- Straub, S.M., Gomez-Tuena, A., Stuart, F.M., Zellmer, G.F., Espinasa-Perena, R., Cai, Y. and Iizuka, Y. 2011. Formation of hybrid arc andesites beneath thick continental crust. *Earth and Planetary Science Letters*, **303**, 337–347.
- Sun, S. -s. and McDonough, W.F. 1989. Chemical and isotopic systematics of oceanic basalts: implications for mantle composition and processes. *Geological Society, London, Special Publications*, **42**, 313–345, <https://doi.org/10.1144/GSL.SP.1989.042.01.19>.
- Tost, M., Price, R.C., Cronin, S.J. and Smith, I.E.M. 2016. New insights into the evolution of the magmatic system of a composite andesite volcano revealed by clasts from distal mass-flow deposits: Ruapehu volcano, New Zealand. *Bulletin of Volcanology*, **78**, 38, <https://doi.org/10.1007/s00445-016-1030-7>.
- Ubide, T., Mollo, S., Zhao, J., Nazzari, M. and Scarlato, P. 2019. Sector-zoned clinopyroxene as a recorder of magma history, eruption triggers, and ascent rates. *Geochimica et Cosmochimica Acta*, **251**, 265–283.
- Villamor, P. and Berryman, K.R. 2006. Evolution of the southern termination of the Taupo Rift, New Zealand. *New Zealand Journal of Geology and Geophysics*, **49**, 23–37.
- Walker, B.A., Bergantz, G.W., Otamendi, J.E., Ducea, M.N. and Cristofolini, E.A. 2015. A MASH Zone Revealed: the Mafic Complex of the Sierra Valle Fértil. *Journal of Petrology*, **56**, 1863–1896, <https://doi.org/10.1093/petrology/egv057>.
- Watson, E.B. and Liang, Y. 1995. A simple model for sector zoning in slowly grown crystals: Implications for growth rate and lattice diffusion, with emphasis on accessory minerals in crustal rocks. *American Mineralogist*, **80**, 1179–1187.
- Wilson, C.J.N., Houghton, B.F., McWilliams, M.O., Lanphere, M.A., Weaver, S.D. and Briggs, R.M. 1995. Volcanic and structural evolution of Taupo Volcanic Zone, New Zealand: a review. *Journal of volcanology and geothermal research*, **68**, 1–28.
- Zellmer, G.F., Sakamoto, N., Matsuda, N., Iizuka, Y., Moebis, A. and Yurimoto, H. 2016. On progress and rate of the peritectic reaction $\text{Fo} + \text{SiO}_2 \rightarrow \text{En}$ in natural andesitic arc magmas. *Geochimica et Cosmochimica Acta*, **185**, 383–393.

3. IMPLICATIONS OF PYROXENITE IN THE SOURCE OF CENOZOIC (EOCENE-RECENT) MAGMATISM IN THE TRIPLE JUNCTION PROVINCE OF PATAGONIAN ARGENTINA

3.1 Introduction

A modern seismic and volcanic gap in the Andean arc represents an important discontinuity in the ongoing ocean-continent orogeny at the western margin of South America (Hayes et al., 2015; Ramos & Kay, 1992). The presence of back arc magmatism in Patagonia to the east of this gap is linked to the subduction of the Chile Rise spreading center over the last 16 Ma (Breitsprecher & Thorkelson, 2009; Boutonnet et al., 2010; Ávila & Dávila, 2020). However, magmas as old as 40 Ma may indicate that ongoing processes within the mantle there have operated for longer than this spreading ridge subduction has been active (Kay et al., 2004). One of the primary ways to infer the characteristics of the mantle is to study the geochemical attributes of basaltic lavas erupted at the Earth's surface. Of particular interest are the pressure, temperature, and composition of that mantle source region, and associated lithologic heterogeneity of that source (Kimura & Kawabata, 2015).

Recently, there has been recognition of pyroxene-rich lithologies in the mantle, and the important role of these pyroxenites in producing magmas in a variety of tectonic settings (e.g., Herzberg, 2006, 2011; Bizimis et al., 2013; Heinonen et al., 2013; Søger et al., 2013, 2015; Lambart et al., 2016). These pyroxene-rich lithologies are thought to represent recycled oceanic crust (Trela et al., 2015), or delamination (“dripping”) of the lower lithospheric mantle (Ducea et al., 2013; Guo et al., 2015). Because they represent smaller and more constrained melting regimes, areas with small-volume basaltic magmatism are considered excellent natural laboratories for

exploring mantle heterogeneity and lithology; they are also important in constraining the temperature and pressure of these source regions (McGee et al., 2017). Small-volume lava flows in the back-arc of Patagonian Argentina provide an excellent opportunity to investigate these mantle source characteristics and their link to subduction phenomena.

There is debate as to whether magmatism in Patagonia is sourced from the sub-slab asthenosphere or if convection brings material in from the south Atlantic. Some works have suggested that interactions between subducting slabs and the underlying asthenosphere are the cause (Gorring & Kay, 2001; Ávila & Dávila, 2020), invoking vertical flow through asthenospheric windows. Others suggest that lateral convection of material from the south Atlantic drives this magmatism (Søager et al., 2021). The arrangement of tectonic plates today, with mid-ocean ridge segments colliding with the continent, favor the first model (Gorring et al., 1997; Breitsprecher & Thorkelson, 2009). Meanwhile the continuous subduction of oceanic crust at the western margin of Patagonia since the Jurassic and the consequent convection cell established there, as well as the presence of ocean islands and elevated melt volumes at the Mid Atlantic Ridge favor the second model (Søager et al., 2021). Therefore, there is still uncertainty about the source of these magmas.

In this work we present six new $^{40}\text{Ar}/^{39}\text{Ar}$ isotopic eruption dates; these magmas range in age from Eocene (~40 Ma ago) to Pleistocene (~2 Ma ago). The Alma Gaucha formation dated in this study (age 20-22 Ma) does not coincide with recognized periods where slab windows occur, conflicting with the slab window model for melt generation. We examine the major and trace element geochemistry of 41 basaltic magmas from the Triple Junction province of Patagonia. We use this geochemistry to test the hypothesis that pyroxenite in the mantle source region is the cause of melt generation over the last 40 Ma. We propose a new third model whereby this pyroxenite is

neither from sub-slab asthenosphere nor the South Atlantic convection cell. Rather, the source in our model is delaminated material that was impregnated into the lithosphere of the Deseado Massif during magmatism in the Mesozoic and the breakup of Gondwana that has since achieved negative buoyancy and therefore melts upon dripping into the asthenosphere. We use thermodynamic models that utilize trace element geochemistry to demonstrate that melt source regions containing volumes of pyroxenite (3-11%) at high pressures (2.6-2.7 GPa) have been the primary contributors to back-arc magmatism through the entire Cenozoic history of magmatism from the Eocene to recent. This work has important implications that contradict tectonic models relying on slab windows for melt generation in this back arc, as well as those that rely on convection of material from the south Atlantic. Our results (e.g., the eruption age of Alma Gaucha formation outside of the period of a slab window, similar trace element chemistry among younger and older magmas, and similarity of modeling outcomes) may suggest new models that do not require an active slab window are needed to describe this magmatism. Furthermore, this work has global implications as to the source of trace element enriched continental small volume magmas: these magmas could be derived from delaminated lithospheric pyroxenites.

3.2 Geologic Background

3.2.1 Cenozoic Magmatism in the Andean Arc and Back Arc

Along the western edge of South America, the subduction of the Nazca and Antarctic plates beneath the westward-moving continent creates an ongoing ocean-continent subduction orogeny (Figure 3.1). There is significant along-strike variation in the seismicity and the style of volcanism (Kay et al., 2004; Hayes et al., 2013). One of the primary factors controlling this variation is the age of the subducting oceanic crust; between 34°S and 52°S latitude in South America, the age of

subducting oceanic crust ranges from as old as 50 Ma in the north to zero at the Chile Triple Junction (Kay et al., 2004). In the north where older crust is subducting, there are abundant stratovolcanoes in the magmatic arc, and continental back-arc magmatism is located nearer to the volcanic arc (Kay et al., 2004). In contrast, near the Chile Triple Junction where a mid-ocean ridge segment is subducting, there are no stratovolcanoes active in the arc and back-arc magmatism is found up to 450 km from the trench.

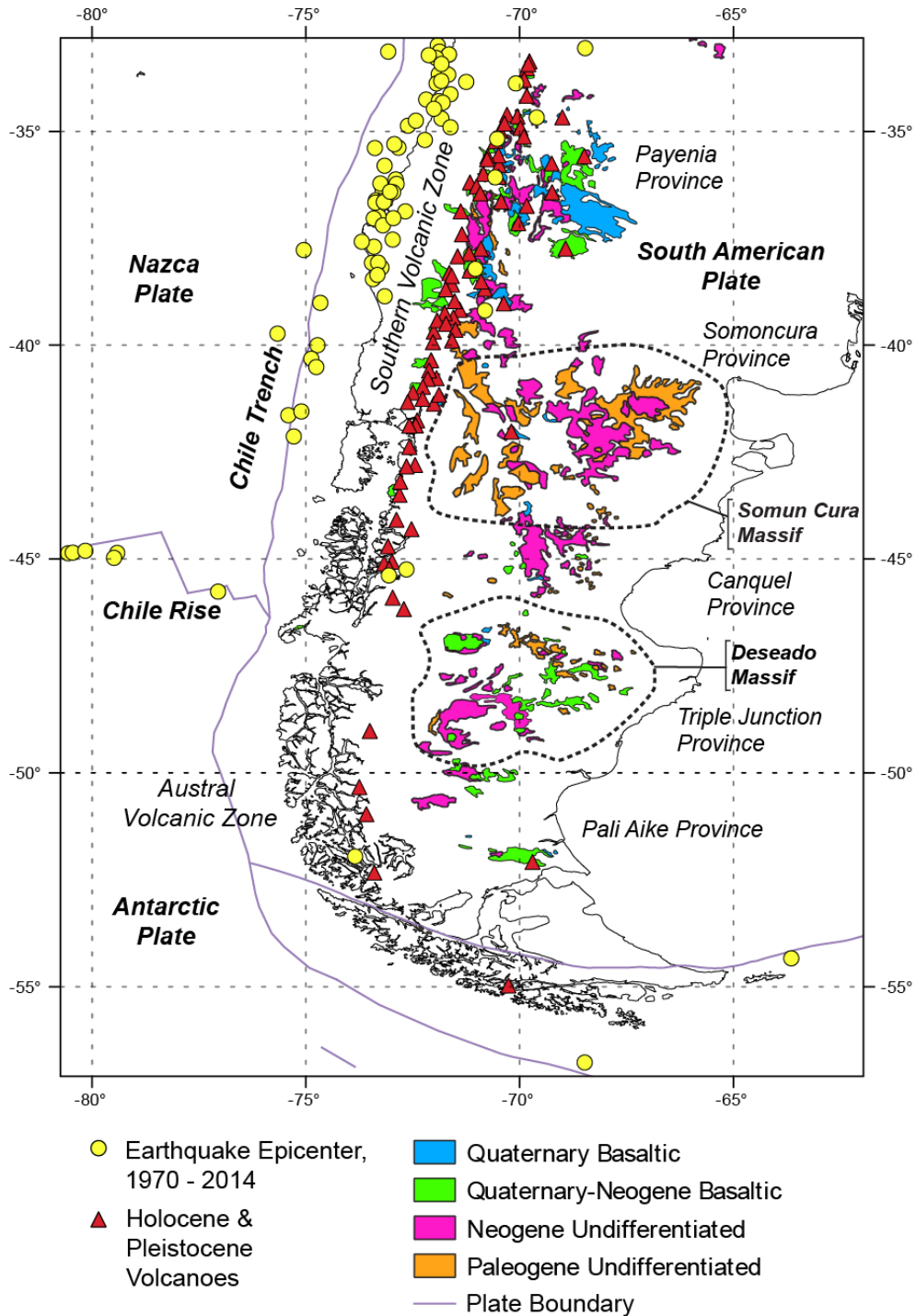


Figure 3.1

Overview map of Patagonia (South America) showing important tectonic and magmatic features. The purple lines represent plate boundaries such as the Chile Rise oceanic spreading

Figure 3.1 (cont'd)

center and the Chile Trench. Earthquakes are represented by yellow circles (Global Catalog of Earthquakes - Humanitarian Data Exchange (USGS ANSS Comprehensive Catalog)), while Holocene and Pliocene volcanoes are shown as red triangles (Smithsonian Institution & Venzke, 2013a, 2013b). The location and ages of Cenozoic lavas are shown by the colored polygons (Gómez et al., 2019). The names of each of the Cenozoic back-arc magmatic provinces are shown in italicized text. Dashed areas show the approximate boundaries of the two Patagonian massifs, the Deseado and Somun Cura (Ramos, 2008). The area of this study is located within the Deseado Massif; see Figure 3.2.

In the area from 34°S and 52°S, the Andean volcanic arc is divided into three segments (Kay et al., 2004; Søger et al., 2021; Figure 3.1). The northernmost segment is the Southern Volcanic Zone (SVZ). At 46°S and stretching to 49°S lies a volcanic and seismic gap east of the Chile Triple Junction where segments of the Chile Rise spreading center and very young adjacent oceanic lithosphere are subducting beneath the continent. Here, the volcanoes of the arc are extinct (Ramos & Kay, 1992). The area is uplifted, evidenced by large glaciated and elevated areas of the Andes (Lagabrielle et al., 2010). The area is also a seismic gap, and no earthquakes of M5.0 or greater have occurred in this 3° latitude stretch since record keeping began (Hayes et al., 2013). South of 49°S is the Austral Volcanic Zone where arc-type volcanic centers reappear in the cordillera (Stern & Kilian, 1996).

Back-arc magmatism occurs almost continuously north to south from 35°S to 52°S in the continental areas to the east of the Andes (Figure 3.1). These extensive back-arc intraplate basalts are ascribed to tectonic causes, where upwellings are in response to subduction-related phenomena

occurring to the west (Gorring et al., 1997; Gorring & Kay, 2001; Massaferrero et al., 2014; Sjøager et al., 2021). Building on the understanding that subduction is a driver of convection cells within the asthenosphere, Sjøager et al. (2021) suggested that all the back-arc magmatism reflected the South Atlantic convection cell, and these continental basalts were analogous to seamounts and ridge segments located in the eastern Atlantic. They modeled isotopic mixing of depleted south Atlantic MORB with the associated seamount chains on the opposite side of the Atlantic Ocean (e.g., Discovery, Bouvet hot-spots). Sjøager et al. (2021) note that low CaO (<9 wt. %) and high whole-rock FeO^T/MnO (up to 79) in Central Patagonia are suggestive of a pyroxenitic, EM-1 type source.

There are five broad back-arc provinces defined by Sjøager et al. (2021); from north to south, they are the Payenia province, the Somuncura province, the Canquel province, the Triple Junction province, and the Pali Aike province. The extent of these five provinces is shown in Figure 3.1. These back-arc volcanic provinces are all thought to be the result of upwellings established by local mantle flow patterns and slab geometries, and the local subcontinental lithospheric and asthenospheric mantle provides the material that melts (Guivel et al., 2006; Massaferrero et al., 2014; Jalowitzki et al., 2017; Sjøager et al., 2021). Sjøager et al. (2013) established that EM-1 (OIB) type asthenospheric materials were the source of volcanism in the southern Payenia province whereas northern Payenia was generated from more MORB (Mid-Ocean Ridge Basalt)-like mantle. Furthermore, Sjøager et al. (2015) put forth a model where these upwellings are mixed peridotite (i.e., MORB) and pyroxenite (i.e., OIB) lithologies that were drawn in and melted due to slab breakoff. Massaferrero et al., (2014) attributed intraplate basalts in the Somuncura and Canquel regions as a response to back-arc thinning and melting of the lithosphere. Ages of back arc magmatism range from Eocene to the Pleistocene (Kay et al., 2004;

Espinoza et al., 2005; Sjøger et al., 2021). The material that is erupted along much of this back-arc magmatic province is ocean-island basalt (OIB) type, trace element enriched magma (Kay et al., 2004; Espinoza et al., 2005;).

This study focuses on magmas of the Triple Junction province. There, Gorrington et al. (1997; 2001) attributed Neogene-Quaternary OIB back-arc to upwelling of material through an asthenospheric window. This window opened in response to mid-ocean ridge segments colliding with the continent and being arrested there, while the plate that represents the eastern side of the mid-ocean ridge is pulled into the mantle by the ostensibly older slab material that is subducting further east. Gorrington & Kay (2001) suggest that small-scale heterogeneities within the asthenosphere are responsible for this trace element enriched magmatism in the Triple Junction Province.

Gorrington & Kay (2001) also divided the timing of this magmatism into two periods: A Plateau phase from 12 to 5 Ma ago with higher volumes of melt (7-10%); and a post-Plateau phase from 5-2 Ma ago with lower melt volumes (1-2%). They also note that in the Northeast region (our sample area, the furthest east magmas in the back-arc) there is not as noticeable of a difference from 12-2 Ma magmas (Gorrington & Kay, 2001). Both Plateau phase and post-Plateau phase magmas are modeled by 2-5% partial melt volumes (Gorrington & Kay, 2001).

3.2.2 Ridge-Trench Interaction and Patagonian Slab Windows

In the Triple Junction province, the tectonic cause of back-arc magmatism is a slab window that has developed since 12-16 Ma ago (Gorrington et al., 1997; Gorrington & Kay, 2001; Guillaume et al., 2010; Ávila & Dávila, 2020). A slab window occurs when a seismic mid-ocean ridge is overridden by continental crust (Thorkelson, 1996). In this model, the western edge of the ocean ridge becomes arrested against the continental crust, while the dense slab descending into the

mantle on the eastern side of the ridge continues pulling the entirety of that plate with it (Breitsprecher & Thorkelson, 2009). This creates a window between these two slabs. Asthenospheric material can upwell through this window. Ideally, this window forms at the weakest areas of the plate, i.e., the ridge itself and the transform faults that connect ridge segments (Thorkelson, 1996; Breitsprecher & Thorkelson, 2009).

There are other geographical areas in the literature where slab windows are recognized: The Central American Cocos-Nazca slab window (e.g., Johnston & Thorkelson, 1997); the Pacific-Juan de Fuca-North America system (e.g., McCrory et al., 2009); the Philippine Sea plate (Huang et al., 2013); and in the Antarctic Peninsula (Breitsprecher & Thorkelson, 2009). In addition to the current slab window model for magmatism since the Miocene period, recent kinematic plate reconstruction models also suggest the possibility of another slab window episode in Patagonia in the Paleocene to Eocene period (Navarrete et al., 2020). All these slab windows are mainly constrained by methods such as lava geochemistry, radiometric dates, and plate kinematic reconstructions (McCrory et al., 2009). The geophysical evidence for slab windows is more sparse because of the transient nature of these phenomena (McCrory et al., 2009). The presence of a modern slab window has been shown in P-wave velocity models of the Philippine Sea plate (Huang et al., 2013). The volcanic & seismic gap in Patagonia is considered evidence for the presence of a slab window (Gorring et al., 1997; Gorring & Kay, 2001). Similarly, in the Central American region, the lack of a Benioff zone is considered evidence for the Cocos-Nazca slab window (Breitsprecher & Thorkelson, 2009).

3.2.3 Tectonic and Magmatic History of the Deseado Massif

The lavas that are the focus of this study are in the Deseado Massif, which is physiographic and geological area of Patagonia (Figure 3.1). It is one of two large basement massifs that make

up Patagonia, the other being the Somun Cura massif to the north (Ramos, 2008). Isotopic evidence in the Re-Os system from Patagonian xenoliths suggests that the oldest lithosphere in the Deseado Massif was formed during the Mesoproterozoic, roughly 1.3 Ga ago (Mundl et al., 2015). The extent of the Deseado Massif is roughly the same as the extent of the Triple Junction Province shown in Figure 3.1. These massifs are bounded by basins to the north and south, and the Andes Mountains to the west (Ramos, 2008). These Patagonian massifs were once part of the supercontinent Gondwana until the breakup which began at ~190 Ma; they were thought to be adjacent to South Africa and the Antarctic Peninsula in the southern extent of the landmass prior to breakup (Pankhurst et al., 1998; Ramos, 2008; Navarrete, Butler, et al., 2020).

There are two periods of magmatism that have affected the Deseado Massif regarding this study:

(A) A period of magmatism represented by the Mesozoic-aged Chon Aike and Bajo Pobre formations. The Bajo Pobre formation is the mafic end member of the largely silicic Chon Aike Large Igneous Province (LIP; Pankhurst et al., 1998). Silicic LIPs are rare on Earth, and they form extensive rhyolite and pyroclastic rocks related to widespread partial melting of the lower crust due to the intrusion of basaltic melts (Pankhurst et al., 1998). The Bajo Pobre and Chon Aike formations formed from ~188-153 Ma in a protracted episode of magmatism related to the breakup of Gondwana (Pankhurst et al., 1998; Navarrete, Butler, et al., 2020). The Chon Aike silicic LIP occurred synchronously with two other mafic large igneous provinces, the Karoo and Ferrar, which are also related to the breakup of Antarctica, Patagonia, South America, and Africa; there is also evidence that subduction of oceanic crust at what is now the western margin of Patagonia also had an influence on the Chon Aike LIP (Pankhurst et al., 1998; Navarrete, Butler, et al., 2020).

(B) A period of magmatism in the Deseado Massif represented by areally extensive, though volumetrically limited, continental basaltic volcanism that occurred from the Eocene until the Pleistocene. This volcanism was alkaline, with enriched trace element chemistry and isotopic signatures that suggest involvement of EM-1-type OIB mantle (Gorring & Kay, 2001; Kay et al., 2004; Espinoza et al., 2005) possibly upwelling through one or more slab windows. Kay et al. (2004) recognizes that early-Miocene volcanism in this part of Patagonia (e.g., Alma Gaucha basalts) is difficult to connect with a tectonic mechanism of magma generation. This is because the volcanic episode does not coincide with either of the slab windows that are thought to have occurred in this part of Patagonia during the Paleocene-Eocene (53-40 Ma ago) and from the mid-Miocene (16 Ma ago to present) (Gorring et al., 1997; Kay et al., 2004; Espinoza et al., 2005; Guillaume et al., 2010; Navarrete, Gianni, et al., 2020). It is this period of volcanism that is the focus of this study.

3.3 Materials and Methods

3.3.1 Samples

Samples were collected from the study area during a field expedition in March 2018. The method of collection was to break free a ~10cm × 10cm × 10cm piece of fresh rock material from the outcrop by striking it with a sledgehammer. The collection site was decided by the most angular area of the rock outcrop, and during sampling we took care to avoid any areas of conspicuous alteration.

Samples were collected from five separate stratigraphic units. These unit names were derived from Programa National de Cartas Geologicas de la Republica Argentina maps and associated materials, specifically numbers: 4969-I bulletin no. 239 (Gobernador Gregores; Panza

et al., 1998); 4769-IV bulletin no. 258 (Monumento Natural Bosques Petrificados; (Panza, 2001); 4769-III bulletin no. 296 (Destacamento la Maria; Panza & Cobos, 2001); 4769-I bulletin no. 319 (El Pluma; Cobos & Panza, 2003); and 4969-II bulletin no. 213 (Tres Cerros; Panza et al., 1994).

The units are as follows, listed from youngest to oldest, with their estimated ages and a brief summary of the descriptions given in the maps:

- (A) La Angelita (Pliocene-Pleistocene) – Mesa-forming melanocratic basalts with olivine \pm plagioclase and occasional ultramafic (olivine \pm clinopyroxene) nodules (Panza, 2001).
- (B) Cerro Mojon (Miocene-Pliocene) – Microvesicular olivine basalts with variably altered crystals (Panza, 2001)
- (C) Basalto de las Lagunas sin Fondo (henceforth BLSF; Mid-Miocene) – Melanocratic porphyritic olivine \pm plagioclase basalts (Cobos & Panza, 2003)
- (D) Alma Gaucha (Early Miocene) – Melanocratic basalts and basanites with altered olivine, clinopyroxene, and feldspar (Panza, 2001).
- (E) Cerro del Doce (Eocene) – Melanocratic olivine basalts (Panza, 2001).

The spatial relationship among units is shown in Figure 3.2.

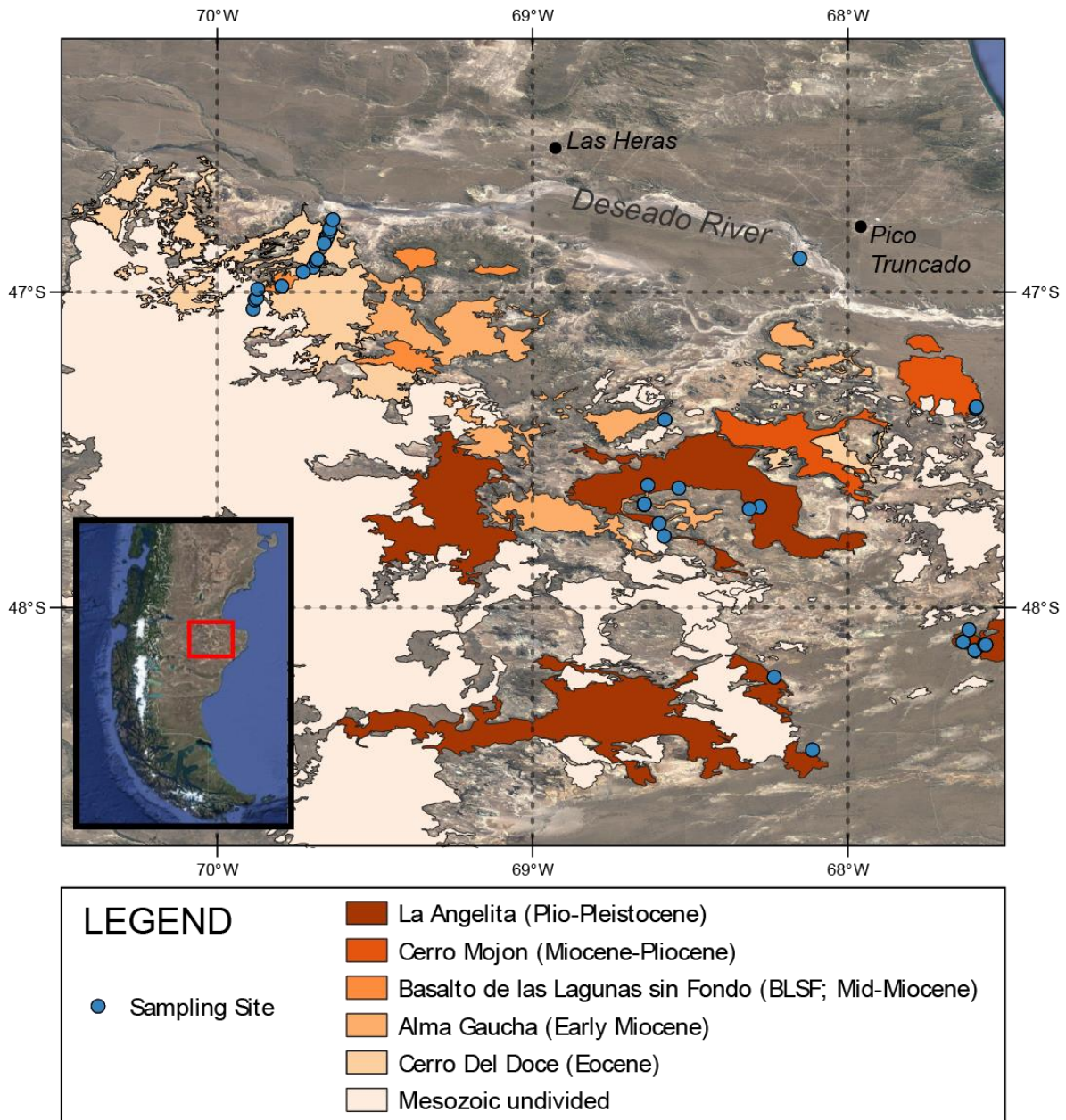


Figure 3.2

Map of the study area showing the extent of Cenozoic and Mesozoic magmatic rocks in the Deseado Massif, Santa Cruz province, Argentina. Colored areas represent the full extent of mapped lava flows from each unit, and circles indicate individual sampling locations. Mesozoic units are shown here to illustrate how closely associated Cenozoic magmatic units are in space

Figure 3.2 (cont'd)

with these Mesozoic volcanics. Inset shows the extent of this mapped area in South America. Base imagery is Google satellite imagery.

3.3.2 Whole Rock Major & Trace Elements

Samples were prepared for whole rock major and trace element analysis at Michigan State University. First samples were cut into billets with a lapidary saw, with care taken to retain only basaltic groundmass; areas of alteration and obvious crystals were trimmed or polished out of the final billets. These billets then had saw marks wet-sanded off their surfaces. Billets were sonic cleaned in deionized water for two five-minute cycles and water was changed between cycles to remove any potential cross-contamination, then dried under hot air.

Billets were first chipped, and then ground into fine powder (rock flour) in an alumina mill. This powder was fused into glass disks for analysis. Fusion occurred in platinum crucibles to prevent any reactivity with elements in the sample. Lithium tetraborate flux was used in a 3:1 ratio with rock flour (9g borate flux to 3g rock flour) and 0.5g of ammonium nitrate was added as an oxidizer, to oxidize all Fe^{2+} into Fe^{3+} . Samples were then melted into a liquid by oscillating them over a Bunsen burner in the platinum crucibles for 20 minutes and then pouring the liquid material into a disk-shaped platinum mold.

Fused glass disks were analyzed for major elements at Michigan State University using a Bruker S4 X-ray fluorescence spectrometer following the methods of Rooney et al. (2012). Fused glass disks used for major element analysis are further analyzed for the concentrations of geologically relevant trace elements following the methods of Rooney et al. (2015). Analysis was completed via laser-ablation inductively coupled plasma mass spectrometry (LA-ICP-MS) using

a Photon-Machines Analyte G2 excimer laser for ablation, coupled to a Thermo Scientific ICAP Q quadrupole ICP-MS, at Michigan State University. Three scans were completed for each sample, and the result of those three analyses was averaged. These averaged results were the elemental concentrations reported.

3.3.3 Ar-Ar Isotopic Dating

$^{40}\text{Ar}/^{39}\text{Ar}$ isotopic age analyses were conducted on basaltic groundmass glass at the University of Nevada, Las Vegas Department of Geosciences Nevada Isotope Geochronology Lab (NIGL). We selected five samples for analysis, with at least one sample from each temporal group (two from La Angelita, one from BLSF, one from Alma Gaucha, and two from Cerro del Doce). We also made sure to obtain dates on lava flows that had not been dated by Gorrying et al. (1997) to add new temporal resolution to magmatism in this part of Patagonian Argentina. We chose the matrix of phenocryst-poor samples that did not show evidence of visible alteration (i.e., brown, green, red, or opaque areas of the groundmass) and have no altered groundmass olivine (Krans, personal communication). Finally, two newly discovered xenolith host magmas were selected for dating (Volcan Auvernia and Estancia True Aike localities).

The laboratory PI at NIGL at the time of analysis, Terry Spell, provided the following general comments regarding $^{40}\text{Ar}/^{39}\text{Ar}$ laboratory procedures:

“Samples analyzed by the $^{40}\text{Ar}/^{39}\text{Ar}$ method at the University of Nevada Las Vegas were wrapped in Al foil and stacked in 6 mm inside diameter sealed fused silica tubes. Individual packets averaged 2 mm thick and neutron fluence monitors (FC-2, Fish Canyon Tuff sanidine) were placed every 5-10 mm along the tube. Synthetic K-glass and optical grade CaF_2 were included in the irradiation packages to monitor neutron induced argon interferences from K and Ca. Loaded

tubes were packed in an Al container for irradiation. Samples irradiated at the Oregon State TRIGA Reactor, Corvallis, OR were in-core for 9.1 hours in the F-12 position, In-Core Irradiation Tube (ICIT) of the 1 MW TRIGA type reactor. Correction factors for interfering neutron reactions on K and Ca were determined by repeated analysis of K-glass and CaF₂ fragments. Measured (⁴⁰Ar/³⁹Ar)_K values were $1.55 (\pm 22.60\%) \times 10^{-2}$. Ca correction factors were (³⁶Ar/³⁷Ar)_{Ca} = $2.31 (\pm 0.77\%) \times 10^{-4}$ and (³⁹Ar/³⁷Ar)_{Ca} = $6.37 (\pm 0.33\%) \times 10^{-4}$. J factors were determined by fusion of 6-10 individual crystals of neutron fluence monitors which gave reproducibility's of 0.09% to 0.11% at each standard position. Variation in neutron fluence along the 100 mm length of the irradiation tubes was <4%. Matlab curve fit was used to determine J and uncertainty in J at each standard position. No significant neutron fluence gradients were present within individual packets of crystals as indicated by the excellent reproducibility of the single crystal fluence monitor fusions.

Irradiated FC-2 sanidine standards together with CaF₂ and K-glass fragments were placed in a Cu sample tray in a high vacuum extraction line and were fused using a 20 W CO₂ laser. Sample viewing during laser fusion was by a video camera system and positioning was via a motorized sample stage. Samples analyzed by the furnace step heating method utilized a double vacuum resistance furnace similar to the Staudacher et al. (1978) design. Reactive gases were removed by three GP-50 SAES getters prior to being admitted to a MAP 215-50 mass spectrometer by expansion. The relative volumes of the extraction line and mass spectrometer allow 80% of the gas to be admitted to the mass spectrometer for laser fusion analyses and 76% for furnace heating analyses. Peak intensities were measured using a Balzers electron multiplier by peak hopping through 7 cycles; initial peak heights were determined by linear regression to the time of gas admission. Mass spectrometer discrimination and sensitivity was monitored by repeated analysis

of atmospheric argon aliquots from an on-line pipette system. Measured $^{40}\text{Ar}/^{36}\text{Ar}$ ratios were $332.89 \pm 0.08\%$ during this work, thus a discrimination correction of 0.8874 (4 AMU) was applied to measured isotope ratios. The sensitivity of the mass spectrometer was $\sim 6 \times 10^{-17}$ mol mV^{-1} with the multiplier operated at a gain of 36 over the Faraday. Line blanks averaged 1.40 mV for mass 40 and 0.01 mV for mass 36 for laser fusion analyses and 15.92 mV for mass 40 and 0.04 mV for mass 36 for furnace heating analyses. Discrimination, sensitivity, and blanks were relatively constant over the period of data collection. Computer automated operation of the sample stage, laser, extraction line and mass spectrometer as well as final data reduction and age calculations were done using LabSPEC software written by B. Idleman (Lehigh University). An age of 28.02 Ma (Renne et al., 1998) was used for the Fish Canyon Tuff sanidine fluence monitor in calculating ages for samples.

For $^{40}\text{Ar}/^{39}\text{Ar}$ analyses a plateau segment consists of 3 or more contiguous gas fractions having analytically indistinguishable ages (i.e., all plateau steps overlap in age at 2σ analytical error) and comprising a significant portion of the total gas released (typically $>50\%$). Total gas (integrated) ages are calculated by weighting by the amount of ^{39}Ar released, whereas plateau ages are weighted by the inverse of the variance. For each sample inverse isochron diagrams are examined to check for the effects of excess argon. Reliable isochrons are based on the MSWD criteria of Wendt & Carl (1991) and, as for plateaus, must comprise contiguous steps and a significant fraction of the total gas released. All analytical data are reported at the confidence level of 1σ (standard deviation).”

3.4 Results

3.4.1 Petrography

Sample petrography was assessed from three aligned high-resolution scans of each thin section collected using PiAutoStage (Steiner & Rooney, 2021). This system provided online delivery of content using images of two high resolution scans of each thin section in cross-polarized light, and one high resolution scan in plane-polarized light. The two cross-polarized light photographs were taken with the section oriented 45° from each other to show extinction and variations in birefringence. The images had calibrated scale bars for the assessment of mineral sizes using the OpenSeaDragon Scalebar javascript developed by the United States NIST. This system provided a significant advantage over traditional microscopes in describing petrographic textures as it permitted full thin section viewing. We chose to utilize this system because it provided on-demand petrographic images with calibrated scale bars and was therefore better suited to making and comparing observations than manual microscopy.

3.4.1.1 *La Angelita (Plio-Pleistocene)*

The La Angelita basalts were porphyritic or glomeroporphyritic (crystals grouped together in aggregates). Samples were mainly olivine or olivine + plagioclase phyrlic, (Figure 3.3 A) and range from 1-70 volume percent crystals, with crystal-rich samples (>40 volume percent crystals) making up 10/14 thin sections. Olivine crystals were typically 0.1-2 mm in size, while feldspar were typically larger in feldspar-phyric samples, 0.5-3 mm. Two samples (TOR0000T8 and TOR0000TA) featured clinopyroxene phenocrysts. Groundmass was commonly plagioclase/pyroxene and ranged from fine-grained to coarse-grained, with fine-grained groundmass more common. Samples TOR0000TI, -TJ, TK, and -TN all had very similar petrography, possibly suggesting they were from the same lava flow; maps and field relations seem

to support this as no visible flow boundaries were observed in the field. Three samples are vesicular, with one (TOR0000TA) representing a scoria collected near the vent. Rounded nodules or subrounded glomerocrysts of clinopyroxene (Figure 3.3 A, B), likely xenolithic in nature, were found in six of 14 La Angelita thin sections.

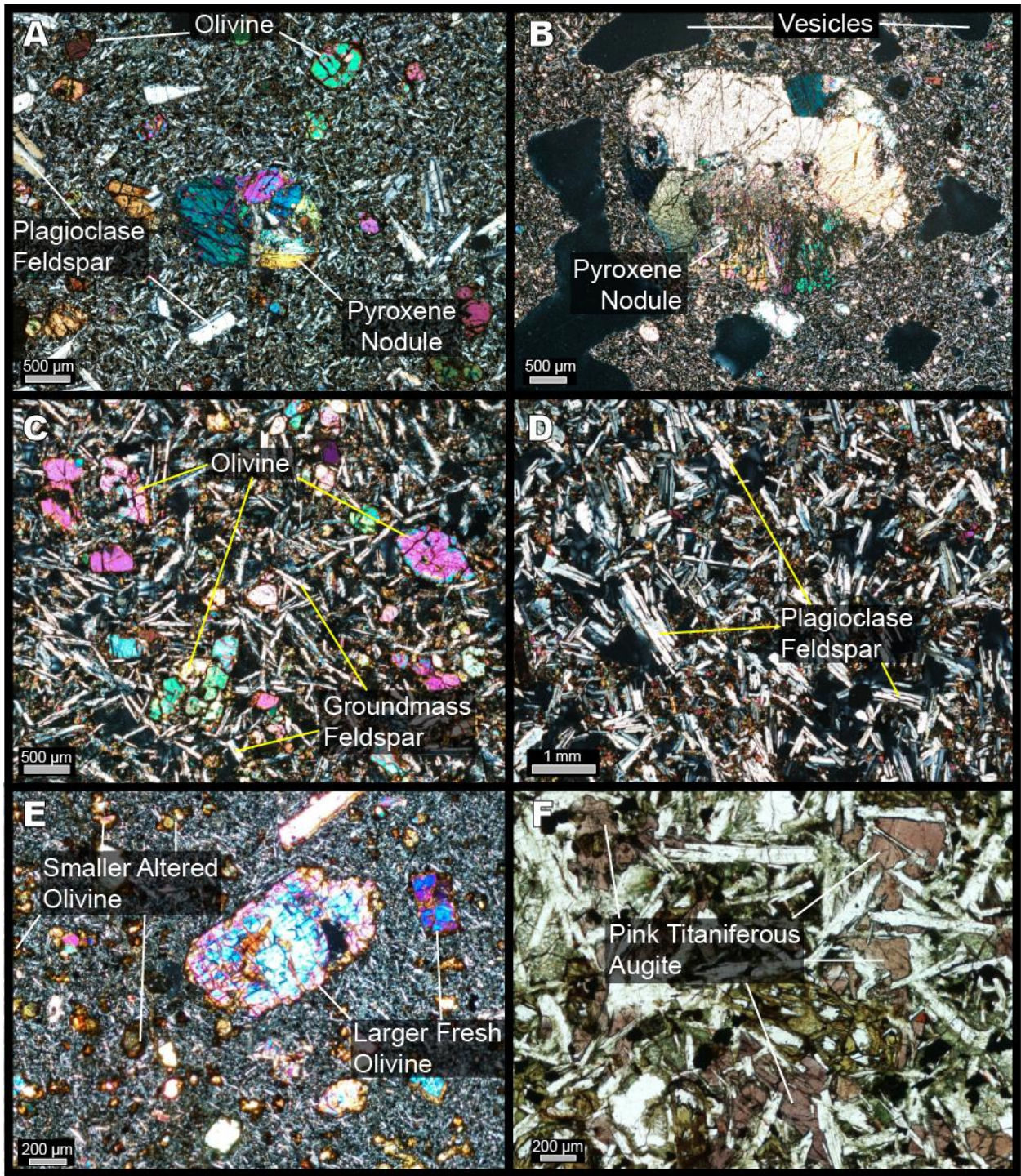


Figure 3.3

Photographs of various mineral phases and textures observed in Patagonian Triple Junction province magmas. Scale bars are shown in the bottom left of individual images. (A) La Angelita

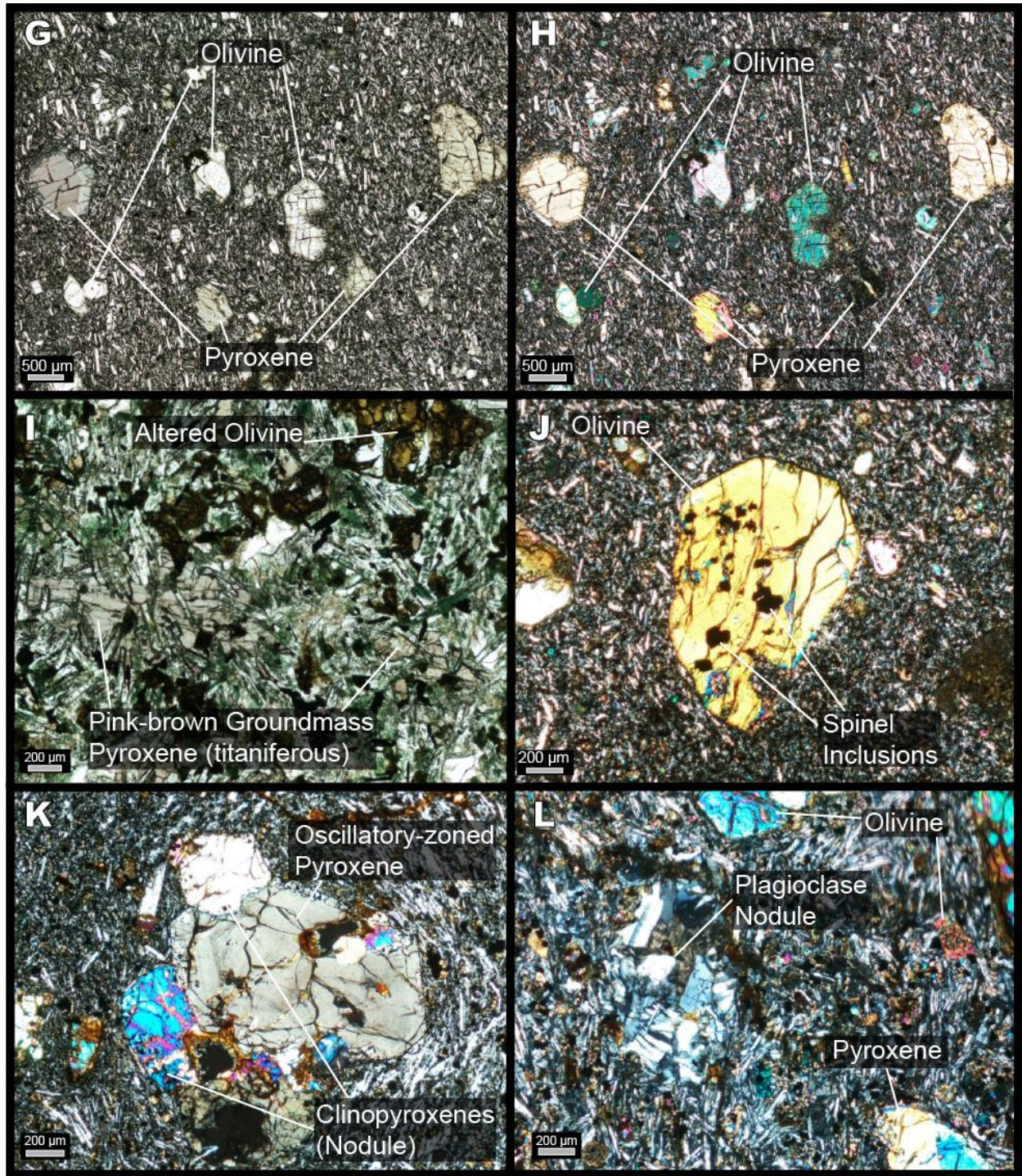


Figure 3.3 (cont'd)

sample TOR0000TH in cross polarized light (XPL) showing olivine and plagioclase feldspar phenocrysts, as well as a rounded pyroxene nodule. Scale bar 500 μm . (B) Vesicular La Angelita sample TOR0000TM in XPL showing rounded pyroxene nodule. Scale bar 500 μm . (C) Cerro

Figure 3.3 (cont'd)

Mojon sample TOR0000TF in XPL showing olivine phenocrysts and coarse feldspar groundmass. Scale bar 500 μm . (D) Cerro Mojon sample TOR0000TD in XPL showing feldspar-rich sample with no phenocryst olivine. Scale bar 1 mm. (E) Basalto de las Lagunas sin Fondo (BLSF) sample TOR0000U2 in XPL showing two subsets of olivine crystals. One subset is small, altered crystals, and the other subset is larger fresh crystals. Also of note is the extremely fine-grained groundmass which is characteristic of BLSF flows in this study. Scale bar 200 μm . (F) Basalto Alma Gaucha sample TOR0000TT in plane polarized light (PPL) showing pink titaniferous groundmass augite. Scale bar 200 μm . (G) Cerro del Doce sample TOR0000U7 in PPL showing green & gray pyroxene and clear olivine. Scale bar 500 μm . (H) Same field of view as (G), but in XPL. Scale bar 500 μm . (I) Cerro del Doce sample TOR0000UA in PPL showing brown-pink titaniferous pink groundmass pyroxene, and also altered olivine. Scale bar 200 μm . (J) Cerro del Doce sample TOR0000U8 in XPL showing spinel inclusions within olivine. Scale bar 200 μm . (K) Cerro del Doce sample TOR0000U0 in XPL showing clinopyroxene nodule. Note oscillatory zoning of the large pyroxene that forms the bulk of the nodule. Scale bar 200 μm . (L) Cerro del Doce sample TOR0000U9 in XPL showing feldspar nodule. Scale bar 200 μm .

3.4.1.2 Cerro Mojon (Miocene-Pliocene)

The two eastern Cerro Mojon flows were olivine phyric, with 20-25% volume percent phenocrysts (Figure 3.3 C). Both samples featured a coarse groundmass of plagioclase and clinopyroxene.

Sample TOR0000TD (4411) was the only sample among the entire sample set that has no phenocryst olivine and featured exclusively plagioclase feldspar phenocrysts (Figure 3.3 D). There was olivine and clinopyroxene in the groundmass of this sample.

3.4.1.3 Basalto de las Lagunas sin Fondo (Mid-Miocene)

The BLSF flows were olivine phyric. Two samples featured a greater proportion of crystals and two distinct size classes of olivine (15 volume percent of 0.1-0.2 mm altered crystals and 5 volume percent of 0.5-1 mm crystals; Figure 3.3 E), while the other more crystal-poor sample did not have a bimodal distribution of crystal sizes. The BLSF flows all had medium- to fine-grained plagioclase and clinopyroxene groundmass.

3.4.1.4 Basalto Alma Gaucha (Early Miocene)

The five Basalto Alma Gaucha samples formed a five-flow stratigraphic sequence (see Figure 3.4 below). Four of the five flows (including the basal flow) were plagioclase and olivine phyric, while one flow (the second flow from the bottom) featured only olivine phenocrysts. Groundmasses ranged from fine- to coarse-grained. Some samples, especially the uppermost flows, showed evidence of alteration in the form of yellow altered olivine. In sample TOR0000TT, the second flow from the bottom, the coarse groundmass/mesostatic pyroxene was pink colored in plane-polarized light (Figure 3.3 F). This strong coloration, a key distinguishing feature, suggests the pyroxene was titanite; other pyroxenes are typically gray or green hued in PPL.

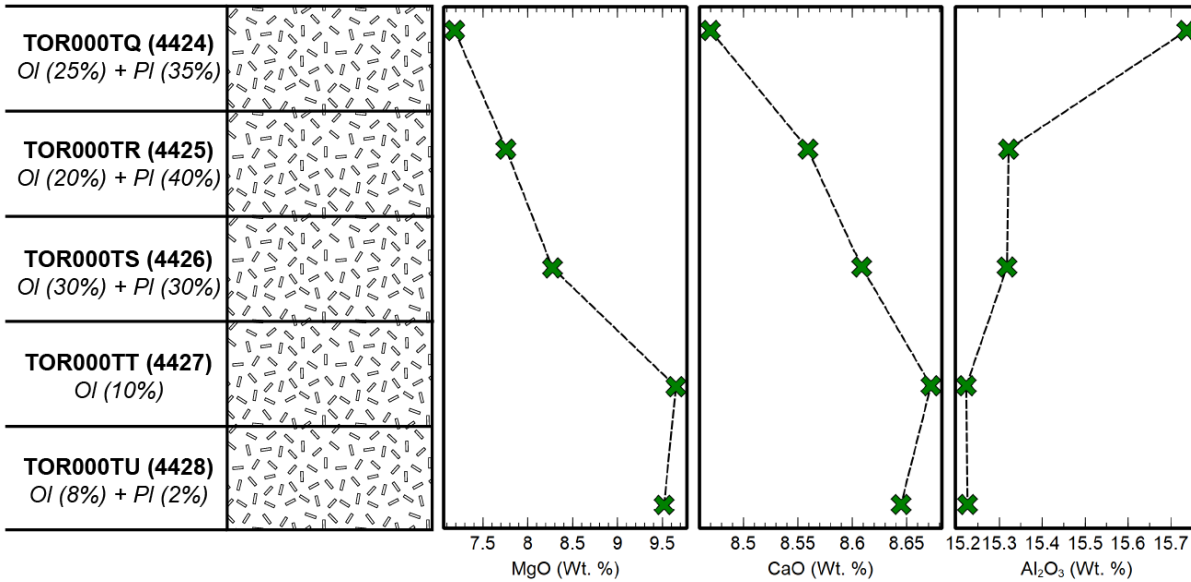


Figure 3.4

Column showing the stratigraphic sequence of sampled Alma Gaucha basalts. Below the sample names are the phases observed petrographically and the mineral proportions by volume (Ol = olivine, Pl = plagioclase feldspar). Also shown are major element oxides MgO, CaO, and Al₂O₃ in weight percent to illustrate how these elements change throughout the section, reflecting crystallization of Mg-rich olivine and Ca-rich plagioclase feldspar.

3.4.1.5 Cerro del Doce (Eocene)

Cerro del Doce basalts were predominantly porphyritic with less abundant glomeroporphyritic texture. Olivine was found in all samples at 5-20% volume percent of each observed thin section. Plagioclase appeared in two samples (TOR0000U0, TOR0000U7), and euhedral clinopyroxene appeared in two as well (TOR0000TY, TOR0000U7). The euhedral clinopyroxene was green to gray hued in plane polarized light (Figure 3.3 G, H). The groundmass clinopyroxene in the Cerro del Doce basalts was largely brown and brownish pink in PPL (Figure 3.3 I), contrasting with the observed crystals. This suggested that the groundmass pyroxene was

titaniferous augite, and further suggests that the larger crystals may have been inherited antecrysts/xenocrysts. Olivine in TOR0000U8 had common inclusions of opaque spinel (Figure 3.3 J). Sieve textures were noted in some samples from this group.

Two samples featured what were likely small xenoliths: sample TOR0000U0 features clinopyroxene nodules (Figure 3.3 K) and TOR0000U9 had a plagioclase feldspar nodule (Figure 3.3 L).

3.4.1.6 Summary of Petrographic Observations

Magmas of the Patagonian Triple Junction province observed petrographically in this study were mostly olivine phyric with few exceptions. Some samples also showed plagioclase feldspar and clinopyroxene. The older units Alma Gaucha (Oligocene) and Cerro del Doce (Eocene) showed qualitative mineralogical evidence (i.e., pink or pink-brown colored pyroxene in plane polarized light) of titaniferous augite in the groundmass. Both the youngest lavas (La Angelita, Plio-Pleistocene in age) and the oldest (Cerro del Doce, Eocene) had xenolithic material, most commonly clinopyroxene nodules. The most common feature that varied among the lavas is the fine- or coarse-grained nature of the groundmass, but they did not vary systematically.

3.4.2 Ar-Ar Isotopic Dating

Six basalt groundmass samples were chosen for $^{40}\text{Ar}/^{39}\text{Ar}$ isotopic age determination. Of these six samples, none returned isochron or plateau ages. Although isochrons are the most accurate and desirable outcome, followed by plateaus, it does not mean that the data are invalid. Plateau ages and isochron give greater confidence in the results. Although our samples did not achieve a plateau with three successive ages within 2σ error of each other, the samples exhibit age spectra that appear “flat”. Spectra that appeared “stepped” or with high variability may be suspect.

Sample TOR0000TD (4411) is the only such spectrum with a stepped appearance, and therefore we treated this result with caution. The remaining five samples did not appear to have the same stepped appearance.

All samples sent for isotopic dating had $^{40}\text{Ar}/^{36}\text{Ar}$ greater than atmospheric. It should be noted here that ages may have been overestimated if there is excess argon, meaning $^{40}\text{Ar}/^{36}\text{Ar} > 295.5$, according to material provided by NIGL. This may be the result of post-eruption alteration. Therefore, these dates may be slightly older than actual eruption ages of the lava flow. The results of these $^{40}\text{Ar}/^{39}\text{Ar}$ isotopic age measurements are given in Table 3.1 and Figure 3.5 below.

The Nevada Isotope Geochronology Lab offered the following comment regarding the interpretation of the stepped spectrum of sample TOR0000TD (4411) in a personal communication from their lab's principal investigator Kevin Konrad in July 2021:

Sample Name (IGSN, Internal)	Programa Nacional de Cartas Geologicas de la Republica Argentina stratigraphic unit	Apparent $^{40}\text{Ar}/^{39}\text{Ar}$ Eruption Age (Given in Ma, millions of years; error given as 1 sigma)	Maximum Eruption Age (Given in Ma, millions of years; error given as 1 sigma)
TOR0000T7, 4406	La Angelita	2.52±0.04	2.01±0.06
TOR0000TD, 4411	La Angelita	5.58±0.11	1.76±0.34
TOR0000TU, 4428	Alma Gaucha	22.26±0.06	20.18±0.11
TOR0000U0, 4434	Cerro del Doce	36.68±0.09	29.54±0.10
TOR0000U4, 4438	Basalto de las Lagunas sin Fondo	9.42±0.02	9.13±0.04
TOR0000UG, 4450	Cerro del Doce	40.18±0.09	38.49±0.09

Table 3.1

Table summarizing results of $^{40}\text{Ar}/^{39}\text{Ar}$ sample dating for the Patagonian Triple Junction Province magmas collected in this study. Apparent eruption ages range from 2.52-40.18 Ma. Maximum eruption ages are given as the lowest single step age from $^{40}\text{Ar}/^{39}\text{Ar}$ results.

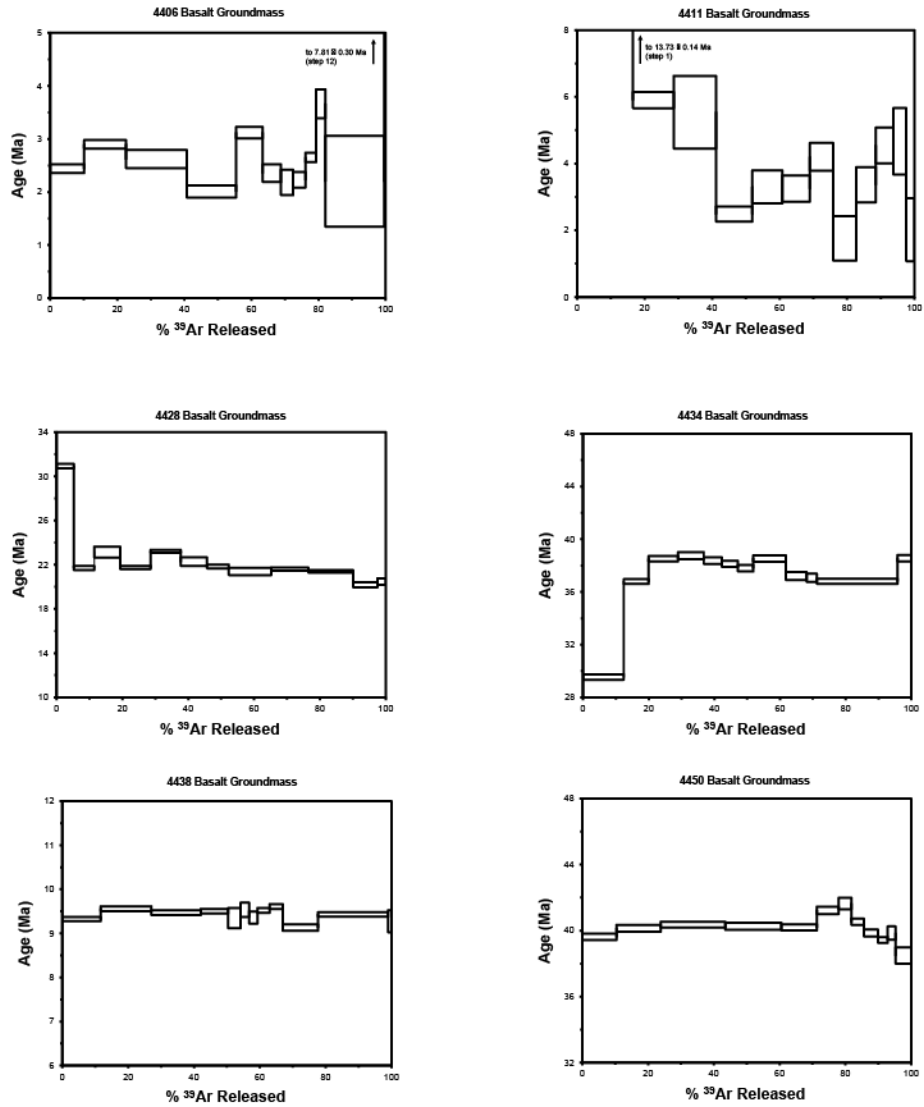


Figure 3.5

Isotopic spectra showing graphical results of ⁴⁰Ar/³⁹Ar dating for Patagonian Triple Junction Province magmas

“This sample produced a very discordant age spectrum with a high initial age (13.73 Ma), falling to an age of 1.76 Ma then increasing. There are no plateau or isochron ages defined by these data. The total gas age is 5.58 ± 0.11 Ma is equivalent to a conventional K/Ar age and is obviously

an overestimate of the true eruptive age. The Ca/K ratios are consistent with outgassing of groundmass. Radiogenic yields (% $^{40}\text{Ar}^*$) are low and strongly indicate alteration. An age spectrum with this form could indicate that excess argon is present, although it is not the classic U-shaped spectrum often associated with excess argon. Excess argon (non-radiogenic initial argon with a $^{40}\text{Ar}/^{36}\text{Ar} > 295.5$ incorporated into the sample, the atmospheric value is 295.5), which can cause anomalously old ages for samples. A lack of an isochron does not allow this assumption to be tested. If an isochron is not obtained then the youngest age on the age spectrum (1.76 Ma here) is a maximum age for the sample, as even this step could be effected by excess argon, i.e. the sample is <1.76 Ma (ages on an age spectrum are calculated assuming that the initial argon is atmospheric in composition, thus they are often referred to as apparent ages).

Another indication of alteration is that the first low temperature steps released an anomalously large amount of the total ^{39}Ar . From analytical data alone this sample would be of low reliability and the total gas age may well be an overestimate of the true age. This suggests alteration of the fine-grained groundmass minerals. Note that this is certainly not an ideal sample, and this age should not be considered reliable.”

Based on this communication regarding the discordant age spectrum, we have chosen to include the youngest single age step recorded from each analysis in Table 3.1. These results, and the $^{40}\text{Ar}/^{36}\text{Ar}$ greater than atmospheric, indicate that all the samples sent for analysis have experienced alteration and may not be reliable. However, we can conclude based on these data that there was back-arc volcanism in the Patagonian back arc over the course of ~39 Ma.

We can compare our results to age estimates and constraints from Programa Nacional de Cartas Geologicas de la Republica Argentina maps to. All results agree with the assigned ages of mapped lithologic units except for TOR0000TD (4411). This sample records an age (5.58 ± 0.11

Ma). This age is more consistent with the geological age of Cerro Mojon formation (5.0 ± 0.11 and 5.2 ± 0.11 Ma, Gorrington et al., 1997) than with the La Angelita unit that it is mapped with (2.0-2.8 Ma). Satellite imagery (Google Earth) is inconclusive whether this flow is an extension of flow GB-5a of Gorrington et al. (1997) or not; they appear to be separated by an area of raised elevation. Comparison of the major- and trace-element geochemistry of GB-5a and TOR0000TD (4411) indicate different compositions (see Section 3.4.4.2). Therefore, although we do approach the apparent eruption age with caution, based on geochemical evidence (see Figure 3.9 and section 3.4.4.2) we do suggest that this flow is not the same as GB-5a.

3.4.3 Major Element Whole Rock Chemistry

3.4.3.1 La Angelita (Plio-Pleistocene)

La Angelita eruptives ranged in composition from basaltic andesite to tephrite in total alkali silica space (Figure 3.6; see Supplemental Document 5), and most of the samples were alkaline basalt. All La Angelita basalts featured MgO contents of >7 wt. % (Fig 3.7). Although there were some observed compatible/incompatible trends (i.e., upward/downward slope to the data with decreasing MgO) in La Angelita basalts, they were unlikely to represent broad fractional crystallization trends within the whole group. This was due to the discrete, small volume nature of individual eruptive centers of the La Angelita basalts (Figure 3.2). For example, samples TOR0000T8-TOR0000TC and sample TOR0000TH were all from the Tres Cerros locality and were within 1 wt. % MgO and 1 wt. % SiO₂ of one another. We therefore suggest that these data be viewed in terms of clusters rather than trends, because individual flows of La Angelita basalt plausibly had unrelated plumbing systems even if they shared a common mantle source. We therefore assigned names to each eruptive center/group of flows for discussion here. They are as

follows: Central, Cerro Vanguardia South, Jaramillo Park, and Tres Cerros. As discussed in Section 4.2, TOR0000TD (4411) is mapped on the geologic map as La Angelita, but it was in the age range of Cerro Mojon. We have reassigned this flow to that group.

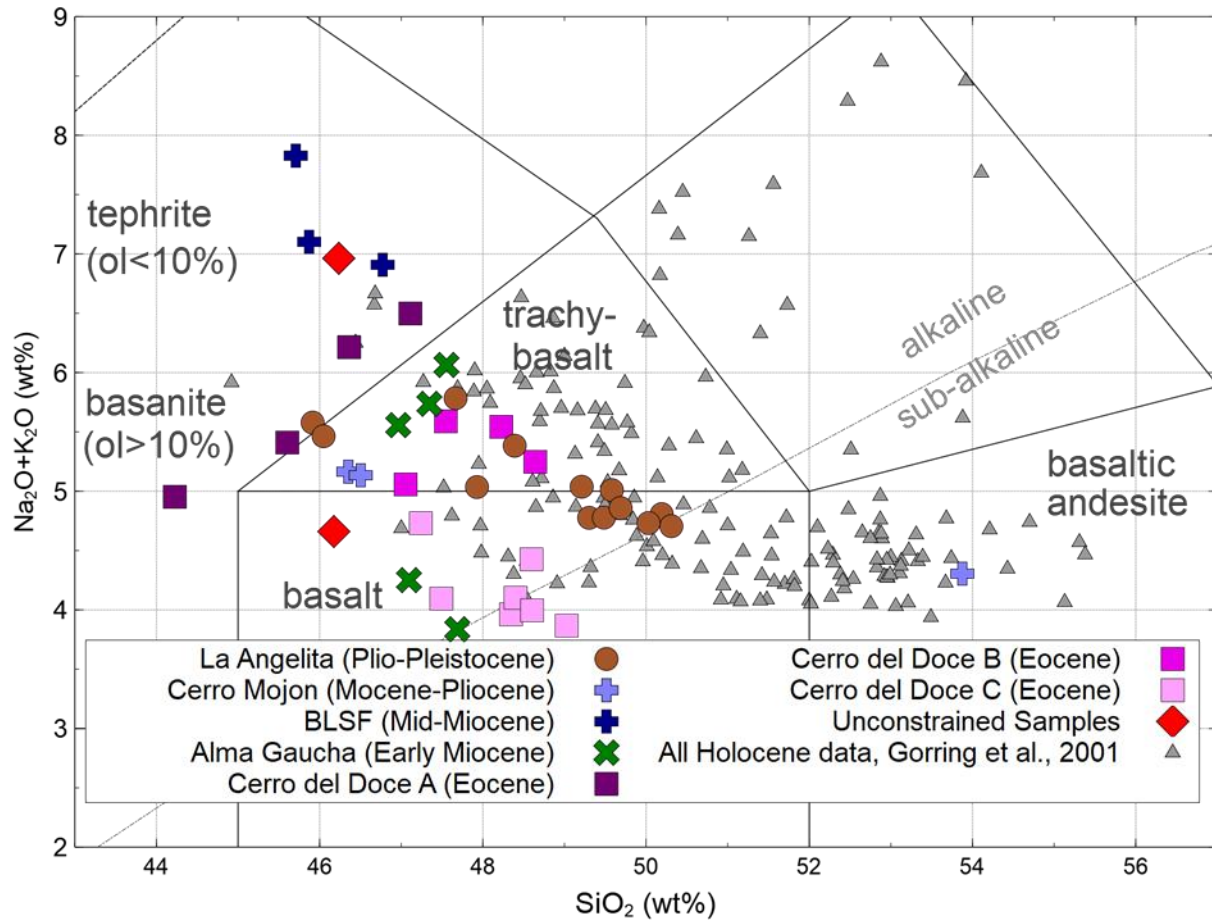


Figure 3.6

Bivariate total alkali silica diagram, where total alkali is major element oxides $\text{Na}_2\text{O} + \text{K}_2\text{O}$. Data from all Holocene volcanic centers in the Patagonian Triple Junction province shown (Gorring & Kay, 2001).

La Angelita basalts from the Central eruptive center had the highest MgO (9.2-9.9 wt %), TiO_2 (2.3-2.4 wt. %), K_2O (1.6 wt %), and P_2O_5 (0.7 wt. %) and the lowest SiO_2 (45.9-46.1 wt. %) of all groups (). The Central eruptive center was very similar in major elements to the Cerro Vanguardia South except FeO^T and MgO, where the Cerro Vanguardia South is lower in FeO^T and MgO. Jaramillo Park basalts had lower MgO, TiO_2 , and K_2O than the Central and Cerro

Vanguardia South groups, and similar SiO_2 . Tres Cerros basalts had the lowest MgO, K_2O , and P_2O_5 of all the groups, but similar TiO_2 and FeO^{T} to the Jaramillo Park group. The Tres Cerros group had the lowest CaO, while the Central and Cerro Vanguardia South were the highest. Al_2O_3 was highest in the Tres Cerros group, and lowest in the Central group, but only ranged from 13.9-15.6 wt % across the whole La Angelita formation. La Angelita basalts had $\text{FeO}^{\text{T}}/\text{MnO}$ ranging from 64.6 to 69.0. Typically $\text{FeO}^{\text{T}}/\text{MnO} > 60$ suggests that magmas are derived from a pyroxenitic rather than peridotitic source (Søager et al., 2015, 2021).

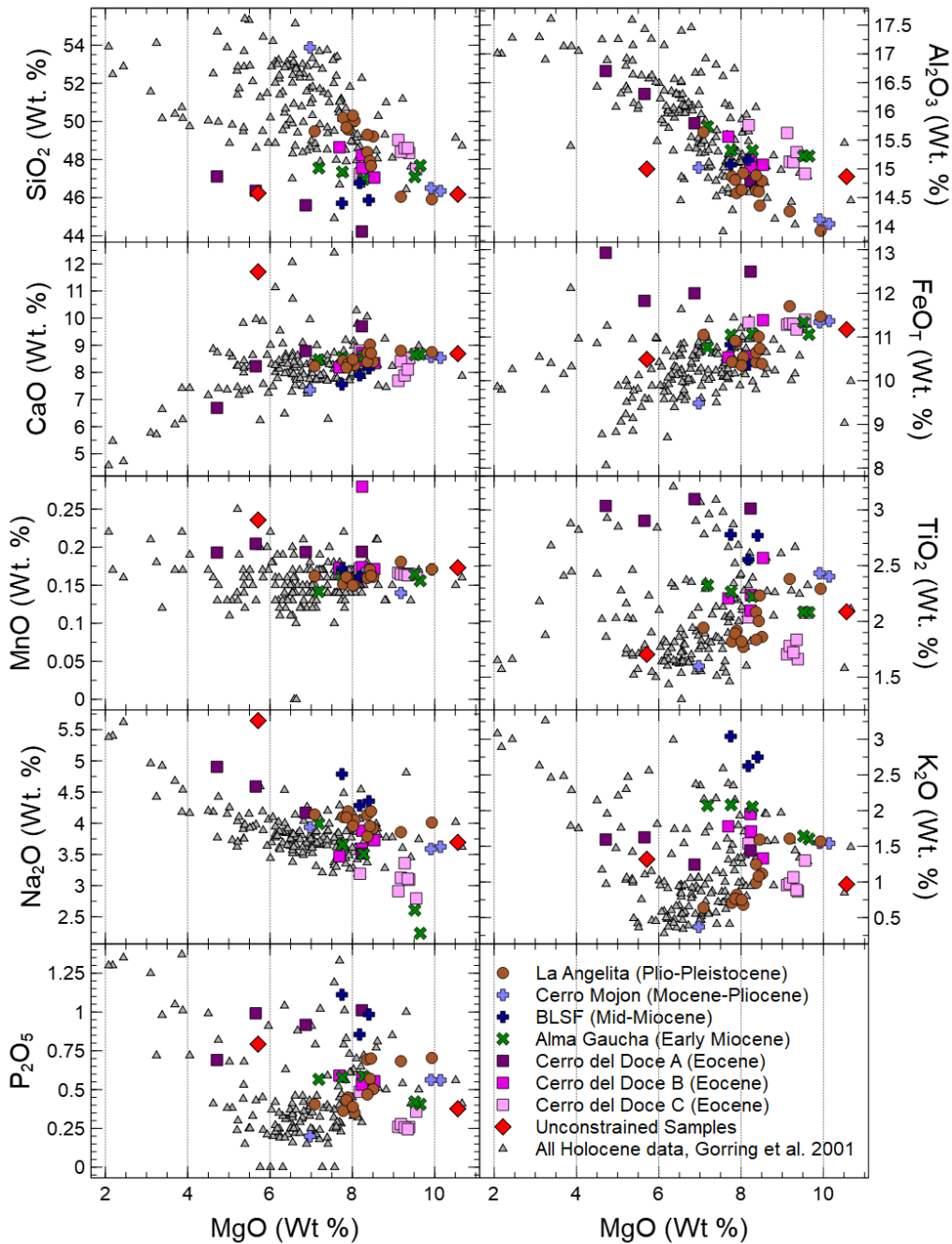


Figure 3.7

Bivariate diagrams of major element oxides vs. MgO in weight percent for Patagonian Triple Junction province magmas. Data from all Holocene volcanic centers in the Patagonian Triple Junction province shown (Gorring & Kay, 2001).

3.4.3.2 Cerro Mojon (Miocene-Pliocene)

Both Cerro Mojon samples collected near the town of Fitz Roy were from the same lava flow and had identical chemistry within analytical uncertainty ($\pm 5\%$ of the measured value on major elements). They had high whole-rock MgO (10 wt. %), CaO of 8.5 wt. %. In most element oxides (FeO^T , TiO_2 , K_2O , Na_2O , Al_2O_3) they were in the same range as the most MgO-rich La Angelita samples. In total alkali-silica space they were alkaline trachybasalts. These basalt samples had FeO^T/MnO of 66.4-66.8.

Sample TOR0000TD (4411) was mapped as La Angelita but our Ar-Ar isotopic dates indicated an age (5.58 ± 0.11 Ma; see section 4.4) consistent with other Cerro Mojon ages from Gorrington et al. (1997) (5.0 ± 0.11 and 5.2 ± 0.11 Ma). This sample is an outlier from the bulk of the other Cenozoic basalts collected in the Triple Junction province of Patagonia. It is the only basaltic andesite and has a full 4 wt. % more SiO_2 than the most silica-rich of the basalts. It is also poor in CaO, P_2O_5 , K_2O , TiO_2 , and FeO^T compared to the rest of the data set. FeO^T/MnO for this sample is 67.8.

3.4.3.3 Basalto de las Lagunas sin Fondo (Mid-Miocene)

Lavas of the BLSF formation were highly alkaline basanites and one tephrite with the highest total alkali of all sampled Triple Junction Province basalts. This came primarily from an increased proportion of K_2O ; these samples had 2.6-3 wt. %. Na_2O was also high (4.3-4.8 wt. %), and they were as Na_2O -rich as the most sodic La Angelita basalts. They also featured high titanium (2.6-2.8 wt. %) and high P_2O_5 (0.9-1.1 wt. %). The BLSF lavas were lower in SiO_2 and CaO than La Angelita and Cerro del Doce basalts. Because there were only three samples from the BLSF, no fractional crystallization trends were apparent. BLSF magmas had FeO^T/MnO from 63.0-65.8.

3.4.3.4 Basalto Alma Gaucha (Early Miocene)

Alma Gaucha basalts were basaltic to trachybasaltic in total alkali silica space. Unlike other sample groups that were singular unrelated flows, the Alma Gaucha formation had a five-flow stratigraphic sequence where wt. % MgO decreased up-section (Figure 3.4). Furthermore, we observed geochemical trends in this sequence that we related to fractional crystallization from high to low MgO. As samples decrease in MgO, SiO₂ and CaO remain relatively unchanged. Element oxides that increased in concentration with decreasing MgO wt. % in Alma Gaucha basalts were Na₂O, P₂O₅, K₂O, TiO₂, and Al₂O₃. Element oxides that had decreasing concentrations with decreasing MgO wt. % were MnO and FeO^T; the concentration of FeO^T only changed by 1 wt %. These trends were consistent with olivine crystallization, but not plagioclase feldspar. Both phases were observed in the petrography. We suggest early fractionation of olivine affecting geochemistry, with crystallization of plagioclase during pre-eruptive storage or during ascent. Alma Gaucha basalts had FeO^T/MnO from 68.0 to 76.0.

3.4.3.5 Cerro del Doce (Eocene)

Lavas of the Cerro del Doce formation were mostly alkaline to subalkaline basalt, with some trachybasaltic compositions and four basanite/tephrite samples. We subdivided the Cerro del Doce basalts into three subgroups: A, B, and C. These groups were coherent in trace elements, and this is how they were initially divided (see next section, Trace Element Whole Rock Chemistry). The basanite/tephrite samples (Group A) feature whole-rock TiO₂, FeO^T, P₂O₅, and Al₂O₃ that was elevated over the other Cerro del Doce basalts and were also the highest concentrations observed in the Cenozoic rocks from the Triple Junction province. Group A magmas showed increasing SiO₂, Na₂O with decreasing MgO, decreasing CaO, FeO^T, and P₂O₅ with decreasing MgO; concentrations of K₂O and TiO₂ do not change considerably. The decreasing concentrations of CaO and P₂O₅ with decreasing MgO suggested crystallization of apatite, but we did not find any

petrographic evidence for this mineral. Group A Cerro del Doce flows had $\text{FeO}^{\text{T}}/\text{MnO}$ between 57.9-67.0.

Fractional crystallization trends were not clear in the remaining Cerro del Doce basalt groups. The Group B lavas were more alkaline and were trachybasaltic in composition. They had intermediate MgO (8-8.5 wt %), lower FeO^{T} , and broadly similar CaO, Al_2O_3 , and MnO to Group C. The Group C lavas were alkaline to subalkaline basalts that had broadly higher MgO contents than Group B, and low whole rock P_2O_5 , TiO_2 , and higher SiO_2 . Group B lavas had $\text{FeO}^{\text{T}}/\text{MnO}$ from 37.5-66.5 and Group C lavas have $\text{FeO}^{\text{T}}/\text{MnO}$ between 65.8 and 69.6.

3.4.4 Whole Rock Trace Element Geochemistry

All Cenozoic magmas of the Triple Junction province from Eocene to Pleistocene age featured rare earth element patterns that were upward sloped from right to left, with Lu at 7-12 \times over chondrite and La from 40-371 \times chondrite (Figure 3.8; see Supplemental Document 5). Another way to express this rare earth element slope is by $(\text{La}/\text{Sm})_{\text{N}}$ and $(\text{Tb}/\text{Yb})_{\text{N}}$, which are chondrite-normalized abundances of the given elements (Figure 3.9).

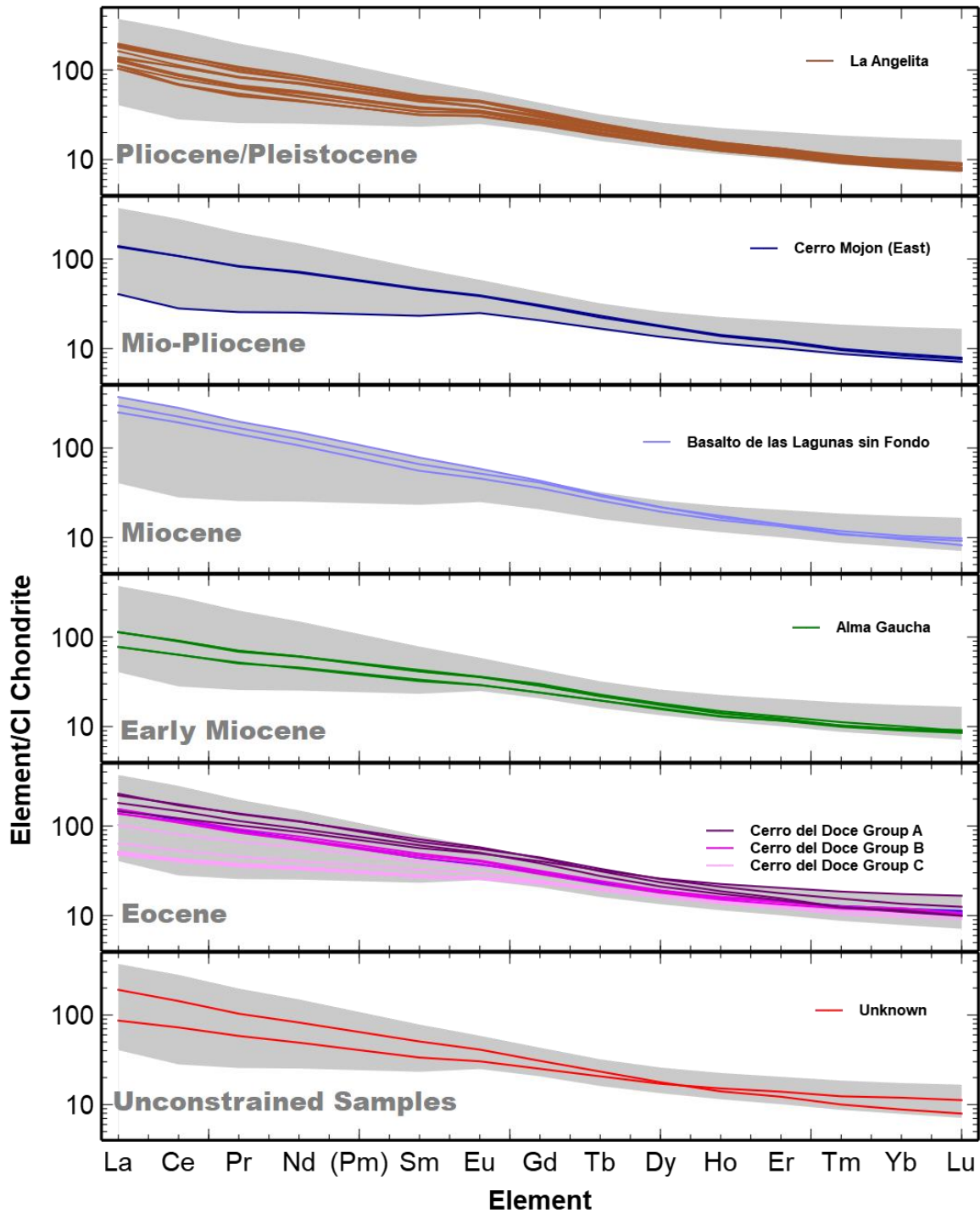


Figure 3.8

Rare earth element concentrations normalized to CI Chondrite (McDonough & Sun, 1995) for Triple Junction Province Patagonian magmas. Promethium (Pm) is not found in terrestrial rock samples, but laboratory convention is to include it on these diagrams to remove an abrupt

Figure 3.8 (cont'd)

jump from Sm to Nd. The interpolated Pm values are calculated as the geometric mean of adjacent chondrite-normalized values of elements Nd and Sm. The gray fields represent the entire dataset from maximum to minimum extremes.

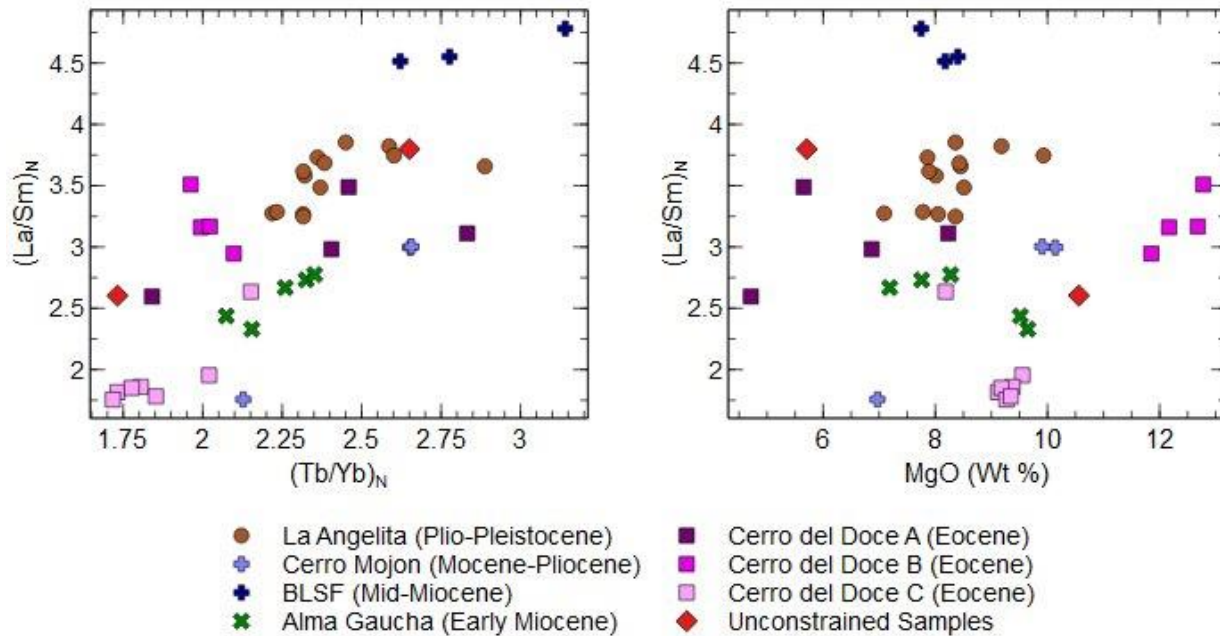


Figure 3.9

Bivariate diagram showing $(La/Sm)_N$, or CI Chondrite-normalized (McDonough & Sun, 1995) lanthanum over samarium concentrations, vs $(Tb/Yb)_N$ for the various Patagonian Triple Junction Province magmas. This diagram is another way to visualize the slope of rare earth element diagrams (Figure 3.8, above) and shows the relative REE slopes of various groups. $(La/Sm)_N$ represents the overall rare earth element slope, which is sensitive to partial melting percentage; $(Tb/Yb)_N$ shows the heavy rare earth element slope, which is sensitive to garnet in the mantle. Because $(La/Sm)_N$ can be sensitive to fractional crystallization, this ratio is also shown plotted vs. MgO. There is some correlation of $(La/Sm)_N$ with MgO, especially in the Eocene Cerro del Doce groups. However, because only the highest-MgO samples were chosen for modeling, the effects of crystallization changing the ratio are not important when considering mantle melting.

3.4.4.1 La Angelita (Plio-Pleistocene)

There was some variability of $(\text{La}/\text{Sm})_N$ among the La Angelita basalts. $(\text{La}/\text{Sm})_N$ or REE slope is associated with the percentage of mantle partial melting; elevated REE slope indicates a lower partial melting percentage. Overall $(\text{La}/\text{Sm})_N$ ranges from 3.25 to 3.85.

Trace element spider diagrams of La Angelita basalts (Figure 3.10) were broadly similar, with a slight negative anomaly in Ti and K, and variable U. A negative sloped pattern was the most common feature of La Angelita basalts with consistent negative anomalies in K and positive anomalies in Pb.

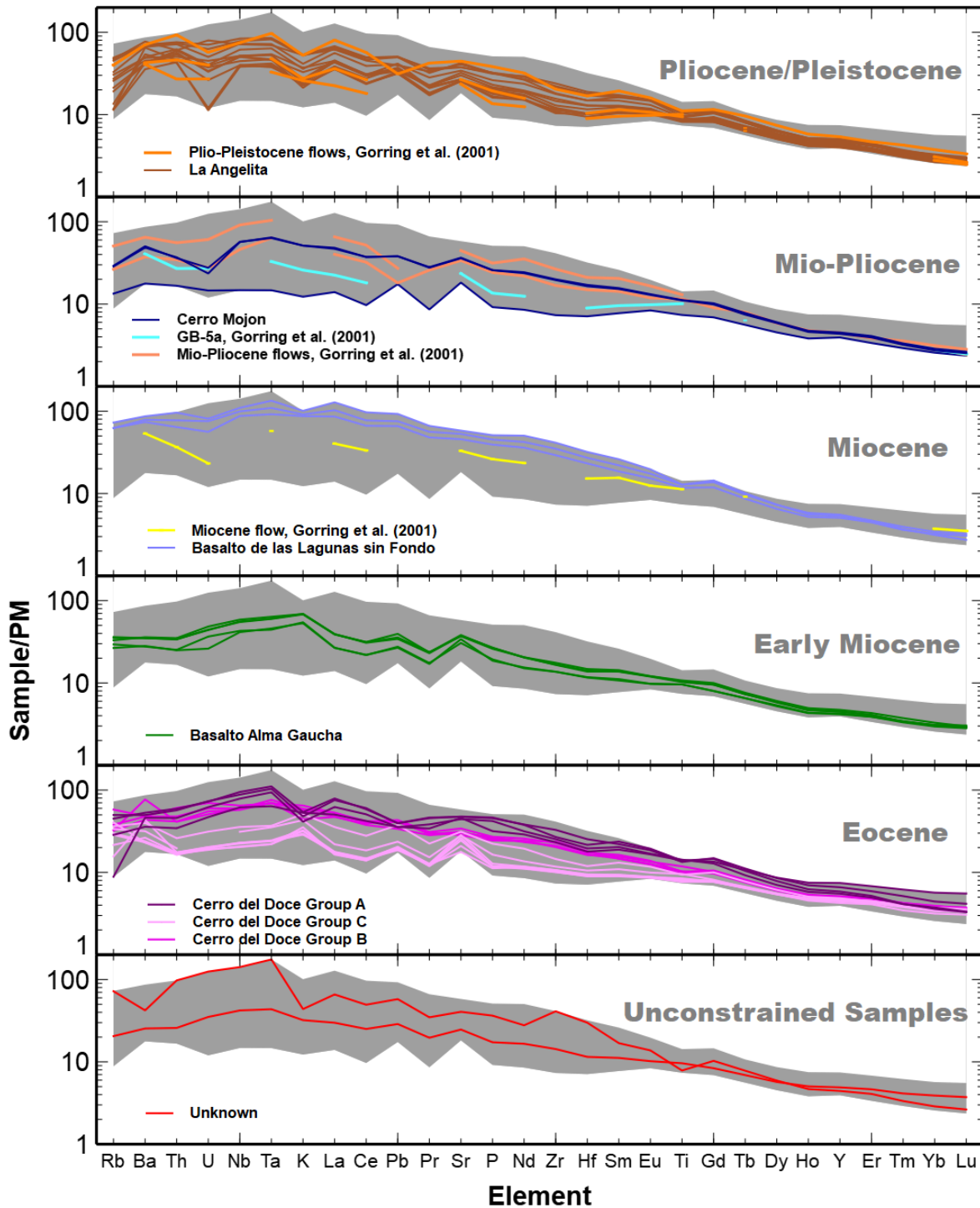


Figure 3.10 (Previous Page)

Trace element spider diagram showing elemental concentrations normalized to pyrolite or Primitive Mantle (PM) (McDonough & Sun, 1995) for the various Patagonian Triple Junction

Figure 3.10 (cont'd)

Province magmas. The gray fields represent the entire dataset from maximum to minimum extremes. Also shown for comparison are the dated magmas from Gorrington & Kay (2001).

3.4.4.2 Cerro Mojon (Miocene-Pliocene)

Cerro Mojon flows collected near Fitz Roy, which we interpreted as from the same flow, had $(La/Sm)_N$ of 3. The southern Cerro Mojon flow was considerably different, with $(La/Sm)_N$ of only 1.76. The northern and southern Cerro Mojon flows were similar in Cr (244-247 ppm in the north vs. 258 ppm in the south) but varied considerably in Ni (231-233 ppm in the north, 171 in the south). The northern flow had a negative U anomaly in the trace element spider diagrams, while the southern flow did not feature a negative U anomaly but did have positive Pb and Sr anomalies (Figure 3.10). In Section 3.4.2 we argued that our dated flow TOR0000TD (4411) appeared to come close to flow GB-5a of Gorrington & Kay, (2001) but argued that they are different flows based on the apparent age of TOR0000TD. We show the trace element chemistry of flow GB-5a in Figure 3.10 with Mio-Pliocene aged lavas from this study. The differences in trace element chemistry further reinforced that our sample TOR0000TD and GB-5a were independent flows from one another.

3.4.4.3 Basalto de las Lagunas sin Fondo (Mid-Miocene)

The three samples of BLSF magmas collected featured variable $(La/Sm)_N$, ranging from 4.51-4.78. These were the highest values observed in all Cenozoic Triple Junction Province magmas (Figure 3.9). Spider diagrams of BLSF magmas (Figure 3.10) showed negative Ti and K anomalies.

3.4.4.4 Basalto Alma Gaucha (Early Miocene)

The early Miocene Alma Gaucha magmas had $(La/Sm)_N$ that range from 2.33-2.77. The trace element spider diagrams (Figure 3.10) showed positive anomalies of Pb and Sr.

3.4.4.5 Cerro del Doce (Eocene)

Group A Cerro del Doce flows (alkaline basanite/tephrite samples) had variable $(La/Sm)_N$, ranging from 2.60-3.49. The Group A spider diagrams (Figure 3.10) were all consistent, showing negative Ti and K anomalies, although they did separate out towards the right side of the plot.

Group B Cerro del Doce flows (alkaline trachybasaltic flows) fell within a narrow range of $(La/Sm)_N$ values, from 2.59-3.51 (Figure 3.9). Spider diagrams of Group B (Figure 3.10) were tightly constrained and showed little variation, with negative Ti anomalies and slight positive Sr and Pb anomalies. TOR0000U6 featured a slight negative K anomaly.

The Group C Cerro del Doce flows (alkaline to subalkaline basalts) had some of the lowest observed $(La/Sm)_N$ values of all Triple Junction Province magmas. The range of $(La/Sm)_N$ was 1.75-2.63 (Figure 3.9). The trace element spider diagrams (Figure 3.10) for Cerro del Doce Group C featured positive Pb, Sr, and K anomalies and a negative Ti anomaly that developed in samples with elevated trace element profiles.

3.4.5 Unconstrained Samples

During the study, two samples were collected that did not have associated units on the Programa Nacional de Cartas Geologicas de la Republica Argentina maps. The first of these samples, TOR0000TP (4423), was collected from near outcrops of the Alma Gaucha and La Angelita formations in the center of the Deseado Massif. The field notes for TOR0000TP indicated that it appeared to be from a dike. The second unconstrained sample, TOR0000TX (4431) was

collected from an outcrop near the Deseado River and field notes from that site suggested it was part of an extrusive lava flow. Panza et al. (1998) classified the location of TOR0000TX as Miocene and based on our modeling results it does fit well with the Miocene-aged Cerro Mojon formation (see Section 3.5.4). It appears that the age of this flow had not been precisely measured based upon a search of the Repositorio Segemar database.

Unconstrained sample TOR0000TP (4423) was spatially located nearby to Alma Gaucha and La Angelita eruptives. It had low MgO (5.71 wt. %) and high alkali ($\text{Na}_2\text{O} + \text{K}_2\text{O} = 6.96$ wt. %), making it one of the most alkaline compositions observed and similar in total alkali silica space to the basanites of the BLSF formation. It also had the highest CaO (wt %) of any other sample collected in the province (11.71 wt. %) making it an extreme outlier from the other samples that have 7.5-10 wt. % CaO. It had elevated $(\text{La}/\text{Sm})_N$ (Figure 3.9) which is also like La Angelita basalts, the BLSF formation, and the low-MgO samples of the Eocene Cerro del Doce group A basanite/tephrite series. Elevated Zr and Hf in TOR0000TP set it apart from any of the observed magma types. The La Angelita basalts were the most plausible group that TOR0000TP may have belonged to when considering trace elements, although they are not a definitive match.

Unconstrained sample TOR0000TX (4431) was not spatially associated with any of the other flows in the study area. It had high whole-rock MgO (10.56 wt. %), and considerably lower alkalis ($\text{Na}_2\text{O} + \text{K}_2\text{O} = 4.66$ wt. %) than unconstrained sample TOR0000TP. The most likely group to assign this sample to is the Cerro del Doce Group C, the subalkaline basalts. It was also like the Doce Group C magmas in major element space.

3.5 Discussion

3.5.1 The Effects of Crustal Contamination on Patagonian Triple Junction Province Magmas

One possible explanation for the incompatible trace element enriched nature of Patagonian triple junction (e.g. Figures 3.8 and 3.10) magmas could be because of crustal contamination. Crustal contamination, also known as assimilation, can affect the isotopic and trace element signatures of magmas. Because assimilation necessarily requires melting of the wall rock material, it is typically observed in magmatic systems that are long-lasting, where large magma volumes pass through the crust, and where magmatism and heat are focused over long periods of time. Crustal contamination is commonly observed in subduction zone volcanic arcs because of prolonged magmatism (e.g., Hildreth & Moorbath, 1988; Price et al., 2012; Walker et al., 2015). Similarly, crustal contamination is commonly observed in periods of LIP magmatism such as the Columbia River Basalt Group (e.g., Wolff et al., 2008), the Proterozoic North American Keweenawan flood basalts (e.g., Nicholson et al., 1997), and the Cenozoic East African LIP (e.g., Rooney, 2017). This leads to the question of whether Patagonian Triple Junction province magmas have in fact experienced any assimilation as a part of their petrogenesis.

Our data suggest that there may be some degree of crustal contamination present in Patagonian Triple Junction province magmas. In Figure 3.11, we show several trace element ratios that are indicators of crustal contamination (Ba/Th vs. Ce/Pb and U , after Søger et al. (2013)). We have plotted the average recommended compositions of the upper and lower continental crust for comparison (Rudnick et al., 2003). In addition, in Figure 3.11 we also plot each individual crustal contamination indicator (Ba/Th , Ce/Pb , and U) vs. MgO to rule out variation in these indicators because of fractional crystallization. Based on these plots, these contamination indicators do not appear affected by fractional crystallization. We observe values of Ba/Th vs.

Ce/Pb that trend towards the upper continental crust for Cerro del Doce group C, Cerro Mojon, and BLSF magmas, and lower continental crust for La Angelita. Meanwhile, in Ba/Th vs. U, we also observe evidence of lower crustal contamination in La Angelita, Cerro del Doce groups A & B, and BLSF magmas. This suggests that minor contamination by upper & lower continental crust is possible.

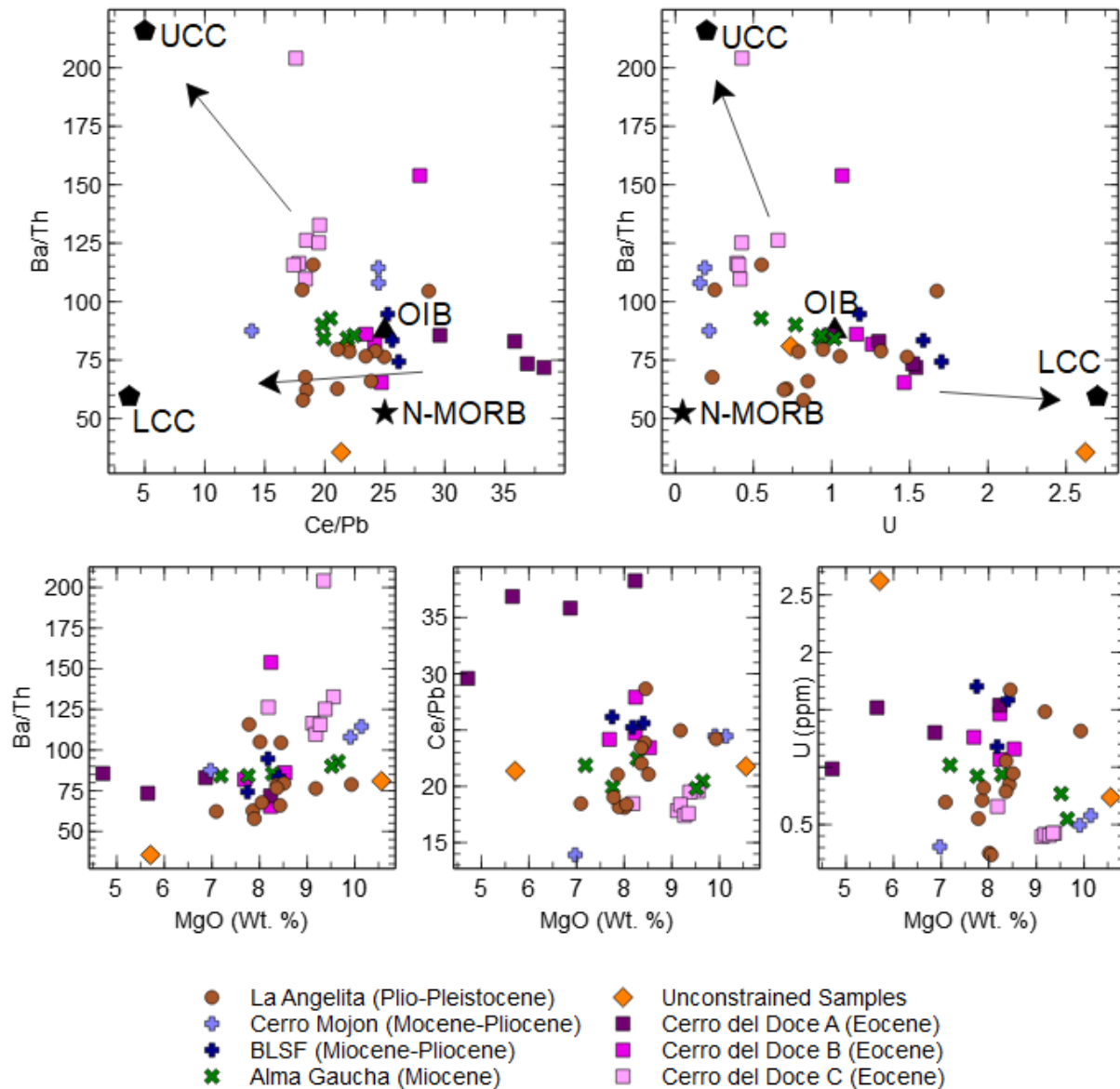


Figure 3.11

Bivariate plots showing trace element concentrations and ratios that are associated with crustal contamination, after Sjøger et al. (2013). UCC is upper continental crust and LCC is lower continental crust. These values are based on those recommended for these reservoirs in Rudnick et al. (2003). OIB and N-MORB are shown for comparison of Patagonian melts with uncontaminated reservoirs; compositions for these two mantle end members are derived from those given in Sun and McDonough (1989). Arrows indicate possible contamination vectors. Also

Figure 3.11 (cont'd)

shown are the three continental contamination indicators versus MgO to rule out variation of these elements due to fractional crystallization.

Gorring & Kay (2001) argue that some crustal-level assimilation-fractional crystallization occurs in the Patagonian Triple Junction province magmas, especially where magmatism is more voluminous, such as the Meseta de la Muerte to the southwest of our study area. However, in the northeastern part of the Triple Junction province the melts are lower volume. The isotopic evidence presented in Kay et al. (2004) for northeastern Triple Junction province magmas shows there is some evidence of crustal contamination in mid-Miocene to recent magmas. We also show this using trace element data derived from this study above in Figure 3.11.

Crustal contamination is still possible in Eocene-early Miocene magmas. Eocene magmas are more voluminous than the more recent ones (Espinoza et al., 2005), meaning that they may have had the opportunity to assimilate some crust. During this study, we collected samples of Eocene magmas (the Cerro del Doce formation) and early Miocene (the Alma Gaucha formation). This is consistent with our results shown in Figure 3.11, which shows Cerro del Doce group C trending towards upper continental crust. Cerro del Doce groups A and B also trend towards lower continental crust. Alma Guacha basalts also trend towards lower continental crust. There are less isotopic data available regarding these older magmas; Gorring & Kay (2001) did not include any Eocene or early Miocene lavas in their study. However, Kay et al. (2004) do give isotopic constraints from Eocene melts found in other parts of the Patagonian back arc, and what appears to be one magma from the Cerro del Doce formation. That Cerro del Doce lava is shown on a plot but is not included in the data tables from that study. It is also not clear whether that Cerro del Doce lava is from the basaltic series, the trachybasaltic series, or the basanitic series that our study

divides them into. What we do know about Paleocene-Eocene melts is that they have even more positive ϵNd values than the northeast mid-Miocene to recent magmas. Kay et al. (2004) show one Cerro del Doce sample has ϵNd of +4, and other Eocene melts in the back-arc range from +3.2 to +5.8 ϵNd . Kay argues against major crustal contamination that would drive ϵNd to negative values during this time. To the southeast of our study area, Espinoza et al. (2005) find OIB-type basalts at Meseta Chile Chico with ϵNd from +4.9-7.0 with little evidence of crustal contamination.

Isotopes from magmas erupted between the Oligocene and Miocene (27-15 Ma eruption ages) show a range of ϵNd from highly positive (+7) to near zero (Kay et al., 2004), also arguing against crustal contamination in these magmas. These isotopic signatures indicate derivation from MORB-like to primitive mantle type isotopic sources (Kay et al., 2004). Major-element and trace-element characteristics of these magmas are consistent with an OIB source which could be isotopically like the primitive mantle reservoir (i.e., ϵNd near zero); magmas are all trace-element enriched and range from sub-alkaline basalt to basanitic.

In the absence of more isotopic constraints on Eocene and early Miocene lavas, we therefore conclude that crustal contamination did play a minor role in petrogenesis. All magmas in this study, from Eocene to recent, likely did not have enough volume or residence time within the crust to assimilate large volumes of crustal material. These magmas do, however, show some trace element indicators that they did incorporate some upper and lower crust during their evolution. The source of this contamination could be to anatexis of the crust in response to uplift and decompression, for which there is evidence in the Deseado Massif (Ávila & Dávila, 2020). While crustal contamination could indeed be involved in details of the petrogenesis of these lavas, the overall trace element enriched signatures require an enriched mantle source to begin with. We suggest that the enriched nature of these magmas may be attributable to source characteristics such

as pyroxenite in the mantle source and low degrees of mantle partial melting. We will explore these hypotheses in later sections of this document, after we discuss the temporal systematics of magmatism in this area of Patagonian Argentina and the relationship to plate tectonics.

3.5.2 The Temporal Progression of Triple Junction Province Magmatism Relative to Slab Windows

A large body of work has been published that ascribes a specific tectonic cause to back-arc magmatism in the Triple Junction province of Patagonia, namely the progression of slab windows (Gorring et al., 1997; Gorring & Kay, 2001; Kay et al., 2004; Breitsprecher & Thorkelson, 2009; Guillaume et al., 2010; Ávila & Dávila, 2020; Navarrete, Gianni, et al., 2020). There are two recognized episodes of slab window magmatism here. The first one from 16 Ma to recent is proposed due to the collision of Chile Ridge segments with the Chile Trench, uplift in the Andes, and coincident magmatism in the back arc (Gorring et al., 1997; Gorring & Kay, 2001; Guillaume et al., 2010). The second, earlier, and proposed slab window episode is thought to have occurred in the Paleocene-Eocene, with some estimates ranging in age from 53-36 Ma, and evidence includes the back-arc magmatism, as well as marine transgression and uplift along the Atlantic margin of Patagonia (Kay et al., 2004; Navarrete, Gianni, et al., 2020). Navarrete et al. (2020) also use plate reconstruction models of Müller et al. (2016) as further evidence for these Paleocene-Eocene slab windows.

There are some issues with ascribing the cause of this back arc magmatism to slab windows. Kay et al. (2004) note that Oligocene-early Miocene magmatism does not appear to correspond to any period of slab-window formation constrained in this section of the Andean subduction system, creating a problem using the slab window model to explain melts from that

period. If the magmas produced in this Oligocene to early Miocene period were due to a different tectonomagmatic cause other than a slab window, we would expect to observe a different composition from those that are thought to come from a slab window. On the contrary, all the magmas from the Eocene to recent sampled in this study are very similar geochemically. We find trace element spider patterns and REE patterns that are enriched and broadly have similar characteristics, including positive Sr and Pb anomalies.. Given that there is no evidence for a Miocene-Oligocene slab window to generate melts in this fashion, the similarities in the geochemical signatures of Eocene-recent Patagonian Triple Junction province magmas would be difficult to explain by different processes. Thus, the slab window hypothesis may not be adequate to explain these similar magmas emerging over 40 Ma. An alternative hypothesis that requires a singular process operating through time is therefore required.

We suggest here that the source of this magmatism (and therefore the process that generated the melts) is persistent over the last 40 Ma even if it is possibly heterogeneous in terms of lithology and melt percentage. A similar explanation has been suggested very recently by Søger et al., (2021) who put forth a model that posits the Patagonian intraplate basalts along the entire back-arc are a reflection of the mantle convection currents beneath the South Atlantic. In this model, the sub-continental lithospheric mantle (SCLM) beneath Patagonia was modified by melts from the African large low shear velocity province (LLSVP). This links magmatism in the Cenozoic to melts that were initially emplaced in the SCLM (melt metasomatism) during the Mesozoic Chon Aike, Karoo, and Ferrar LIPs which occurred contemporaneously with the breakup of Gondwana during the Jurassic. Similar material to that of metasomatized the SCLM of Patagonia in the Mesozoic is still erupting today along hot spots near the southern Mid Atlantic Ridge (e.g., Bouvet, Discovery seamounts, the Shona ridge, and Tristan/Gough). Søger et al. (2021) also note that

many of the South Patagonian melts have characteristics (i.e., high whole-rock $\text{FeO}^{\text{T}}/\text{MnO}$ and low CaO) that are consistent with derivation from pyroxenite material.

Pyroxenite is a mantle lithology that recently has been recognized as important in generating melt, especially at hot spots (OIB). Evidence for mixed peridotite-pyroxenite source lithology is implicated at many hot spot upwellings such as Hawaii (e.g., C. Herzberg et al., 2007; Herzberg, 2006, 2011; Bizimis et al., 2013), the Canary Islands (e.g., Herzberg, 2011), the Galapagos Islands (e.g., Trela et al., 2015), and the Karoo LIP (e.g., Heinonen et al., 2013). Blobs of pyroxenite in a peridotite matrix (i.e., a lithologically heterogeneous mantle) have been shown to produce melt, and this melting is a function of potential temperature, fraction of pyroxenite, and fertility of the pyroxenite (Lambart et al., 2016). Studies that examined magmas and the minerals crystallized from those magmas in the northern part of the Patagonian back arc also conclude that these heterogeneities of pyroxenite are important contributors to magma generation (Søager et al., 2013, 2015). We therefore hypothesize that although tectonic perturbations may trigger melting events, the cause of the back-arc magmatism is likely attributable to pyroxenite heterogeneity in the melting source region. We observe whole-rock $\text{FeO}^{\text{T}}/\text{MnO}$ in whole rocks in this study that are mostly >60 (except for samples TOR0000TP, an unconstrained sample, and TOR0000U0, an Eocene basanite) and CaO contents <9 wt. %, both measures that indicate it is likely that pyroxenite was a major contributor to melts (Søager et al., 2021). These pyroxenite heterogeneities could have been impregnated into the Patagonian SCLM during the LIP magmatism of the Mesozoic. It also stands to reason that the melted material is derived in the asthenosphere, and convection has carried this asthenospheric material in response to flow within the mantle. We will explore these concepts in later sections of this document. First, we must derive some constraints on the mantle conditions of these Patagonian Triple Junction province basalts.

3.5.3 Estimation of Mantle-Equilibrated Primary Magmas using PRIMACALC2

Magmas that erupt at the Earth's surface have typically gone through at least some degree of evolution that must be corrected for to establish the primary composition that was last in equilibrium with the mantle. The most primitive melts found at the surface are those that have high whole-rock MgO and Mg# (molar Mg/Mg+Fe), but even these have generally crystallized some olivine. Therefore, we must correct for this olivine crystallization. This was accomplished by using the PRIMACALC2 modeling software of Kimura and Ariskin (2014). PRIMACALC2 creates a provisional primary basalt, and then uses the thermodynamic COMAGMAT3.72 program to iteratively constrain a forward evolution path that converges with the observed magma composition. Trace element concentrations in the primary basalt are then calculated by adding back the calculated mass of olivine the melt lost.

Before modeling melts in PRIMACALC2, we selected melts that had only experienced olivine crystallization (as opposed to olivine \pm clinopyroxene \pm plagioclase feldspar). Samples were selected based on the presence of only porphyritic phenocryst olivine. One exception to this is sample TOR0000TU of the Alma Gaucha basalt; this flow, the base of stratigraphy, has minor feldspar. These feldspars are small and most likely crystallized either during ascent or post-eruption, and thus have not exerted a major control on the basalt's geochemistry. The sample above TOR0000TU in the stratigraphy has only olivine and was also utilized in this modeling. Based on Kimura and Ariskin (2014), PRIMACALC2 is capable of back-correcting other mineral phases. However, we have an abundance of high-MgO samples that only show petrographic evidence of olivine crystallization (or olivine with minor feldspar that is likely a post-emplacement phase), and therefore have chosen to use the simplest back-correction scenarios. This gave us seven samples for back correction: one from the La Angelita formation (Pliocene-Pleistocene; 2-3 Ma eruption

age); two from the Cerro Mojon formations (Miocene; 5 Ma eruption age); two from the Alma Gaucha formation (early Miocene; 22 Ma eruption age); one from the Cerro del Doce formation (Eocene; 35-40 Ma eruption age); and one of unconstrained age that was collected just south of the Deseado River.

During PRIMACALC2 simulations, the main input variables were left identical for all modeled melts. Crystallization mode was set to isobaric; this is the default setting that represents a magma that ponds temporarily and cools via crystallization. Because all magma groups show geochemical evidence of this crystallization, we think this is a reasonable assumption for the Patagonian back-arc magmas. Initial oxygen fugacity buffer was set to QFM (Quartz-Fayalite-Magnetite), which is appropriate for MORB or OIB type samples (Kelley and Cottrell, 2009; Kimura and Kawabata, 2014), consistent with the geochemical information we have presented. Runs were performed at both 1 and 2 weight percent H₂O, which are within the ranges of water contents found in primary back-arc basin basalts given in Kelley and Cottrell (2009). It should be noted that the La Angelita basalt at 1 wt. % H₂O returned a pressure of 0.0 GPa and therefore we consider this run to have failed. This may be related to the fact that the model also produced an F% (melting fraction) of 0%

The results of the seven back-corrected melts that were last in equilibrium with the mantle are presented in Table 3.2. In this table we have also included an estimated age for that magma based on the unit is from or constrained from Ar-Ar dates provided in this study or from Gorrington et al. (1997). Because not all PRIMACALC2 simulations were successful at the 1 wt. % H₂O, but were successful at 2 wt. %, we will base our discussion around these results. Lowering the water content of the primary basalt had the effect of increasing all output variables. The exception to this

is TOR0000TM, the La Angelita basalt that failed the 1 wt. % H₂O simulation, which failed to return a pressure or reasonable temperature estimates.

Sample	TOR-TE	TOR-TF	TOR-TM	TOR-TT	TOR-TU	TOR-TX	TOR-U5
Formation	Cerro Mojon	Cerro Mojon	La Angelita	Alma Gaucha	Alma Gaucha	N/A	Cerro del Doce
Age	5 Ma	5 Ma	2 Ma	22 Ma	22 Ma	N/A	40 Ma
Mg# of Primary Basalt	66	66	66	68	66	67	66
Fe ²⁺ /Fe(T)	0.83	0.83	0.83	0.84	0.84	0.84	0.84
FeO/MnO	76.8	75.2	76.6	80.4	80.8	74.8	81.8
TWC (Katz)	1291	1295	1272	1385	1354	1289	1374
TDC (Herz)	1460	1449	1471	1449	1445	1460	1445
P (GPa)	2.9	2.8	3.1	2.4	2.5	2.8	2.5
F% (Herz)	1	2	0	17	11	1	14
(La/Sm) _N	3.00	3.00	3.74	2.32	2.43	2.60	1.95
%XFrac	13	13	14	16	14	13	15
MgO PM	31	30	32	29	28	32	28
Primary Magma CaO (Wt. %)	7.69	7.72	7.78	7.60	7.69	7.84	7.67
Primary Magma FeO ^T /MnO	74.7	74.6	79.1	81.7	79.6	73.1	80.1

Table 3.2

Table summarizing the results of PRIMACALC2 modeling simulations to back correct for olivine fractionation and establish Primary magma compositions. Sample names have had the 0000 between the TOR and the -## omitted and replaced with a dash (-) to save space. F% is percent partial melt; %XFrac represents the weight percent of olivine that has been added back into the primary melt; P is pressure; TWC is wet temperature in °C; TDC is dry temperature in °C; Fe²⁺/FeT is the calculated percentage of Fe in the 2+ oxidation state over the total Fe in the sample; MgO PM is the weight percent of MgO calculated for the mantle in equilibrium with the sample. (La/Sm)_N from non-corrected magmas is shown for a comparison to predicted F%.

The results of PRIMACALC2 simulations reveal primary magmas that are very similar in composition, as well as pressure & temperature of crystallization. Modeled primary melts from this study have consistently deep predicted melt segregation pressures. Our results show melt segregation at depths of 2.4-3.1 GPa. Modeled wet melt temperature (TWC(Katz)) range from 1272-1385°C, while modeled mantle melting fraction (F%) range from 0-16%.

Several correlations exist in the PRIMACALC2 modeling results. F% decreases as age decreases; pressure of melt segregation decreases as wet temperature (TWC(Katz)) increases; and F% increases as wet temperature increases. This suggests that as time progresses, melts are cooler, they are derived at higher pressure, and they have a lower fraction of partial melt. The La Angelita basalt, TOR0000TM, modeled in this study shows a 0% fraction of partial melt even at 2 wt. % H₂O, but we interpret this as an extremely low (<1%) melt fraction.

Typically (La/Sm)_N is inversely correlated with partial melting percentage or melting fraction (F%), where elevated (La/Sm)_N suggests lower percentage of partial melts (Rollinson, 2014). We observe lower (La/Sm)_N in Eocene melts and higher values in younger melts, suggesting that the percentage of partial melting was higher in older melts and lower in younger melts. This is consistent with six of the seven the modeled melts. Melts with low (La/Yb)_N from the Alma Gaucha and Cerro del Doce formations have high partial melting percentages predicted by PRIMACALC2. Conversely, melts with high (La/Sm)_N from the Cerro Mojon and La Angelita formations have low partial melting percentages (Table 3.2). The only magma that is inconsistent with this inverse correlation is the unconstrained sample TOR0000TX, which has moderate (La/Sm)_N and a low partial melting percentage predicted by PRIMACALC2. This could be a function of low La in the magma's source.

The major element compositions of back-corrected, mantle equilibrated melts predicted by PRIMACALC2 simulations also indicate derivation from a pyroxenite-type source mantle. Peridotite melts have whole-rock $\text{FeO}^{\text{T}}/\text{MnO} < 60$ and CaO contents from 9-12.5 weight percent; meanwhile, pyroxenite melts have whole-rock $\text{FeO}^{\text{T}}/\text{MnO} > 60$ and CaO contents that are broadly < 9 wt. %. The Patagonian primary melts simulated in this study have low CaO contents in a narrowly defined range (7.60-7.84 wt. %), and $\text{FeO}^{\text{T}}/\text{MnO}$ greater than 60 (73.1-81.7), which is consistent with derivation from pyroxenitic mantle domains. These results are seen in melts that span in age from the Eocene to the Pliocene/Pleistocene. This modeling outcome supports the initial hypothesis that pyroxenitic mantle is consistently melting through time.

3.5.4 Exploring Adiabatic Mantle Melting of Patagonian Back Arc Basalts using Ocean Basalt Simulator version 1 (OBS-1)

In the previous section we discussed the back correction of olivine primary melts using PRIMACALC2 modeling software (J.-I. Kimura & Ariskin, 2014). This model calculates the mantle equilibrium based on major elements, and then applies a correction to the trace element concentrations of that sample based on the major-element results and how much olivine was added back into the melt to make it a primary mantle-equilibrated composition. We also note that back-corrected mantle equilibrated major element compositions have high $\text{FeO}^{\text{T}}/\text{MnO}$ and low CaO that are consistent with derivation from pyroxenite-rich mantle domains. However, the estimated mantle conditions from major elements are prone to greater uncertainty than those derived from trace elements (J. Kimura & Kawabata, 2015; Baziotis et al., 2018). Therefore, we have taken the back-corrected trace element compositions for primary Patagonian back-arc basalts and used these

as inputs in the trace-element mass balance thermodynamic model of adiabatic mantle melting Ocean Basalt Simulator version 1 (OBS1; J. Kimura & Kawabata, 2015).

This mantle melting simulator provides different insights into various mantle parameters, most importantly for this study the proportion of pyroxenite in the source mantle. The parameters OBS1 estimates include the mantle potential temperature (T_P °C), the proportions of various mantle lithologies present in the source mantle (pyroxenite, primitive mantle peridotite, and depleted MORB peridotite), the melting fraction (F%) and the depth of the melting column (J. Kimura & Kawabata, 2015). We can make some pre-modeling predictions of some of these quantities based on trace element ratios. Magmas with $(Tb/Yb)_N > 1.85$ indicates melting in the presence of garnet, and thus melting at greater depths (Nelson et al., 2019). Most Patagonian Triple Junction province magmas have $(Tb/Yb)_N > 1.85$; those that do not (specifically Eocene Cerro del Doce Group C magmas) have $(Tb/Yb)_N$ between 1.75-1.85, indicating the melting may have occurred near the transition zone between garnet and spinel in the mantle. The depth of this transition is thought to be temperature-dependent based on petrological experiments (e.g., Klemme and O’Niel, 2000), but is typically 20-26 kbar (2.0-2.6 GPa) between 1200° and 1400° C. These elevated $(Tb/Yb)_N$ values all indicate deep melting.

Mantle potential temperature is a measure of the temperature of the mantle if it were to ascend adiabatically to the surface. It is often used to compare the temperature of the “ambient” mantle (i.e., the depleted upper mantle beneath mid-ocean ridges) to that of thermal anomalies/mantle plumes. The ambient mantle potential temperature is typically 1200-1400°C, while plumes can exceed this by several hundred degrees (Herzberg et al., 2007).

The simulator outputs two pressures that are meant to represent a melting column: the first pressure is the pressure of melt segregation, or the final pressure in the mantle where the melt is

extracted from the melting lithology (in other words segregated) and rises buoyantly on its own; the second pressure is the pressure where the first melt is formed at triple junctions. We report the final pressure of melt segregation.

The fitting strategy employed during this study was to adjust the various fitting parameters manually. OBS-1 offers a Monte Carlo macro fitting program that we opted not to use due to the time (2-3 hours) required by Excel to run each Monte Carlo simulation and the possibility of these simulations not returning any viable results. Effective results were achieved manually because we were able to allow one element to be just outside of the acceptable tolerances. The primary fitting parameters that controlled the output basalt were the pyroxenite fraction, PM peridotite fraction, potential temperature, and melt segregation depth; these were adjusted to fit the calculated model basalt to the trace element pattern of the target basalt.

There is an option to change the mixing model between melt metasomatism (T) and melt-melt mixing (X). In the metasomatism (T) model, a pyroxenite melt alters (metasomatizes) the peridotite lithology, and then a melt of that peridotite is the simulated melt. The reaction of these two (the solid peridotite and pyroxenite melt) then reduces the solidus temperature of the new metasomatized peridotite. In the alternate end member mixing model (X), the peridotite and pyroxenite both generate a partial melt, and these two melts mix to provide the simulated melt composition. Kimura & Kawabata (2015) note that in natural systems the process would likely be somewhere between the two extremes. We opted to utilize the melt metasomatism (T) assumption for most of our fitting results, but we have generated some results that satisfy our criteria for a successfully modeled melt that utilize the melt-melt mixing (X) process.

Neither of the pyroxenite compositions included in the OBS1 package were sufficient to match our observed lavas. The pyroxenites included in OBS1 were: Py-MORB which is assumed

to be an N-MORB (normal MORB) of Pearce & Parkinson (1993); and Py-UCC, which is unattributed in the main text of Kimura & Kawabata (2015) but we assume by the abbreviation UCC to represent a composition consistent with upper continental crust. To find other geologically relevant pyroxenite compositions, we looked to the recent work on mantle melting by Brown et al. (2020). In their melting models they used three different natural pyroxenite compositions, MIX1G, G2, and KG1. They used these compositions to constrain potential temperature and pyroxenite percentage in Icelandic basalts using their REEBOX-Pro software. G2 pyroxenite is also important to the modeling performed by Lambart et al. (2016) where that group sought to parameterize the melting of mantle pyroxenite. We used these compositions in further modeling attempts with OBS1, and we were able to obtain successful fits using these three geologically relevant pyroxenite compositions (see below).

Because the given compositions in Brown et al. (2020) did not include the full suite of elements needed for input into OBS1, we had to interpolate these missing elements (specifically Sr, Eu, Tb, Ho, Tm). This interpolation estimate was accomplished by taking the geometric mean of the adjacent chondrite-normalized element concentrations, and then converting this to a ppm concentration. For example, for Sr, the elements Pr and Nd are adjacent. In the G2 pyroxenite, the chondrite-normalized abundance of Pr is 7.54 and the chondrite-normalized abundance of Nd is 6.84. The geometric mean of these two is 7.18, and this chondrite-normalized value corresponds to 151.6 ppm Sr assumed in the pyroxenite. This method assumes that the pyroxenite trace element patterns are “smooth”, meaning that there are not negative or positive anomalies in the interpolated elements.

We considered a run a possible solution when it was able to reproduce the observed melt within the fitting window for the Monte Carlo calculation for 25/26 trace elements. We also

attempt to fit most of the strongly incompatible elements (i.e., the right side of spider diagrams produced by OBS1) to under 10% relative standard deviation and to represent the same approximate slope of the incompatible elements. The parameters with the greatest effect on the strongly incompatible elements are the mantle potential temperature and the melt segregation depth. An example of the trace element spider diagram fit and the fitting window we observed for one such successful run on TOR0000TE is shown below in Figure 3.12 and Figure 3.13. Isotopes were not constrained by this study and were therefore not considered in the fitting parameters, only trace elements. Results are summarized in Table 3.3, below.

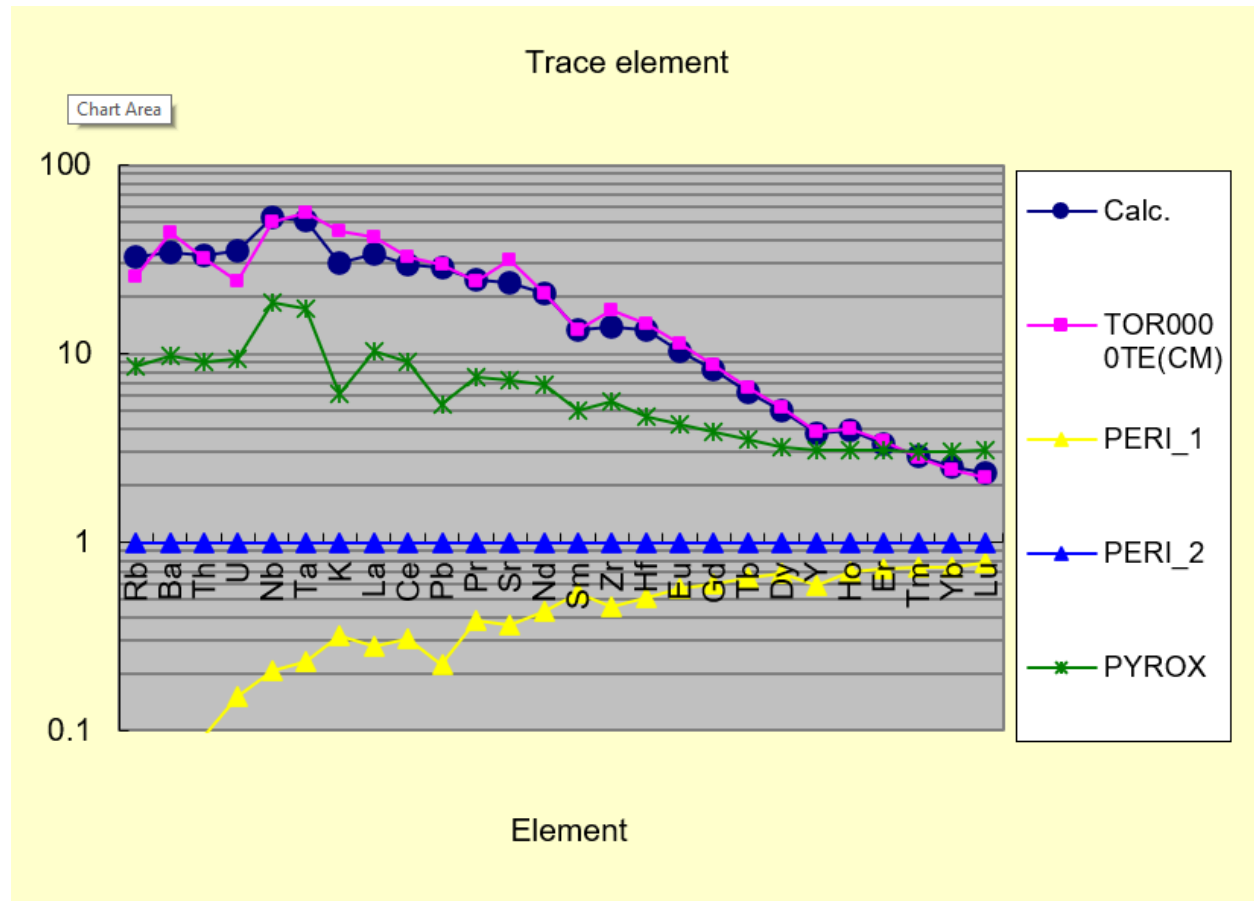


Figure 3.12

OBS1 trace element spider profile (normalized to primitive mantle of Sun & McDonough, 1989) of sample TOR0000TE (Cerro Mojon, Mio-Pliocene) using the pyroxenite composition G2, considered a successful fit and therefore a possible solution. Slope on heavily incompatible elements (the right side of the diagram) was considered a critical constraint on the success of the fit. The dark blue line represents the melt calculated by OBS1 because of mixing the three end members in user-specified proportions: PYROX, green (in this instance the G2 pyroxenite composition of Brown et al. (2020)); PERI_2, bright blue, which represents the primitive or previously unmelted mantle; and PERI_1, yellow, which represents the depleted mantle component. The pink line represents the measured composition of the lava. Elements are displayed

Figure 3.12 (cont'd)

as concentrations divided by primitive mantle (PM); in this case PM values are from (Sun & McDonough, 1989).

FITTING WINDOW FOR MONTE CARLO CALCULATION												
ELEMENT	Rb	Ba	Th	U	Nb	Ta	K	La	Ce	Pb	Pr	Sr
LIMIT(RD%)	50	50	100	50	30	30	30	30	30	50	30	30
CALC(RD%)	26.6	21.9	5.3	44.2	5.5	8.8	32.2	17.5	8.8	3.8	2.3	24.7
Calc (ppm)	20.61	241.28	2.84	0.73	37.71	2.08	7619	23.37	53.00	2.28	6.86	502

Nd	Sm	Zr	Hf	Eu	Gd	Tb	Dy	Y	Ho	Er	Tm	Yb	Lu
30	30	30	30	30	20	20	20	20	20	20	20	20	20
0.4	0.1	18.9	8.1	9.9	6.0	4.0	3.9	1.1	2.7	4.4	1.1	4.7	5.7
28.34	5.96	156	4.11	1.72	4.88	0.68	3.66	17.26	0.64	1.58	0.21	1.25	0.17

Figure 3.13

Monte Carlo simulation fitting window from OBS1 that was the second control on successful fit for elements. The view has been split into two to fit within the width constraints of this document. 25/26 elements match between the observed and the simulated melt. In this case K was slightly outside of the window of success at 32.2 of an acceptable 30 relative deviation % limit. However, considering the low percentage relative deviation (RD%) for the right side of the diagram (i.e., the bottom row of elements in the figure; also, the most incompatible) we considered the slight mismatch excess of 2.2% relative deviation on the element potassium to be within acceptable tolerances.

Sample Name	Melting Model	Pyroxenite Source	Pyroxenite Fraction	Peri-2 (Primitive mantle) fraction	Mantle potential temp. (T_P , °C)	Melt Seg. Depth (GPa)
TOR0000TE (Cerro Mojon)	T	G2	7%	60%	1385	2.7
TOR0000TE (Cerro Mojon)	T	MIX1G	11%	70%	1380	2.7
TOR0000TF (Cerro Mojon)	T	G2	8%	60%	1385	2.7
TOR0000TF (Cerro Mojon)	T	MIX1G	10%	70%	1360	2.6
TOR0000TM (La Angelita)	T	MIX1G	11%	70%	1360	2.6
TOR0000TT (Alma Gaucha)	X	KG1	11%	60%	1380	2.7
TOR0000TT (Alma Gaucha)	T	KG1	3%	50%	1390	2.7
TOR0000TT (Alma Gaucha)	T	MIX1G	8%	50%	1370	2.6
TOR0000TU (Alma Gaucha)	T	KG1	5%	70%	1380	2.6
TOR0000TX (Unconstrained)	T	MIX1G	8%	50%	1380	2.6
TOR0000U5 (Cerro del Doce)	X	G2	10%	60%	1380	2.7
TOR0000U5 (Cerro del Doce)	T	MIX1G	3%	70%	1370	2.6

Table 3.3

Table summarizing the result of OBS1 simulations on Patagonian triple junction province melts that were first back corrected in PRIMACALC2 to reflect equilibrium with the mantle. Melting models are melt metasomatism (T) and melt-melt mixing (X), discussed in text.

From the results shown in Table 3.3, it is evident that solutions are non-unique, and successful fits can be generated by using different pyroxenite compositions and melting models. The pyroxenite MIX1G is the most common pyroxenite to provide a successful fit, and the melt-

metasomatism melting model (T) is the most commonly successful. With many unsuccessful fits, the melt mixing model (X) often overestimated the least incompatible elements, i.e., those on the left side of the spider diagram. The necessary pyroxenite fraction ranges from 3-11% and the needed proportion of primitive mantle is 50-70%. Mantle potential temperatures vary little from 1370-1390 °C, and the pressure of final melt segregation is also consistently 2.6-2.7 GPa. This pressure corresponds to roughly 86-89 km depth if it is assumed that 1 GPa is equivalent to 33 km depth; this is consistent with depths estimated from pressure in Kimura & Kawabata (2015). These pressure estimates are also in the same range of pressure estimates calculated by the major element models for back correction in PRIMACALC2, which were 2.4-3.1 GPa (79-102 km depth). The greater range in PRIMACALC2 compared to OBS1 may represent the greater uncertainty associated with using major elements instead of trace elements.

Based on the depths of melting constrained by PRIMACALC2 and OBS1, it seems unlikely that the lithosphere is the source of these melts. There are several constraints on the thickness of the lithosphere in this area. One such study, which uses heat flow measurements to infer lithospheric thickness, suggests that the lithosphere beneath this part of Patagonia is at present ~25-50 km thick, having been thinned by a widening slab window spreading to the northeast (Ávila & Dávila, 2018). The thinnest part of the lithosphere is beneath Gobernador Gregores in Ávila & Dávila's (2018) heat flow model. Xenolith studies of garnet and spinel peridotites from Pali Aike that utilized mineral thermometry and barometry suggested lithospheric thicknesses between 60 and 80 km (Zaffarana et al., 2014). Meanwhile, waveform inversion seismic models predict a lithospheric lid thinner than 65 km broadly throughout Patagonia (Robertson Maurice et al., 2003). All these estimates suggest thinner lithosphere than even the shallowest of melt segregation pressures in our modeling results, which is 2.4 GPa or 79 km depth.

Based on the results of PRIMACALC2 and OBS1 modeling, we can make some conclusions. Pyroxenites (G2, KG1, MIX1G) and primitive mantle material are necessary lithologies for generating mantle melts in this area. This is supported by the low CaO and high FeO/MnO of these melts, as well as the isotopic results of Gorry and Kay (2001) which show ϵ_{Nd} values near that of the primitive mantle. Multiple constraints on the thickness of the lithosphere in the area estimate a lithosphere thinner than 65 km (Ávila & Dávila, 2018; Robertson Maurice et al., 2003; Zaffarana et al., 2014). Based on the depth of melt segregation estimated by OBS1 (86-89 km depth), the asthenosphere and not the lithosphere is the most likely location of these melting lithologies. A recent paper by Chiasera et al. (2021) conducted mantle equilibration modeling on Ethiopian flood basalts using the Hydrous Adiabatic Mantle Melting Simulator (HAMMS), which was designed by the same individuals that created OBS1. In this paper, the authors argued that the modeled depth of melt segregation represents the depth of the lithosphere-asthenosphere boundary where the magmas last equilibrate with the mantle (Chiasera et al., 2021). This may also be true of the Patagonian melts studied in this paper; if we assume this is the case, then this represents thicker lithosphere in the Patagonian back arc than that suggested by others (e.g., Robertson Maurice et al., 2003, Ávila & Dávila, 2018).

The mantle modeled in this work is homogeneous with respect to depth of melt segregation (constrained by PRIMACALC2 and OBS1 results) and potential temperature (constrained by OBS1 results). These calculations are in line with the geochemical evidence (e.g., $(\text{Tb}/\text{Yb})_{\text{N}}$), which suggests these melts were in equilibrium with garnet at depths greater than 2.0 GPa. Furthermore, the predicted melting fractions (F%) that decrease through time in the modeled results are consistent with observed $(\text{La}/\text{Yb})_{\text{N}}$ values that increase from older to younger melts.

Finally, the predictions of pyroxenite contribution are consistent with the elevated $\text{FeO}^{\text{T}}/\text{MnO}$ and CaO contents.

3.5.5 Dripping Pyroxenite in the Source of Eocene-Recent Patagonian Triple Junction Province Magmas

The OBS1 modeling results presented in the previous section suggest that pyroxenite is a necessary material in the source mantle to explain the observed melt compositions. The pyroxenites that provide successful fits are trace element enriched pyroxenites from Brown et al. (2020) which are considered geologically relevant; the somewhat depleted N-MORB pyroxenite and UCC pyroxenite that came pre-loaded into OBS1 did not return successful fits. This is consistent with studies that find LREE-enriched pyroxenites in central Patagonian SCLM-derived xenoliths as well as LREE-depleted pyroxenes in peridotites, and those with flat REE patterns (Melchiorre et al., 2015, 2020). These same studies suggest the SCLM beneath Patagonia is extremely heterogeneous, with EM-1 type materials, depleted MORB mantle materials, and primitive mantle type mantle materials (Melchiorre et al., 2015, 2020). This is consistent with the idea that enriched pyroxenite domains exist within mixed depleted and primitive mantle domains in the Patagonian SCLM. The results from OBS1 simulations indicate Peri-2 (primitive mantle) percentages of 50-70%. These results suggest a considerable proportion of the contributing mantle material to Triple Junction province melts was previously unmelted mantle (PM or pyrolite) that is also possibly richer in pyroxene (Green & Ringwood, 1967; Anderson & Bass, 1984; Kesson et al., 1998; Yang et al., 2019).

A recent model put forth by Søger et al. (2021) suggests that westward flow of mantle material driven by subduction has drawn in plume-type material from the southern Mid Atlantic

Ridge. These plume-type materials are compositionally similar to the modern ocean island basalts erupted near this ridge (Søager et al., 2021). This model does not require a slab window to produce melts. However, this model relies on mantle material being transported up to 4000 km laterally from the ridge before it melts beneath the continental back-arc. On the eastern side of the Mid Atlantic Ridge, these ocean island basalts erupt as seamounts ~1000 km from the ridge. Søager et al. (2021) argue that it is possible that the asthenosphere beneath the continents moves at an accelerated rate relative to the continents. To make this argument they point to a 2014 study by Colli et al., where several estimates of asthenospheric mantle flow velocities are presented based on uncertainties in asthenospheric channel depth and mantle viscosity; Søager et al. (2021) utilize a value of 24.1 cm/s from Table 1 of Colli et al. (2014). They use this velocity to suggest that if that mantle flow velocity were to remain constant through time, the difference between asthenospheric flow and plate motion would be sufficient to draw mid-Atlantic ridge material beneath the South American continent. However, Colli et al. (2014) conclude in their paper that the velocity of flow in the asthenosphere is transient in time based on their models and observations. Furthermore, there is considerable uncertainty in the constraints on mantle viscosity (e.g. Mao and Zhong, 2021). Because of this uncertainty, we propose a simpler explanation here: rather than having material transported long distances by mantle flow before melting, the material was instead stored in the Patagonian lithosphere.

The most recent magmatism in the Patagonian Triple Junction province prior to the Eocene was the Jurassic-aged (188-153 Ma ago) Chon Aike silicic large igneous province that is also associated with the Karoo and Ferrar LIPs that signified the breakup of Gondwana (Navarrete et al., 2020; Pankhurst et al., 1998). It is plausible that hot, dense lithosphere (i.e., dense due to pyroxenite) was created during this LIP event and was not affected by destabilization until it had

become sufficiently negatively buoyant. Recent studies (e.g., Heinonen et al., 2015) suggest the Karoo LIP saw olivine crystallization temperatures as high as $1481 \pm 35^\circ\text{C}$ based on Al-in-olivine thermometry, indicating that the lithospheres of the affected continental terranes were heated to at least 200°C above ambient mantle temperatures. It is posited here that the Karoo LIP generated magma that transited the lithosphere; as this occurred, dense pyroxenite zones were created, especially at the base of the lithosphere. These dense materials emplaced in the lithospheric mantle then may have cooled and subsequently delaminated over the last 40 Ma in response to the asthenospheric flow established by subduction at the western margin of South America.

One possible explanation for the observed modeled trends in PRIMACALC2 results of decreasing F% and increasing pressure of melting versus decreasing age could be due to what is called “drip magmatism”, whereby dense, unstable parts of the lithospheric mantle gradually descend into the mantle and undergo “damp” melting due to dehydration/devolatilization within these domains (Furman et al., 2016). There are several lines of evidence that may support this hypothesis. First, the series of slab window events and subduction-related events through the last 40 Ma in Patagonia could provide the necessary convective motion necessary to cause the destabilization of these deep lithospheric components (Massaferro et al., 2014; Søger et al., 2021). Furman et al. (2016) also note that uplift is a necessary component to lithospheric drip magmatism, and the Patagonian crust is undergoing dynamic uplift effects (Ávila & Dávila, 2020). Modeling results that show a time-progressive decrease in F% and increase in melting P may represent melting of this lithospheric material as it descends and the depletion of easily fusible (i.e., pyroxene-rich) material. The decreasing F% may also be a function of the increased pressure that inhibited the system from producing elevated melt fractions, or a depletion of the “dampness” that triggered larger-scale melting in the Eocene.

It is possible that subduction-related convective motion in the mantle, but not necessarily slab windows, are responsible for triggering the melting that caused Patagonian Triple Junction province magmas. Our results suggest that lithospheric material was formed during Mesozoic LIP magmatism. This dense, pyroxenitic material then subsequently dripped into the asthenosphere. Melting of these dripping pyroxenites are responsible for the observed Eocene-recent Patagonian Triple Junction melts. Further geophysical studies into the mantle, age dating, isotopic study, and modeling are necessary to fully constrain this link, but our observations and the associated interpretations should be integrated into the ongoing debate on sources of magmatism in the Patagonian back arc.

3.6 Conclusions

Cenozoic magmas of the Patagonian Triple Junction province that occurred from 40Ma ago until recently have trace-element enriched compositions. The results of this study and trace element modeling performed herein demonstrate that these melts are generated in the asthenosphere at pressures from 2.6-2.7 GPa, and that all magmas require a contribution from pyroxenitic mantle domains. Previous models (e.g., Gorrying et al., 1997; Gorrying & Kay, 2001; Guillaume et al., 2010; Ávila & Dávila, 2018) assigned tectonic causes to these magmas due to the temporal association of mid-ocean ridge collisions with the South American continent in both the Miocene-Pleistocene and the Paleocene-Eocene. These ridge collisions are thought to have precipitated the opening of slab windows in the mantle that asthenospheric material upwelled through. However, our results show that magmatism like that from the purported slab window periods occurred outside of the range of constrained ridge collision.

We conclude here Patagonian Triple Junction province magmas are the result of dense lithospheric material rich in pyroxenite dripping into the asthenosphere and melting due to devolatilization. Slab windows are thus not necessary to explain the magmatism. Instead, the pyroxenite heterogeneities stored within the lithospheric mantle are destabilized and are the cause of these magmatic events when they melt. Søger et al. (2021) suggest a model where convection pulls this material from a series of ocean islands and ridges in the southern Mid-Atlantic Ridge 4000 km away. These ocean islands and ridges in the Atlantic are themselves the remnants of plume-related magmatism and convection established in the Mesozoic during the breakup of the supercontinent Gondwana. Our alternative model presented here suggests vertical transport from the lithosphere, rather than lateral transport from the Atlantic mid-ocean ridge. Cenozoic magmatic deposits from this study are also associated spatially with Mesozoic volcanic units from Gondwana-related silicic breakup magmatism. We posit that pyroxene-rich mantle domains emplaced in the SCLM through melt metasomatism during this Mesozoic LIP activity are being destabilized by subduction-related convection. These pyroxenite domains are thus the source of these lithospheric drips. Furthermore, our observations may suggest that destabilization of the lithosphere and preferential melting of pyroxenites/pyroxene-rich lithologies are applicable processes to small-volume mafic magmas globally.

BIBLIOGRAPHY

BIBLIOGRAPHY

- Anderson, D.L. and Bass, J.D. 1984. Mineralogy and composition of the upper mantle. *Geophysical Research Letters*, **11**, 637–640, <https://doi.org/10.1029/GL011i007p00637>.
- Ávila, P. and Dávila, F.M. 2018. Heat flow and lithospheric thickness analysis in the Patagonian asthenospheric windows, southern South America. *Tectonophysics*, **747–748**, 99–107, <https://doi.org/10.1016/j.tecto.2018.10.006>.
- Ávila, P. and Dávila, F.M. 2020. Lithospheric thinning and dynamic uplift effects during slab window formation, southern Patagonia (45°–55° S). *Journal of Geodynamics*, **133**, 101689, <https://doi.org/10.1016/j.jog.2019.101689>.
- Baziotis, I., Kimura, J.-I., Pantazidis, A., Klemme, S., Berndt, J. and Asimow, P.D. 2018. Geophysical source conditions for basaltic lava from Santorini volcano based on geochemical modeling. *Lithos*, **316–317**, 295–303, <https://doi.org/10.1016/j.lithos.2018.07.027>.
- Bizimis, M., Salters, V.J.M., Garcia, M.O. and Norman, M.D. 2013. The composition and distribution of the rejuvenated component across the Hawaiian plume: Hf-Nd-Sr-Pb isotope systematics of Kaula lavas and pyroxenite xenoliths: Kaula Lavas And Pyroxenites. *Geochemistry, Geophysics, Geosystems*, **14**, 4458–4478, <https://doi.org/10.1002/ggge.20250>.
- Boutonnet, E., Arnaud, N., Guivel, C., Lagabrielle, Y., Scalabrino, B. and Espinoza, F. 2010. Subduction of the South Chile active spreading ridge: A 17Ma to 3Ma magmatic record in central Patagonia (western edge of Meseta del Lago Buenos Aires, Argentina). *Journal of Volcanology and Geothermal Research*, **189**, 319–339, <https://doi.org/10.1016/j.jvolgeores.2009.11.022>.
- Breitsprecher, K. and Thorkelson, D.J. 2009. Neogene kinematic history of Nazca–Antarctic–Phoenix slab windows beneath Patagonia and the Antarctic Peninsula. *Tectonophysics*, **464**, 10–20, <https://doi.org/10.1016/j.tecto.2008.02.013>.
- Cobos, J.C. and Panza, J.L. 2003. *4769-IV Bulletin No. 319 (El Pluma)*.
- Colli, L., Bunge, H.-P., Smethurst, M., Clark, S., Iaffaldano, G., Tassara, A., Guillocheau, F., and Bianchi, M.C. 2014. Rapid South Atlantic spreading changes and coeval vertical motion in surrounding continents: Evidence for temporal changes of pressure-driven upper mantle flow. *Tectonics*, **33**, 1304–1321, <https://doi.org/10.1002/2014TC003612>.
- Ducea, M.N., Seclaman, A.C., Murray, K.E., Jianu, D. and Schoenbohm, L.M. 2013. Mantle-drip magmatism beneath the Altiplano-Puna plateau, central Andes. *Geology*, **41**, 915–918, <https://doi.org/10.1130/G34509.1>.

- Espinoza, F., Morata, D., et al. 2005. Petrogenesis of the Eocene and Mio–Pliocene alkaline basaltic magmatism in Meseta Chile Chico, southern Patagonia, Chile: Evidence for the participation of two slab windows. *Lithos*, **82**, 315–343, <https://doi.org/10.1016/j.lithos.2004.09.024>.
- Furman, T., Nelson, W.R. and Elkins-Tanton, L.T. 2016. Evolution of the East African rift: Drip magmatism, lithospheric thinning and mafic volcanism. *Geochimica et Cosmochimica Acta*, **185**, 418–434, <https://doi.org/10.1016/j.gca.2016.03.024>.
- Global catalog of earthquakes - Humanitarian Data Exchange (USGS ANSS Comprehensive Catalog). n.d.<https://data.humdata.org/dataset/catalog-of-earthquakes1970-2014>.
- Gómez, J., Schobbenhaus, C. and Montes, N.E. 2019. *Geological Map Of South America At a Scale of 1: 5M*, <https://doi.org/10.32685/10.143.2019.929>.
- Gorring, M.L. and Kay, S.M. 2001. Mantle Processes and Sources of Neogene Slab Window Magmas from Southern Patagonia, Argentina. *Journal of Petrology*, **42**, 1067–1094, <https://doi.org/10.1093/petrology/42.6.1067>.
- Gorring, M.L., Kay, S.M., Zeitler, P.K., Ramos, V.A., Rubiolo, D., Fernandez, M.I. and Panza, J.L. 1997. Neogene Patagonian plateau lavas: Continental magmas associated with ridge collision at the Chile Triple Junction. *Tectonics*, **16**, 1–17, <https://doi.org/10.1029/96TC03368>.
- Green, D.H. and Ringwood, A.E. 1967. The stability fields of aluminous pyroxene peridotite and garnet peridotite and their relevance in upper mantle structure. 10.
- Guillaume, B., Moroni, M., Funicello, F., Martinod, J. and Faccenna, C. 2010. Mantle flow and dynamic topography associated with slab window opening: Insights from laboratory models. *Tectonophysics*, **496**, 83–98, <https://doi.org/10.1016/j.tecto.2010.10.014>.
- Guivel, C., Morata, D., et al. 2006. Miocene to Late Quaternary Patagonian basalts (46–47°S): Geochronometric and geochemical evidence for slab tearing due to active spreading ridge subduction. *Journal of Volcanology and Geothermal Research*, **149**, 346–370, <https://doi.org/10.1016/j.jvolgeores.2005.09.002>.
- Guo, Z., Wilson, M., Zhang, M., Cheng, Z. and Zhang, L. 2015. Post-collisional Ultrapotassic Mafic Magmatism in South Tibet: Products of Partial Melting of Pyroxenite in the Mantle Wedge Induced by Roll-back and Delamination of the Subducted Indian Continental Lithosphere Slab. *Journal of Petrology*, **56**, 1365–1406, <https://doi.org/10.1093/petrology/egv040>.
- Hayes, G.P., Smoczyk, G.M., Benz, H.M., Furlong, K.P. and Villaseñor, A. 2015. *Seismicity of The Earth 1900-2013, Seismotectonics of South America (Nazca Plate Region)*.
- Heinonen, J.S., Luttinen, A.V., Riley, T.R. and Michallik, R.M. 2013. Mixed pyroxenite–peridotite sources for mafic and ultramafic dikes from the Antarctic segment of the Karoo

- continental flood basalt province. *Lithos*, **177**, 366–380, <https://doi.org/10.1016/j.lithos.2013.05.015>.
- Heinonen, J.S., Jennings, E.S. and Riley, T.R. 2015. Crystallisation temperatures of the most Mg-rich magmas of the Karoo LIP on the basis of Al-in-olivine thermometry. *Chemical Geology*, **411**, 26–35, <https://doi.org/10.1016/j.chemgeo.2015.06.015>.
- Herzberg, C. 2006. Petrology and thermal structure of the Hawaiian plume from Mauna Kea volcano. *Nature*, **444**, 605–609, <https://doi.org/10.1038/nature05254>.
- Herzberg, C. 2011. Identification of Source Lithology in the Hawaiian and Canary Islands: Implications for Origins. *Journal of Petrology*, **52**, 113–146, <https://doi.org/10.1093/petrology/egq075>.
- Herzberg, C., Asimow, P.D., et al. 2007. Temperatures in ambient mantle and plumes: Constraints from basalts, picrites, and komatiites: Mantle temperatures inferred from volcanoes. *Geochemistry, Geophysics, Geosystems*, **8**, n/a-n/a, <https://doi.org/10.1029/2006GC001390>.
- Hildreth, W. and Moorbath, S. 1988. Crustal contributions to arc magmatism in the Andes of Central Chile. *Contributions to Mineralogy and Petrology*, **98**, 455–489, <https://doi.org/10.1007/BF00372365>.
- Huang, Z., Zhao, D., Hasegawa, A., Umino, N., Park, J.-H. and Kang, I.-B. 2013. Aseismic deep subduction of the Philippine Sea plate and slab window. *Journal of Asian Earth Sciences*, **75**, 82–94, <https://doi.org/10.1016/j.jseas.2013.07.002>.
- Jalowitzki, T., Gervasoni, F., et al. 2017. Slab-derived components in the subcontinental lithospheric mantle beneath Chilean Patagonia: Geochemistry and Sr–Nd–Pb isotopes of mantle xenoliths and host basalt. *Lithos*, **292–293**, 179–197, <https://doi.org/10.1016/j.lithos.2017.09.008>.
- Johnston, S.T. and Thorkelson, D.J. 1997. Cocos-Nazca slab window beneath Central America. *Earth and Planetary Science Letters*, **146**, 465–474, [https://doi.org/10.1016/S0012-821X\(96\)00242-7](https://doi.org/10.1016/S0012-821X(96)00242-7).
- Kay, S.M., Gorrington, M. and Ramos, V.A. 2004. Magmatic sources, setting and causes of Eocene to Recent Patagonian plateau magmatism (36°S to 52°S latitude). 13.
- Kesson, S.E., Fitz Gerald, J.D. and Shelley, J.M. 1998. Mineralogy and dynamics of a pyrolite lower mantle. *Nature*, **393**, 252–255, <https://doi.org/10.1038/30466>.
- Kimura, J. and Kawabata, H. 2015. OceanBasaltSimulator version (OBS1): Trace element mass balance in adiabatic melting of a pyroxenite-bearing peridotite. *Geochemistry, Geophysics, Geosystems*, **16**, 267–300, <https://doi.org/10.1002/2014GC005606>.
- Kimura, J.-I. and Ariskin, A.A. 2014. Calculation of water-bearing primary basalt and estimation of source mantle conditions beneath arcs: PRIMACALC2 model for WINDOWS.

- Klemme, S., O'Neill, H.S. 2000. The near-solidus transition from garnet lherzolite to spinel lherzolite. *Contributions to Mineralogy and Petrology*, **138**, 237-248.
- Lagabrielle, Y., Scalabrino, B. and Suárez, M. 2010. Mio-Pliocene glaciations of Central Patagonia: New evidence and tectonic implications. *Andean Geology*, **25**.
- Lambart, S., Baker, M.B. and Stolper, E.M. 2016. The role of pyroxenite in basalt genesis: Melt-PX, a melting parameterization for mantle pyroxenites between 0.9 and 5 GPa. *Journal of Geophysical Research: Solid Earth*, **121**, 5708–5735, <https://doi.org/10.1002/2015JB012762>.
- Loske, W., Marquez, M., Giacosa, R., Pezzuchi, H. and Fernandez, M.I. 1999. U/Pb Geochronology of the pre-Permian basement rocks in the Macizo del Deseado, Santa Cruz Province, Argentine Patagonia. *In: Resumen Congreso Geologico Argentino*. 1.
- Mao, W. and Zhong, S. 2021. Constraints on Mantle Viscosity from Intermediate-Wavelength Geoid Anomalies in Mantle Conversion Models with Plate Motion History. *Journal of Geophysical Research: Solid Earth*, **126**. <https://doi.org/10.1029/2020JB021561>.
- Massaferro, G.I., Haller, M.J., Dostal, J., Pécskay, Z., Prez, H., Meister, C. and Alric, V. 2014. Possible sources for monogenetic Pliocene–Quaternary basaltic volcanism in northern Patagonia. *Journal of South American Earth Sciences*, **55**, 29–42, <https://doi.org/10.1016/j.jsames.2014.07.001>.
- McCrory, P.A., Wilson, D.S. and Stanley, R.G. 2009. Continuing evolution of the Pacific–Juan de Fuca–North America slab window system—A trench–ridge–transform example from the Pacific Rim. *Tectonophysics*, **464**, 30–42, <https://doi.org/10.1016/j.tecto.2008.01.018>.
- McDonough, W. and Sun, S. 1995. The composition of the Earth. *Chemical Geology*, **31**, 223-253
- McGee, L.E., Brahm, R., et al. 2017. A geochemical approach to distinguishing competing tectono-magmatic processes preserved in small eruptive centres. *Contributions to Mineralogy and Petrology*, **172**, 44, <https://doi.org/10.1007/s00410-017-1360-2>.
- Melchiorre, M., Coltorti, M., Gregoire, M. and Benoit, M. 2015. Refertilization process in the Patagonian subcontinental lithospheric mantle of Estancia Sol de Mayo (Argentina). *Tectonophysics*, **650**, 124–143, <https://doi.org/10.1016/j.tecto.2015.02.015>.
- Melchiorre, M., Faccini, B., Grégoire, M., Benoit, M., Casetta, F. and Coltorti, M. 2020. Melting and metasomatism/refertilisation processes in the Patagonian sub-continental lithospheric mantle: A review. *Lithos*, **354–355**, 105324, <https://doi.org/10.1016/j.lithos.2019.105324>.
- Müller, R.D., Seton, M., et al. 2016. Ocean Basin Evolution and Global-Scale Plate Reorganization Events Since Pangea Breakup. *Annual Review of Earth and Planetary Sciences*, **44**, 107–138, <https://doi.org/10.1146/annurev-earth-060115-012211>.

- Mundl, A., Ntaflos, T., Ackerman, L., Bizimis, M., Bjerg, E.A. and Hauzenberger, C.A. 2015. Mesoproterozoic and Paleoproterozoic subcontinental lithospheric mantle domains beneath southern Patagonia: Isotopic evidence for its connection to Africa and Antarctica. *Geology*, **43**, 39–42, <https://doi.org/10.1130/G36344.1>.
- Navarrete, C., Butler, K.L., Hurley, M. and Márquez, M. 2020a. An early Jurassic graben caldera of Chon Aike silicic LIP at the southernmost massif of the world: The Deseado caldera, Patagonia, Argentina. *Journal of South American Earth Sciences*, **101**, 102626, <https://doi.org/10.1016/j.jsames.2020.102626>.
- Navarrete, C., Gianni, G., Massaferro, G. and Butler, K. 2020b. The fate of the Farallon slab beneath Patagonia and its links to Cenozoic intraplate magmatism, marine transgressions and topographic uplift. *Earth-Science Reviews*, **210**, 103379, <https://doi.org/10.1016/j.earscirev.2020.103379>.
- Nelson, W.R., Hanan, B.B., Graham, D.W., Shirey, S.B., Yirgu, G., Ayalew, D., Furman, T. 2019. Distinguishing plume and metasomatized lithospheric mantle contributions to post-flood basalt volcanism on the southeastern Ethiopian Plateau. *Journal of Petrology*, **60**, 1063–1094, <https://doi.org/10.1093/petrology/egz024>.
- Nicholson, S.W., Schulz, K.J., Shirey, S.B. and Green, J.C. 1997. Rift-wide correlation of 1.1 Ga Midcontinent rift system basalts: implications for multiple mantle sources during rift development. *Canadian Journal of Earth Sciences*, **34**, 504–520, <https://doi.org/10.1139/e17-041>.
- Pankhurst, R.J., Leat, P.T., Sruoga, P., Rapela, C.W., Márquez, M., Storey, B.C. and Riley, T.R. 1998. The Chon Aike province of Patagonia and related rocks in West Antarctica: A silicic large igneous province. *Journal of Volcanology and Geothermal Research*, **81**, 113–136, [https://doi.org/10.1016/S0377-0273\(97\)00070-X](https://doi.org/10.1016/S0377-0273(97)00070-X).
- Panza, J.L. 2001. 4769-IV bulletin no. 258 (*Monumento Natural Bosques Petrificados*).
- Panza, J.L. and Cobos, J.C. 2001. 4769-III bulletin no. 296 (*Destacamento la Maria*).
- Panza, J.L., Zubia, M.A. and Godeas, M.C. 1994. 4969-II bulletin no. 213 (*Tres Cerros*).
- Panza, J.L., Marin, G. and Zubia, M.A. 1998. 4969-I Bulletin No. 239 (*Gobernador Gregores*).
- Pearce, J.A. and Parkinson, I.J. 1993. Trace element models for mantle melting: application to volcanic arc petrogenesis. *Geological Society, London, Special Publications*, **76**, 373–403, <https://doi.org/10.1144/GSL.SP.1993.076.01.19>.
- Price, R.C., Gamble, J.A., Smith, I.E.M., Maas, R., Waight, T., Stewart, R.B. and Woodhead, J. 2012. The Anatomy of an Andesite Volcano: a Time–Stratigraphic Study of Andesite Petrogenesis and Crustal Evolution at Ruapehu Volcano, New Zealand. *Journal of Petrology*, **53**, 2139–2189, <https://doi.org/10.1093/petrology/egs050>.

- Ramos, V.A. 2008. Patagonia: A paleozoic continent adrift? *Journal of South American Earth Sciences*, **26**, 235–251, <https://doi.org/10.1016/j.jsames.2008.06.002>.
- Ramos, V.A. and Kay, S.M. 1992. Southern Patagonian plateau basalts and deformation: Backarc testimony of ridge collisions. *Tectonophysics*, **205**, 261–282, [https://doi.org/10.1016/0040-1951\(92\)90430-E](https://doi.org/10.1016/0040-1951(92)90430-E).
- Renne, P.R., Swisher, C.C., Deino, A.L., Karner, D.B., Owens, T.L. and DePaolo, D.J. 1998. Intercalibration of standards, absolute ages and uncertainties in $^{40}\text{Ar}/^{39}\text{Ar}$ dating. *Chemical Geology*, **145**, 117–152, [https://doi.org/10.1016/S0009-2541\(97\)00159-9](https://doi.org/10.1016/S0009-2541(97)00159-9).
- Robertson Maurice, S.D., Wiens, D.A., Koper, K.D. and Vera, E. 2003. Crustal and upper mantle structure of southernmost South America inferred from regional waveform inversion: South America waveform inversion. *Journal of Geophysical Research: Solid Earth*, **108**, <https://doi.org/10.1029/2002JB001828>.
- Rollinson, H. R. 2014. Using geochemical data: Evaluation, presentation, interpretation. Routledge.
- Rooney, T.O. 2017. The Cenozoic magmatism of East-Africa: Part I — Flood basalts and pulsed magmatism. *Lithos*, **286–287**, 264–301, <https://doi.org/10.1016/j.lithos.2017.05.014>.
- Rooney, T.O., Hart, W.K., Hall, C.M., Ayalew, D., Ghiorso, M.S., Hidalgo, P. and Yirgu, G. 2012. Peralkaline magma evolution and the tephra record in the Ethiopian Rift. *Contributions to Mineralogy and Petrology*, **164**, 407–426.
- Rooney, T.O., Morell, K.D., Hidalgo, P. and Fraceschi, P. 2015. Magmatic consequences of the transition from orthogonal to oblique subduction in P anama. *Geochemistry, Geophysics, Geosystems*, **16**, 4178–4208.
- Rudnick, R.L., Gao, S., Holland, H.D. and Turekian, K.K. 2003. Composition of the continental crust. *The crust*, **3**, 1–64.
- Smithsonian Institution and Venzke, E. 2013a. Volcanoes of the World, v. 4.3.4 (Holocene).
- Smithsonian Institution and Venzke, E. 2013b. Volcanoes of the World, v. 4.3.4 (Pleistocene).
- Søager, N., Holm, P.M. and Llambías, E.J. 2013. Payenia volcanic province, southern Mendoza, Argentina: OIB mantle upwelling in a backarc environment. *Chemical Geology*, **349–350**, 36–53, <https://doi.org/10.1016/j.chemgeo.2013.04.007>.
- Søager, N., Portnyagin, M., Hoernle, K., Holm, P.M., Hauff, F. and Garbe-Schönberg, D. 2015. Olivine Major and Trace Element Compositions in Southern Payenia Basalts, Argentina: Evidence for Pyroxenite–Peridotite Melt Mixing in a Back-arc Setting. *Journal of Petrology*, **56**, 1495–1518, <https://doi.org/10.1093/petrology/egv043>.

- Søager, N., Holm, P.M., Massafarro, G.I., Haller, M. and Traun, M.K. 2021. The Patagonian intraplate basalts: A reflection of the South Atlantic convection cell. *Gondwana Research*, **91**, 40–57, <https://doi.org/10.1016/j.gr.2020.12.008>.
- Staudacher, T., Jessberger, E., Dorflinger, D. and Kiko, J. 1978. Journal of Physics E: Scientific Instruments A refined ultrahigh-vacuum furnace for rare gas analysis. *Journal of Physics E: Scientific Instruments*, **11**.
- Steiner, R.A. and Rooney, T.O. 2021. PiAutoStage: An Open-Source 3D Printed Tool for the Automatic Collection of High-Resolution Microscope Imagery. *Geochemistry, Geophysics, Geosystems*, **22**, e2021GC009693, <https://doi.org/10.1029/2021GC009693>.
- Stern, C.R. and Kilian, R. 1996. Role of the subducted slab, mantle wedge and continental crust in the generation of adakites from the Andean Austral Volcanic Zone. *Contributions to Mineralogy and Petrology*, **123**, 263–281, <https://doi.org/10.1007/s004100050155>.
- Sun, S. -s. and McDonough, W.F. 1989. Chemical and isotopic systematics of oceanic basalts: implications for mantle composition and processes. *Geological Society, London, Special Publications*, **42**, 313–345, <https://doi.org/10.1144/GSL.SP.1989.042.01.19>.
- Thorkelson, D.J. 1996. Subduction of diverging plates and the principles of slab window formation. *Tectonophysics*, **255**, 47–63, [https://doi.org/10.1016/0040-1951\(95\)00106-9](https://doi.org/10.1016/0040-1951(95)00106-9).
- Trela, J., Vidito, C., et al. 2015. Recycled crust in the Galápagos Plume source at 70 Ma: Implications for plume evolution. *Earth and Planetary Science Letters*, **425**, 268–277, <https://doi.org/10.1016/j.epsl.2015.05.036>.
- Walker, B.A., Bergantz, G.W., Otamendi, J.E., Ducea, M.N. and Cristofolini, E.A. 2015. A MASH Zone Revealed: the Mafic Complex of the Sierra Valle Fértil. *Journal of Petrology*, **56**, 1863–1896, <https://doi.org/10.1093/petrology/egv057>.
- Wendt, I. and Carl, C. 1991. The statistical distribution of the mean squared weighted deviation. *Chemical Geology: Isotope Geoscience section*, **86**, 275–285, [https://doi.org/10.1016/0168-9622\(91\)90010-T](https://doi.org/10.1016/0168-9622(91)90010-T).
- Wolff, J.A., Ramos, F.C., Hart, G.L., Patterson, J.D. and Brandon, A.D. 2008. Columbia River flood basalts from a centralized crustal magmatic system. *Nature Geoscience*, **1**, 177–180, <https://doi.org/10.1038/ngeo124>.
- Yang, Z., Li, J., Jiang, Q., Xu, F., Guo, S., Li, Y. and Zhang, J. 2019. Using Major Element Logratios to Recognize Compositional Patterns of Basalt: Implications for Source Lithological and Compositional Heterogeneities. *Journal of Geophysical Research: Solid Earth*, **124**, 3458–3490, <https://doi.org/10.1029/2018JB016145>.
- Zaffarana, C., Tommasi, A., Vauchez, A. and Grégoire, M. 2014. Microstructures and seismic properties of south Patagonian mantle xenoliths (Gobernador Gregores and Pali Aike). *Tectonophysics*, **621**, 175–197, <https://doi.org/10.1016/j.tecto.2014.02.017>.

4. FRACTIONAL CRYSTALLIZATION AND CRUSTAL CONTAMINATION: EVOLUTION OF LATE-STAGE MAGMAS FROM THE PORCUPINE MOUNTAINS IN THE 1.1 GA MID-CONTINENT RIFT

4.1 Introduction

Large igneous provinces (LIPs) occur on oceanic crust as plateaus and seamount chains, or on continents as continental flood basalts (CFBs), and they represent the eruption of massive volumes of basaltic magma ($0.21 \times 10^6 - 4 \times 10^6 \text{ km}^3$; Stein et al., 2015 and references therein). These LIPs are associated with upwellings of thermally and chemically anomalous material that decompresses and partially melts as it rises from deeper parts of the Earth's solid mantle, known as mantle plumes (Ernst, 2014; Schmerr et al., 2010). Importantly, LIPs are associated with the breakup of continental landmasses; intensive basaltic magmatism is temporally associated with the opening of many oceanic basins (S. Stein et al., 2018; White & McKenzie, 1989). Examples of this phenomenon can be found in flood basalt packages such as: (1) the Parana-Etendeka sequence that marks the breakup of eastern Gondwana and the opening of the southern Atlantic ocean, (2) the Deccan Volcanic Province that formed when India separated from Africa, (3) the North Atlantic Igneous Province where Greenland and northern Europe rifted apart to form the north Atlantic Ocean, and (4) the Ethiopian Flood Basalt Province, which preceded continental rifting in East Africa as well as the formation of the Red Sea and Gulf of Aden, and is viewed as a potentially incipient ocean basin (White & McKenzie, 1989). The breakup and the magmatism are often protracted and can last for millions of years. The latest stages are often buried offshore at the newly formed continent-ocean margin.

The latest stages of continental breakup that are buried offshore are represented by packages of lavas and sediments called seaward dipping reflectors (McDermott et al., 2018). These seaward dipping reflectors are considered diagnostic of magma-rich volcanic margins (i.e., those that form in association with plumes) and necessarily require elevated mantle potential temperatures to produce the magma volumes observed (Paton et al., 2017). Constraining the evolution of these margins, especially the final stages when seaward dipping reflectors are produced, is therefore fundamental to understanding the role of mantle plumes in continental breakup (Brown & Leshner, 2014; McDermott et al., 2018). One way to understand the relationship between plumes and breakup is to study the lavas themselves, but because of burial, surficial weathering, erosion, and eventual dissection by plate boundaries, most LIPs that occurred before the Mesozoic eon (~250 Ma ago) are no longer preserved except for the plumbing systems (Ernst, 2014).

One notable exception to this is the ~1.1 Ga Keweenaw LIP. The Keweenaw LIP is a CFB that has exposed lava flows (surficial) and intrusive residues (deep plumbing) at the Earth's surface in the Lake Superior region of North America (Cannon, 1992; Stein et al., 2015; Swanson-Hysell et al., 2019). The Keweenaw LIP lava flows were erupted into an extended basin called the Mid-Continent Rift, but the rift failed to progress to seafloor spreading due to compression associated with the contemporaneous Grenville orogeny (Cannon, 1992; C. A. Stein et al., 2015; S. Stein et al., 2018). These compressive forces inverted the rift and left a tilted section of the volcanic and sedimentary package exposed and available for observation (Cannon, 1992; S. Stein et al., 2018; Swanson-Hysell et al., 2019). Included in this package of rocks are late stage lava flows interbedded with sediments that are analogous to seaward dipping reflectors (S. Stein et al.,

2018); these lava flows therefore allow for investigation of how mantle plumes and the continental crust interact in the final stages of LIP magmatism before continental breakup.

Here we present an analysis of the geochemical, petrographic, and stratigraphic evidence from magmatic rocks of the Porcupine Mountains in northern Michigan. These materials represent the main stage of volcanism, the shutdown of the main stage, and an apparent pulse of new late-stage material. This later pulse, which is interbedded with sediments and therefore analogous to seaward dipping reflectors, is geochemically distinct from the preceding main stage volcanic rocks. Incompatible trace elements are enriched in the basalts from this later pulse, and isotopic evidence suggests extensive crustal contamination of these magmas. Furthermore, there are similarities among the main stage volcanic products, the evolved products related to the shutdown of main stage volcanism, and the final pulse of magmatism. These characteristics suggest a complex interplay of igneous processes (fractional crystallization, assimilation of continental crust, and mixing) that led to the genesis and subsequent evolution of the final pulse of magmatism. We integrate the characteristics of the magmas into the already-established framework for the evolution of the MCR and the Keweenaw LIP. These results also provide insight into the role that LIP magmas play in the latest stages of volcanism prior to continental breakup. They suggest that a waning flux of magma results in the generation of evolved, crustally-contaminated lavas. Later pulses of plume melt material may rejuvenate, exploit, and hybridize with the contents of preexisting magma plumbing systems to produce the lava flows intercalated with sediments known as seaward dipping reflectors during continental breakup.

4.2 Geologic Background

4.2.1 Defining the Mid-Continent Rift

The MCR is a failed rift located in the center of North America. The rift formed during the Proterozoic, at around 1.1 billion years ago (Cannon, 1992; S. Stein et al., 2018). It is an arcuate structure with its western limb buried beneath Iowa and Minnesota, its eastern limb buried beneath the lower peninsula of Michigan, and exposures along the shorelines and islands of Lake Superior (Figure 4.1). The full extent of the rift is primarily known through geophysical imaging (C. A. Stein et al., 2015; S. Stein et al., 2018). Specifically, it is visible on gravity and magnetic maps of North America (Stein et al., 2015, 2018 and references therein; Figure 4.1). The gravity map (Figure 4.1 A) indicates that the material is dense given the positive anomaly, and the magnetics map (Figure 4.1 B) indicates that the material is highly magnetized; these geophysical signatures of dense, magnetic material are due to the large volume of mainly basaltic lava that filled in the preexisting rift structure (C. A. Stein et al., 2015; Thomas & Teskey, 1994). For this reason, the MCR is fundamentally inseparable from the Keweenawan LIP.

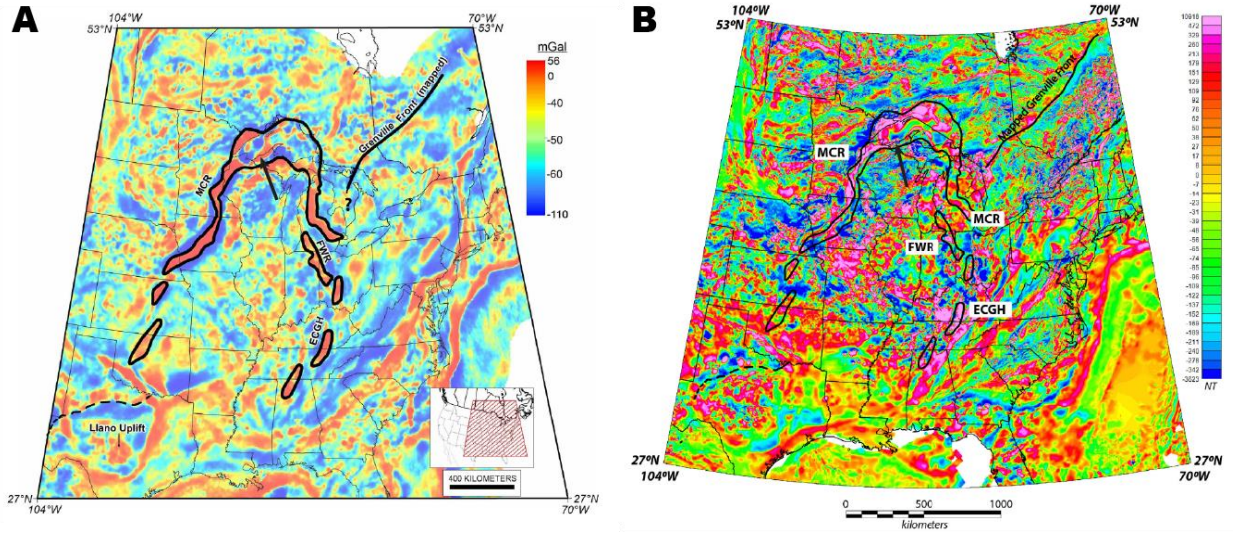


Figure 4.1

Gravity (A) and magnetic (B) anomaly maps of the Midwest region of the United States of America defining the extent of the Mid-Continent Rift (MCR). The Fort Wayne Rift (FWR) structure and East Continent Gravity High (ECGH) structure are considered by S. Stein et al. (2018) to be extensions of the mid-continent rift. Black arrow in each figure points to this study's geographic area in northern Michigan. Figures modified from S. Stein et al. (2018).

The Keweenawan LIP is a CFB that erupted contemporaneously with the development of the MCR (Cannon, 1992; D. W. Davis & Green, 1997; C. A. Stein et al., 2015). Other CFB provinces around the globe from the Cenozoic all have similar average thicknesses of around 1 km or less when the erupted volcanic rock volume of the province is divided by the areal extent; in contrast, the MCR/Keweenawan LIP has an average thickness of 5 km when calculated this way (Stein et al., 2015 and references therein). The rift itself was already developing within the core of Laurentia prior to the onset of magmatism; this allowed the erupting lavas to fill in the relatively narrow rift basin (Stein et al., 2015). This was a protracted process that unfolded over the course

of 25 million years (1110 Ma-1085 Ma; Stein et al., 2015; Swanson-Hysell et al., 2014; Swanson-Hysell et al., 2019).

4.2.2 Structural and Magmatic Evolution of the Mid-Continent Rift

4.2.2.1 Mid-Continent Rift Development Prior to Initiation of Magmatism

The development of both the MCR and the Keweenaw LIP in the interior of Laurentia is set within the larger backdrop of large-scale global tectonism. Between 1200-1000 Ma, the supercontinent of Rodinia is thought to have formed via assembly of continental landmasses on Earth (Li et al., 2008; Stein et al., 2018; Swanson-Hysell et al., 2019). The Grenvillian orogeny is the term given to the assembly of other continental terranes (e.g., the Amazonia, Kalahari cratons) along the margin of Laurentia during this time. The assembly of the supercontinent Rodinia and the contemporaneous Grenvillian orogeny are thought to have played an overarching role in the initiation of the MCR, as well as the eventual cessation of magmatism and inversion (i.e., closure) of the rift (Stein et al., 2015; Swanson-Hysell et al., 2019).

Part of the formation of the MCR basin preceded the magmatism of the Keweenaw LIP (e.g., Stein et al., 2015; Swanson-Hysell et al., 2019). The initiation of rifting is very poorly constrained; the onset of magmatism began at around 1108 Ma (Davis & Green, 1997; Swanson-Hysell et al., 2014). Some magmatism is thought to predate the 1108 Ma onset, such as intrusive rocks from 1115-1100 Ma in the Thunder Bay area (Keays and Lightfoot, 2015) and 1144 Ma lamprophyre dikes near the Coldwell Complex in Marathon, Ontario (Piispa et al., 2018). Meanwhile extension is thought to have begun around 1120 Ma (C. A. Stein et al., 2015). Paleogeographic reconstructions of Laurentia place the MCR in the interior of the continent (Li et al., 2008; C. A. Stein et al., 2015). It is thought that part of the development of the MCR is attributable to rotation of a microplate within Laurentia called the Illinois microplate (Merino et

al., 2013; C. A. Stein et al., 2015). Paleomagnetic reconstructions of the continents also show Laurentia moving rapidly ($>25\text{cm/yr}$) from a position near the poles at 1140 Ma to near the equator at 1080 Ma (Davis & Green, 1997; Swanson-Hysell et al., 2019). This rapid equator-ward motion and the recognized rotation of the Illinois microplate together likely created the conditions favorable for the formation of MCR rift structures and subsequent eruption of the Keweenaw LIP contained within its boundaries (Merino et al., 2013; Swanson-Hysell et al., 2019).

4.2.2.2 *Extent and Timing of Magmatism of the Keweenaw Large Igneous Province*

The Keweenaw LIP is anomalous among LIPs (C. A. Stein et al., 2015). While most LIPs occur prior to rifting and continental breakup (e.g., Parana-Etendeka, Ethiopia, Karoo/Ferrar; Ernst, 2014), the Keweenaw LIP erupted into an already-developed rift structure known as the Mid-Continent Rift (MCR) that had formed in the interior of Laurentia (Cannon, 1992; Stein et al., 2015). Paleomagnetic data indicate that over the course of the Keweenaw LIP's activity, Laurentia was undergoing extremely rapid motion ($>25\text{ cm/yr}$) from high latitudes to the equator (Swanson-Hysell et al., 2019). Furthermore, the extensional MCR structure and contemporaneous Keweenaw LIP occur during a time of intensive compressional tectonism of the Grenville orogeny associated with the assembly of the supercontinent Rodinia (Li et al., 2008; S. Stein et al., 2018; Swanson-Hysell et al., 2019). Finally, while most LIPs erupt in a very short time scale (1-5 Ma; Ernst, 2014), the duration of the Keweenaw LIP is protracted. It spans $\sim 25\text{ Ma}$ in a series of apparent pulses that are separated by periods of quiescence (Nicholson et al., 1997a; Swanson-Hysell et al., 2014, 2019).

There are multiple localities around the Lake Superior region where MCR/Keweenaw volcanic rocks are found. We will discuss many of these localities in the course of this work. Figure 4.2 shows the locations of these volcanic rocks and their associated names, along with the

paleomagnetic polarity of these lavas. Mamainse Point is often thought of as the most complete stratigraphic section of Keweenaw volcanics.

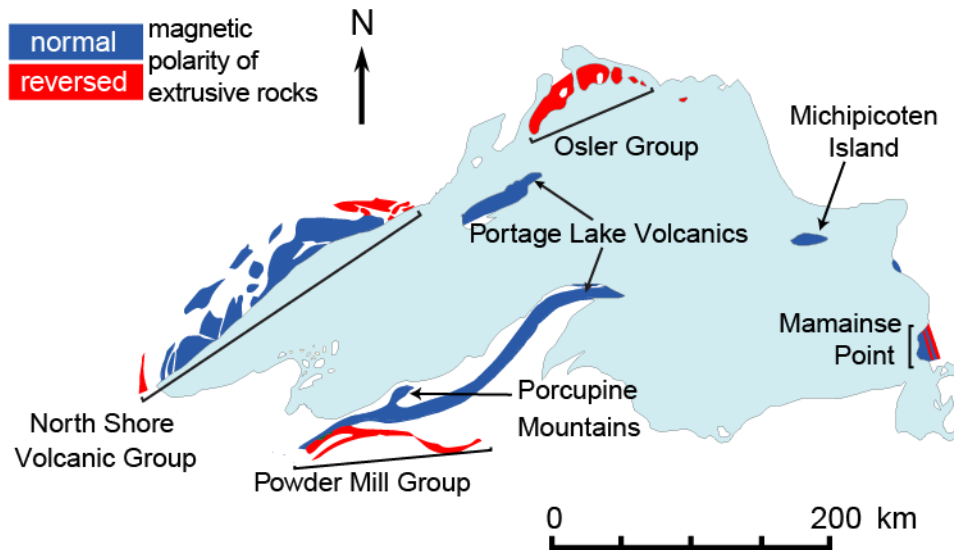


Figure 4.2

Map of the Lake Superior region showing the various locations where MCR/Keweenaw magmatic rocks are exposed. Red areas represent reversed magnetic polarity, while blue areas represent normal polarity. Figure modified from Swanson-Hysell et al. (2014).

The magmatic activity associated with the Keweenaw LIP occurs in discrete pulses of volcanic activity, and researchers have divided these pulses into four stages (D. W. Davis & Green, 1997; Nicholson et al., 1997; Vervoort et al., 2007). The stages are the early stage (~1109-1104 Ma); the latent stage (1104-1098 Ma); the main stage (1198-1190 Ma); and the late stage (1190-1183 Ma).

These pulses are divided by period and by the paleomagnetic polarity measured within these rocks. The most complete record of magmatism associated with the Keweenaw LIP can be found at Mamainse Point, Ontario (Shirey et al., 1994). There, magmatic rocks that dip into Lake Superior provide a continuous stratigraphic section from the Early Stage through the Latent

Stage and into the end of the Main Stage of volcanism. Late-stage magmatism is not present at Mamainse Point.

Early-stage rocks feature exclusively reversed magnetic polarity. They are found in the Powder Mill group of Michigan and Wisconsin; at the base of the North Shore Volcanic group and the associated Duluth Complex intrusions; in the Osler Group near Thunder Bay, Ontario; and at the base of the Mamainse Point sequence.

The Latent Stage is only recognized from materials at Mamainse Point, and both normal & reversed magnetic polarity rocks are observed here. Latent Stage basalts show heavy crustal contamination isotopically (e.g., negative ϵ_{Nd} ; Shirey et al., 1994) and can be modeled by magma mixing between basalt and rhyolites found in the area (Klewin & Berg, 1991).

The Main Stage volcanics are found in all localities, but the Osler Group main stage rocks are very limited in extent. The magnetic polarities of the Main Stage and the Late-Stage rocks are both normal. The Main Stage is the period of the most voluminous magmatism.

Late-Stage volcanic rocks are uncommon and are recognized in only a few places: The Lake Shore Traps of the northeastern Keweenaw Peninsula interbedded within the Copper Harbor Conglomerate that lies over the Portage Lake Volcanics; at Michipicoten Island; and a series of undated flows in the Porcupine Mountains that are interbedded within the Copper Harbor Conglomerate. The Copper Harbor Conglomerate is a volcanogenic, stromatolite-bearing alluvial fan conglomerate conformably overlying Portage Lake Volcanics that is interpreted as rift-fill deposited after main-phase magmatism ended (Elmore, 1984). This work focuses on the magmatic stratigraphy of the Porcupine Mountains, which ranges in age from the end of Main Stage volcanism and is assumed to extend into the Late Stage with the flows interbedded with the Copper Harbor Conglomerate.

4.2.3 The Porcupine Mountains Volcanic Complex

The Porcupine Mountains and the associated volcanic complex is in the northwestern Upper Peninsula of Michigan on the shores of Lake Superior (Figure 4.3). The volcanic complex includes basaltic flows of the Portage Lake Volcanics, but also features a series of intermediate and felsic material that overlies the basaltic lavas. The Portage Lake Volcanics are products of the Main Phase of volcanism in this area. The Copper Harbor Conglomerate thins considerably around the Porcupine Mountains volcanic complex, and early interpretations of these volcanics drew comparisons to Icelandic central volcanoes (Nicholson et al., 1991). Within the volcanic complex, there are upper and lower rhyolite units surrounding a unit that was named the Porcupine Andesite (Cannon et al., 1995). These units thin with distance from the Porcupine Mountains. Spatial associations of these units are shown in Figure 4.3.

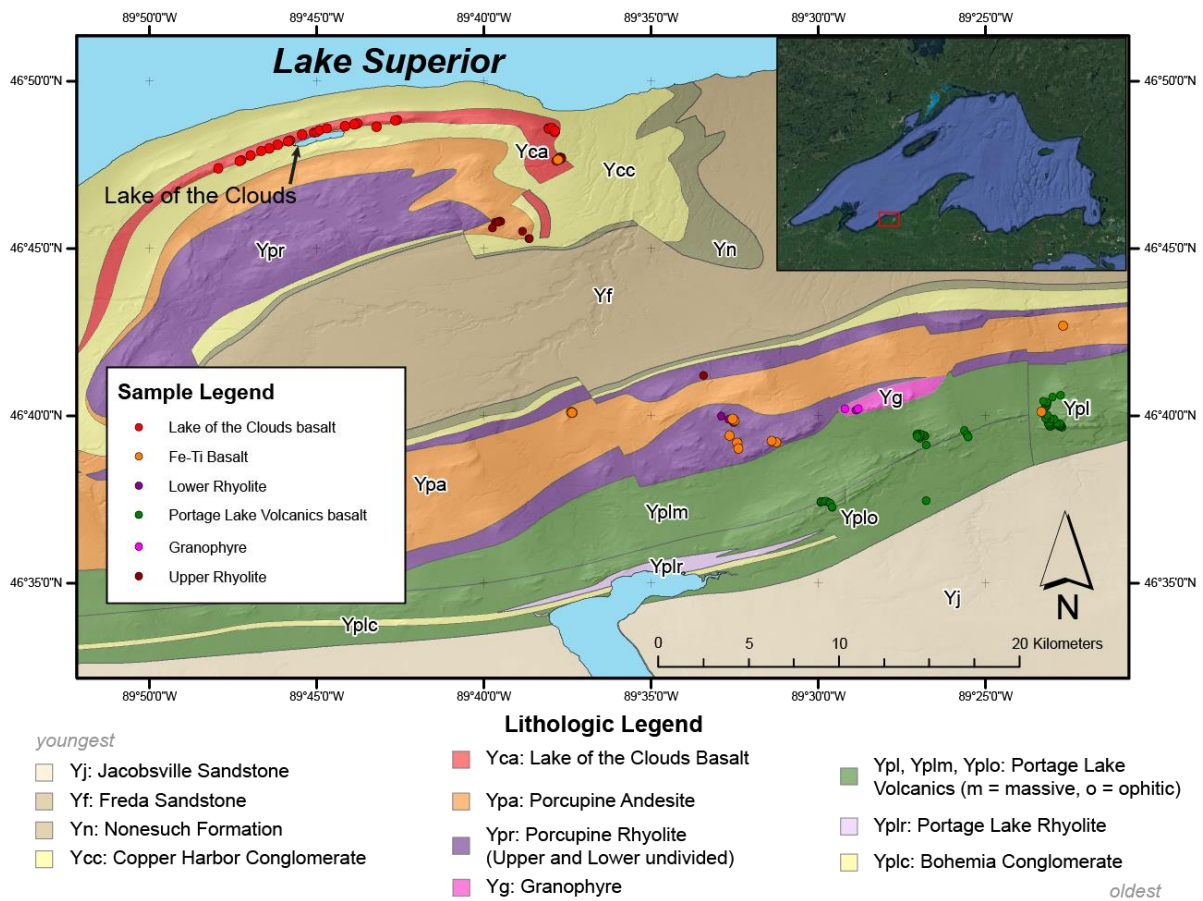


Figure 4.3

Geologic map of the Porcupine Mountains volcanic complex. Colored regions indicate the mapped extent of each unit from Cannon et al. (1995), while the points represent the sampling sites of rocks described in this study. This map figure was initially created by Jacob Bonessi and modified by Chris Svoboda for use in this document. Lake of the Clouds basalt, Fe-Ti Basalt, and Upper & Lower Rhyolite are designations from this study. Inset map in upper right-hand corner shows Google Earth aerial imagery of the Lake Superior region, and the red square indicates the extent of the map area shown.

There are flows of basaltic material interbedded within the Copper Harbor Conglomerate in this area (Cannon et al., 1995), stratigraphically above the Porcupine Volcanics. Cannon et al. (1995) refers to these as the Copper Harbor Andesite. In this work, we refer to these flows as the Lake of the Clouds basalt because of the association of this geographical feature with the base of the flows (Figure 4.3). Relative thicknesses of the volcanic and sedimentary rocks in the area are estimated from the map of Cannon et al. (1995) (Figure 4.4). The Lake of the Clouds basalts are the youngest volcanic material recognized in this area, and they are thought to be from a pulse of magmatism during the Late Stage. Nicholson et al. (1997) suggest that these basalts interbedded within the Copper Harbor Conglomerate may be similar in age to the Lake Shore Traps that are found at the eastern tip of the Keweenaw peninsula at High Rock Bay.

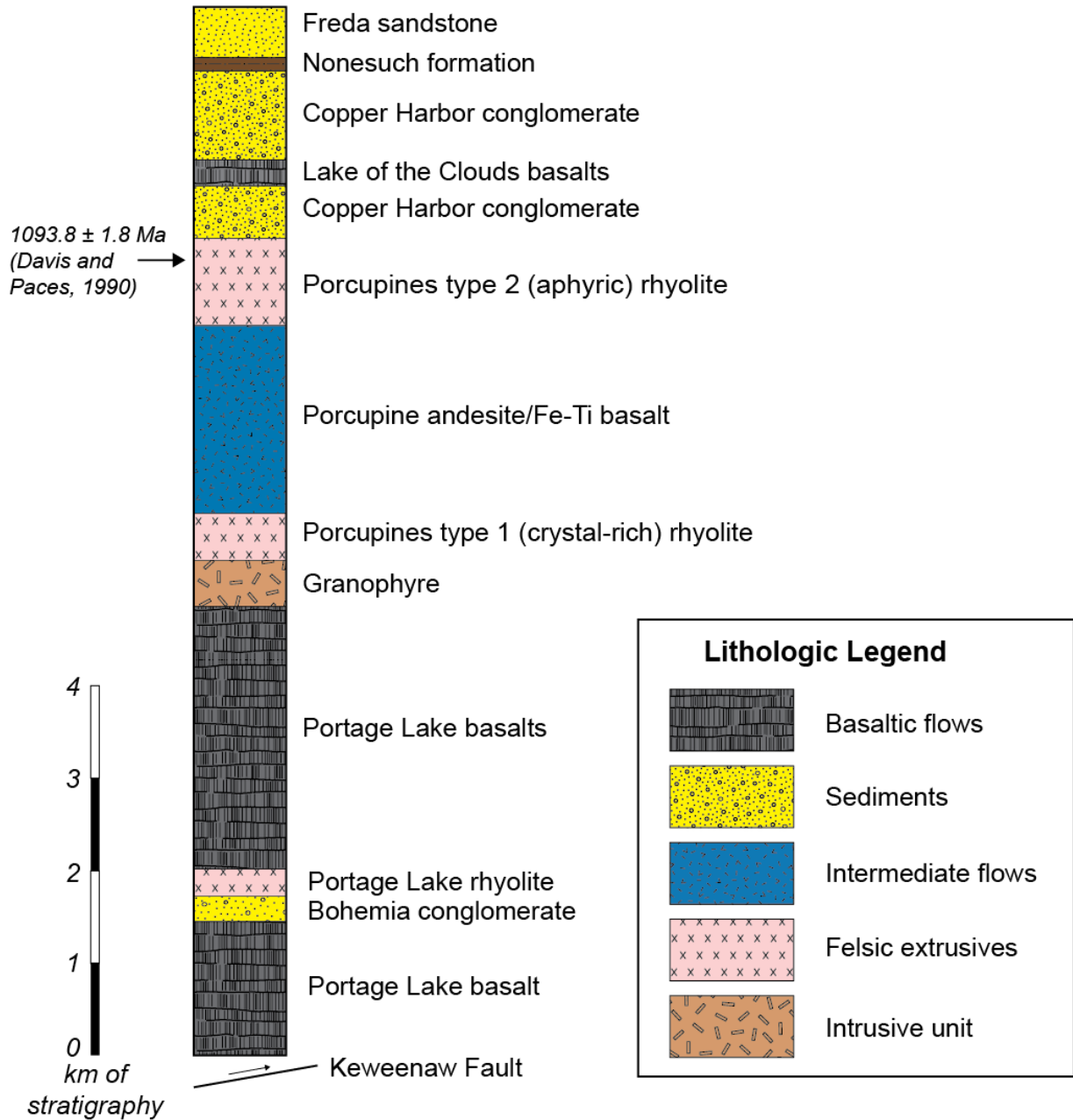


Figure 4.4

Stratigraphic column showing the various igneous and sedimentary rock units in the Porcupine Mountains. Developed from the map of Cannon et al. (1995).

4.2.4 Temporal Constraints on Portage Lake and Porcupine Mountains Volcanism

There are few constraints on the age of the Porcupine Volcanics and associated units. Simple prismatic zircon crystals from an ash flow within the upper Porcupine Volcanics rhyolite yield a concordant $^{207}\text{Pb}/^{206}\text{Pb}$ age of 1093.6 ± 1.8 Ma (Zartman et al., 1997). These authors do note that these concordant dates are derived from two crystals, and other zircons isolated from the same unit show variable $^{207}\text{Pb}/^{206}\text{Pb}$ ages, ranging from 1080-1137 Ma. The uncertainties on these analyses are larger than those of the concordant zircons. The range of dates from this one flow may suggest this rhyolite eruption may have intermixed many inherited zircon crystals.

The Portage Lake Volcanics lie beneath the Porcupine Volcanics, and these rocks have recently been precisely dated by Swanson-Hysell et al. (2019). While it has not been proven that the Portage Lake Volcanics are completely laterally continuous along the length of the Keweenaw peninsula, it is assumed (e.g., Cannon & Nicholson, 2001). The dates on the Portage Lake Volcanics are $^{206}\text{Pb}/^{238}\text{U}$ dates from chemically abraded zircon crystals measured under a thermal ionization mass spectrometer. They come from two large, evolved flows at the eastern end of the Keweenaw peninsula: The Copper City flow (lower in the volcanic stratigraphy); and the Greenstone flow (higher in the volcanic stratigraphy). The Copper City flow yields an age of 1093.37 ± 0.53 Ma, and the Greenstone flow yields an age of 1091.59 ± 0.27 Ma. The Copper City flow age is within error of the ages for the Porcupine Volcanics found in Zartman et al. (1997). This may suggest the silicic Porcupine Volcanics were erupted directly on top of the Portage Lake Volcanics while basaltic magmatism was still ongoing in what is now the eastern Keweenaw peninsula.

There are no isotopic ages available for the Lake of the Clouds basalts. They have been considered possibly contemporaneous with the Lake Shore Traps basalts found at the eastern tip

of the Keweenaw peninsula because they are interbedded within the Copper Harbor Conglomerate (Nicholson et al., 1997). There are two dates available for the Lake Shore Traps. Davis & Paces (1990) find $^{207}\text{Pb}/^{235}\text{U}$ vs. $^{206}\text{Pb}/^{238}\text{U}$ concordia intercept ages of 1087.2 ± 1.6 Ma. Meanwhile, the chemically abraded thermal ionization mass spectrometry methods of Swanson-Hysell et al. (2019) find ages of 1085.57 ± 0.25 Ma. These ages are within uncertainty of one another and indicate that the Lake Shore Traps are from a younger pulse of magmatism that occurred ~ 5 Ma after cessation of the PLV. If the assumption of Nicholson et al. (1997) is correct, then the Lake of the Clouds basalts would be roughly the same age and another part of this pulse of late-stage magmatism. This later pulse also includes the Michipicoten Island formation in eastern Lake Superior (Figure 4.2), which is correlated with the Mamainse Point formation (Annells, 1974; Fairchild et al., 2017) and has constrained eruption ages of 1084.35 ± 0.20 Ma and 1083.52 ± 0.23 Ma.

4.3 Materials and Methods

4.3.1 Samples

This study includes samples from the Porcupine Volcanics (Porcupine Andesite, $n = 13$; Porcupine Rhyolite, $n = 16$), the Lake of the Clouds basalts ($n = 38$), and a granophyre body associated with the Portage Lake & Porcupine Volcanics ($n = 5$). The sampling locations are shown in Figure 4.2. Collection method was by hand via a sledgehammer from the massive core of flows, away from vesicular flow tops/bottoms. In the field, the Porcupine Andesite outcrops very poorly. Here, we refer to samples of the Porcupine Andesite as Fe-Ti basalts based on their major and trace element characteristics. These samples are collected from within the area of noted outcrops in Cannon et al. (1995), dikes in rhyolite, and flows intercalated within the Lake of the Clouds

basalts and Portage Lake volcanics. We have divided the Porcupine Volcanics rhyolites into upper (aphyric) and lower (phyric) units.

4.3.2 Whole rock major & trace elements

Samples were prepared for whole rock and trace element analysis in an identical manner to procedures outlined in Section 2.4 of this document. In brief, whole rock samples were cut, washed, and polished. They were then chipped, then subsequently powdered in an alumina mill. The fine powder was mixed in a 1:3 ratio with lithium tetraborate flux and 1:1 ratio with ammonium nitrate oxidizer to convert all Fe into Fe³⁺, then oscillated over a Bunsen burner to create a liquid. This liquid was poured into non-reactive platinum molds and allowed to quench, producing sample glasses. These glasses were analyzed for major elements on a Bruker S4 X-ray fluorescence spectrometer. For trace elements they were analyzed on a Thermo Scientific ICAP-Q quadrupole ICP-MS with a Photon-Machines Analyte G2 laser used for ablation of sample material. Three scans were completed with the LA-ICP-MS and trace element results presented are the average of these three runs.

4.3.3 Isotopes

Isotopic analyses were conducted at the University of Hawaii Manoa School of Earth Science and Technology (SOEST) after initial processing at Michigan State University by Andrew LaVigne. The isotopic analyses incorporated in this study include three samples from the Lake of the Clouds basalts (TOR000054, TOR00005F, and TOR00005I), one Fe-Ti basalt (TOR00004R), one rhyolite from the lower rhyolite unit in the stratigraphy of the Porcupine Mountains (TOR000047), and one from the Portage Lake Volcanics (TOR0000KC). These samples were analyzed for Hf, Nd, and Pb isotopes; here we consider only Hf and Nd isotopes. Pb isotopes for samples of this antiquity are difficult to interpret due to the possibility of open-system behavior in

these isotope systems. In brief, the procedure for isotopic measurement was to crush and pick glassy, unaltered basaltic groundmass material. This material was then leached in hydrochloric acid to draw the specific isotopes into solution, and then individual isotopes were separated from one another in resin columns. Finally, separated solutions were analyzed on a Nu Plasma HR multi-collector ICP-MS at the University of Hawaii Manoa SOEST. For more specific procedures, the reader is referred to Andrew's master's thesis (LaVigne, 2019) and references therein.

4.4 Results

4.4.1 Petrography

4.4.1.1 Lake of the Clouds Basalts & Fe-Ti Basalts

Lake of the Clouds basalts and Fe-Ti basalts are similar petrographically and are treated together here. Both exhibit a paucity of phenocrysts. Only six of 39 thin sections contained phenocrysts. Within these six samples the volume percentage of these crystals are 1-2% and all observed phenocrysts are plagioclase, with one exception. This exception is sample TOR00005E (9504A), which contains 5 volume percent altered olivine. Phenocrysts are more common in the Fe-Ti basalts than in that of the Lake of the Clouds basalts; five of seven Fe-Ti basalts examined petrographically contained phenocrysts, while only one of 32 Lake of the Clouds basalt thin sections did.

We use the petrographic nomenclature for flood basalt textures developed by Krans et al. (2018). The most common texture observed in Fe-Ti basalt and Lake of the Clouds thin section is aphyric-intergranular, with aphyric-microcrystalline samples and aphyric-ophitic representing the remaining sections. Groundmass phases are plagioclase, clinopyroxene, and opaque Fe-Ti oxides

in sub-equal but varying abundances. Chlorite, calcite, and opaque oxide are observed as vesicle- or void-filling alteration phases.

4.4.1.2 Granophyres

Granophyre samples are holocrystalline and contain predominantly quartz and potassium feldspar with conspicuous characteristic granophyric intergrowth textures. Granophyre samples were observed with a JEOL6610LV scanning electron microscope (SEM) under low-vacuum operation (60 Pa) at 15 kV. We observed several accessory phases that were assessed with energy dispersive X-ray spectroscopy (EDS). These accessory phases include apatite, sphene, oxides showing two-phase exsolution, and several Fe-silicate phases that were most likely pyroxene, biotite, and/or amphibole.

4.4.1.3 Rhyolites

Petrographically, the rhyolites can be divided, and this division is consistent with stratigraphic location. Lower (type 1) rhyolites are phyrlic (>40 volume % crystals) with abundant, subequal amounts of subhedral brecciated quartz and feldspar (potassium and albite) with minor (1%) oxides and amphibole in a fine-grained matrix. The upper (type 2) rhyolites are aphyric rhyolites, composed of devitrified groundmass with minor quartz fragments.

4.4.2 Major Elements

4.4.2.1 Lake of the Clouds Basalts

Lake of the Clouds basalts range between 4-8 wt. % MgO (Figure 4.5; see Supplemental Document 6). Lake of the Clouds basalts as a group have higher overall TiO₂, P₂O₅, Na₂O, and K₂O than Portage Lake Volcanics basalts but lower CaO, while Al₂O₃, FeO, and MnO are like the Portage Lake Volcanics. TiO₂, Al₂O₃, and P₂O₅ concentrations decrease with decreasing MgO contents, while CaO and FeO increase. Overall, the Lake of the Clouds basalts extend to lower

MgO contents than the Portage Lake Volcanics, which all contain >6 wt. % MgO. Na₂O and K₂O oxides are largely scattered when considered vs. MgO (Figure 4.5). One Lake of the Clouds basalt shows strong enrichment in TiO₂ and P₂O₅ (TOR000053) and another strong enrichment in Al₂O₃ (TOR0000JY), but petrographic thin sections were unavailable for these samples. Both are low MgO (~3.9 wt. %) and are possibly affected by accumulation of minerals. TOR0000JY has trace element characteristics consistent with Lake of the Clouds basalts but is found within the stratigraphy of the Portage Lake Volcanics.

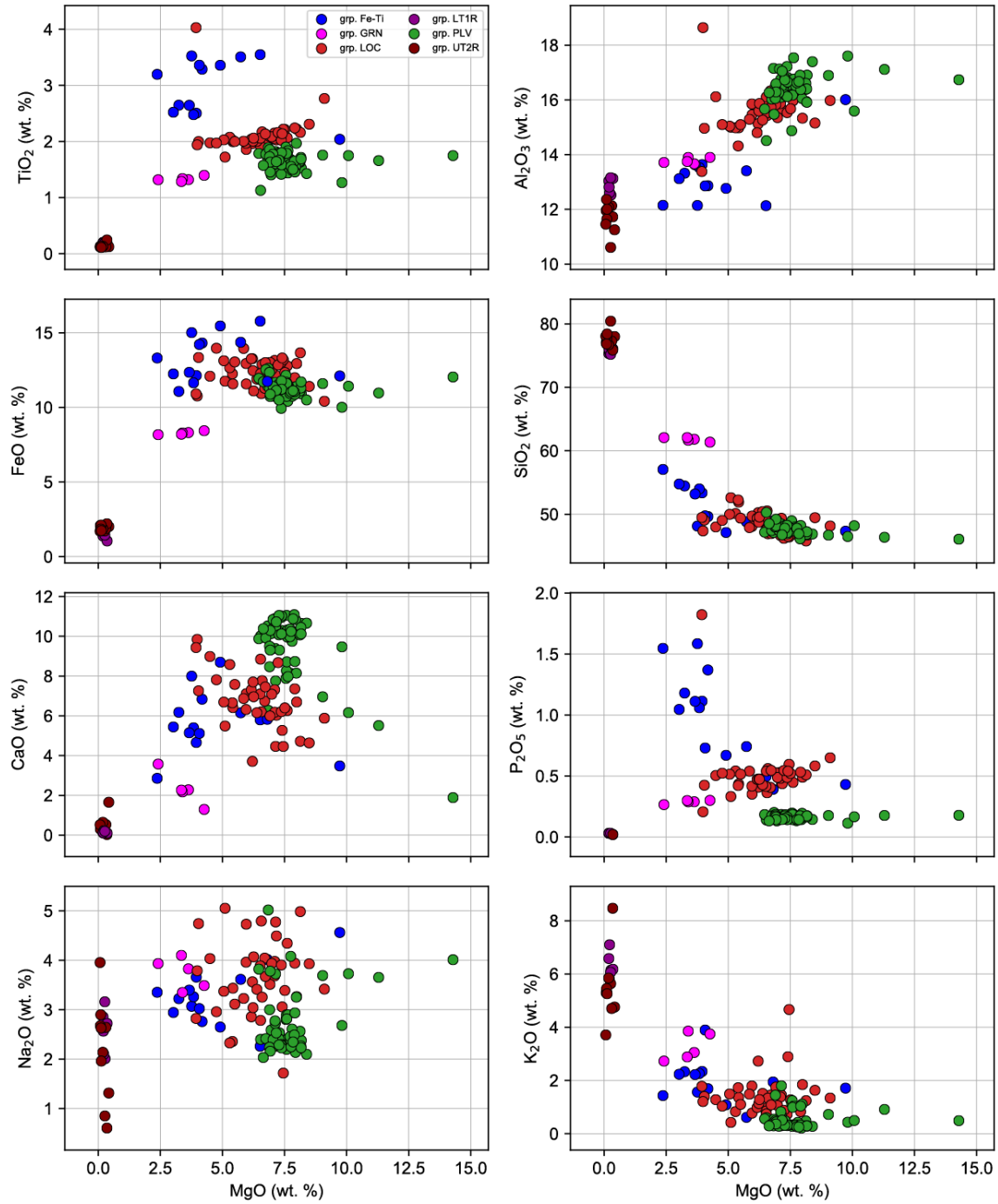


Figure 4.5 (Previous Page)

Bivariate diagrams of major element oxides vs. MgO in weight percent for Porcupine Mountains volcanics samples. Sample group abbreviations in key are as follows: Fe-Ti = Fe-Ti

Figure 4.5 (cont'd)

basalts; LT1R = Lower Type 1 rhyolite; GRN = Granophyre; PLV = Portage Lake Volcanics; LOC = Lake of the Clouds basalts; UT1R = Upper Type 2 rhyolite. These abbreviations will be used consistently among all figures in this paper to identify these groups. FeO shown is Fe²⁺ and represents 85% of FeO^T

4.4.2.2 Granophyres

The five granophyre samples range from 2.4 - 4.2 wt. % MgO (Figure 4.5). Major element oxides TiO₂, and K₂O decrease with decreasing MgO, while MnO, CaO, and Na₂O increase; P₂O₅, Al₂O₃, and FeO do not change with decreasing MgO. The granophyres are depleted in TiO₂, FeO, Al₂O₃, and CaO and have greater overall K₂O when compared to Lake of the Clouds basalts. MnO, P₂O₅, and Na₂O are in about the same concentrations as Lake of the Clouds basalts.

4.4.2.3 Fe-Ti Basalts

Fe-Ti basalts range from 2.4 - 6.8 wt. % MgO, with one high MgO sample (TOR00005E) at 9.7 wt. % MgO (Figure 4.5). Based on petrographic observations of disseminated, altered olivine crystals in this sample, it is likely that TOR00005E's major element chemistry (specifically high MgO) reflects this olivine accumulation. Fe-Ti basalts are moderately to strongly enriched in TiO₂, MnO and P₂O₅ compared to the Portage Lake Volcanics and Lake of the Clouds basalts; FeO is enriched compared to Lake of the Clouds and Portage Lake Volcanics basalts in most Fe-Ti basalts, except at lower MgO contents when FeO overlaps with the Lake of the Clouds basalts.

4.4.2.4 Lower Type 1 Rhyolites

Type 1 rhyolites are crystal-rich tuffs that are almost entirely depleted in MgO, TiO₂, CaO, and P₂O₅. Type 1 rhyolites vary considerably in Al₂O₃, Na₂O, and K₂O, consistent with

crystallization of alkali-rich feldspars. Lower Type 1 rhyolites have a more SiO₂ than Type 2 rhyolites.

4.4.2.5 Upper Type 2 Rhyolites

Type 2 rhyolites, aphyric tuffs, are almost entirely depleted in MgO, TiO₂, CaO, and P₂O₅. Al₂O₃, Na₂O, and K₂O vary considerably in Type 2 rhyolites, consistent with crystallization of alkali-rich feldspars (Na and K). Type 2 rhyolites are poor in Al₂O₃ compared to Type 1 rhyolites.

4.4.3 Trace Elements

4.4.3.1 Lake of the Clouds Basalts

Lake of the Clouds basalts feature chondrite-normalized rare earth element (REE) patterns with slopes that are steeper than the Portage Lake Volcanics, especially in La-Eu (Figure 4.6; see Supplemental Document 6), with concentrations of all trace elements enriched over those in the Portage Lake Volcanics. They are also offset vertically from the Portage Lake Volcanics patterns. All Lake of the Clouds basalt REE patterns feature negative Eu anomalies consistent with crystallization of plagioclase feldspar. Eu/Eu* shows the magnitude of a europium anomaly by dividing the measured Eu content by the expected/interpolated Eu concentration, Eu* (Eu* = $\sqrt{Sm_{CN} + Gd_{CN}}$). Eu/Eu* of Lake of the Clouds basalts ranges from 0.81-0.99. These values do not co-vary with Sr or MgO content (Figure 4.7).

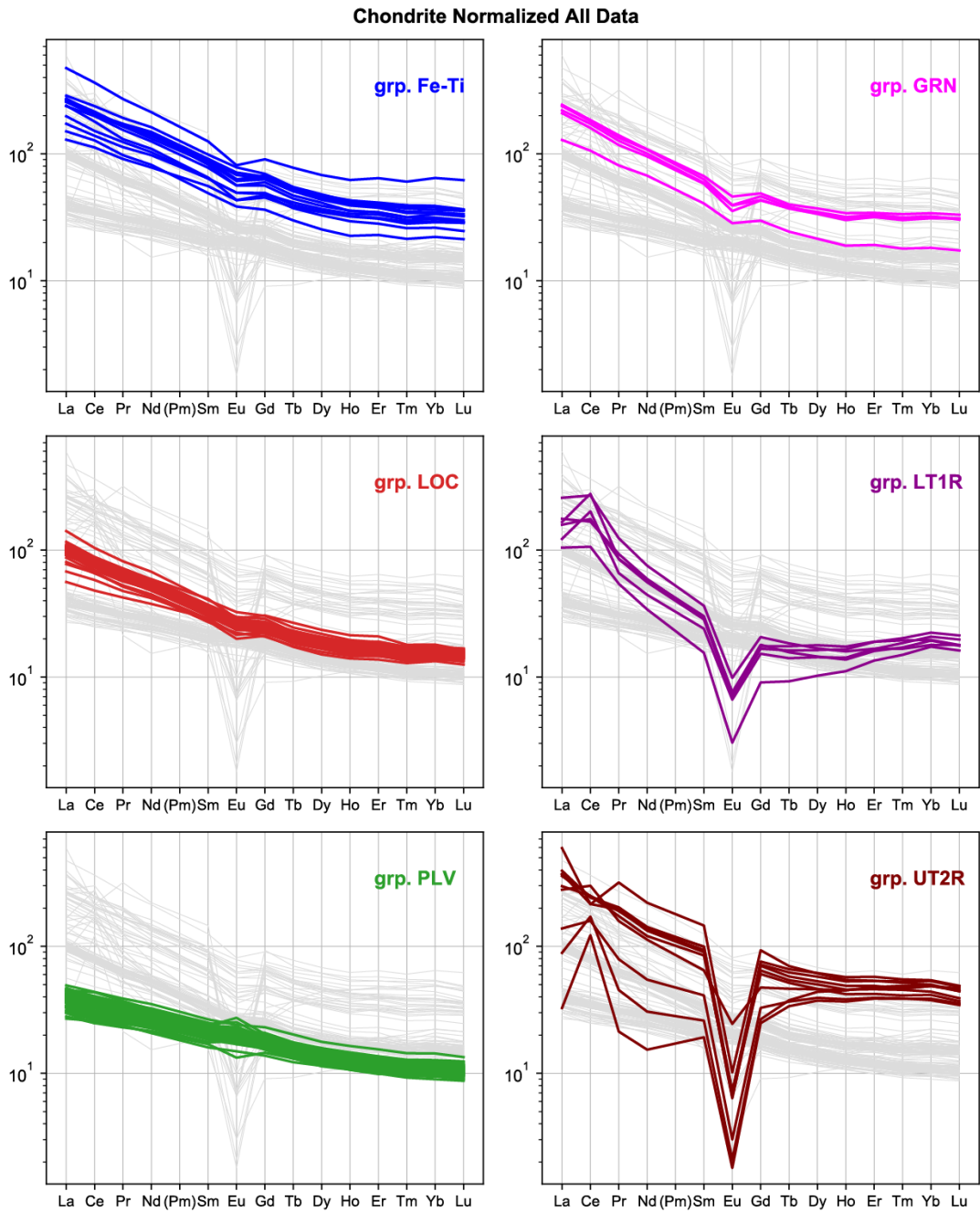


Figure 4.6

Rare earth element (REE) diagrams showing concentrations of REE in Porcupine Mountains magmas normalized to chondrite (Boynton, 1984). The element Pm is not found in nature and its value in this figure represents the geometric mean of the adjacent elements Nd & Sm.

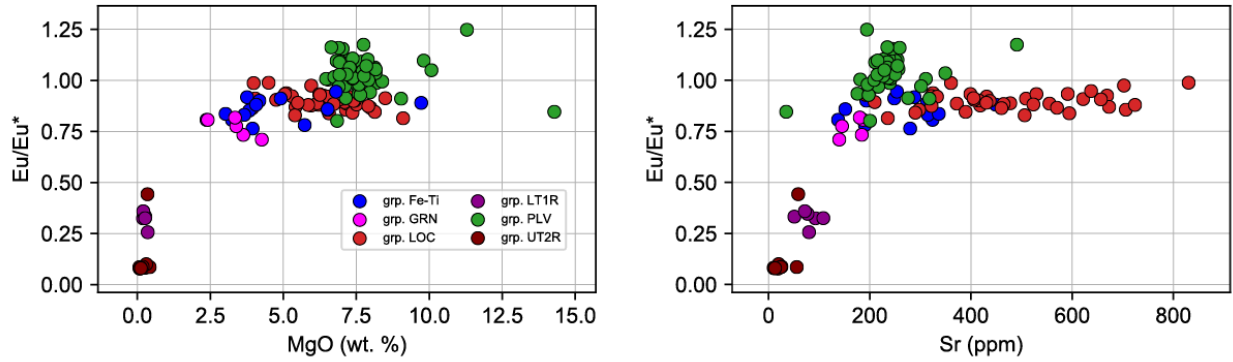


Figure 4.7

Bivariate diagram showing Eu/Eu^ (measured/interpolated Eu) vs. MgO and Sr for Porcupine Mountains magmas.*

Primitive-mantle normalized trace element spider diagrams for Lake of the Clouds basalts (Figure 4.8) show negative Ti anomalies that also appear in the Portage Lake Volcanics and a trough in U-Ta. Lake of the Clouds basalts appear to co-vary on a diagram of chondrite normalized La/Yb ($(La/Yb)_{CN}$) vs. Tb/Yb ($(Tb/Yb)_{CN}$; Figure 4.9). The Lake of the Clouds basalts also have La/Tb like Groups 5a and 5c of the Mamainse Point Volcanic Group in this plot, although Mamainse Point samples have lower $(La/Yb)_{CN}$ and $(Tb/Yb)_{CN}$ than Porcupine Mountains samples. $(La/Yb)_{CN}$ (REE slope) ranges from 3.9-8.2, $(Tb/Yb)_{CN}$ (heavy rare earth element (HREE) slope) ranges from 1.2-1.5, and $(La/Sm)_{CN}$ (light rare earth element (LREE) slope) ranges from 1.9-3.5 for Lake of the Clouds basalts. $(La/Yb)_{CN}$ and $(Tb/Yb)_{CN}$ do not vary with decreasing MgO (Figure 4.10).

Primitive Mantle Normalized (Sun & McDonough, 1989) - ALL DATA

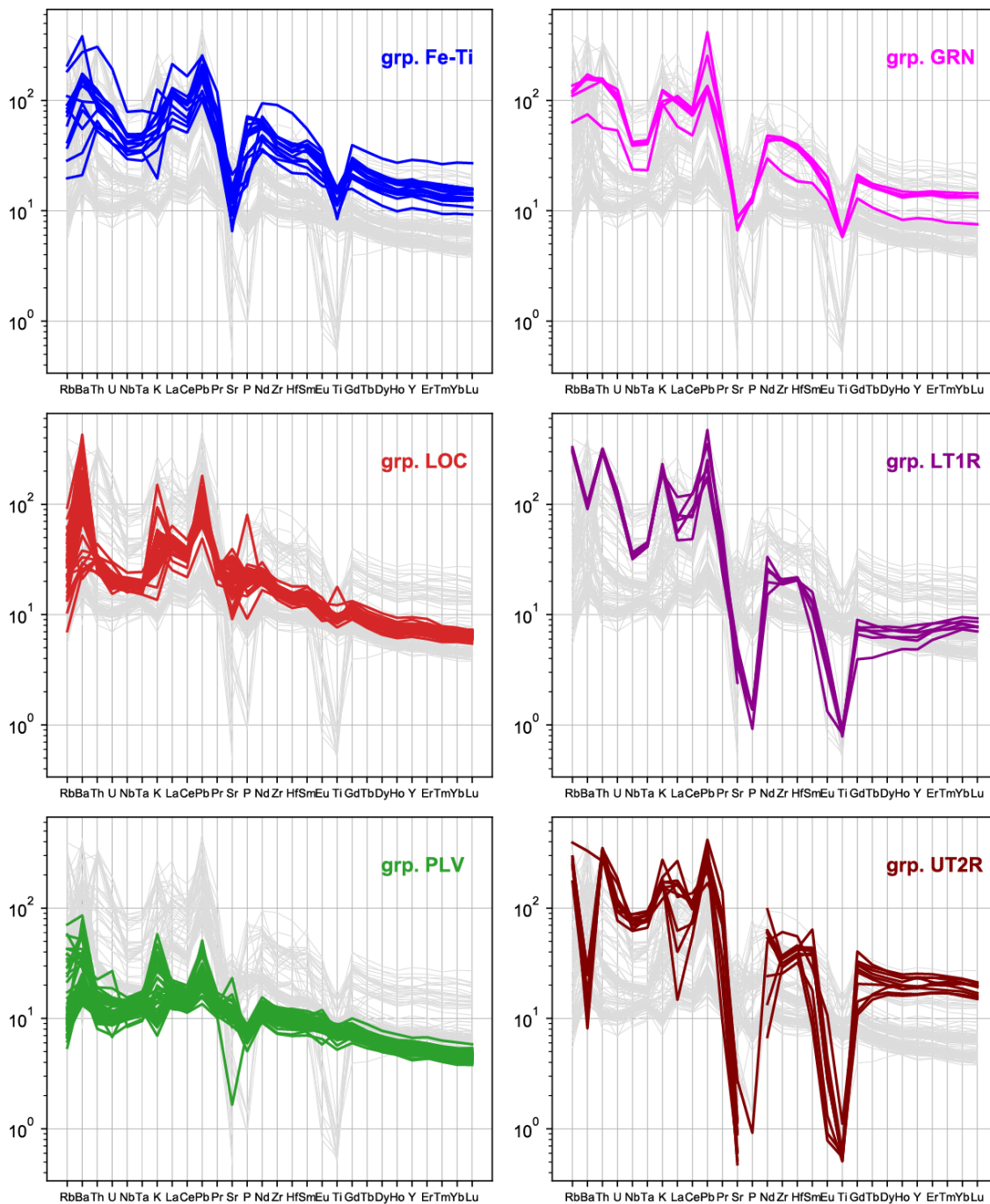


Figure 4.8

Trace element spider diagrams showing concentrations of incompatible trace elements in Porcupine Mountains magmas normalized to the Primitive Mantle (Sun & McDonough, 1989).

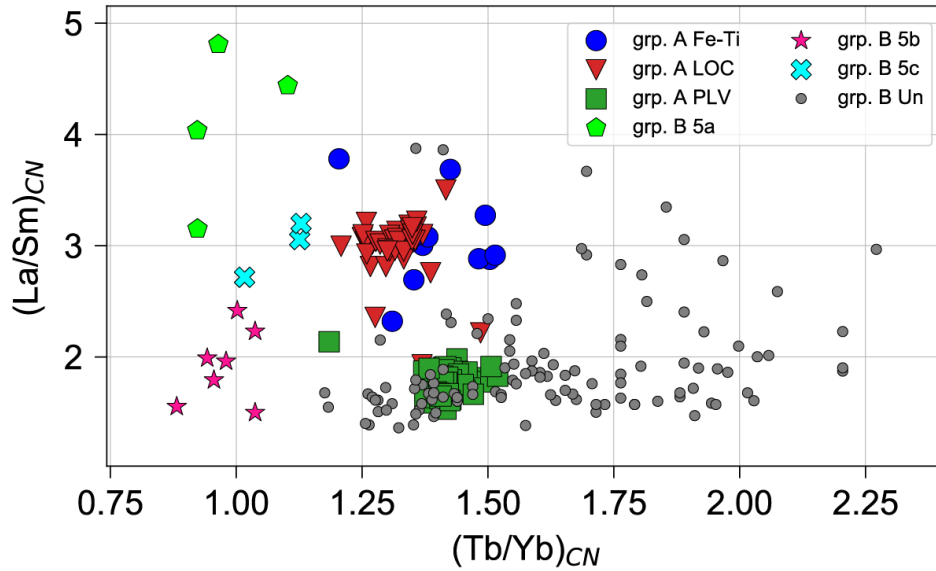


Figure 4.9

Plot of chondrite-normalized La/Yb vs chondrite-normalized Tb/Yb in Porcupine Mountains volcanic rocks (samples labeled with prefix A). Shown for comparison are Mamainse Point Volcanic Group magmas; Types 5a, b, and c (grp. B samples in legend) are divided to show similarities between these groups remaining Mamainse Point magmas are undivided. Evolved rocks from the Porcupine Mountains are not shown on this plot as mineral phases can affect these elements .

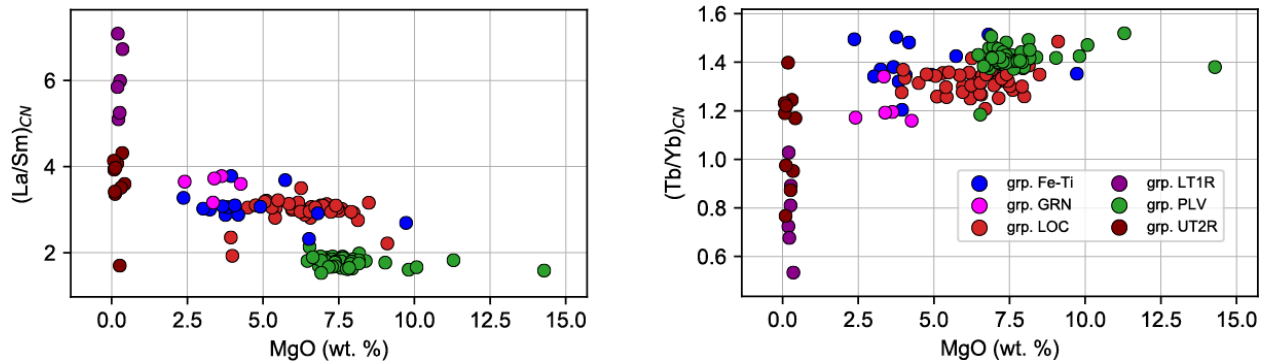


Figure 4.10

Bivariate diagrams showing chondrite-normalized La/Sm and Tb/Yb vs. MgO in all Porcupine mountains volcanic rocks. These elemental ratios in Lake of the Clouds basalts and Fe-Ti basalts do not co-vary with MgO, indicating that these ratios are not altered by fractional crystallization. We observe a large spread in $(La/Sm)_{CN}$ and $(Tb/Yb)_{CN}$ in the rhyolites (LT1R and UT2R).

4.4.3.2 Granophyres

Chondrite-normalized REE diagrams have negative Eu anomalies consistent with plagioclase feldspar crystallization (Eu/Eu^* from 0.71-0.81; Figure 4.7). The REE diagrams overlap with the Fe-Ti basalts, and one granophyre overlaps with Lake of the Clouds basalts (Figure 4.6). Primitive mantle normalized trace element spider diagrams show negative Nb-Ta, Sr, P, and Ti anomalies. Granophyre $(La/Yb)_{CN}$ ranges from 6.5-7.4, $(Tb/Yb)_{CN}$ ranges from 1.2-1.3, and $(La/Sm)_{CN}$ ranges from 3.2-3.8.

4.4.3.3 Fe-Ti Basalts

Fe-Ti basalts exhibit negative Eu anomalies in chondrite-normalized REE patterns (Figure 4.6). The magnitude of these Eu anomalies, Eu/Eu^* , overlap with Lake of the Clouds basalts (Figure 4.7). On primitive-mantle normalized trace element spider diagrams, there are negative anomalies in Sr, Ti, and Nb-Ta. $(La/Yb)_{CN}$ ranges from 4.5-9.16, $(Tb/Yb)_{CN}$ ranges from 1.2-1.5

(Figure 4.10), and $(La/Sm)_{CN}$ ranges from 2.3-3.8 for Fe-Ti basalts, and these values overlap considerably with Lake of the Clouds basalts.

4.4.3.4 Lower Type 1 Rhyolites

Type 1 rhyolites have negative to flat HREE slopes with $(Tb/Yb)_{CN}$ from 0.5-1.0 (Figure 4.10). Chondrite normalized REE patterns show negative Eu anomalies (Eu/Eu^* from 0.26-0.36) consistent with extensive plagioclase feldspar crystallization (Figure 4.7). Primitive mantle normalized trace element diagrams show negative anomalies in Nb-Ta, Sr, P, and Ti. Type 1 rhyolite have $(La/Sm)_{CN}$ from 5.1-7.1

4.4.3.5 Upper Type 2 Rhyolites

Upper Type 2 rhyolites have unusual REE patterns that vary greatly, especially in LREE elements La-Sm. Type 2 rhyolites feature the most pronounced negative Eu anomalies on REE plots (Eu/Eu^* from 0.08 to 0.44; Figure 4.6, Figure 4.7). On trace element spider diagrams (Figure 4.8), there are negative Eu, Ti, and Sr anomalies; P is below detection limit in most of the Type 2 rhyolites. Upper Type 2 rhyolites have overall much higher concentrations of HREE than lower Type 1 rhyolites (Figure 4.6).

4.4.4 Isotopes

Results of isotopic analyses are shown in Figure 4.11. Six samples from the Porcupine Mountains were analyzed here, including one Fe-Ti basalt sample, three Lake of the Clouds basalts, one Portage Lake Volcanics basalt, and one lower Type 1 rhyolite. We present Nd and Hf isotopic data.

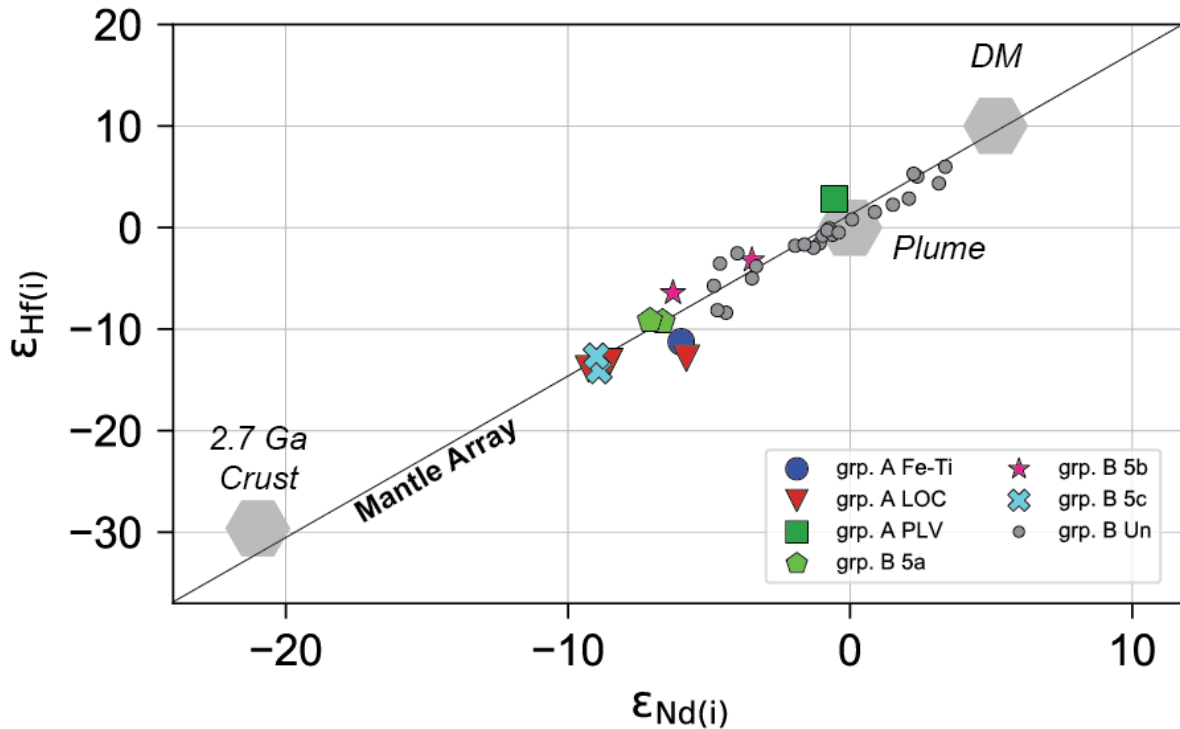


Figure 4.11

Age-corrected ($i = \text{initial at 1100 Ma}$) isotopic results (Hf, Nd) for Porcupine Mountains magmatic rocks (samples with prefix A in the legend). Mamainse Point formation samples (those with prefix B in the legend) shown for reference. Groups 5a, 5b, and 5c of the Latent Stage at Mamainse Point are selected for comparison and remaining Mamainse Point isotopes are shown but are undifferentiated. Shown for reference is the Mantle Array (Chauvel et al., 2008). The precise compositions of the end members given here (plume, continental crust, and the depleted mantle (DM)) are not well constrained and they are therefore illustrated as gray hexagons representing this uncertainty. Isotope end members from Rooney et al., 2022.

Isotopic results shown here have been back corrected to a consistent 1100 Ma value, in essence the time of their formation. Decay constants used for these corrections were 1.867×10^{-11} for ^{176}Lu (Söderlund et al., 2004) and 6.54×10^{-12} for ^{147}Sm . Conversion of Hf and Nd isotopic

ratios into ϵ_{Hf} and ϵ_{Nd} notation requires Chondritic Uniform Reservoir (CHUR) values, and we use the values presented in Bouvier et al. (2008): $^{176}\text{Hf}/^{177}\text{Hf}$ (0.282785), $^{176}\text{Lu}/^{177}\text{Hf}$ (0.0336), $^{143}\text{Nd}/^{144}\text{Nd}$ (0.51263), and $^{147}\text{Sm}/^{144}\text{Nd}$ (0.196). These values are also corrected to 1100 Ma. Existing Nd isotopic data from Shirey et al. (1994) were used for the MPVG samples, and new Hf isotope compositions were acquired on the same samples (Rooney et al., 2022). Shown in Figure 4.11, the plot of ϵ_{Hf} vs ϵ_{Nd} , is the mantle array, which shows a linear mixing relationship between depleted mantle, primitive mantle, and crustal materials. From this point forward, all isotopic ratios and ϵ isotopic notations are described in terms of the initial, 1100 Ma corrected values.

We observe highly negative ϵ_{Hf} and ϵ_{Nd} isotopic signatures for Fe-Ti basalts and Lake of the Clouds basalts. Lake of the Clouds basalts have ϵ_{Hf} ranging from -12.9 to -13.9 and ϵ_{Nd} ranging from -5.8 to -9.3. The Fe-Ti basalt has an ϵ_{Hf} of -11.25 and an ϵ_{Nd} of -6.0. The Portage Lake Volcanics basalt analyzed has an ϵ_{Hf} of 2.8 and the Type 1 rhyolite has an ϵ_{Hf} of -16.2.

For the Portage Lake Volcanics basalt and the Type 1 rhyolite, Nd isotopic analysis failed. Nicholson et al. (1997) provide average ϵ_{Nd} for Portage Lake Volcanics magmas of 0.4 and 0.6 for low- and high-TiO₂ samples respectively. We have therefore assigned an ϵ_{Nd} of 0.5, the average of the two Portage Lake groups, to the Portage Lake Volcanics in our isotopic plots based on the averages in Nicholson et al. (1997). For the Type 1 rhyolite, there are no averages of Porcupine Volcanics felsic rocks provided, so we have not assigned it a value. The Lake of the Clouds and Fe-Ti basalt ϵ_{Hf} and ϵ_{Nd} values are comparable to that of Groups 5a, 5b, and 5c from the Mamainse Point formation.

4.4.5 Alteration

Although steps were taken during field work to minimize the effects of alteration (e.g., taking samples from flow interiors, avoiding obvious veins), the Keweenaw/MCR volcanic

rocks are ~1.1 Ga old and have been subjected to the effects of post-magmatic alteration processes (Davis et al., 2021; Paces, 1988). Paces (1988) indicates oxidation/hydration and burial metamorphism are the two major processes observed in Portage Lake Volcanics, and we can extrapolate this to suggest the Porcupine Volcanics most likely experienced the same processes. Despite this, many that work in the region have concluded that flow interiors are indicative of the initial compositions of the Keweenawan magmatic rocks (e.g., Davis et al., 2021; Nicholson & Shirey, 1990; Paces, 1988; Shirey et al., 1994).

Thin sections observed in this study do show petrographic evidence of alteration. Oxide, calcite, and chlorite are all observed; these are common phases consistent with burial metamorphism and oxidation/hydration by meteoric water. Furthermore, we observe geochemical variability, in the Fe-Ti basalts, Lake of the Clouds basalts, and Portage Lake Volcanics of the large-ion lithophile elements (LILE), specifically K, Rb, Ba, Sr, and Pb. These elements are fluid-mobile. The variability observed is most likely attributable to removal from or introduction to the lava flows from post-eruption hydrous alteration. Davis et al. (2021) reached the same conclusion in their geochemical study of the Portage Lake Volcanics; the authors of that study opted not to place interpretive emphasis on those elements. We will also adopt this method in this study; the analyses of the Portage Lake Volcanics presented in that study and in this study are the same. It should be noted that silicic rock samples presented in this study (e.g., the granophyres, upper rhyolites, and lower rhyolites) do not present the same variability in LILE.

4.5 Discussion

4.5.1 Magmatic Pulses Evident in the Porcupine Mountains & Inferences from the Volcanic Stratigraphy

The stratigraphic and geologic relationships observed in the Porcupine Mountains suggest that two distinct pulses of magmatism occurred there. The first of these pulses is represented by the thick basaltic main-stage Portage Lake Volcanics succession, and conformably overlying units of the Porcupine Volcanic Group (Figure 4.2). The appearance of the intermediate and silicic rocks above the Portage Lake Volcanics signals some sort of shift or perturbation in the Portage Lake Volcanics magma plumbing system.

The second distinct pulse of magmatism in the Porcupine Mountains is the series of lava flows interbedded within the Copper Harbor Conglomerate. In this study these flows are referred to as the Lake of the Clouds basalts. Cannon et al. (1995) refers to these flows as the Copper Harbor andesite, but our geochemical results show the bulk of this formation, where we have sampled it, are basaltic. These basalts have a distinctive geochemistry in comparison to the Portage Lake Volcanics and are enriched in incompatible trace elements (Figure 4.8). Further on in this work we will describe the petrogenesis of this unique Lake of the Clouds pulse.

The Porcupine Mountains Volcanics (rhyolites and andesite/Fe-Ti basalts) conformably overlie the Portage Lake Volcanics in the study area. The presence of volcanoclastic sediments, the Copper Harbor Conglomerate, overlying the Porcupine Mountains Volcanics supports the idea that magmatism then ceased locally until the Lake of the Clouds basalts were erupted. An argument could also be made that the rhyolite and andesite sequence of the Porcupine Volcanic Group was a distinct pulse of magmatism. However, based on the dates given above and the conformable contacts of the rhyolite with the Portage Lake Volcanics (Figure 4.2), we will treat them as the end

of the first pulse. In the upcoming sections, we will treat the formation of each of the units in the volcanic stratigraphy of the Porcupine Mountains. The main scope of this work, however, is the formation of the mafic lithologies: the Fe-Ti Basalts and the Lake of the Clouds basalts.

4.5.2 Formation of Porcupine Mountains Rhyolites

One possible explanation for the intermediate & silicic rocks in the Porcupine Mountains is a loss of magma supply. Davis et al. (2021) concludes in their study that as the Portage Lake system evolved, magma flux rates increased; this resulted in increased eruption rates at the expense of assimilation and fractional crystallization. Conversely, the presence of the rhyolites at the top of the stratigraphy here supports the loss of magma supply. If elevated magma flux produces waning assimilation and fractional crystallization, then the inverse must also be true: reduced magma flux thus increases the importance of these processes, and we observe the evidence for these processes taking over at the top of the Portage Lake Volcanics stratigraphy.

Rhyolites are necessarily the product of either extensive fractional crystallization or assimilation. The crystalliferous nature of the Lower Type 1 rhyolite may provide evidence of the crystallization of evolved phases (e.g., potassium feldspar, albite, quartz) and the formation of these phases most likely plays a part in their petrogenesis. The highly negative ϵ_{HF} of these samples is also evidence of assimilation or a crustal origin. The unusual slope of the Lower Type 1 Rhyolites trace element spider diagrams (Figure 4.8) could be evidence of the melting of a different source than the Portage Lake Volcanics. This could also signal that the mineralogy is related to anatexis and disaggregation of preexisting granitic continental crust.

The formation of the Upper Type 2 Rhyolite aphyric tuffs is more difficult to constrain because of the lack of crystals to link to fractional crystallization. The trace element patterns (Figure 4.8) more closely mirror those of the Portage Lake Volcanics and suggest that the Type 2 rhyolites are

derived from evolution of the basalts. The extreme negative anomalies in the elements Sr, P, Eu, and Ti evident in these patterns do give some clue as to the phases that crystallized; the elements in question suggest feldspars (Sr, Eu), apatite (P), and Fe-Ti oxides (Ti) are the phases that were removed. These same elements are depleted to a lesser extent in the granophyres found in the study area. Thus, the granophyres may represent an intermediate step in the extreme fractional crystallization between Portage Lake basalt and Type 2 rhyolite. Another possibility is that the Upper Type 2 Rhyolites are liquids that were extracted from granophyric mushes. Either way, we can infer based on the trace element similarities to the Portage Lake Volcanics basalts that the Upper Type 2 Rhyolites & granophyres are likely related to the basalts via extreme fractional crystallization.

These observations of the Type 1 and Type 2 rhyolites and the interpretations based on them are presented here as an embryonic stage of understanding. They are not meant to be conclusive or authoritative, but rather an initial step. Because of the complexity of rhyolite petrogenesis and this work's focus on the mafic lithologies present in the Porcupine Mountains, further assessment or modeling of the silicic magmas is required but is beyond the scope of this work. Future analysis of the silicic component of the Porcupine Mountains stratigraphy should be considered within the overall conceptual framework of magmatism that we will present here.

4.5.3 Assimilation and Fractional Crystallization in the Genesis of the Porcupine Mountains Volcanics Fe-Ti Basalts

4.5.3.1 Comparison to Group 5 at Mamainse Point

The Porcupine Andesite, here termed Fe-Ti basalts, are an important volumetric component of the Porcupine Mountains stratigraphy (e.g., Figures 4.3 and 4.4) but their petrogenesis has remained elusive. In the field, they outcrop poorly, and this study only recovered a few samples

from the area delineated as Porcupine Andesite in geologic maps. However, importantly, these compositions are also found within the stratigraphy of the Portage Lake and Lake of the Clouds basalts (Figure 4.3) as well as intrusions in rhyolite bodies. This indicates that they are persistent and common magma in the study area; therefore, elucidating their genesis and evolution is important to constraining and understanding the magmatic system that produced the volcanic rocks found in the Porcupine Mountains.

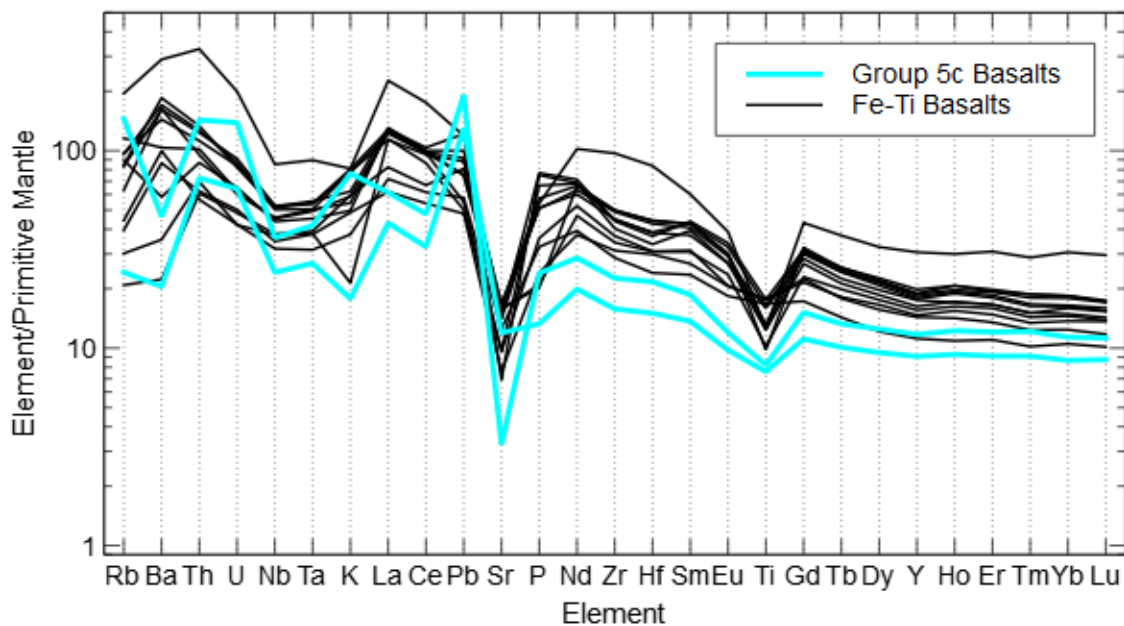


Figure 4.12

Trace element spider diagram that shows similarities between Group 5c basalts from Mamainse Point and the Fe-Ti basalts from the Porcupine Mountains.

One important observation about the Fe-Ti basalts is that they closely resemble Group 5c magmas from the Mamainse Point formation (Figure 4.12). Some of these important similarities are overall trace element values that are elevated 10-100 times primitive mantle values, and negative excursions in Sr and Ti. Other Group 5 (5a and 5b) magmas from Mamainse Point are

not as enriched in trace elements and are not close approximations. Klewin and Berg (1991) conclude that Group 5c magmas are the product of assimilation and fractional crystallization of Group 5b from Mamainse Point, which are already fractionated and contaminated products of Group 3b magmas of the Early Stage of magmatism. Isotopic evidence is presented in Figure 4.11 that the Fe-Ti basalts are also contaminated by crustal materials, shown by the negative, unradiogenic, crustal ϵ_{Nd} and ϵ_{Hf} values.

Groups 3 and 5 occur at Mamainse Point after voluminous early-stage magmatism (Group 2) has waned and immediately below the Great Conglomerate. This shutdown of the Mamainse Point system represented a loss of magma supply, and this supports the hypothesis presented earlier in this work that the silicic and intermediate rocks in the Porcupine Mountains are the result of a loss of magma supply as well. As explained by Davis et al. (2021), assimilation & fractional crystallization (AFC) decrease when magma flux is high and increase when magma flux is low. Therefore, I will now attempt to use a numerical trace element formulation to model the evolution of these Fe-Ti basalts.

4.5.3.2 Trace Element REAFC/AFC/FC Modeling Rationale and Procedure

Recent modeling of the Portage Lake Volcanics has indicated that the combined processes of recharge, eruption, assimilation, hybridization, and fractional crystallization are all necessary to explain the geochemical variability of these magmas (Davis et al., 2021). One key observation that led to this modeling is that Portage Lake Volcanics magmas mostly fit into a narrow range of MgO contents (6-8 wt. %) while incompatible trace elements sensitive to crystallization of minerals typical in basaltic magma evolution (Sr for plagioclase, Cr for clinopyroxene, and Ni for olivine) varied considerably. Davis et al. (2021) used the constant mass REAFC (recharge, eruption, assimilation, and fractional crystallization) model developed by Lee et al. (2014).

Following the methods of Davis et al. (2021), we use the constant-mass REAFC architecture (Lee et al., 2014) to model the trace element evolution of the Fe-Ti basalts. Constant mass means that the mass of the magma chamber (the liquid volume) did not change with evolution. Our laboratory developed a Python code using the constant mass REAFC architecture of Lee et al. (2014), with added functionality. In addition to the magma evolution trajectory for REAFC, our formulation also considers pure Rayleigh fractional crystallization trajectories (Gast, 1968; Lee et al., 2014; Rollinson, 2014) as well as assimilation-fractional crystallization (AFC; DePaolo, 1981). The model considers the evolution of trace elements versus changing MgO concentrations in response to recharge, eruption, assimilation, and fractional crystallization processes. The specific elements and their reason for incorporation in the model is given in Table 4.1.

<i>Element</i>	<i>Reason for Incorporation</i>
Ni	Compatible element in major phase olivine
Cr	Compatible element in major phases clino- and orthopyroxene and accessory phase spinel
Sr	Compatible element in major phase plagioclase feldspar
Nb	Incompatible element in major and accessory phases
La	Incompatible element in major and accessory phases.

Table 4.1

Trace elements considered in the constant mass REAFC model, with explanation for their incorporation.

The model requires the input of several magma compositions. These include the parental magma composition, the recharging magma composition (which can be and often is the same as the parental magma), and the assimilant. We opted to use the same composition for the parental and recharging magma. For this modeling, we attempted several compositions as “primitive” starting compositions. The first of these was the highest-MgO sample in the Fe-Ti basalt group (TOR00005E with 9.74 wt. % MgO). However, because this high-MgO sample could be due to accumulation of olivine, and Klewin and Berg concluded that the Group 5c were derived from already-fractionated melts, we attempted the model with two other magmas with lower MgO that qualitatively appeared to be where evolutionary trends began. These were TOR00005G (5.73 wt. % MgO) and TOR0000JZ (6.52 wt. % MgO). It should also be noted that TOR0000JZ is the Fe-Ti basalt that is found in the Portage Lake Volcanics stratigraphy. All these starting compositions had considerable variability in the five trace elements examined.

Models were first attempted with the assimilant composition used in Davis et al. (2021), which is a granitoid leucosome partial melt of 2.7 Ga crust (Steiner, 2014). We kept the Sr value of this leucosome for some of the runs presented below as it may be representative of a potential assimilant; see table 4.2 below. However, for the other elements (Ni, Cr, Nb, and La) the

leucosome did not present acceptable modeling results. Instead, an average of three Archean granite gneisses that are known to contaminate Midcontinent Rift rocks in Wisconsin (Seifert et al., 1992) was utilized as an alternative for most or all assimilant compositions.

In addition to magma compositions, the REAFC model requires a fractionating crystal assemblage as an input. The model uses the input proportions of minerals to calculate a bulk D value, or partition coefficient, for each element. The concentrations of trace elements are controlled by bulk mineral-melt partition coefficient values, D . Partition coefficients greater than one (1) are compatible in the bulk solid assemblage and will decrease in concentration as fractional crystallization/AFC/REAFC proceeds, while partition coefficients less than one (1) are incompatible in the bulk solid assemblage and will concentrate in the liquid mass. Most individual mineral-melt partition coefficients are from Table 4.1 of Rollinson (2014) while others are derived from the Geochemical Earth Reference Model (GERM) website and references therein. MELTS models were attempted to constrain the fractionating phases but were inconclusive.

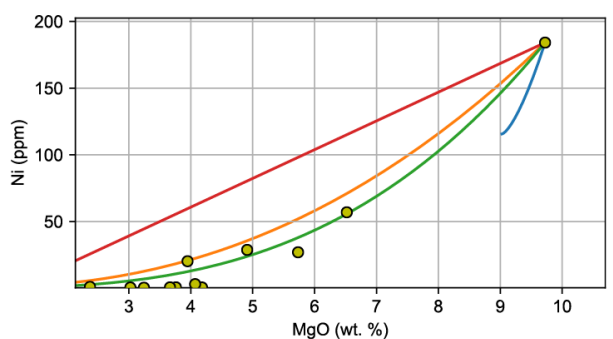
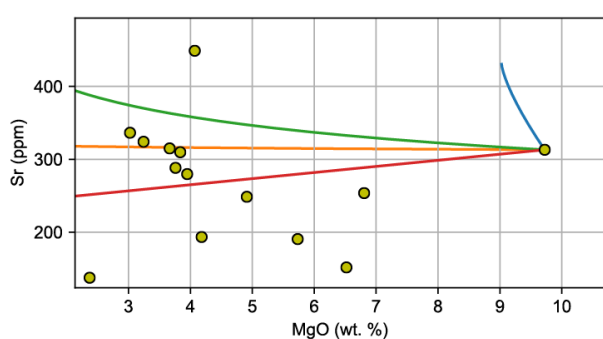
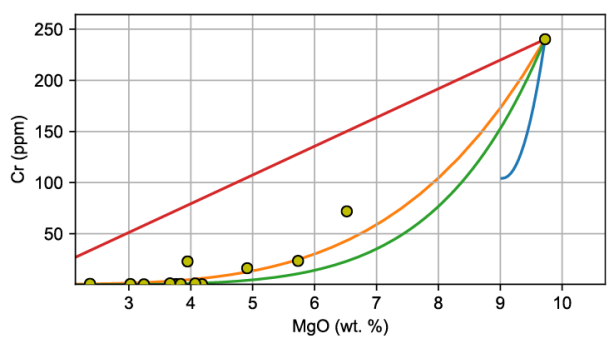
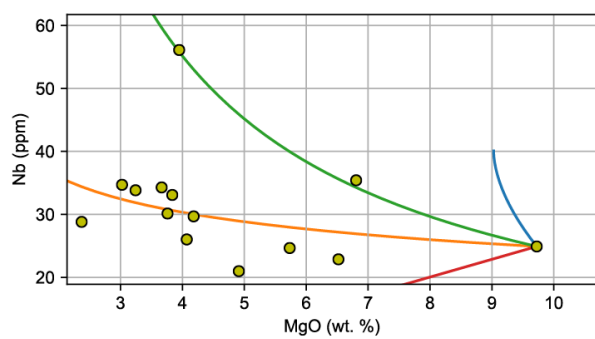
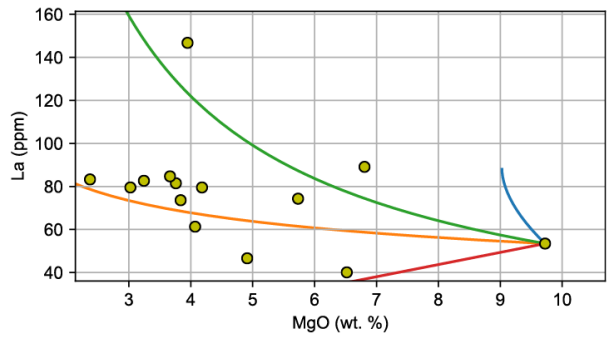
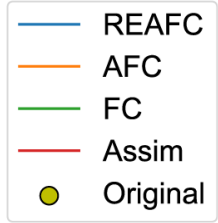
Model Run	A	B	C
Starting Magma	TOR00005E	TOR00005G	TOR0000JZ
Starting MgO	9.74	5.73	6.52
Starting Sr	313	190	152
Starting Nb	24.9	24.7	22.9
Starting La	53.5	74.3	40.1
Starting Cr	240	23.4	71.9
Starting Ni	184	26.9	56.9
Assimilant MgO	1.37 (a)	1.37 (a)	1.37 (a)
Assimilant Sr	243 (a)	1143 (b)	1143 (b)
Assimilant Nb	1.34 (a)	1.34 (a)	1.34 (a)
Assimilant La	6.21 (a)	6.21 (a)	6.21 (a)
Assimilant Cr	5.46 (a)	5.46 (a)	5.46 (a)
Assimilant Ni	4.09 (a)	4.09 (a)	4.09 (a)
Olivine %	43	22	22
Clinopyroxene %	0	27	27
Plagioclase %	46	40	40
Magnetite %	7	7	7
Ilmenite %	4	4	4
Eruption %	60	40	30
Crystallization %	25	45	55
Assimilation %	15	15	15

Table 4.2

Run conditions and compositions used in the various REAFC/AFC/FC models to describe the evolution of the Fe-Ti basalts. For assimilant compositions, (a) indicates that the value used is the average of three granite gneisses presented in Seifert et al., 1992 while (b) indicates that the value used is the leucosome of Steiner, 2014. For REAFC, the starting magma and recharging magma are the same composition.

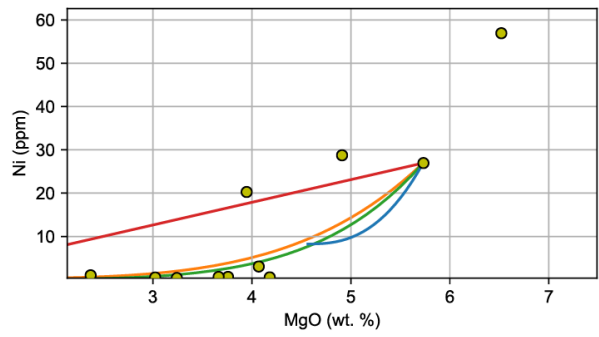
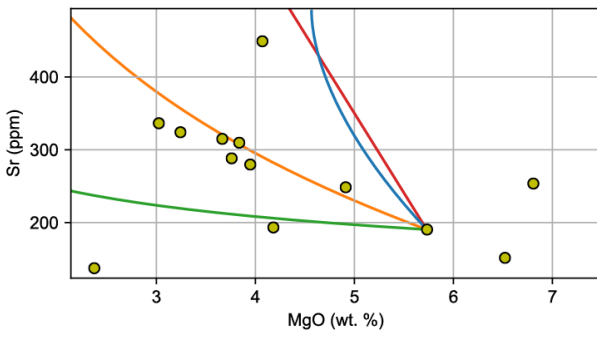
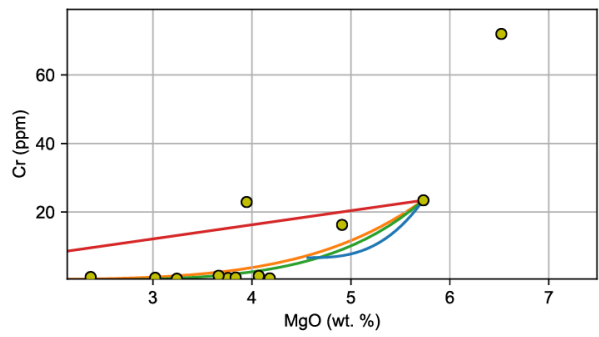
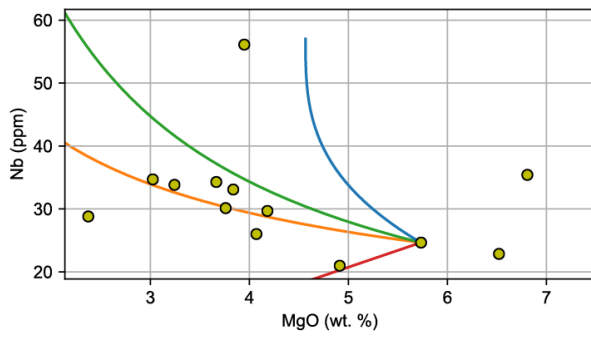
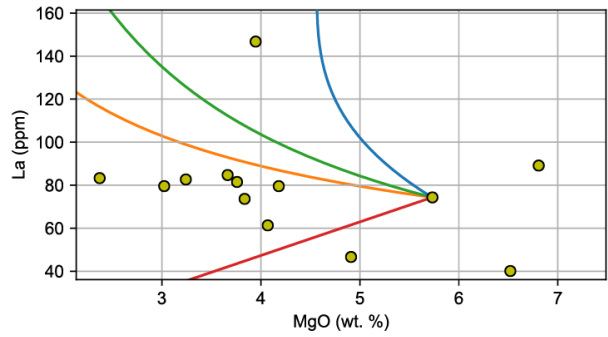
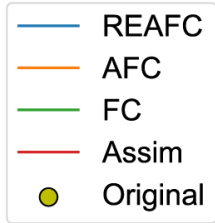
Run with eruption at 0.6, crystallization at 0.25, assimilation at 0.15
 olivine = 0.43, opx = 0.0, cpx = 0.0, plag = 0.46, ilmenite = 0.07, magnetite = 0.04, apatite = 0.0

TOR00005E



Run with eruption at 0.4 crystallization at 0.45, assimilation at 0.15
 olivine = 0.22, opx = 0.0, cpx = 0.27, plag = 0.4, ilmenite = 0.07, magnetite = 0.04, apatite = 0.0

TOR00005G



Run with eruption at 0.3, crystallization at 0.55, assimilation at 0.15
 olivine = 0.22, opx = 0.0, cpx = 0.27, plag = 0.4, ilmenite = 0.07, magnetite = 0.04, apatite = 0.0

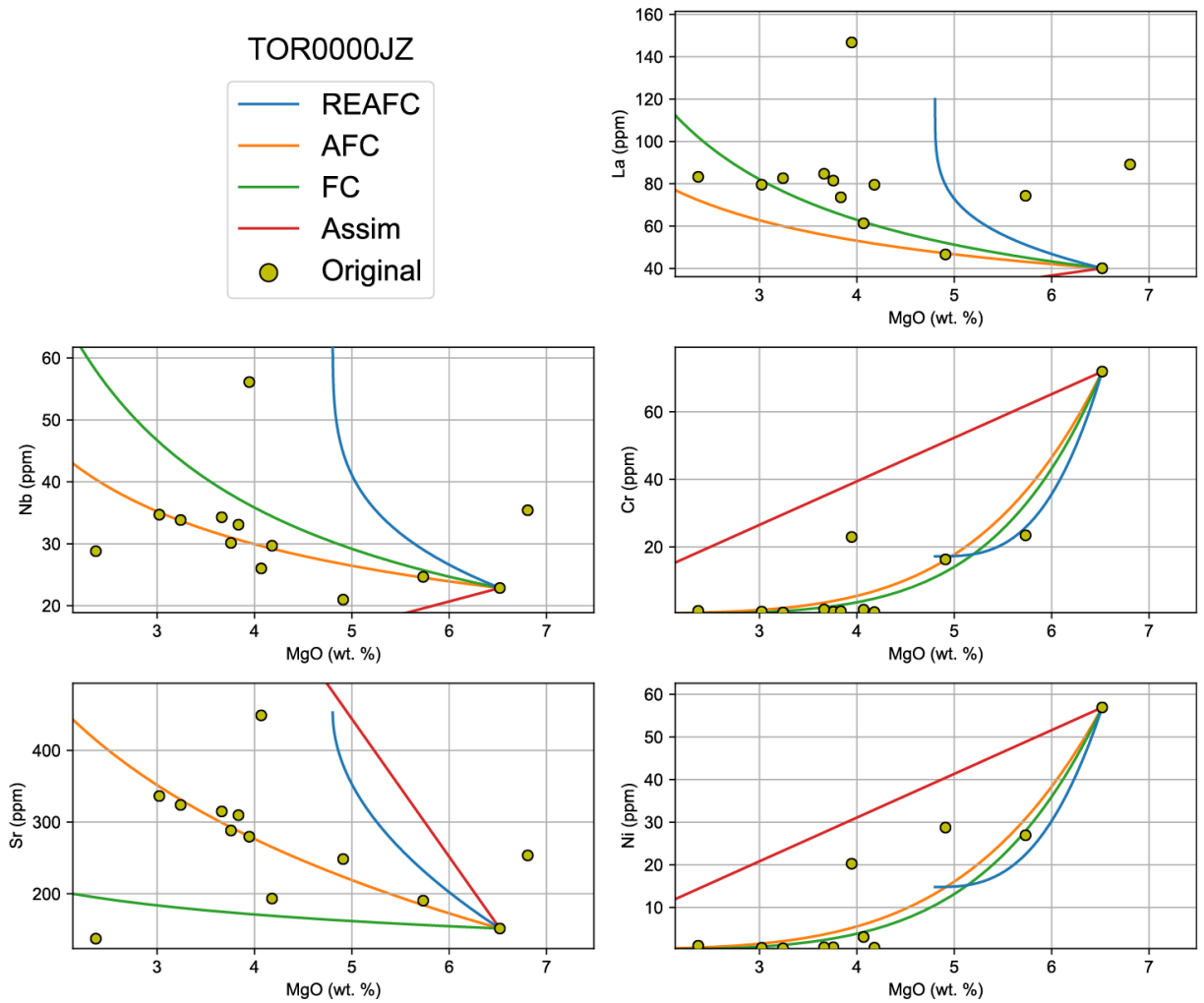


Figure 4.13 (This page & two previous)

Results of trace element magma evolution simulations for magmas TOR00005E, TOR00005G, and TOR0000JZ. Legend entry abbreviations are as follows: REAFC = Recharge, evacuation, assimilation, fractional crystallization (blue line); AFC = assimilation-fractional crystallization (orange line); FC = fractional crystallization (green line); Assim = Assimilation (pure mixing between parental magma and assimilant; red line). High-MgO sample TOR00005E in the first set of plots is omitted from further diagrams.

4.5.3.3 Modeling Outcomes & Implications for Rift Volcanism

The REAFC/AFC/FC models were implemented by varying the amounts of evacuation and assimilation. Our modeling outcomes presented in Figure 4.13 suggest that REAFC processes are unlikely to have generated the chemical systematics observed in the Fe-Ti basalts. One of the main indicators against REAFC is that the REAFC curves do not go below 4.5 wt. % MgO (depending on the starting composition) while observed melts go below 3 wt. % MgO. Instead, the AFC, and fractional crystallization trajectories at 15% assimilation best circumscribe our observed data set. In this model, the assimilation model is pure mass-balance mixing between the parental magma and the assimilate.

The crystallizing mineral assemblage for the models indicate either troctolite (olivine + plagioclase feldspar) or gabbro (olivine + plagioclase feldspar + clinopyroxene) with minor oxide constituents common to all three models (ilmenite + magnetite). These phase assemblages are consistent with the most common rock types found in the Duluth Complex of Minnesota, oxide-bearing troctolites and gabbros (Miller Jr. et al., 2002). While the Duluth Complex is not unequivocally the intrusive complex where the magmas of the Porcupine Mountains evolved, it still provides a suitable analog for comparison. Keays and Lightfoot's (2015) model for the Mid-Continent rift suggests a series of intrusive complexes emplaced across the rift axis, and because of similar primitive materials being delivered from the plume to these complexes, similar fractionating assemblages are expected.

Because assimilation is an important component of these magmas' evolution, the intrusions that formed the Fe-Ti basalts are likely located close to the margin of the intrusive complex in contact with continental crust. Our models use compositions of Archean materials (Seifert et al., 1992) in the simulations, suggesting that the country rocks assimilated in the formation of the Fe-

Ti basalts are Archean in age. Miller Jr. et al (2002) show that mafic intrusions of the Beaver Bay Complex, which is associated with younger lavas in Minnesota, are in contact with Paleoproterozoic and Archean country rocks. This supports the notion that the intrusive system where assimilation is an important factor must necessarily be in direct contact with the assimilated materials.

With the complexity and size of the magmatic system in question, it is difficult to estimate the volume of continental crust that the modeled 15% assimilation suggested represents. It is not certain from these models what fraction of the assimilated material was represented by the initial, fractionated starting basalt and what fraction was assimilated during the evolution of the even more evolved magmas. Another uncertainty lies in how open or closed the magma system that produced these specific magmas is with respect to the bulk magmatic system. Finally, a volume of the Portage Lake volcanics & associated intrusive rocks is not readily available in the literature, only a gross volume of all Mid-Continent Rift materials. Thus, estimating this volume of crust assimilated is not within the scope of this work but may be accomplished by future works.

The models presented here do strongly support a hypothesis that the Fe-Ti basalts formed by extensive assimilation and fractional crystallization of a troctolitic or gabbroic assemblage in an intrusive complex that hosts evolved magmas derived from the Portage Lake Volcanics-type magmas. This evolutionary sequence is also consistent with the formation of Group 5c magmas from Mamainse Point (Klewin and Berg, 1991). The Group 5 magmas at Mamainse Point represent a shutdown of the magmatic system and loss of magma flux there. Furthermore, evolved compositions and increased assimilation are associated with lower magmatic flux (Davis et al., 2021). Therefore, when the Fe-Ti basalts, the rhyolitic magmas found at the top of the Portage Lake stratigraphy, and subsequent deposition of the Copper Harbor Conglomerate in the Porcupine

Mountains are considered together, it becomes clear that these magmas represent the cessation of the main stage of flood basalt volcanism in this part of the rift.

4.5.4 The Genesis & Evolution of the Lake of the Clouds Basalts

4.5.4.1 The Lake of the Clouds magmatic pulse

The Lake of the Clouds basalts appear to be a unique pulse of magmatism that occurred after the shutdown of the Portage Lake Volcanics & associated intermediate to felsic rocks (e.g., Fe-Ti basalts, rhyolites) in the Porcupine Mountains area. They differ from the Portage Lake basalts in several ways. These include elevated concentrations of major element oxides TiO_2 and P_2O_5 (Figure 4.5), trace element patterns that are offset upwards from the Portage Lake Volcanics (Figure 4.8), and REE that have a higher slope from La to Sm (Figure 4.6 & Figure 4.9). $(\text{La}/\text{Sm})_{\text{CN}}$ is a measure of REE enrichment and thus a proxy for partial melting percentage, where elevated values are indicative of lower percentage partial melts. This elevated $(\text{La}/\text{Sm})_{\text{CN}}$ is evidence that the Lake of the Clouds basalts are produced by a separate pulse of magmatism that represented reduced melting volume from the mantle source when compared to the Portage Lake Volcanics of the main stage.

Another observation of the Lake of the Clouds basalts is that they are some of the most crustally-contaminated compositions found in the MCR when compared with the Mamainse Point dataset (Figure 4.11). We observe highly negative ϵ_{Nd} and ϵ_{Hf} in the Lake of the Clouds basalts, consistent with crustal assimilation. The only other compositions from the MCR that have such highly negative ϵ_{Nd} and ϵ_{Hf} values are from Group 5 from Mamainse Point & the Fe-Ti basalts lower in the Porcupine Mountains stratigraphy. These magmas are affected by AFC processes (Klewin and Berg, 1991). Our major element, trace element, and isotopic results indicate that the Lake of the Clouds basalts must have experienced additional processing (i.e., fractional

crystallization and assimilation) of parental magma compositions as they extend to MgO contents as low as 4 wt. %. Due to the proximity of the Portage Lake Volcanics to the Lake of the Clouds basalts, it is plausible that the Lake of the Clouds basalts were another pulse of magma but were processed through the same plumbing system as the Portage Lake Volcanics. We began with this hypothesis: that the magma plumbing system that produced the Portage Lake Volcanics and Porcupine Volcanics was the same one that Lake of the Clouds magmas were later passed through. We will therefore employ the same REAFC model used by Davis et al. (2021) and detailed in Section 4.5.3.2 of this work.

Crystallization in the Portage Lake Volcanics was accompanied by low degrees of assimilation of 2.7 Ga crustal material that was emplaced during the Algoman/Kenoran orogeny (Card & Ciesielski, 1986; Davis et al., 2021). The specific major & trace element composition used in the modeling of Davis et al. (2021) was a leucosome found in the Wawa subprovince basement in contact with Duluth Complex of Minnesota. This granitoid composition represents a partial melt of 2.7 Ga crust due to interaction with Keweenawan intrusive igneous rocks (Davis et al., 2021; Steiner, 2014). We will utilize this same assimilant composition for our REAFC modeling because it has already been shown to produce successful modeling results with other Keweenawan basalts.

4.5.4.2 Modeling Procedure

to establish a crystallizing assemblage, we opted to use MELTS_Excel software (Gualda & Ghiorso, 2015). This software simulates a thermodynamically constrained major element evolution path for an input magma from a calculated liquidus temperature. Davis et al. (2021) used this software to confirm the REAFC phase assemblage. We have done the reverse, where we use this software to establish an assemblage for input into the trace element model. We do use some constraints from Davis et al. (2021); they suggest that the PLV magma system is at 4 kbar depth and has a temperature of 1160° C based on their MELTS_Excel modeling results. We used the

same pressure (4 kbar) and we selected the assemblage that MELTS_Excel predicts for TOR00008D at 1160° C. At this temperature and pressure, the input basalt has crystallized to 26% of the initial liquid and has a crystallizing assemblage of 50% olivine, 43% plagioclase feldspar, and 7% spinel. This set of simulated pressure, temperature, crystallization, and assemblage has MgO contents of 4.3 weight percent in the residual liquid (74% liquid remaining), which is the average MgO content we observe in the most evolved Lake of the Clouds basalts. We interpret this simulation to represent a major-element crystallization path for the evolution of the Lake of the Clouds basalts. This assemblage is therefore used as the input into the Python REAFC program to model the trace element data.

Like the work of Davis et al. (2021), we sought to find a model that creates an “envelope” around the observed Lake of the Clouds data set. We then interpret the space within that envelope to be the range of processes that contributed to the evolution of the Lake of the Clouds basalt.

4.5.4.3 Modeling Results

The REAFC/AFC/fractional crystallization models were implemented by varying the amounts of evacuation and assimilation. Our modeling outcomes presented in Figure 4.14 suggest that REAFC processes are unlikely to have generated the chemical systematics observed in the Lake of the Clouds basalts; instead, the assimilation, AFC, and fractional crystallization trajectories at 15% assimilation best circumscribe our observed data set. In this model, the assimilation model is pure mass-balance mixing between the parental magma and the assimilant. The result of this model is shown below in Figure 4.14. In the figure we observe that the REAFC model predicts trace element concentrations that extend to elevated values that we do not observe. MgO contents predicted for REAFC also do not go below 7.5 wt. % MgO. We also observe that there is a larger spread of the element Sr in Figure 4.14 than the elements Nb & Ni. This is likely

attributable to post-emplacement alteration of these basalts (noted in Section 4.4.5). Because Sr is an element with a fluid-mobile large ion lithophile character, it is more likely to have been perturbed by transition metal Ni and high-field strength element Nb, which are less mobile under hydrothermal alteration (Rollinson, 2014).

Run with eruption at 0.59, crystallization at 0.26, assimilation at 0.15
 olivine = 0.5, opx = 0.0, cpx = 0.0, plag = 0.43, ilmenite = 0.0, magnetite = 0.0, apatite = 0.0, User specified = 0.07, 0.0, 0.0, 0.0
 LOC Basalts with LOC (TOR00008D) as starting comp and recharge comp

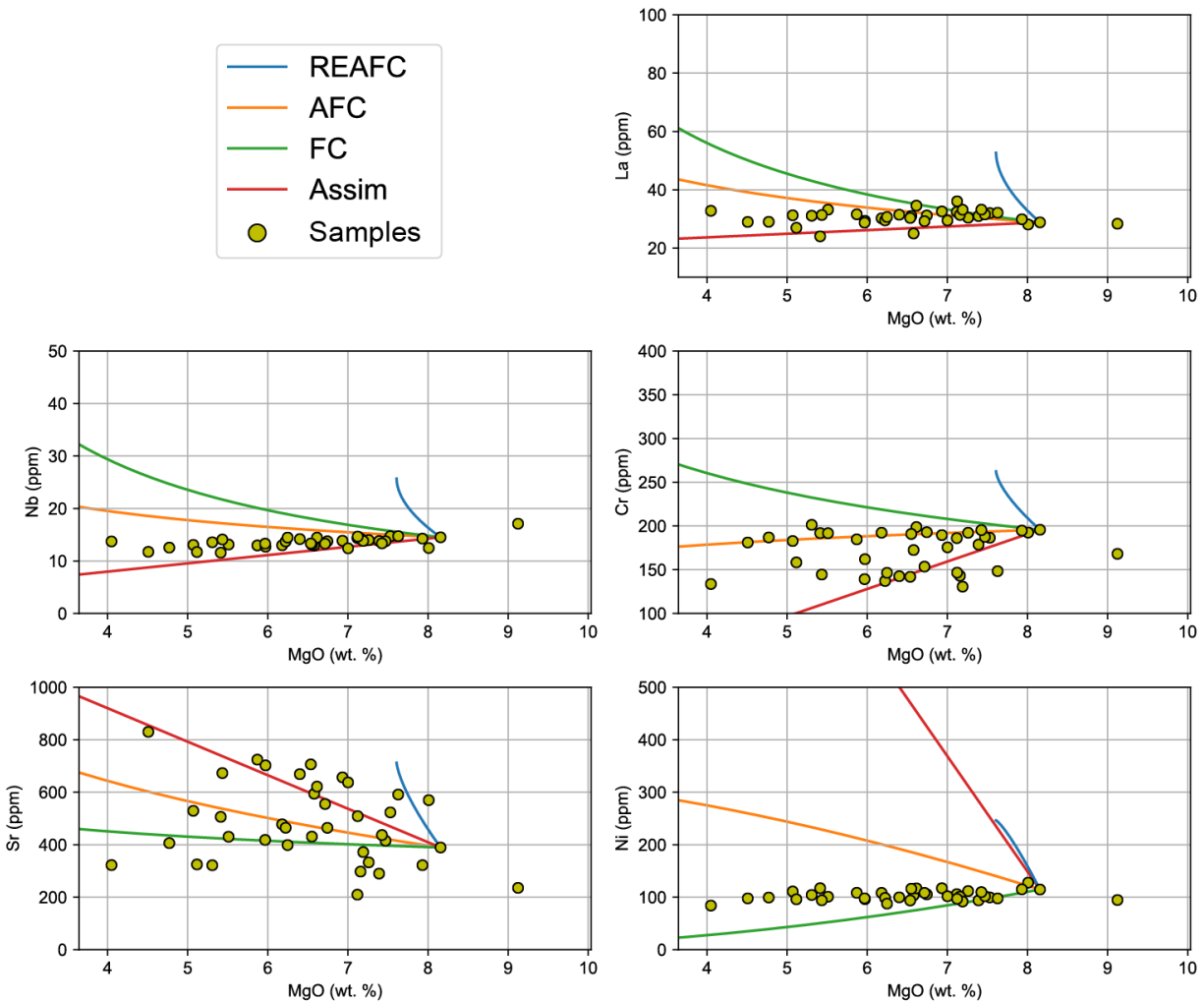


Figure 4.14

Results of trace element magma evolution simulations showing a possible solution using TOR00008D as the parental and recharging magma, and the leucosome granitoid melt liquid composition of Steiner (2014) as the assimilant. Legend entry abbreviations are as follows: REAFC = Recharge, evacuation, assimilation, fractional crystallization (blue line); AFC = assimilation-fractional crystallization (orange line); FC = fractional crystallization (green line); Assim = Assimilation (pure mixing between parental magma and assimilant; red line). User specified mineral in the second header column is spinel.

4.5.4.4 Modeling Conclusions & Synthesis

Based on our trace element modeling results, we can conclude that the processes fractional crystallization with or without assimilation have resulted in the observed compositions of Lake of the Clouds basalt. The Lake of the Clouds magmas crystallized an assemblage of olivine (50%), plagioclase feldspar (43%), and spinel (7%) as predicted by MELTS_Excel models. These processes likely occurred in magma chambers at 4 kbar depth in the crust.

The trace element modeling presented here suggests 15% assimilation of continental crust. This number is consistent with the results in Section 4.5.3.3 of this work. This 15% figure may represent melts of the crust that remained partially molten from previous magmatic episodes it may take more careful calculations that are beyond the scope of this work to deconvolve the relative contributions of assimilation at this stage versus the contributions from previous assimilation events. Another confounding factor in the estimation of the true volume of continental crust is that we have suggested there may be ongoing heating & anatexis of the crust through the latent heat of crystallization and thermal diffusion in the time between the Lake of the Clouds and the cessation of the Portage Lake Volcanics. The 15% figure may rather be viewed as a time-integrated total amount of crust assimilated through all the magmatic episodes. The modeling results presented here do add further support to the hypothesis that AFC of these mixed magmas occurred.

Unlike the Portage Lake Volcanics evolution that was dominated by flux of large volumes of magma through the crust (Davis et al., 2021), the Lake of the Clouds basalts is likely the result of a more limited magma supply. A smaller pulse is consistent with the trace elements of this study. Typically REE slope (i.e., $(La/Sm)_{CN}$) is controlled by percentage of partial melt (Rollinson, 2014). At lower partial melt percentages, incompatible elements (light REE) are partitioned into the liquid

while more-compatible elements (heavy REE) remain in the solid residue. Thus, higher percentages of partial melting such as those observed in voluminous main-phase Portage Lake basalts result in the low $(La/Sm)_{CN}$ observed in that magma series (Figure 4.9). Conversely, lower partial melting results in elevated the $(La/Sm)_{CN}$ observed in the Lake of the Clouds basalts (Figure 4.9). Therefore, the Lake of the Clouds basalts are from a smaller, possibly singular pulse of magma rather than multiple large pulses as observed in the main phase. This also likely explains why REAFC (i.e. continued replenishment of the magma chamber while magmas erupt) is unlikely for the Lake of the Clouds basalts. This singular pulse was likely of a lower percentage partial melt as evidenced by the trace element data presented above. Thus, the trace element data is consistent with a limited magma supply from the mantle.

A similar relationship is observed between these REE & isotope measures in Group 5a & 5c from Mamainse Point as compared to the Lake of the Clouds & Fe-Ti basalts (Figure 4.6). Klewin and Berg (1991) acknowledge that variation in mantle partial melting is responsible for differences between groups 5b (high percentage partial melt) and groups 5a & 5c (low percentage partial melting). Therefore, we recognize this symmetry between the Mamainse Point Volcanic Group samples and the Porcupine Mountains volcanics here. This symmetry between the Mamainse Point latent stage Group 5 magmas late stage basalts (i.e., Fe-Ti, Lake of the Clouds) of the Porcupine Mountains is also evident in the highly negative, unradiogenic Nd and Hf isotopes. Similar processes are thus likely at play in the genesis of the Fe-Ti basalts, Lake of the Clouds basalts and the Latent Stage at Mamainse Point.

4.5.4.5 Implications of Different Assimilants Used in Modeling Outcomes

The AFC models presented above utilize two separate assimilants. For the Fe-Ti basalts, models were first attempted with the assimilant used by Davis et al. (2021), which is a leucosome

found at the footwall of the Duluth Complex first presented by Steiner (2014). However, this composition was unsuccessful in providing relevant modeling outcomes. A new assimilant composition was developed using the Sr of the Steiner melt, but other modeled elements were derived from the average granite-gneiss presented in Seifert et al. (1992). These granite-gneisses are also Archean in age but are instead found at the contact between lower Keweenawan basalt flows and older Archean granites (Seifert et al., 1992). Conversely, the Lake of the Clouds basalts were successfully modeled using the leucosome melt of Steiner (2014).

Both modeling outcomes suggest a 15% contribution of each individual assimilant; lower volumes of assimilation do not provide satisfactory modeling results. Furthermore, observed isotopic values for the Fe-Ti basalts and the Lake of the Clouds basalts are comparable and highly negative in ϵ_{Nd} and ϵ_{Hf} . This supports that the assimilation in each case is extensive. However, the major difference between these assimilants lies in the concentrations of incompatible trace elements. The leucosome of Steiner (2014) has relatively high Nb and La (14.5 ppm and 28.8 ppm respectively), while the granite-gneiss of Seifert et al. (1992) is much lower in these elements (1.34 ppm Nb, 6.21 ppm La). The two compositions also differ greatly in Ni and Cr. It is also noted here that the Type 1 and Type 2 Rhyolites in the Porcupine Mountains do differ in trace element abundances, and different assimilants may be part of what gives rise to these two different compositions.

The presence of two assimilant compositions implies there is a spatial heterogeneity in the physical location where the different magmas stalled and interacted with Archean-aged country rock. There are thus two different options for this variation: laterally (in the x or y direction, meaning a different place along or across the rift axis) or vertically (z, at a different depth in the plumbing system). Keays and Lightfoot (2015) do suggest that there may be multiple edifices

along the rift axis contributing to the pile of lavas that accumulates in the Mid-Continent Rift basin, and it is therefore plausible that the Fe-Ti basalts and the Lake of the Clouds basalts emerged from different vents. However, examples of the Fe-Ti basalt are ubiquitous throughout the Porcupine Mountains stratigraphy. They are found as flows interbedded with the Portage Lake Volcanics, flows within the Lake of the Clouds stratigraphy, and as flows in the unit mapped as Porcupine Andesite, and as dikes within Porcupine Volcanic Group rhyolites (Figure 4.3). These suggest, but are not conclusive, that all these melts likely emerged from the same edifice. While it is still possible that the Lake of the Clouds and Portage Lake basalts emerged from a different vent and were interbedded with flows of the Fe-Ti basalts from the Porcupine Mountains, the simpler explanation is that they all came from the same edifice.

The incompatible trace elements of the modeled contaminants also provide some constraints on the depth-dependence hypothesis. Incompatible trace elements are concentrated more in the upper continental crust than the lower crust. The assimilated composition for the Fe-Ti basalts has 6 ppm La and 1.34 ppm Nb; these values are more like the composition of average lower continental crust given in Rudnick and Gao (2003), which are 8 ppm La and 5 ppm Nb. On the other hand, the assimilated composition for the Lake of the Clouds basalt has 28.8 ppm La and 14.5 ppm Nb. These values are like the values for average upper continental crust (31 ppm La, 12 ppm Nb, Rudnick and Gao, 2003). MELTS models from both this study and Davis et al. place some constraints on the depths of the Portage Lake Volcanics and Lake of the Clouds basalts as having crystallized at ~4 kbar, which is consistent with shallower, upper continental crust. Furthermore, the crystallizing assemblage in the Lake of the Clouds model is olivine + plagioclase + oxides, while the likely Fe-Ti basalt modeled crystallizing assemblage is gabbroic (olivine + plagioclase + clinopyroxene) with oxides. Clinopyroxene is stable at greater pressures. Therefore,

it is plausible based on this reasoning that the Fe-Ti basalts are the result of AFC at greater depths than that of the Lake of the Clouds basalts or the Portage Lake basalts.

The origin of the Fe-Ti basalts at depth may also explain several of the field observations in the Porcupine Mountains. First, these magmas are found throughout the Porcupine Mountains stratigraphy but are not a common component. This could be because of the difficulty these melts would have escaping from the deepest parts of the plumbing system without being further processed or homogenized with other more voluminous magma components in shallower reservoirs. The presence of this Porcupine Andesite as its own unit that comes after the cessation of the Portage Lake Volcanics and one of the rhyolites may be evidence that these Fe-Ti basalts were erupted en masse only after the massive basaltic volcanism stopped and a rhyolitic “cap” stopping the eruption were cleared out of the plumbing system.

There is one flaw in this model of the Fe-Ti basalts having been produced at greater depths. Typically, one would expect magmas from the deep parts of the magmatic plumbing system to have greater whole-rock MgO; the Fe-Ti basalts are all relatively depleted in MgO except for TOR00005E which has > 9 wt. % MgO. However, we hypothesize that this magma was affected by accumulated high-MgO olivine. Therefore, the bulk of the observed Fe-Ti basalts range from 3-7 wt. % MgO. I speculate here that these could be magmas that are evolved from and segregated from the most primitive magmas from the lowest parts of the plumbing system where they remain to assimilate crustal material until eruption. Attempts to model the evolution of the Fe-Ti basalt magmas at various depths using MELTS were unsuccessful, likely due to limitations of the software.

It is also possible that the assimilant of the Fe-Ti basalt is deep crust that had been exhumed to shallower depths due to rifting-related uplift and exhumation of deeper crustal lithologies; this

would explain the low-MgO, evolved character of the Fe-Ti basalt magmas but lower-crustal character of the proposed assimilant. While it remains unclear whether the Fe-Ti basalt assimilation took place at greater or shallower depths than the Lake of the Clouds, we conclude here that the magmas most likely had a depth-dependent difference in the assimilants.

4.5.5 Porcupine Mountains Volcanic Complex and the Local Cessation of Main Stage Volcanism

We have shown above that the Lake of the Clouds basalts in the Porcupine Mountains are likely formed from a new pulse of magma with a lower percentage partial melt. These magmas evolved by fractional crystallization of olivine, plagioclase feldspar, and spinel and assimilation of 2.7 Ga continental crust. We posit that the stratigraphy of the Porcupine Mountains volcanic group (i.e., the Porcupine Rhyolites, Andesite, and the granophyre) represent some intrusive and extrusive products of a magma vent of the Portage Lake Volcanics that lost its magma supply during the Main Stage and thus produced these evolved products. When the magma supply was cut off, some of these evolved compositions erupted, but many of them could have plausibly remained in a hot, partly crystalline mush that was dominated by basaltic melts, but also included some granophyric to rhyolitic.

The latent heat released by ongoing crystallization could have kept the entire magmatic plumbing system hot and partially molten for a long period of time, as well as created anatexis of the remaining crust in the area. Studies have shown that magma bodies & crystal mushes can be rejuvenated and remobilized after periods of magmatic quiescence (e.g., Jackson et al., 2018; Szymanowski et al., 2017). Furthermore, rapid burial by conglomeratic sediments may have also served to insulate both the lava flows and the plumbing system (Bornhorst & Barron, 2011; S. Stein et al., 2018). We suggest that the magma plumbing system remaining hot would be even

more plausible given the massive magma volumes represented by the Portage Lake Volcanics, other main-stage lavas, and the cumulate body of the Duluth complex (Merino et al., 2013; Miller Jr et al., 2002).

After a hiatus in magmatism, represented by the Copper Harbor Conglomerate, the local central vent's relict magma system was a conduit exploited by another pulse of basaltic magmatism. This pulse likely had a mantle-equilibrated composition with a lower percentage partial melt than the Portage Lake Volcanics. Within the relict magma system, the magmas underwent assimilation and fractional crystallization.

We posit here that the Lake of the Clouds basalts are partially analogous to the latent stage basalts at Mamainse Point, where magmatic flux had waned locally but new inputs of material from the mantle still occurred. These inputs are possibly of considerably lower volume than those that drove main stage magmatism, as shown by elevated $(La/Sm)_{CN}$ in both the Lake of the Clouds basalts and Mamainse Point Groups 5a & 5c (Figure 4.9). These latent stage basalts from Mamainse Point are similarly contaminated by continental crust.

Swanson-Hysell et al. (2019, 2021) suggest that the long duration of the Keweenaw LIP magmatism can be explained by plume material travels along thinned lithosphere via a process called upside-down drainage (Sleep, 1997; Swanson-Hysell et al., 2014). This upside-down drainage system where plume material periodically flows laterally along the topography of the lithosphere could explain the later pulse of material arriving at the relict Porcupine Mountains plumbing system and forming the Lake of the Clouds basalts.

Based on this upside-down drainage model, we would suggest that the Porcupine Mountains volcanic group and Lake of the Clouds could have its own discrete plumbing system (i.e., a magma mush complex) like that of but independent from (1) the Duluth Complex; (2) the

northeastern Keweenaw peninsula Portage Lake; and (3) the Mamainse Point formation. The granophyre in the Porcupine Mountains could be an exposed upper remnant of that magmatic system, while the remains may be buried beneath the Keweenaw Fault. This system could have also fed the Portage Lake flows locally.

Davis et al. (2021) suggest that the Portage Lake Volcanics are fed from an intrusion like the layered series of the Duluth Complex. Davis et al. (2021) also acknowledged similarities in age, petrographic, and geochemical characteristics between the Beaver Bay complex within the Duluth Complex and the Greenstone Flow. This could mean the Beaver Bay complex is a feeder for the Greenstone Flow, which is found at Isle Royale and in the northeast Keweenaw Peninsula (Doyle, 2016; Fairchild et al., 2017). This could mean that Portage Lake Volcanics -type material was erupting broadly across the MCR from multiple vents. The model of MCR magmatism put forth in Keays & Lightfoot (2015; fig. 14) suggests many disparate intrusive complexes evolved across the width (and possibly length) of the developing MCR as well. The model of Miller & Nicholson (2013) supports this possibility of multiple discrete magma centers.

Upside-down drainage could also explain why the Portage Lake Volcanics appears to shut down in the Porcupine Mountains before more main-stage Portage Lake Volcanics flows are erupted in the northeastern Keweenaw peninsula (Swanson-Hysell et al., 2019; Zartman et al., 1997). The absence of the notable Greenstone and Copper City flows in the Portage Lake Volcanics stratigraphy within the Porcupine Mountains also supports the notion of continuing magmatism in other parts of the MCR while having ceased in some places. The large Greenstone flow is found on Isle Royale (King, 2008) but not in the Porcupine Mountains (Cannon et al., 1995), giving further support to a spatial disparity in the eruption of Portage Lake Volcanics materials. Therefore, we posit here that what is now the northeastern Keweenaw Peninsula was

still receiving magmatic input while the Porcupine Mountains shut down. This is evidenced by the thick cap of silicic and intermediate rocks overlying the Portage Lake Volcanics in the Porcupine Mountains. Magmatism in both locations (Porcupine Mountains and the northeast Keweenaw peninsula) is later rejuvenated by a pulse that may have flowed in via upside down drainage. This is shown by the Lake of the Clouds basalts in the Porcupine Mountains and the Lake Shore Traps basalts to the northeast.

Further comparisons of the Lake of the Clouds basalts, Lake Shore Traps basalts, and Group 5 materials from Mamainse Point are likely to further elucidate more geochemical similarities. There is also a need for more precise geochronological constraints on the Porcupine Volcanics and the Lake of the Clouds basalts. Swanson-Hysell et al. (2019) found pegmatitic segregations in the Portage Lake Volcanics Greenstone and Copper City flows. These horizons were used to extract zircons that were then used for precise dating. Our field work did not reveal any pegmatitic horizons in Lake of the Clouds basalts, but further field study may identify them. These comparisons are useful for establishing parallels in the processes active in the final stages of LIP magmatism before continental breakup.

4.6 Conclusions

In this study we present the major element, trace element, isotopic, petrographic, and stratigraphic relationships among magmatic rocks in the Porcupine Mountains Volcanic Complex in northern Michigan. A series of evolved and intermediate volcanic rocks (i.e., the Porcupine rhyolites & Fe-Ti basalts) conformably overlie the Portage Lake Volcanics there. We conclude that these are related to the shutdown of one in a series of magmatic vents erupting main stage Keweenawan LIP materials. The dates from the Porcupine Volcanic complex of 1093.6 ± 1.8 Ma (Zartman et al., 1997) and the Greenstone flow of 1091.59 ± 0.27 Ma (Swanson-Hysell et al., 2019)

overlap within uncertainty. This may reflect continued eruption of main-stage Portage Lake Volcanics type material into the Mid-Continent Rift from one edifice (the Beaver Bay complex in Minnesota feeding the Greenstone Flow) while another goes dormant (the Porcupine Mountains). Then all magmatism ceases in the MCR, shown by the sedimentation of the Copper Harbor Conglomerate that is ubiquitous along the Keweenaw peninsula.

After this period of sedimentation and magmatic quiescence, there is a renewed pulse of magmatism. This is shown by lavas interbedded within the Copper Harbor Conglomerate in both the Porcupine Mountains, herein defined as the Lake of the Clouds basalt, and flows at the very northeastern most Keweenaw Peninsula at High Rock Bay called the Lake Shore Traps. The Lake of the Clouds basalts are trace-element enriched magmas contaminated extensively by continental crust.

We conclude that the Lake of the Clouds pulse of magmatism evolved via assimilation, and fractional crystallization. Similarly, Fe-Ti basalts found in the Porcupine Mountains Volcanics group also evolved by assimilation and fractional crystallization processes. The main differences between these two is in the modeled assimilated and crystallizing phase assemblage that produced them. Extensive assimilation of crustal materials (modeled at 15% for the Lake of the Clouds and Fe-Ti basalts) most profound of these processes, resulting in highly nonradiogenic isotopic values. During the residence of these residual materials, latent heat of crystallization may be responsible for anatexis of continental crust and the continued mushy state of these intrusive rocks. These anatectic melts are incorporated into the Lake of the Clouds pulse of volcanism, resulting in the isotopic results presented in this study.

The primitive materials of the Lake of the Clouds basalts are likely low-volume plume melts that are channeled to the relict Porcupine Mountains Volcanic Complex intrusive complex

via upside down drainage. This intrusive complex may have remained hot and partially molten due to the latent heat of crystallization and insulative burial beneath conglomeratic sediments. The residual materials are likely a complex analogous to those intrusive rocks found in the Duluth Complex. This complex is potentially buried beneath the Keweenaw fault locally but may also have been distal to the area where these basalts were emplaced.

These results suggest that the loss of magma supply locally can produce evolved and intermediate compositions to erupt near the vent. Similar compositions may persist within the magmatic plumbing system of these vents as mushes for long periods of time, especially in extremely hot regions where magma had been intensively focused. Further magma inputs channeled along sub-lithospheric drainage networks could exploit these relict mush zones. The products would further crystallize within these zones. These interpretations apply to the MCR here but can likely be extrapolated to other interpretations for the evolution of plume-influenced LIP magma systems globally.

Our results also have important implications for understanding the role of plume magmatism in continental breakup, especially later stages of the process. Small pulses of plume melt material at the end of a LIP such as the Lake of the Clouds basalt may be analogous to seaward dipping reflectors that are otherwise buried or eroded in rifted margins that progress to oceanic spreading. At the latest stage of continental rifting prior to continental breakup, plume material and the continental crust may interact to produce lava flows that intercalate with sediments, and these packages form the base of passive continental margins.

BIBLIOGRAPHY

BIBLIOGRAPHY

- Annells, R. N. 1974. *Keweenaw volcanic rocks of Michipicoten Island, Lake Superior, Ontario, an eruptive centre of proterozoic age* **218**
- Bornhorst, T. J., & Barron, R. J. 2011. Copper deposits of the western Upper Peninsula of Michigan. *Geological Society of America Field Guide*, **24**, 83–99.
- Boynton, W. V. 1984. Cosmochemistry of the Rare Earth Elements: Meteorite Studies. In *Developments in Geochemistry*, **2**, 63–114). Elsevier. <https://doi.org/10.1016/B978-0-444-42148-7.50008-3>
- Bouvier, A., Vervoort, J. D., & Patchett, P. J. 2008. The Lu–Hf and Sm–Nd isotopic composition of CHUR: Constraints from unequilibrated chondrites and implications for the bulk composition of terrestrial planets. *Earth and Planetary Science Letters*, **273**, 48–57. <https://doi.org/10.1016/j.epsl.2008.06.010>
- Brown, E. L., & Lesher, C. E. 2014. North Atlantic magmatism controlled by temperature, mantle composition and buoyancy. *Nature Geoscience*, **7**, 820–824.
- Cannon, W. F. 1992. The Midcontinent rift in the Lake Superior region with emphasis on its geodynamic evolution. *Tectonophysics*, **213**, 41–48. [https://doi.org/10.1016/0040-1951\(92\)90250-A](https://doi.org/10.1016/0040-1951(92)90250-A)
- Cannon, W. F., & Nicholson, S. W. 2001. *Geologic map of the Keweenaw Peninsula and adjacent area, Michigan*. <https://doi.org/10.3133/i2696>
- Cannon, W. F., Nicholson, S. W., Woodruff, L. G., Hedgman, C. A., & Schulz, K. J. 1995. Geologic map of the Ontonagon and part of the Wakefield 30' x 60' quadrangles, Michigan. IMAP, Article 2499. <https://doi.org/10.3133/i2499>
- Card, K. D., & Ciesielski, A. 1986. DNAG #1. Subdivisions of the Superior Province of the Canadian Shield. *Geoscience Canada*. <https://journals.lib.unb.ca/index.php/GC/article/view/3439>
- Chauvel, C., Lewin, E., Carpentier, M., Arndt, N. T., & Marini, J.-C. 2008. Role of recycled oceanic basalt and sediment in generating the Hf–Nd mantle array. *Nature Geoscience*, **1**, 64–67. <https://doi.org/10.1038/ngeo.2007.51>
- Davis, D. W., & Green, J. C. 1997. Geochronology of the North American Midcontinent rift in western Lake Superior and implications for its geodynamic evolution. *Canadian Journal of Earth Sciences*, **34**, 476–488. <https://doi.org/10.1139/e17-039>
- Davis, D. W., & Paces, J. B. 1990. Time resolution of geologic events on the Keweenaw Peninsula and implications for development of the Midcontinent Rift system. *Earth and Planetary Science Letters*, **97**, 54–64. [https://doi.org/10.1016/0012-821X\(90\)90098-I](https://doi.org/10.1016/0012-821X(90)90098-I)

- Davis, W. R., Collins, M. A., Rooney, T. O., Brown, E. L., Stein, C. A., Stein, S., & Moucha, R. 2021. Geochemical, petrographic, and stratigraphic analyses of the Portage Lake Volcanics of the Keweenawan CFBP: Implications for the evolution of Main stage volcanism in Continental Flood Basalt Provinces. Geological Society, London, Special Publications, SP518-2020–2221. <https://doi.org/10.1144/SP518-2020-221>
- DePaolo, D. J. 1981. Trace element and isotopic effects of combined wallrock assimilation and fractional crystallization. *Earth and Planetary Science Letters*, **53**, 189–202. [https://doi.org/10.1016/0012-821X\(81\)90153-9](https://doi.org/10.1016/0012-821X(81)90153-9)
- Doyle, M. 2016. *Geologic and geochemical attributes of the Beaver River Diabase and Greenstone Flow: Testing a possible intrusive-volcanic link in the 1.1 Ga Midcontinent Rift*.
- Ernst, R. E. 2014. Large igneous provinces. Cambridge University Press.
- Ersoy, E. Y. 2013. PETROMODELER (Petrological Modeler): A Microsoft® Excel© spreadsheet program for modelling melting, mixing, crystallization and assimilation processes in magmatic systems. *TURKISH JOURNAL OF EARTH SCIENCES*, **22**, 115–125.
- Fairchild, L. M., Swanson-Hysell, N. L., Ramezani, J., Sprain, C. J., & Bowring, S. A. 2017. The end of Midcontinent Rift magmatism and the paleogeography of Laurentia. *Lithosphere*, **9**, 117–133. <https://doi.org/10.1130/L580.1>
- Gast, P. W. 1968. Trace element fractionation and the origin of tholeiitic and alkaline magma types. *Geochimica et Cosmochimica Acta*, **32**, 1057–1086.
- Gualda, G. A., & Ghiorso, M. S. 2015. MELTS _ E xcel: AM icrosoft E xcel-based MELTS interface for research and teaching of magma properties and evolution. *Geochemistry, Geophysics, Geosystems*, **16**, 315–324.
- Jackson, M. D., Blundy, J., & Sparks, R. S. J. 2018. Chemical differentiation, cold storage and remobilization of magma in the Earth’s crust. *Nature*, **564**, 405–409. <https://doi.org/10.1038/s41586-018-0746-2>
- Keays, R. R., & Lightfoot, P. C. 2015. Geochemical Stratigraphy of the Keweenawan Midcontinent Rift Volcanic Rocks with Regional Implications for the Genesis of Associated Ni, Cu, Co, and Platinum Group Element Sulfide Mineralization. *Economic Geology*, **110**, 1235–1267. <https://doi.org/10.2113/econgeo.110.5.1235>
- King, N. 2008. Geologic Map of Isle Royale National Park. *National Park Service, US Department of the Interior*, 1.
- Klewin, K. W., & Berg, J. H. 1991. Petrology of the Keweenawan Mamainse Point lavas, Ontario: Petrogenesis and continental rift evolution. *Journal of Geophysical Research*, **96**, 457. <https://doi.org/10.1029/90JB02089>

- Krans, S. R., Rooney, T. O., Kappelman, J., Yirgu, G., & Ayalew, D. 2018. From initiation to termination: A petrostratigraphic tour of the Ethiopian Low-Ti Flood Basalt Province. *Contributions to Mineralogy and Petrology*, **173**, 37. <https://doi.org/10.1007/s00410-018-1460-7>
- LaVigne, A. 2019. *Terminal Stage of a Dying Rift*. Michigan State University.
- Lee, C.-T. A., Lee, T. C., & Wu, C.-T. 2014. Modeling the compositional evolution of recharging, evacuating, and fractionating (REFC) magma chambers: Implications for differentiation of arc magmas. *Geochimica et Cosmochimica Acta*, **143**, 8–22. <https://doi.org/10.1016/j.gca.2013.08.009>
- Li, Z. X., Bogdanova, S. V., Collins, A. S., Davidson, A., De Waele, B., Ernst, R. E., Fitzsimons, I. C. W., Fuck, R. A., Gladkochub, D. P., Jacobs, J., Karlstrom, K. E., Lu, S., Natapov, L. M., Pease, V., Pisarevsky, S. A., Thrane, K., & Vernikovsky, V. 2008. Assembly, configuration, and break-up history of Rodinia: A synthesis. *Precambrian Research*, **160**, 179–210. <https://doi.org/10.1016/j.precamres.2007.04.021>
- McDermott, C., Lonergan, L., Collier, J. S., McDermott, K. G., & Bellingham, P. 2018. Characterization of seaward-dipping reflectors along the South American Atlantic margin and implications for continental breakup. *Tectonics*, **37**, 3303–3327.
- Merino, M., Keller, G. R., Stein, S., & Stein, C. 2013. Variations in Mid-Continent Rift magma volumes consistent with microplate evolution: Variations in Mid-Continent Rift magma. *Geophysical Research Letters*, **40**, 1513–1516. <https://doi.org/10.1002/grl.50295>
- Miller, J., & Nicholson, S. 2013. *Geology and Mineral Deposits of the 1.1Ga Midcontinent Rift in the Lake Superior Region – An Overview*. **50**.
- Miller Jr, J. D., Green, J. C., Severson, M. J., Chandler, V. W., Hauck, S. A., Peterson, D. M., & Wahl, T. E. 2002. *RI-58 Geology and mineral potential of the Duluth Complex and related rocks of northeastern Minnesota*.
- Nicholson, S. W., Schulz, K. J., Shirey, S. B., & Green, J. C. 1997a. Rift-wide correlation of 1.1 Ga Midcontinent rift system basalts: Implications for multiple mantle sources during rift development. *Canadian Journal of Earth Sciences*, **34**, 504–520. <https://doi.org/10.1139/e17-041>
- Paces, J. B. 1988. *Magmatic processes, evolution and mantle source characteristics ...* **436**.
- Paces, J. B., & Bell, K. 1989. Non-depleted sub-continental mantle beneath the Superior Province of the Canadian Shield: Nd-Sr isotopic and trace element evidence from Midcontinent Rift basalts. *Geochimica et Cosmochimica Acta*, **53**, 2023–2035. [https://doi.org/10.1016/0016-7037\(89\)90322-0](https://doi.org/10.1016/0016-7037(89)90322-0)
- Paton, D.A., Pindel, J., McDermott, K., Bellingham, P., & Horn, B. 2017. Evolution of seaward-dipping reflectors at the onset of oceanic crust formation at volcanic passive margins: Insights from the South Atlantic. *Geology*, **45**, 439-442. <https://doi-org/10.1130/G38706.1>

- Piispa, E.J., Smirnov, A.V., Pesonen, L.J., & Mitchell, R.H. 2018. Paleomagnetism and Geochemistry of ~1144-Ma Lamprophyre Dikes, Northwestern Ontario: Implications for the North American Polar Wander and Plate Velocities. *Journal of Geophysical Research Solid Earth*, **123**, 6195-6214. <https://doi.org/10.129/2018JB015992>
- Rollinson, H. R. 2014. Using geochemical data: Evaluation, presentation, interpretation. Routledge.
- Rooney, T. O., Nelson, W. R., Dosso, L., Furman, T., & Hanan, B. 2014. The role of continental lithosphere metasomes in the production of HIMU-like magmatism on the northeast African and Arabian plates. *Geology*, **42**, 419–422. <https://doi.org/10.1130/G35216.1>
- Rooney, T.O., Konter, J.G., Finlayson, V.A., Lavigne, A., Brown, E.L, Stein, C.A., Stein, S., & Moucha, R. 2022. Constraining the Isotopic Endmembers Contributing to 1.1 Ga Keweenaw Large Igneous Province Magmatism. *Contributions to Mineralogy and Petrology*, in review.
- Satkoski, A. M., Bickford, M. E., Samson, S. D., Bauer, R. L., Mueller, P. A., & Kamenov, G. D. 2013. Geochemical and Hf–Nd isotopic constraints on the crustal evolution of Archean rocks from the Minnesota River Valley, USA. *Precambrian Research*, **224**, 36–50. <https://doi.org/10.1016/j.precamres.2012.09.003>
- Schmerr, N., Garnero, E., & McNamara, A. 2010. Deep mantle plumes and convective upwelling beneath the Pacific Ocean. *Earth and Planetary Science Letters*, **294**, 143–151.
- Seifert, K.E., Peterman, Z.E., and Thieben, S.E. 1992. Possible crustal contamination of Midcontinent Rift igneous rocks: examples from the Mineral Lake intrusions, Wisconsin. *Canadian Journal of Earth Sciences*, **29**, 1140-1153. <https://doi.org/10.1139/e92-092>
- Shirey, S. B., Klewin, K. W., Berg, J. H., & Carlson, R. W. 1994. Temporal changes in the sources of flood basalts: Isotopic and trace element evidence from the 1100 Ma old Keweenaw Mamainse Point Formation, Ontario, Canada. *Geochimica et Cosmochimica Acta*, **58**, 4475–4490. [https://doi.org/10.1016/0016-7037\(94\)90349-2](https://doi.org/10.1016/0016-7037(94)90349-2)
- Sleep, N. H. 1997. Lateral flow and ponding of starting plume material. *Journal of Geophysical Research: Solid Earth*, **102**, 10001–10012.
- Söderlund, U., Patchett, P. J., Vervoort, J. D., & Isachsen, C. E. 2004. The ¹⁷⁶Lu decay constant determined by Lu–Hf and U–Pb isotope systematics of Precambrian mafic intrusions. *Earth and Planetary Science Letters*, **219**, 311–324. [https://doi.org/10.1016/S0012-821X\(04\)00012-3](https://doi.org/10.1016/S0012-821X(04)00012-3)
- Stein, C. A., Kley, J., Stein, S., Hindle, D., & Keller, G. R. 2015. North America’s Midcontinent Rift: When rift met LIP. *Geosphere*, **11**, 1607–1616. <https://doi.org/10.1130/GES01183.1>
- Stein, S., Stein, C. A., Elling, R., Kley, J., Keller, G. R., Wysession, M., Rooney, T., Frederiksen, A., & Moucha, R. 2018. Insights from North America’s failed Midcontinent Rift into the

- evolution of continental rifts and passive continental margins. *Tectonophysics*, **744**, 403–421. <https://doi.org/10.1016/j.tecto.2018.07.021>
- Steiner, A. 2014. Genesis of Sulfide Mineralization within the Footwall Granite of the Maturi Cu-NI-PGE Deposit of the South Kawishiwi Intrusion, Duluth Complex, Minnesota (2014-07-07).
- Sun, S. -s., & McDonough, W. F. 1989. Chemical and isotopic systematics of oceanic basalts: Implications for mantle composition and processes. *Geological Society, London, Special Publications*, **42**, 313–345. <https://doi.org/10.1144/GSL.SP.1989.042.01.19>
- Swanson-Hysell, N. L., Burgess, S. D., Maloof, A. C., & Bowring, S. A. 2014. Magmatic activity and plate motion during the latent stage of Midcontinent Rift development. *Geology*, **42**, 475–478. <https://doi.org/10.1130/G35271.1>
- Swanson-Hysell, N. L., Hoaglund, S. A., Crowley, J. L., Schmitz, M. D., Zhang, Y., & Miller, J. D. 2021. Rapid emplacement of massive Duluth Complex intrusions within the North American Midcontinent Rift. *Geology*, **49**, 185–189. <https://doi.org/10.1130/G47873.1>
- Swanson-Hysell, N. L., Ramezani, J., Fairchild, L. M., & Rose, I. R. 2019. Failed rifting and fast drifting: Midcontinent Rift development, Laurentia's rapid motion and the driver of Grenvillian orogenesis. *GSA Bulletin*, **131**, 913–940. <https://doi.org/10.1130/B31944.1>
- Szymanowski, D., Wotzlaw, J.-F., Ellis, B. S., Bachmann, O., Guillong, M., & von Quadt, A. 2017. Protracted near-solidus storage and pre-eruptive rejuvenation of large magma reservoirs. *Nature Geoscience*, **10**, 777–782.
- Thomas, M. D., & Teskey, D. J. 1994. An interpretation of gravity anomalies over the Midcontinent Rift, Lake Superior, constrained by GLIMPCE seismic and aeromagnetic data. *Canadian Journal of Earth Sciences*, **31**, 682–697. <https://doi.org/10.1139/e94-061>
- Vervoort, J. D., Wirth, K., Kennedy, B., Sandland, T., & Harpp, K. S. 2007. The magmatic evolution of the Midcontinent rift: New geochronologic and geochemical evidence from felsic magmatism. *Precambrian Research*, **157**, 235–268. <https://doi.org/10.1016/j.precamres.2007.02.019>
- White, R., & McKenzie, D. 1989. Magmatism at rift zones: The generation of volcanic continental margins and flood basalts. *Journal of Geophysical Research: Solid Earth*, **94**, 7685–7729.
- Zartman, R. E., Nicholson, S. W., Cannon, W. F., & Morey, G. B. 1997. U – Th – Pb zircon ages of some Keweenawan Supergroup rocks from the south shore of Lake Superior. *Canadian Journal of Earth Sciences*, **34**, 549–561. <https://doi.org/10.1139/e17-044>

5. CONCLUSION AND SYNTHESIS

The three preceding chapters of this dissertation propose mechanisms for the creation and evolution of magmas in variable tectonic and magmatic settings. These mechanisms are all united by the framework of that every one of them occurs within a column of liquid magma and crystalline mush that extends from the mantle, through the crust in a series of dikes and sills, and to the eruptive vent at the surface. This column is called a transcrustal magmatic system. A schematic diagram of one of these vertically extensive magmatic systems is shown in Figure 1.1.

In each chapter, the physical extent of the transcrustal magmatic system is varied. In chapter two, the findings indicate that the magmatic system at Ohakune is focused primarily in the middle to lower crust. At Ohakune, fractional crystallization and magma mixing dominate while assimilation is not yet an important process. The minerals erupted at Ohakune are all mafic and record high pressures. This contrasts with the proximal stratovolcano Ruapehu which erupts a greater proportion of felsic minerals (feldspars) and mafic minerals that are overall poorer in MgO. This indicates Ruapehu has a more vertically extensive magmatic plumbing system that is spread throughout the crust, rather than being focused deep. There is also evidence that the Ruapehu magmatic system was at one time analogous to that of Ohakune, suggesting there may be an evolutionary trajectory in transcrustal magmatic systems with repeated and sustained intrusion of melts.

The magmatic plumbing system investigated in chapter four in the Porcupine Mountains, although found in a rift setting rather than a subduction zone like Ohakune, represents a much larger, longer lived, and massive version of a transcrustal magmatic system. While modern Ruapehu has been active for on the order of 300ka (Tost et al., 2016), geochronological constraints

on the Portage Lake volcanics indicate that the Main Stage of the Mid-Continent Rift (e.g. Swanson-Hysell et al., 2021) was active for an order of magnitude longer. The difference in age between the Copper City and Greenstone flows in the PLV stratigraphy is 1-2 million years. Indeed, the Duluth Complex in northern Minnesota can be thought of as a gigantic relict transcrustal magmatic system that stretches 225 km along the coastline of Lake Superior and was at least 11 km thick (Miller Jr. et al., 2002). The Portage Lake Volcanics and Lake Shore Traps in the Keweenaw peninsula were fed by a similar magmatic system. The results of the study in chapter four constrain the pressure and temperature of the active part of the transcrustal magmatic system to 4 kbar and $\sim 1160^{\circ}$ C. They also show extensive magma mixing, crystallization, and extensive anatexis of the surrounding continental crust. This shows that transcrustal magmatic systems, while variable on spatial scales, have commonalities in their structure and the processes ongoing within them. However, the relative contributions of each process (mixing, crystallization, and assimilation) vary with time and spatial scales.

Chapter three focused less on the crustal dynamics of a magmatic system and focused more on the mantle melting region. Indeed, with some magmatic episodes in Patagonia represented by only one flow, the crustal portion of the transcrustal magmatic system there was likely almost nonexistent. Where Ohakune was a juvenile system, Ruapehu was more mature, and the Porcupine Mountains volcanic complex was extremely progressed, the Patagonian system was likely an infant by comparison. However, the mantle is an important part of the transcrustal system as this is where the melts originate. The results of the study in chapter three indicate that pyroxene-rich lithologies within the mantle (pyroxenite) are responsible for the small-volume magmas found in Patagonia. However, transcrustal magmatic systems likely develop progressively; these first pulses of magma may be what begin the preconditioning of the crust to develop into advanced magmatic

systems like those detailed in the other two chapters of this dissertation. Furthermore, these melting pyroxenites may serve to metasomatize the surrounding and overlying mantle and make them more likely to melt in the future. The early stages of magmatism may thus precondition not only the crust but the mantle to sustain large and long-lived transcrustal magmatic systems.

The methods and findings in this dissertation can be applied to future investigations of magmatic systems. These future investigations may be geochemical or geophysical in nature. The conceptual framework of a transcrustal magmatic system as a mantle melting region connected to a series of dikes and sills in the crust where magmas evolve and then erupt at a vent on the surface provides a physical model to unite observations and interpretations of volcanism at all sites and scales.

BIBLIOGRAPHY

BIBLIOGRAPHY

- Miller Jr, J. D., Green, J. C., Severson, M. J., Chandler, V. W., Hauck, S. A., Peterson, D. M., & Wahl, T. E. 2002. *RI-58 Geology and mineral potential of the Duluth Complex and related rocks of northeastern Minnesota*.
- Swanson-Hysell, N. L., Hoaglund, S. A., Crowley, J. L., Schmitz, M. D., Zhang, Y., & Miller, J. D. 2021. Rapid emplacement of massive Duluth Complex intrusions within the North American Midcontinent Rift. *Geology*, **49**, 185–189. <https://doi.org/10.1130/G47873.1>
- Tost, M., Price, R.C., Cronin, S.J. and Smith, I.E.M. 2016. New insights into the evolution of the magmatic system of a composite andesite volcano revealed by clasts from distal mass-flow deposits: Ruapehu volcano, New Zealand. *Bulletin of Volcanology*, **78**, 38, <https://doi.org/10.1007/s00445-016-1030-7>